Projecting long-term past and future climate change within the context of post-closure performance assessments for disposal of radioactive waste

Natalie S Lord

A dissertation submitted to the University of Bristol in accordance with the requirements for award of the degree of Doctor of Philosophy in the Faculty of Science.

School of Geographical Sciences, September 2017.

Word count: 64,000

Abstract

Multi-millennial transient simulations of climate changes have various important applications, such as for investigating key past geologic events for which high resolution proxy data are available, or for projecting the long-term impacts of future climate evolution on the performance of geological repositories for radioactive waste disposal. However, due to the high computational requirements of current General Circulation Models (GCMs), long-term simulations can generally only be performed with less complex models and/or at lower spatial resolution. In this thesis, two tools are developed which can be used to rapidly project long-term (>1000 years) changes in climate and one of its primary forcings – atmospheric CO_2 concentration.

A multi-exponential analysis is performed on a series of atmospheric CO_2 decay curves predicted by an Earth system model, producing an empirical response function that can rapidly project the long-term response of atmospheric CO_2 to any plausible cumulative CO_2 release. With increasing total emissions, the buffering and CO_2 uptake by the ocean on anthropogenic timescales is found to progressively saturate, whilst CO_2 uptake due to carbonate weathering processes progressively increases in importance to compensate. In contrast, the uptake timescale and relative importance of the silicate feedback is almost unchanged.

Long-term "continuous" projections of climate evolution are then produced using a statistical emulator calibrated using GCM simulations with varying orbital configurations and atmospheric CO_2 concentrations. The emulator is applied to model climate in the late Pliocene and over the next 1 million years. For both periods, emulated climate varies on an approximately precessional timescale, with evidence of increased obliquity response at times. Uncertainties include the emulator's inability to represent true transient changes in the climate system, and its limited range of fixed ice sheet configurations. The climate data produced is suitable for use in modelling performed for a post-closure safety assessment for a radioactive waste repository.

Acknowledgements

First and foremost, I would like to acknowledge the RWM and NDA for funding this project, along with AMEC Foster Wheeler, who undertook the project on behalf of RWM via a framework contract, and Quintessa Limited, who provided support to AMEC Foster Wheeler. I would also like to acknowledge the University of Bristol for hosting the project.

I am hugely grateful to my three supervisors, Dan Lunt, Andy Ridgwell, and Mike Thorne, and have found our meetings and discussions to be enjoyable, stimulating, and useful. Thanks to Dan for his enthusiasm, encouragement and advice in our weekly meetings. Thanks to Andy for his guidance and support, as well as for providing such an enjoyable setting for our weekly meetings, surrounded by My Little Pony figures. And finally, thanks to Mike for patiently providing me with a thorough background of the history of, and issues associated with, radioactive waste disposal, along with his support and advice. I am also grateful to all for allowing me to attend several international conferences and meetings, which have been an invaluable and fun experience.

My sincere thanks to Michel Crucifix, for allowing me to use his GP emulator package. Thanks also for taking the time to provide me with training and instruction in its application, advice on the interpretation of its results, and for replying to my many emails containing queries. I have very much enjoyed our collaboration.

I would like to thank my Progress Panel, Penny Johnes, Sandra Arndt, and Tony Payne, who provided different perspectives of the project, along with helpful discussions and advice. Thanks also to Greg Tourte and the UM Users group for answering my computing queries and providing support with any issues. Thank you to Alex Farnsworth and Emma Stone for their help with changing the Greenland and Antarctic ice sheet configurations in HadCM3. My thanks also to Nabila Bounceur, for providing advice and answering my queries about the use of emulators.

I would also like to thank Working Group 6 of the MODARIA research project, for several enjoyable meetings in Vienna and elsewhere containing useful discussions about the disposal of radioactive wastes and the long-term environmental changes that are relevant to it.

And finally, a huge thank you to my family and friends. Your support, encouragement, and understanding has been invaluable, and I am truly grateful.

Author’s declaration

I declare that the work in this dissertation was carried out in accordance with the requirements of the University's *Regulations and Code of Practice for Research Degree Programmes* and that it has not been submitted for any other academic award. Except where indicated by specific reference in the text, the work is the candidate's own work. Work done in collaboration with, or with the assistance of, others, is indicated as such. Any views expressed in the dissertation are those of the author.

SIGNED: ..... DATE:.....

Contents

List of Figures

List of Tables

Abbreviations

Chemical symbols

ALK	alkalinity
C	carbon
Ca	calcium
Ca^{2+}	calcium ion
$CaCO_3$	calcium carbonate
$CaSiO_3$	calcium silicate
CH_4	methane
CO_2	carbon dioxide
CO_3^{2-}	carbonate ion
$\delta^{11}B$	isotopic composition of boron
$\delta^{18}O$	isotopic composition of oxygen
DIC	dissolved inorganic carbon
H_2O	water
HCO_3^-	bicarbonate ion
Mg	magnesium
pCO_2	partial pressure of CO_2
PO_4	phosphate
SiO_2	silicate

Mathematical symbols

ϖ	longitude of perihelion
ε	obliquity
e	eccentricity
cos	cosine
sin	sine
δ	correlation length scales for emulator
v	nugget for emulator

General

^{O}C	degrees Celsius
^{O}N / ^{O}S / ^{O}E / ^{O}W	degrees North / South / East / West
ΔT	change in temperature
~	approximately
AIC	Akaike Information Criterion

AIS	Antarctic ice sheet
AMOC	Atlantic meridional overturning circulation
AOGCM	atmosphere-ocean general circulation model
AP	after present
AR5	IPCC Fifth Assessment Report
BEIS	Department for Business, Energy and Industrial Strategy
BGL	below ground level
BIOCLIM	Modelling Sequential Biosphere Systems under Climate Change for Radioactive Waste Disposal
BP	before present
CE	Common Era
cGENIE	cGENIE Earth system model (EMIC)
CMIP5	Coupled Model Intercomparison Project Phase 5
DJF	December-January-February (winter)
DOE	U.S. Department of Energy
EAIS	East Antarctic ice sheet
EIS	Environmental Impact Statement
EMBM	Energy-Moisture Balance atmosphere
EMIC	Earth system model of intermediate complexity
ENSO	El Niño Southern Oscillation
ESM	Earth system model
GBq	gigabecquerels
GCM	general circulation model
GDF	Geological Disposal Facility
GHG	greenhouse gas
GrIS	Greenland ice sheet
GP	Gaussian Process
HadCM3	Hadley Centre coupled Model (GCM)
HadISST	Hadley Centre sea-ice and sea surface temperature data set
HLW	High Level Waste
IAEA	International Atomic Energy Agency
ICRP	International Commission on Radiological Protection
ILW	Intermediate Level Waste
IODP	Integrated Ocean Drilling Program
IPCC	Intergovernmental Panel on Climate Change
JJA	June-July-August (summer)
kg m^{-2}	kilograms per square metre
kyr	thousand years
LHC	Latin hypercube
LLW	Low Level Waste
LLWR	Low Level Waste Repository

m	metre
mm day^{-1}	millimetres per day
mol yr^{-1}	moles per year
MOC	Meridional Ocean Circulation
MODARIA	MOdelling and DAta for Radiological Impact Assessments
MOSES2.1	Met Office Surface Exchange Scheme (land surface)
Myr	million years
NAO	North Atlantic Oscillation
NADW	North Atlantic Deep Water
NDA	Nuclear Decommissioning Authority
NH	Northern Hemisphere
NRC	U.S. Nuclear Regulatory Commission
ODP	Ocean Drilling Program
PC	principal component
PCA	principal component analysis
PCPA	post-closure performance assessment
PETM	Paleocene-Eocene Thermal Maximum
Pg C	petagrams of carbon
ppmv	parts per million by volume
R^2	R-squared
RCM	Regional Climate Model
RCP	Representative Concentration Pathway
RMSE	root mean squared error
SAT	surface air temperature
sd	standard deviation
SNF	spent nuclear fuel
SST	sea surface temperature
SVD	singular value decomposition
TBq	terabecquerels
Tmol yr^{-1}	teramoles per year
TOA	top of atmosphere
TRIFFID	Top-down Representation of Interactive Foliage and Flora Including Dynamics (dynamic vegetation model)
UNSCEAR	United Nations Scientific Committee on the Effects of Atomic Radiation
VLLW	Very Low Level Waste
W m^{-2}	Watts per square metre
W m^{-2} °C^{-1}	Watts per square metre per degree Celsius
WAIS	West Antarctic ice sheet
WG6	Working Group 6 (MODARIA)
wt%	weight percent
yr	years

CHAPTER 1

Introduction

Over time, the Earth's climate can undergo significant changes. These changes can occur at different spatial scales, with global, regional and/or local variations, as well as at different temporal scales, on timescales of seconds up to millions of years or more. It is known from palaeo data, which can be interpreted as a proxy for climate, that global climate in the past experienced large variations, ranging from hypothesised "Snowball Earth" conditions in the late Neoproterozoic (>650 million years (Myr) Before Present (BP)) when extreme glaciations may have covered the majority of the Earth's surface with ice, to the "hyperthermal" interval that occurred during the Paleocene-Eocene Thermal Maximum (PETM; ~55 Myr BP), to the glacial-interglacial cycles that are associated with the waxing and waning of ice sheets in the Northern Hemisphere, and that have been a dominant feature of the Earth's climate system over the past several million years. Climate in the future will also undergo changes, driven by the natural forcings that have driven climate changes in the past, but also by the increasing atmospheric concentrations of carbon dioxide (CO_2) that are a result of anthropogenic activities.

Research into future changes in climate often focuses on shorter timescales that are deemed to be immediately relevant to society, typically changes occurring over years to hundreds of years up to several millennia (IPCC, 2013). However, projections of future climatic changes occurring on relatively long timescales, of tens of thousands of years or more, also have a number of applications, one of the primary ones being to the long-term disposal of radioactive

wastes. The extended timescales involved in the decay of radioactivity in these wastes to safe levels means that disposal facilities must continue to function effectively long into the future. It is, therefore, essential to consider the potential impacts of long-term climate evolution and associated landscape change on a proposed waste repository.

This thesis proposes a framework for how long-term climate change can be addressed in the context of radioactive waste disposal, and develops several tools based on climate models of different complexities. These tools can be used to project the possible long-term evolution of both past and future climates, as will be demonstrated. It also includes an illustrative case study, in which the proposed methodology is applied to the potential site of a radioactive waste repository.

In this introductory chapter, background information about the disposal of radioactive wastes is given, along with a description of the forcings associated with long-term climate change, and a review of previous studies that modelled future climate evolution. Finally, the aims of the thesis are outlined, and the framework for addressing climate change in the context of radioactive waste disposal is presented.

1.1 Disposal of radioactive waste

In this section, background information about radioactive waste is provided (Sections 1.1.1 and 1.1.2), along with an explanation of why long-term climate change is relevant to its disposal (Section 1.1.3).

1.1.1 Radioactive waste

Radioactive waste is defined as material that is of no further use, and that contains levels of radioactivity that are above a certain level, as defined by legislation (e.g. Radioactive Substances Act, 1993). It is produced from a range of sources, including medical, industrial, research, and defence activities, as well as during nuclear energy production. Waste comes in a huge range of forms and quantities, depending on the source and site of its production. It is organised into four main categories in the UK, defined by the level of radioactivity the waste contains and the amount of heat that this radioactivity produces. These categories are:

- High Level Waste (HLW), which may also include Spent Nuclear Fuel (SNF)

- Intermediate Level Waste (ILW)
- Low Level Waste (LLW)
- Very Low Level Waste (VLLW)

In the UK, the Nuclear Decommissioning Authority (NDA), a non-departmental public body reporting to the Department for Business, Energy and Industrial Strategy (BEIS), is responsible for the long-term management of radioactive waste. This includes responsibility for the decommissioning and clean-up of nuclear facilities, the safe management of all waste products (both radioactive and non-radioactive), and the implementation of policy on the long-term management of waste. It releases an inventory of radioactive waste and nuclear materials in the UK every 3 years. Information from the latest inventory (NDA, 2016) is presented in Table 1.1, including the definition for each category of waste, and the projected inventory in 2125 CE (Common Era). Of the total volume of waste, approximately 96% has already been produced, mostly making up existing nuclear facilities (e.g. reactors, reprocessing plants, etc) which will be decommissioned and cleaned up when they reach the end of their operating lifetime within the next ~100 years. The remaining 4% will be produced in the future from planned operations. As can be seen from Table 1.1, the majority of the radioactive waste inventory is made up of VLLW and LLW (>90%), with less than 0.03% comprising HLW. However, HLW contains more than 95% of the radioactivity in all radioactive waste, at 3,200,000 terabecquerels (TBq) in 2150 CE (NDA, 2016).

Radioactivity can be highly hazardous to all forms of life, since ionizing radiation has enough energy to cause chemical changes in cells which damages them. This damage may be temporary or permanent, and may result in the cell dying or becoming abnormal. It can also lead to cancer, due to the DNA in cells being damaged and misrepaired. Ultimately, the amount and type of ionizing radiation and the length of exposure will determine the extent and severity of damage, which will also be affected by the type of exposure, i.e. external or internal. External exposure occurs when the radioactive source is outside the organism which is exposed to it, such as an airline passenger exposed to cosmic radiation or a worker at a nuclear power plant being exposed to activated components during maintenance work. Internal exposure occurs when the source of radiation enters the organism, through inhalation, ingestion or injection, via wounds or across the intact skin (as occurs with tritium). A summary of the sources and effects of ionizing radiation can be found in various reports from the International Commission on Radiological Protection (ICRP) and the UN Scientific Committee on the Effects of Atomic Radiation (UNSCEAR), including ICRP (2007) and UNSCEAR (2000). As a result of the dangers associated with radiation,

Table 1.1. Types of nuclear waste, including their definition, examples of wastes, and total packaged volume forecast up to 2125 CE after waste packaging (m^3). Source: Taken from NDA (2016).

Type	Definition (NDA, 2016)	Examples	Total volume in 2125 (m^3)
HLW	Wastes in which the temperature may rise significantly as a result of their radioactivity, so this factor has to be taken into account in the design of storage or disposal facilities	SNF, and the residue produced during reprocessing of SNF	1,500
ILW	Wastes exceeding the upper boundaries for LLW, but which do not require heating to be taken into account in the design of storage or disposal facilities	Redundant nuclear fuel casing, core components, and graphite blocks from nuclear reactors	449,000
LLW	Wastes containing radioactivity not exceeding 4 gigabecquerels (GBq) per tonne of alpha activity, or 12 GBq per tonne of beta/gamma activity	Items and materials associated with the daily operation of nuclear facilities, including protective equipment, plant items, ion-exchange resins, and sludges	1,600,000
VLLW	A sub-category of LLW, comprising wastes that can be disposed of with municipal commercial or industrial waste, or can be disposed of in specified landfill sites	Items and materials from hospitals and universities, structural building materials, and excavated soils produced during decommissioning of nuclear facilities	2,720,000

radiative waste is regulated by governments, who follow the guidance of international organisations such as the ICRP, the International Atomic Energy Agency (IAEA) and the UNSCEAR, and its management is carefully controlled in order to protect human health and the environment.

The total radioactivity (expressed as nuclear decays per second and measured in Bequerels, Bq, s^{-1}) of a radioactive isotope reduces over time, as the unstable atomic nuclei emit radiation in the form of particles, such as alpha (helium nuclei), beta (electrons and positrons) or gamma (photons) (it is these emitted particles that result in damage to cells). This process causes the nucleus to lose energy, thus transitioning to a stable isotope in one or more steps. The expected decay rate of a radionuclide is described by its half-life, which is a measure of the time taken for half of its radioactive atoms to decay. The half-lives of different radionuclides vary greatly, ranging from seconds or shorter (e.g. oxygen-22 – 2.25 seconds) up to a million years or longer (e.g. caesium-135 – 2.3 Myr). The total radioactivity, type of radioactivity, half-life, and biological and environmental factors, play a role in determining the level of risk that the waste poses to humans, non-human biota, and the environment.

1.1.2 Long-term disposal

At present, radioactive waste in the UK is managed in a number of ways and at various locations, as illustrated in Figure 1.1. Re-use and recycling of VLLW and LLW materials is carried out where possible, in order to reduce the total amount of waste that is to be disposed. LLW that is not suitable for recycling is disposed of in the national Low Level Waste Repository (LLWR) in Cumbria, England, a near-surface facility in which ~1 million cubic metres of LLW has been deposited since 1959 (NDA, 2010). A new shallow LLW repository has also been constructed near to the Dounreay site in Caithness, Scotland, which began receiving waste in 2015.

For ILW, a final disposal solution has not yet been decided in the UK. As a result, waste is generally currently stored in treated or untreated form in a variety of containers (e.g. tanks, vaults, silos, and drums) at nuclear sites. If necessary, it may also be transferred and stored off-site. Several other countries have adopted geological disposal for the long-term disposal of ILW. An example of such a facility is the SFR facility in Forsmark, Sweden, which is a repository for LLW and ILW constructed ~50 m below the Baltic Sea. Geological disposal is discussed in more detail below.

The UK's (excluding Scotland) and many other countries' preferred final disposal solution for SNF and HLW (and in some cases ILW) is deep geological disposal. This involves building a

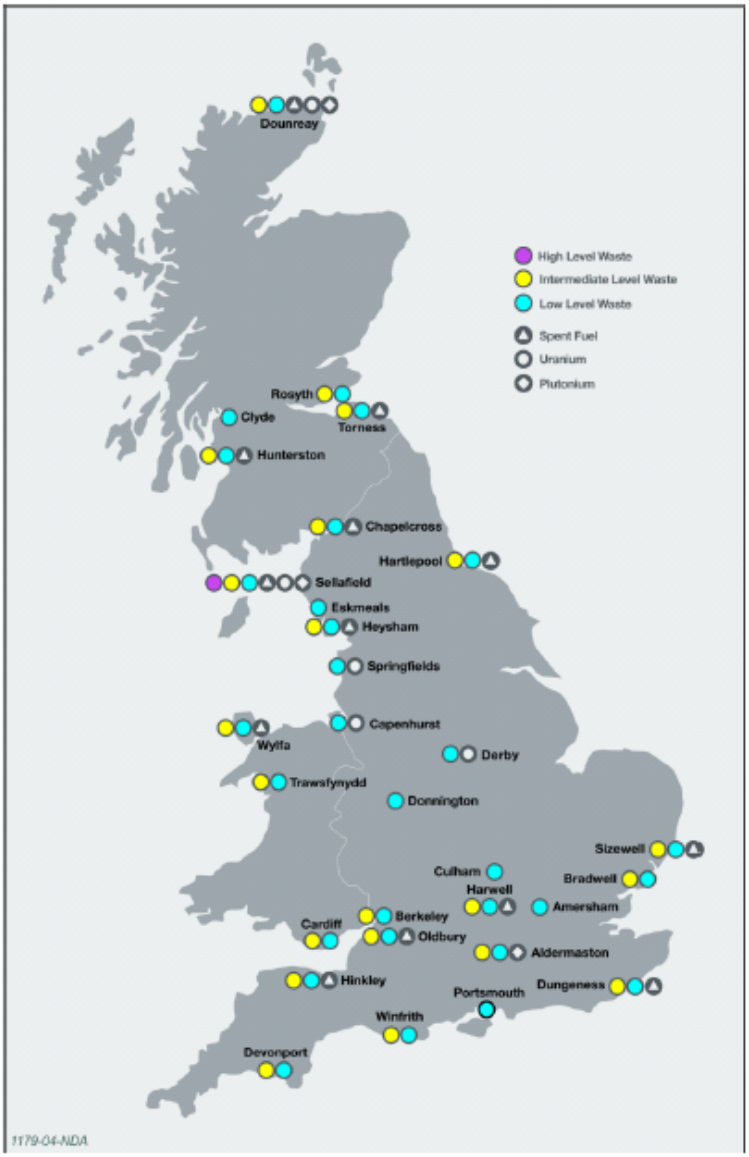

Figure 1.1. Sites where radioactive waste and materials are currently stored. Source: Taken from DECC (2014) (p. 16).

highly-engineered Geological Disposal Facility (GDF) deep underground, generally between 200 and 1000 m below ground level (BGL). An illustrative example of such a facility is shown in Figure 1.2. GDFs are designed and constructed such that they provide a multi-barrier system, which aims to keep the waste and its radioactivity contained and isolated for long periods of time to minimise and slow radionuclide release and therefore potential damage to the environment. Figure 1.3 shows a schematic of such a multi-barrier system as used for ILW and HLW, and the barriers may typically include (NDA, 2010):

- The form of the waste: i.e. a stable, solid form.
- The waste container: provides a physical barrier around the waste and is designed to keep the waste contained for 1000 years or longer, e.g. in a copper canister.

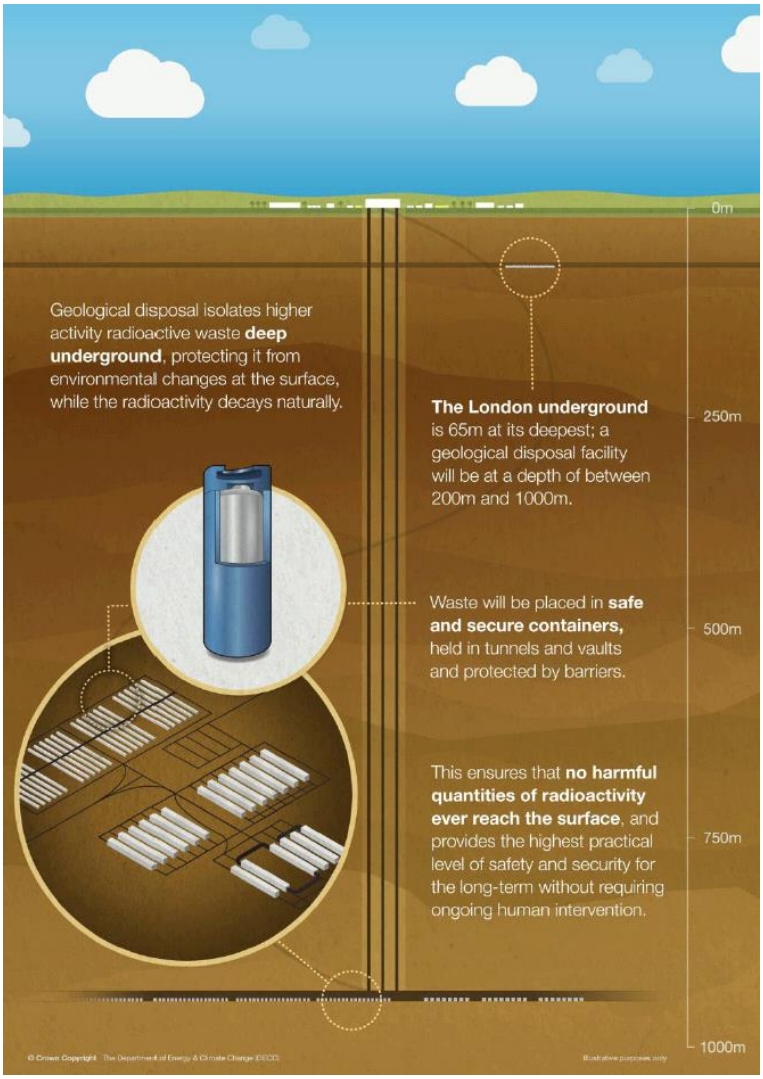

Figure 1.2. Illustrative schematic of a geological disposal facility. Source: Taken from DECC (2014) (p. 23).

- The buffer or backfill: the material placed immediately around the waste aims to act as a physical barrier to limit water movement, and/or provide a chemical barrier, e.g. cement to provide a high pH environment that ensures low solubility and a high degree of sorption for many radionuclides.
- Mass backfill and sealing systems: used to fill and seal excavated access tunnels and shafts, aiming to control the movement of water to repository depth.
- Geological barrier: comprises the host rock that the facility is constructed in, as well as the surrounding rocks. It aims to provide the long-term containment and isolation of the waste, whilst also protecting the engineered barriers. Therefore, it should ideally be geologically stable with low seismicity and low levels of groundwater inflow.

As with a repository for ILW, no such facility yet exists in the UK. However, there are proposals for the construction of deep GDFs for HLW and SNF both in Olkiluoto, Finland and in

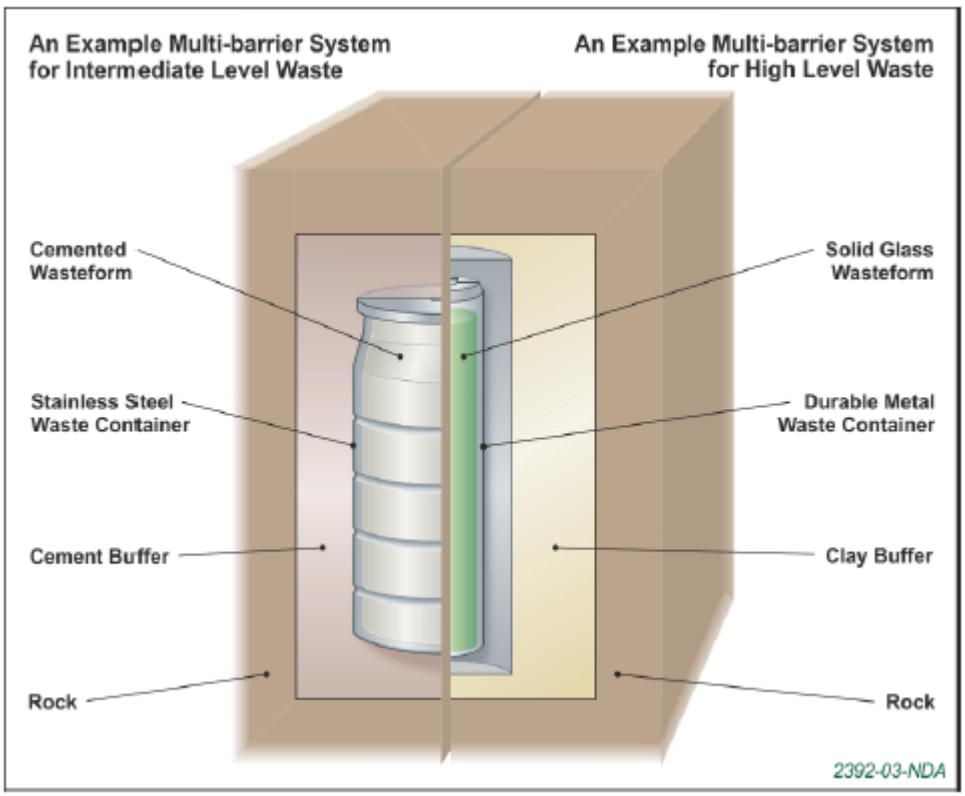

Figure 1.3. Schematic of a multi-barrier system. Source: Taken from DECC (2014) (p. 19).

Forsmark, Sweden. As mentioned previously, the Forsmark site already hosts the SFR repository for LLW and ILW, and the proposed KBS-3 type facility for SNF and HLW will be located 400-500 m BGL in a granitic type of host rock. The planned facility at Olkiluoto is also a KBS-3 type and, if approved, will be located at a depth of 400-450 m BGL in crystalline bedrock. The US has also selected a site for the proposed first US repository for spent nuclear fuel and high-level waste, in Yucca Mountain, Nevada. If approved, the Yucca Mountain facility will be constructed approximately 300 m BGL in a flat-topped ridge comprised of volcanic tuff.

1.1.3 The relevance of long-term climate change

The significant timescales involved in the decay to safe levels of radionuclides incorporated in radioactive wastes means that GDFs must continue to function effectively for long timescales. For repositories containing LLW and ILW, such as the UK's LLWR facility (LLWR, 2011), this operating lifetime is up to 100 kyr (thousand years). For HLW and SNF, repositories such as the proposed KBS-3 facility at Forsmark in Sweden (SKB, 2011) must remain functional for up to 1 Myr. Over such long timescales, both global and regional climate will undergo significant changes, which may have significant impacts on the functioning of the facility. It is,

therefore essential to consider long-term climate evolution and associated landscape change in post-closure performance assessments (PCPAs) in order to evaluate a geological disposal system's response to and robustness against a variety of potential environmental changes, driven by both natural (e.g. orbital variations) and anthropogenic (e.g. emissions from combustion of fossil fuels, land-use change and cement production) forcings.

In order to identify what climate changes may be of relevance to different waste repositories and how they might be impacted by these changes, facilities can be categorised based on various criteria, as shown in Figure 1.4 taken from the final report of MODARIA Working Group 6 (2016). These categories include the mode of construction, the geological context, the hydrogeological context, the coastal context and the potential for extreme climates.

For repositories in glaciated environments for example, the environmental change that is likely to have the most significant impact is the passage of an ice sheet margin across the site (Becker et al., 2014). Whether the accompanying changes in the hydrological regime are likely to have a large impact can be inferred from the hydrogeological and geological context, whilst the mode of construction will give an indication of how vulnerable the facility is to surface denudation and permafrost formation. For HLW repositories, the timing and severity of the glaciation may be of particular importance, as this will determine the remaining radionuclide inventory that can be impacted by the altered hydrogeological conditions that occur during passage of the ice sheet. It will also determine the duration of the period of permafrost conditions prior to glaciation and, therefore, be a key factor in determining whether the permafrost develops to repository depth (SKB, 2011).

Thus, different repositories have different key timescales that need to be considered, based in part on the climate-change processes that are expected to have the most significant impact on the facility. In the case of the UK's LLWR for example, the coming centuries will be key as sea-level rise and the resultant coastal erosion are expected to affect the site on these timescales (Fish et al., 2010), whereas permafrost is projected to impact Sweden's SFR disposal facility on timescales of tens of millennia (SKB, 2014). In contrast, the key timescale for the proposed HLW and SNF repositories in Sweden and Finland is 100 kyr or longer (SKB, 2011, Kjellström et al., 2009, Pimenoff et al., 2011). In this context, the timing of the next glacial inception and amplitude of future glacial-interglacial cycles are key.

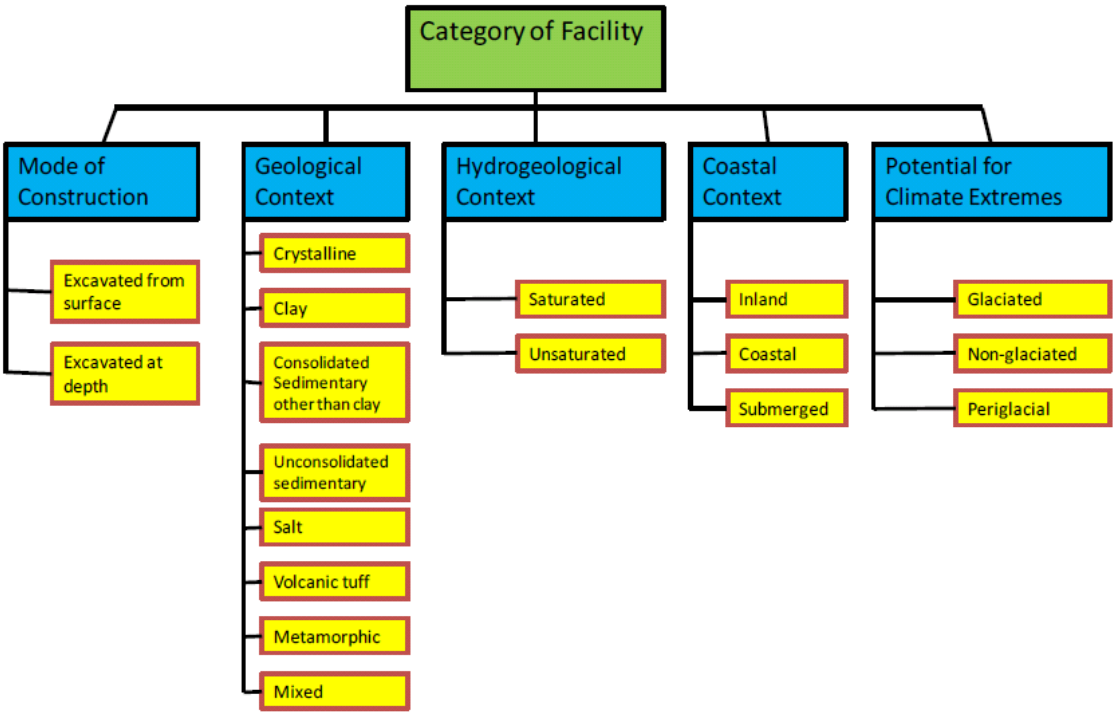

Figure 1.4. Categories of facilities. Source: Taken from Figure 2.1 (p. 25) of MODARIA Working Group 6 (2016).

1.2 Long-term climate change

The evolution of future climate is critical for the assessment of the safety of long-term storage of nuclear waste in geological repositories. However, in contrast to climates that occurred in the past, no observational data exist for the future; as such, scientists are reliant entirely on models for their predictions (or, more correctly, alternative projections under various assumptions, notably in respect to anthropogenic emissions of greenhouse gases). This necessitates a careful consideration of the uncertainties inherent in the projections, which encompass the evolution of atmospheric carbon dioxide concentrations on both short (10^1–10^2 years) and long (10^4–10^6 years) timescales in response to carbon cycle processes, and the climatic response to CO_2 and variations in Earth's orbital parameters. In this section, a summary of the main forcings and feedbacks affecting future climate change occurring on timescales of tens of thousands of years or more is provided (Sections 1.2.1 and 1.2.2).

1.2.1 Forcings of long-term future climate change

1.2.1.1 Orbital parameters

On timescales of up to 1 Myr, the primary external forcing of the Earth system is variation in incoming solar radiation at the top of the atmosphere. This variation results from changes in the Earth's astronomical parameters, which determine the seasonal and latitudinal distribution of incoming radiation. For example, Figure 1.5 (bottom panel) illustrates fluctuations in insolation at 60 degrees North (° N) in June for the last 1 Myr. The key astronomical parameters are eccentricity (the extent to which the orbit of the Earth around the sun is elliptical), obliquity (the angle of the axis of rotation relative to the plane of the orbit of the Earth around the Sun), and the precession (the timing of aphelion or perihelion relative to the vernal equinox). Due primarily to the gravitational effects of other bodies in the solar system, these three astronomical parameters vary on timescales of ~400 kyr and ~100 kyr (eccentricity), ~40 kyr (obliquity), and ~20 kyr (precession). Precession and obliquity modify the latitudinal and seasonal distribution of incoming radiation but do not affect the total global annual mean insolation. Eccentricity affects both the distribution of radiation and the total amount of radiation (albeit to a small degree), and also modulates the precession parameter.

For both the past and future, the development of the three orbital parameters (precession, obliquity and eccentricity) can be calculated with relatively little uncertainty for up to tens of millions of years (e.g. Laskar et al., 2004). For the next ~100 kyr, the eccentricity of the Earth's orbit will be relatively low, which will reduce the impact of precessional changes and will result in obliquity having a greater influence on climate (Ganopolski et al., 2016). Minima in June insolation at 65° N in the next 100 kyr occur at approximately 17, 54, 77 and 97 kyr After Present (AP), making glacial inception more likely around these times. However, as will be discussed later, increased radiative forcing due to higher atmospheric CO_2 concentrations may result in a delay in glacial inception for one glacial cycle or more.

1.2.1.2 Atmospheric CO_2

As a direct result of the astronomical forcing, Earth's climate has swung between glacial and interglacial states over at least the last 1 Myr (Figure 1.5; middle panel), despite the changes in orbital characteristics providing only a relatively weak forcing. The reason for the large response is likely due to positive feedbacks in the Earth system that amplify the eccentricity

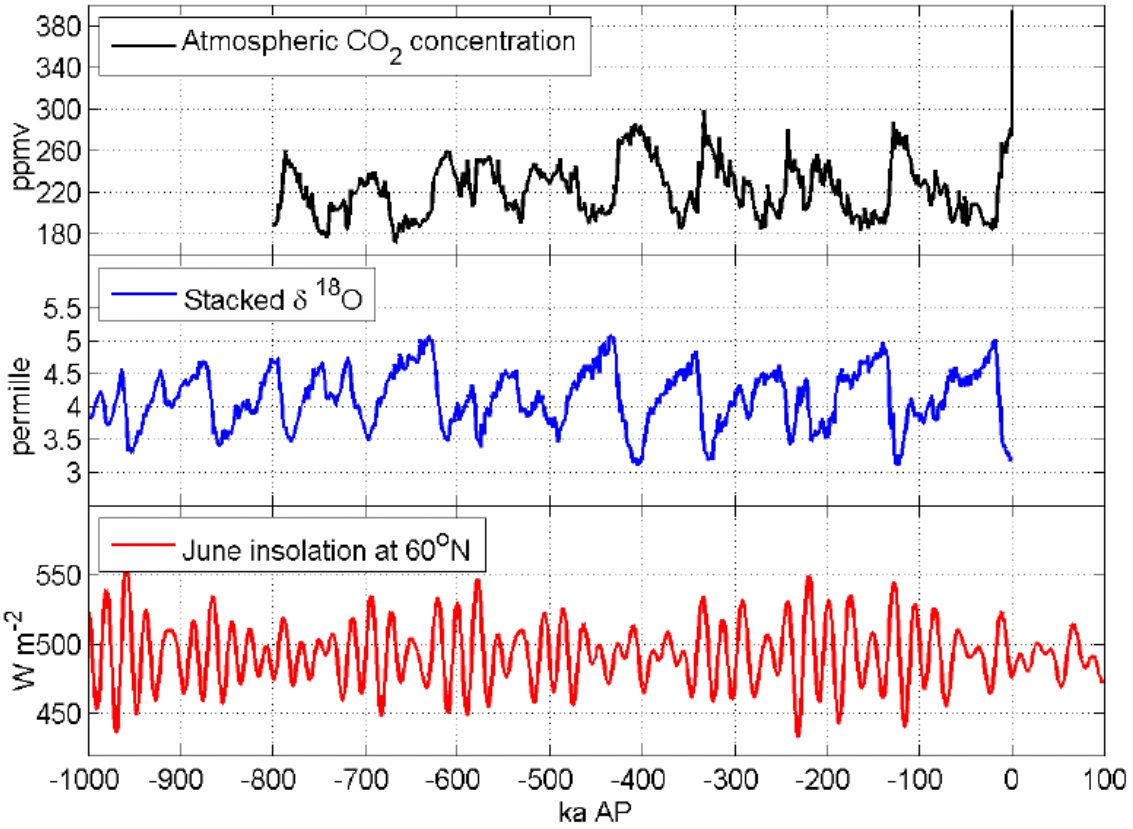

Figure 1.5. Top panel: CO_2 composite record for the last 1 Myr (Luthi et al., 2008), and the observed annual average atmospheric CO_2 concentration of 393.8 parts per million by volume (ppmv) in 2012 CE (www.esrl.noaa.gov). High values of CO_2 correspond to a warmer climate (interglacial state). Middle panel: Stack of 57 benthic $\delta^{18}O$ records for the last 1 Myr (Lisiecki and Raymo, 2005), which is used a proxy for global ice volume and temperature. High values of $\delta^{18}O$ correspond to a colder climate (glacial state). Bottom panel: June insolation at 60° N for the last 1 Myr and the next 100 kyr (Berger, 1978, Berger and Loutre, 1991). Source: Taken from Figure 3.1 (p. 34) of MODARIA Working Group 6 (2016).

forcing. The primary feedback is associated with the carbon cycle. Ice-core records indicate that glacial periods are associated with relatively low concentrations of CO_2 (Figure 1.5; top panel) and methane (CH_4). However, the mechanism by which CO_2 changes through glacial-interglacial cycles is currently uncertain. Likely contributing effects are physical processes such as temperature dependence of the solubility of CO_2 in the ocean, ocean circulation affecting the lifetime of CO_2 in the ocean, and biogeochemical processes associated with the biological pump, such as iron fertilisation in the Southern Ocean increasing during glacial episodes (See Figure 6.5 of Ciais et al., 2013). Feedbacks associated with the carbon cycle are so poorly understood that it is common practice to consider CO_2 changes in the past as a forcing on the climate system, rather than a feedback, and to impose CO_2 concentrations in long-term palaeoclimate simulations. Furthermore, anthropogenic emissions of CO_2 provide a genuine external climate forcing. Therefore, for the remainder of this thesis, CO_2 will be considered as a forcing on the climate system.

There is a significant amount of uncertainty relating to the future evolution of atmospheric CO_2 concentration. Firstly, it is not possible to know how anthropogenic CO_2 emissions will develop over the next few hundred years or longer in response to human activities, particularly combustion of fossil fuels, cement production and land use change. However, it is likely that, at least for the remaining part of the 21st century, CO_2 will continue to be released to the atmosphere, and thus the atmospheric CO_2 concentration will continue to increase (IPCC, 2013). CO_2 emissions scenarios are often developed for use in modelling studies, based on different assumptions about future socioeconomic developments that aim to cover the range of possible futures. For example, the Fifth Assessment Report (AR5) of the Intergovernmental Panel Climate Change (IPCC, 2013) uses four Representative Concentration Pathways (RCPs), which describe changes in radiative forcing over time, and have different year 2100 radiative forcing targets, of 2.6, 4.5, 6.0 and 8.5 Watts per square metre (W m^{-2}). These end-of-century targets roughly represent low (RCP2.6), medium (RCP4.5 and RCP6.0) and high (RCP8.5) levels of climate forcing, and extensions to the scenarios also exist that project emissions to 2300 CE.

Secondly, there is uncertainty about the atmospheric lifetime of emitted anthropogenic CO_2, related to how long it will remain in the atmosphere before it is removed by the natural carbon cycle, thus returning CO_2 concentrations back towards pre-industrial values. There is increasing evidence that a significant proportion will remain in the atmosphere for very long timescales, due to its removal over tens to hundreds of thousands of years by a range of carbon cycle processes (Archer et al., 1997, Archer and Ganopolski, 2005, Lenton and Britton, 2006, Ridgwell and Hargreaves, 2007). Transient simulations performed using Earth system Models of Intermediate Complexity (EMICs) containing representations of the long-term carbon cycle suggest that, even 10 kyr after CO_2 emissions have ceased, between 15 and 30% of emissions remain in the atmosphere following total cumulative emissions of approximately 200–5000 petagrams of carbon (Pg C; 1 Pg = 10^{15} g) (Eby et al., 2009). It is estimated that, neglecting natural carbon cycle variations, it may take up to 1 Myr or more for pre-industrial CO_2 values to be restored following an anthropogenic CO_2 perturbation (Lenton and Britton, 2006, Colbourn et al., 2015), with higher total emissions taking a greater amount of time to be removed. The long-term evolution of an atmospheric CO_2 perturbation is found to be dependent on the total emissions released, rather than the rate of release (Eby et al., 2009), hence the amount of CO_2 released over the coming centuries will affect the lifetime of the perturbation. Based on current emissions trends, CO_2 originating from anthropogenic activities is expected to act as a significant forcing on climate for the next few tens of thousands of years or longer, in combination with variations in the orbital parameters. Notwithstanding this, it is also important to consider

scenarios in which humanity carries out large-scale carbon-cycle geoengineering, in which anthropogenic CO_2 is effectively reduced to zero, and the system follows a "natural" trajectory as it would have in the absence of human industrialisation.

A third source of uncertainty is associated with natural variations in the carbon cycle. In the absence of anthropogenic emissions, atmospheric CO_2 concentrations have fluctuated over the past few million years, often demonstrating a strong correlation with temperature (Petit et al., 1999, Luthi et al., 2008). During the late Quaternary, atmospheric CO_2 has varied between ~180 and 280 ppmv on glacial-interglacial timescales, and it is expected that fluctuations will continue into the future, although of an unknown magnitude. For reference, pre-industrial concentrations of atmospheric CO_2 were ~280 ppmv, and current concentrations are ~400 ppmv.

1.2.1.3 Other forcings

Other external forcings include palaeogeographical (changes in topography and bathymetry due to plate tectonics) and solar luminosity changes, but these act on much longer timescales than 1 Myr and as such can be neglected (unless the period considered includes a significant change in ocean gateways, such as the closure of the Panama Seaway that occurred in the past). In addition, the 11-year sunspot cycle, and longer timescale luminosity changes, such as those associated with the Maunder Minimum, can also be neglected as they occur on timescales shorter than those of relevance here. A similar comment applies to volcanic forcing, although the possibility of a supervolcano occurring over the timescale of interest is non-zero.

1.2.2 Climate feedbacks

There are multiple feedbacks, both positive and negative, that mediate the climate system response to the orbital and CO_2 forcings.

As stated previously, over the last million years the Laurentide and Fennoscandian ice sheets (and the smaller Alpine, Himalayan and Patagonian glaciers) have fluctuated in synchrony with CO_2, and paced by astronomical forcings. The orbital pacing of ice sheets is still not well understood, but the essence of Milankovic theory is thought to be broadly correct. That is, that the insolation in Northern Hemisphere summer is critical for determining the state of the Earth system, as this governs the likelihood of snow surviving summer ablation in regions where there is sufficient continental area to build up a large ice sheet. Thus, periods of low summer insolation

in the Northern Hemisphere are generally associated with increasing ice volume. However, the system is highly non-linear and state dependent; for example, the Last Glacial Maximum, one of the periods of greatest ice volume in the last 2 Myr, had similar astronomical forcing to the present day. These ice sheets play an important role in the atmosphere and ocean systems. They affect the radiation balance due to their high albedo (relative to vegetation or bare soil), affect atmospheric circulation directly through generation of Rossby waves and due to their effect on temperature, affect precipitation due to their orography, and can also affect ocean properties and circulation through interaction with the atmosphere and through the input of fresh melt-water.

Ocean circulation changes also play a role in the Earth system and their effect is important both for regional and millennial-scale variability. Of particular importance are millennial scale variations in temperature, which are recorded in ice and sediment cores, in particular in the North Atlantic during the last glacial-interglacial cycle. Antarctic and Greenland ice-cores show a “bipolar seesaw”, whereby one pole warms as the other cools or remains at a steady temperature, before the pattern reverses (e.g. Broecker, 1998, Stenni et al., 2010). The mechanisms behind these events are not fully understood and are not captured by all model simulations (e.g. Smith and Gregory, 2012), but are likely linked to changes in ocean circulation and the strength of overturning in the North Atlantic (Wolff et al., 2009) associated with the inputs of freshwater associated with the decay of ice sheets.

Other processes such as changes in atmospheric dust and vegetation feedbacks likely played some role in shaping the exact nature of the glacial cycles. Dust is known to have varied over these timescales (Mahowald et al., 1999, Lambert et al., 2008) and could interact with the climate system through affecting the albedo of fresh snow (Warren, 1984), absorption and/or scattering of radiation in the atmosphere (Tegen, 2003), and ocean fertilisation (Jickells et al., 2005) for example. These processes may be very important, but their effect is much more uncertain than the effects of orbital and CO_2 changes.

1.3 Previous modelling of long-term future climate change

Many previous studies have addressed future climate change, based on various assumptions about future boundary conditions (e.g. CO_2 forcing, ice sheet extents) and using a range of modelling approaches. In this section, previous modelling studies that have attempted to project future climate evolution are reviewed, particularly those that model long timescales.

The review is divided into four categories, based on the length of time considered: the evolution of climate on the order of centuries (up to 2300 CE; Section 1.3.1), tens of thousands of years (up to 50 kyr; Section 1.3.2), 100 kyr (Section 1.3.3), and 1 Myr (Section 1.3.4) AP. These timescales are chosen in part due to their relevance to the disposal of nuclear wastes, and also because they generally require the use of different modelling techniques and/or focus on different features of the Earth system and climate.

In general, simulations up to 2300 CE have used state-of-the-art Earth System Models (ESMs) and General Circulation Models (GCMs) in the context of the IPCC. These models are the most complex of the range of available models, in terms of the processes and physics included, and have relatively high spatial and temporal resolutions. However, they are extremely computationally expensive and relatively slow, meaning they are more suited to running relatively short transient simulations of several hundred years to a few millennia. Simulations up to 50 kyr have focussed on CO_2-induced climate warming and ignored orbital forcings, whilst those simulations up to 100 kyr have focussed on the onset of the next glaciation. When modelling timescales of several millennia or longer, reduced complexity models are often employed, such as EMICs. These generally have lower resolutions and include more parameterizations, and consequently require significantly less computing power and time than GCMs, making it feasible to run long-term continuous simulations and large ensembles of simulations. Finally, simulations up to 1 Myr have used conceptual models to predict future glacial-interglacial cycles. These are highly simplified models based on a small number of parameters, and generally do not include any physical processes, which makes them very quick to run. Where GCMs have been applied to predict changes occurring on multi-millennial timescales or longer, “snapshot” simulations have been performed, representing specific future time-slices or climatic conditions.

As mentioned in the previous section, there are several uncertainties associated with future climate forcings, particularly relating to the future evolution of atmospheric CO_2 concentration. In addition to these, the responses of the Greenland and Antarctic ice sheets (GrIS, AIS) to changes in surface air temperature (SAT) and precipitation are also uncertain, as are the resulting impacts on climate, ocean circulation and global sea level. However, changes in sea level are beyond the scope of this work, and changes in SAT in response to increased melting of the ice sheets generally only occurs locally to these two ice sheets (Lunt et al., 2004, Toniazzo et al., 2004, Ridley et al., 2005) and thus is not likely to be relevant to any currently planned or proposed radioactive waste repositories.

As a result of these uncertainties, modelling studies must make a range of assumptions or empirical estimates about the future, which may include, but are not limited to, anthropogenic CO_2 emissions (total emissions and timescale of release), the timing and magnitude of natural CO_2 variations, the evolution of atmospheric CO_2 in response to anthropogenic and natural variations (in the absence of an interactive coupled carbon cycle model), and the response of the ice sheets to climate change (in the absence of an interactive coupled ice sheet model).

1.3.1 Evolution until 2300 CE

Changes in climate that occur on timescales of decades to several centuries are relevant to policy decisions, and hence have been addressed in detail in a wide range of studies. Therefore, only a brief description of the key findings is presented here; for a more detailed summary of current knowledge and understanding, please refer to the IPCC AR5 (IPCC, 2013).

Based on the Coupled Model Intercomparison Project Phase 5 (CMIP5; Taylor et al., 2012) climate projections, for which a range of state-of-the-art GCMs were forced using four RCP emissions scenarios, it was estimated that the global annual average surface air temperature for 2081–2100 will be higher than for the 1986–2005 reference period, by 0.3–1.7 degrees Celsius (°C; RCP2.6), 1.1–2.6°C (RCP4.5), 1.4–3.1°C (RCP6.0) and 2.6–4.8°C (RCP8.5) (IPCC, 2013), as illustrated in Figure 1.6. The range in predictions for each RCP scenario is a result of differences in the models used to make each prediction. At the end of the 21st century, globally averaged changes over land will be greater than changes over the ocean, and the greatest warming is projected to occur in the Arctic region, assuming that there is not a strong reduction in Atlantic Meridional Overturning Circulation (AMOC). A reduction in Northern Hemisphere snow cover and retreat of permafrost will occur over the course of the century, in response to increased global temperatures and changes in precipitation and ablation.

High latitude regions are projected to experience an increase in temperature and precipitation by almost all climate models (IPCC, 2013), which generally results in high latitude surface waters becoming less dense and hence more stable, potentially affecting the strength of the AMOC. SATs in Central Europe are very likely to continue to increase over the next hundred years, based on the results of the CMIP5 simulations (IPCC, 2013). Under the RCP4.5 scenario, annual mean temperatures in Europe and western North America are projected to have increased by 2–3.5°C and 2–3.4°C (25th–75th percentiles of model simulations) in 2081–2100 compared with the period 1986–2005, respectively. Annual mean precipitation increases

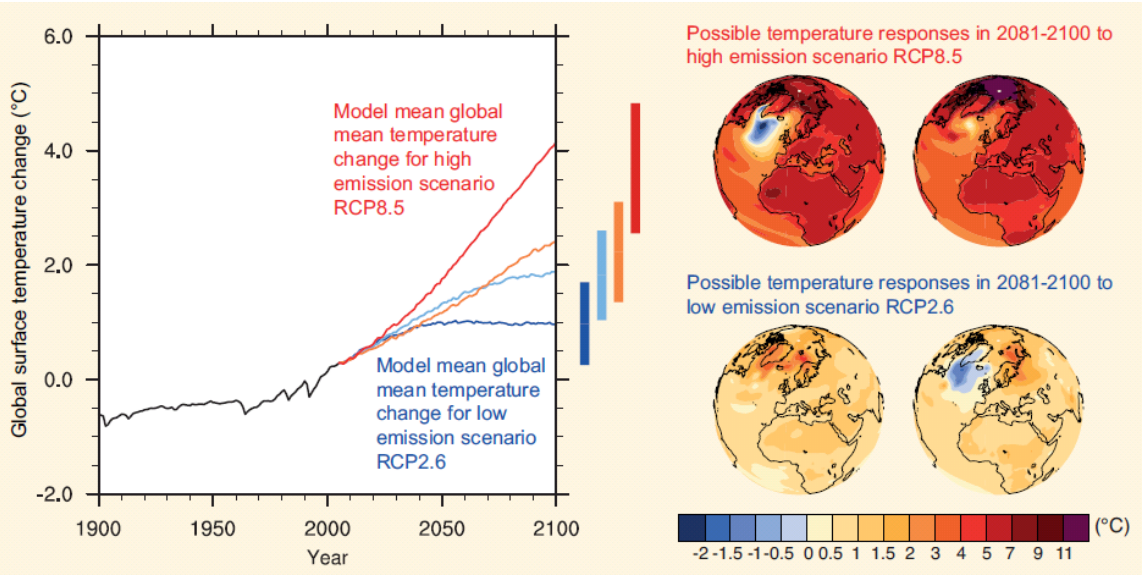

Figure 1.6. Change in global mean temperature averaged across all CMIP5 models (relative to 1986–2005) for the four RCP scenarios: RCP2.6 (dark blue), RCP4.5 (light blue), RCP6.0 (orange) and RCP8.5 (red) (left). Likely ranges for global temperature change by the end of the 21st century are indicated by vertical bars. Note that these ranges apply to the difference between two 20-year means, 2081–2100 relative to 1986–2005, which accounts for the bars being centred at a smaller value than the end point of the annual trajectories. For the highest (RCP8.5) and lowest (RCP2.6) scenario, illustrative maps of surface temperature change at the end of the 21st century (2081–2100 relative to 1986–2005) are shown for two CMIP5 models (right). These models are chosen to show a rather broad range of response, but this particular set is not representative of any measure of model response uncertainty. Source: Taken from Figure 1 of FAQ12.1 (p.1037) of Collins et al. (2013).

by 0–10% and 2–6% for the same period. The length, frequency, and/or intensity of warm spells or heat waves are also very likely to increase in these regions.

1.3.2 Evolution until 50 kyr AP

A consequence of the slow removal of excess atmospheric CO_2, combined with the slow response times of parts of the climate system, is that changes in global climate are projected to continue to occur long after anthropogenic CO_2 emissions have been reduced or have stopped entirely. In fact, the lag in the response of SAT to changes in radiative forcing caused by increasing atmospheric CO_2 means that, even if radiative forcing were stabilised, global SAT would only reach steady state after several centuries to millennia (IPCC, 2013). This means that a large proportion of the climate change that will occur over the next hundred years or so is unavoidable, unless net CO_2 emissions are strongly negative for a significant period of time (IPCC, 2013), such as through the development of carbon-neutral energy production accompanied by the removal from the atmosphere and long-term storage of excess CO_2 (carbon sequestration through geoengineering). Variations in emissions of other gases will further affect the global temperature response, with a termination of aerosol emissions likely to contribute to warming. Conversely, a

termination of emissions of greenhouse gases (GHG) with relatively short-lifetimes, such as methane (~10 years), nitrous oxide (~100 years) and hexofluoroethane (~10 kyr), will have a cooling effect.

For modelling timescales of tens of thousands of years, models of a lower complexity and/or resolution, such as EMICs, are often used in place of GCMs. This is because their relatively fast running time generally makes them more suitable for simulations that cover long periods of time, as well as for running larger ensembles of simulations. In terms of future climate forcings, it is likely that atmospheric CO_2 will act as a dominant influence for at least several tens of thousands of years, due to its relatively high concentration and slow uptake by some components of the carbon cycle (Shaffer et al., 2009, Ganopolski et al., 2016). Only when atmospheric CO_2 declines back towards pre-industrial values are orbital variations likely to become increasingly influential.

Various modelling studies have addressed the subject of climate change on multimillennial timescales of up to 50 kyr AP. These studies have generally focussed on the response of climate to anthropogenic emissions up to ~10 kyr AP, along with several studies which have investigated the longer-term impact of climate change on the Greenland ice sheet. In these studies, anthropogenic CO_2 is emitted to the atmosphere, either as an instantaneous pulse (Frolicher et al., 2014), or over decades to centuries, where emissions or the atmospheric CO_2 concentration are initially increased before they are either held constant (Huybrechts et al., 2011, Li et al., 2013) or reduced over various timescales (e.g. several hundred years) (Lenton, 2000, Lenton et al., 2006, Mikolajewicz et al., 2007, Solomon et al., 2009, Friedlingstein et al., 2011, National Research Council, 2011, Clark et al., 2016), or a combination of these approaches (Plattner et al., 2008, Vizcaino et al., 2008, Eby et al., 2009, Zickfeld et al., 2013). Many of the studies prescribe CO_2 emissions and use models that include a representation of the carbon cycle in order to predict atmospheric CO_2 concentrations, whereas others prescribe atmospheric CO_2 concentrations directly (Huybrechts et al., 2011, Li et al., 2013), or else use an empirical response function to project the evolution of atmospheric CO_2 following emissions (Charbit et al., 2008).

In the simulations, changes in climate occur long after CO_2 emissions have declined or been reduced to zero. Peak warming generally occurs several decades to millennia after the peak CO_2 concentration is reached (Eby et al., 2009, Friedlingstein et al., 2011, Frolicher et al., 2014), due to the slow response time of the oceans. The amount of warming that occurs in response to increased atmospheric CO_2 ultimately depends on the sensitivity of the climate to a doubling of CO_2, which is estimated [likely/highly likely] to be in the range 1.5°C to 4.5°C (IPCC, 2013). In the

simulations, the maximum warming ranges from 0.32°C to 10.8°C, depending on the CO_2 scenario and model used. Following the initial period of warming, global temperature then generally begins to slowly decline, excluding simulations where the atmospheric CO_2 concentration is held at a constant elevated value. Some studies demonstrate a temporary reversal of this cooling trend several hundreds to thousands of years into the simulation, which is attributed to changes in ocean processes (Vizcaino et al., 2008, Eby et al., 2009). After 10 kyr AP, Eby et al. (2009) find that 15–20% of the atmospheric CO_2 perturbation remains, whilst up to 75% of the maximum temperature anomaly persists, suggesting that the lifetime of warming may be significantly longer than that of excess atmospheric CO_2.

Increased global temperatures will have further impacts on other parts of the climate and Earth system, including changes in precipitation, storm events and sea level (Vizcaino et al., 2008, Kjellström et al., 2009, Solomon et al., 2009, National Research Council, 2011). Several studies suggest that the AMOC may weaken in response to warming, resulting in cooling over the North Atlantic and parts of north-western Europe (Mikolajewicz et al., 2007, Vizcaino et al., 2008, Kjellström et al., 2009). The reduction in strength of the AMOC is found to be generally dependent on the magnitude of warming (Lenton et al., 2006), and whilst some studies suggest that it recovers following this weakening within the time period studied (Plattner et al., 2008, Li et al., 2013), others find that higher CO_2 reduces this recovery (Vizcaino et al., 2008, Zickfeld et al., 2013). Mikolajewicz et al. (2007) find that high CO_2 emissions result in a collapse of the AMOC, which does not recover for several thousand years. It has also been suggested that deglaciation of Greenland may occur if global mean temperature increases of 1.9–4.6°C occur (Meehl et al., 2007), or local warming of higher than 2.5°C (Huybrechts and de Wolde, 1999), with the rate and magnitude of melt increasing with increased warming. Many studies simulate a partial or complete melt of the GrIS within the next 50 kyr for various CO_2 scenarios (Ridley et al., 2005, Lenton et al., 2006, Huybrechts et al., 2011), with some showing no regrowth within a simulation time of up to 20 kyr (Charbit et al., 2008, Vizcaino et al., 2008). Melting of the GrIS may cause local increases in temperature, accompanied by cooling in winter over the Barents sea due to changes in sea-ice cover, atmospheric circulation and poleward heat transport (Lunt et al., 2004). Winkelmann et al. (2015) estimate a substantial melting of the Antarctic ice sheet (>50 m of sea level equivalent) after 10 kyr under the most extreme CO_2 emissions scenarios, using the PISM ice sheet model.

1.3.3 Evolution until ~100 kyr AP

On timescales of up to 100 kyr, variations in the orbital parameters act as a significant forcing on climate, through their impact on the seasonal and latitudinal distribution of insolation received by the Earth. It has been previously mentioned that glacial-interglacial cycles have been a dominant feature of the Earth's climate system for several million years, and such cycles are expected to continue into the future. However, it is possible that these natural cycles will be disrupted by anthropogenic climate change, although to what extent is currently uncertain.

As with modelling of multimillennial timescales, EMICs are often used for transient simulations on 100 kyr timescales, although a small number of studies use GCMs to simulate snapshots of climate at specific times and/or conditions in the future, whilst some studies make use of conceptual models. The models are forced by changes in future insolation and a range of natural and anthropogenic CO_2 scenarios are considered, often with the aim of predicting when the next glacial inception may occur.

Imbrie and Imbrie (1980) forced a simple conceptual non-linear model, tuned on data from the last 150 kyr, with climatic variations on orbital frequencies (lower than 19 kyr for one cycle), thus ignoring anthropogenic and natural CO_2 forcing. The 100 kyr future simulation suggested that, purely under orbital forcing, the current interglacial might have ended ~6 kyr BP, when a global cooling trend began. This cooling is projected to continue for the next 23 kyr, with the next glacial maximum occurring at ~60 kyr AP.

Loutre and Berger (2000b) used the Louvain-la-Neuve two-dimensional Northern Hemisphere climate model (LLN 2-D NH), an EMIC, to simulate the possible evolution of climate over the next 130 kyr. A range of simulations were performed with a modern-day GrIS configuration, with constant natural CO_2 concentrations ranging from 210 to 290 ppmv. In addition, several scenarios with variable CO_2 were performed, including one where CO_2 linearly increased to 750 ppmv within 200 years, before decreasing to natural values by 1 kyr AP, and a second "natural" scenario, using CO_2 concentrations derived from Vostok ice-core data, but shifted towards the future by 130 kyr (Jouzel et al., 1993). This natural scenario was also used to force a version of the model with no GrIS, along with three other constant CO_2 scenarios of 210, 250 and 290 ppmv. For a constant CO_2 concentration of 210 ppmv, glacial inception is imminent, with increases in ice beginning at the present day. The next glaciation occurs at around 50 kyr AP when atmospheric CO_2 is 270 ppmv or lower, whereas, if it is higher than this, no inception occurs before 130 kyr AP at the earliest.

A subsequent study by Berger and Loutre (2002) also used the LLN 2-D NH model to simulate the climate from 200 kyr BP to 130 kyr AP under a number of CO_2 forcing scenarios. Two natural scenarios were simulated, one with a constant CO_2 concentration of 210 ppmv, and one using CO_2 concentrations derived from the Vostok ice-core (Jouzel et al., 1993), as in Loutre and Berger (2000b). The "global warming" scenario of Loutre and Berger (2000b) was also modelled, where CO_2 increased to 750 ppmv within 200 years, before decreasing to natural values by 1 kyr AP. Consistent with the results of Loutre and Berger (2000b), ice growth occurred almost continuously from present day in the simulation with a CO_2 concentration of 210 ppmv, whereas glacial inception was delayed until after 50 kyr AP in the anthropogenic and naturally variable CO_2 scenarios.

Lunt et al. (2004) used a GCM, the IPSL_CM4_D model, to carry out snapshot simulations of 67 and 178 kyr AP in the context of the BIOCLIM project (Texier et al., 2003), which aimed to examine long-term future climate change and its implications for radioactive waste disposal. These time periods were chosen because they represent super-interglacial orbital conditions, and a future glaciated state, respectively. The 178 kyr simulation showed a cooling relative to modern in the Central European region of the order of 0.5 and 1°C in December-January-February (DJF) and June-July-August (JJA) respectively. This was primarily due to the presence of a Fennoscandian ice sheet, as the CO_2 concentration was the same as the pre-industrial value (280 ppmv). The BIOCLIM project also carried out dynamical downscaling using a regional climate model (RCM), and found that in the RCM, the winter temperature change was significantly greater over Europe than in the GCM, decreasing by as much as 4°C compared with modern (BIOCLIM, 2003b).

Berger et al. (2003) simulated the coming 130 kyr using the LLN 2-D NH model for a range of CO_2 scenarios, including constant natural CO_2 concentrations of 210, 250 and 290 ppmv and variable natural CO_2 derived from the Vostok ice-core (Jouzel et al., 1993). Two variable anthropogenic emissions scenarios were also modelled, following the same trajectory as the "global warming" scenario of Loutre and Berger (2000b), but reaching maximum CO_2 concentrations of 550 and 750 ppmv. For a constant atmospheric CO_2 concentration of 210 ppmv, glacial inception was imminent. However, in all other scenarios the current interglacial lasted until at least 50 kyr AP.

A study by Cochelin et al. (2006), using the "green" McGill Paleoclimate Model (MPM), an EMIC which simulates the area between 75° S and 75° N, included a range of natural CO_2 scenarios with constant atmospheric CO_2 of between 240 and 300 ppmv. Additionally, several

anthropogenic emissions scenarios were modelled, for which an initial increase in CO_2 was followed by a gradual reduction until constant concentrations of 280, 290 and 300 ppmv were achieved. In the absence of anthropogenic CO_2 emissions, three possible future climate evolutions were identified. Glacial inception was predicted to be imminent for constant atmospheric CO_2 concentrations of 270 ppmv or less, was predicted to occur at ~50 kyr AP for CO_2 of 280–290 ppmv, and does not occur within the next 100 kyr for CO_2 concentrations over 300 ppmv. Similar development pathways also occurred for the simulations which included a period of intense global warming. For CO_2 concentrations of 290 ppmv or lower, glaciation occurs at ~50 kyr AP, whilst for 300 ppmv or higher the current interglacial period lasts for at least the next 100 kyr. These results suggest the atmospheric CO_2 threshold for the next glacial inception may lie between 290 and 300 ppmv.

A study by Pimenoff et al. (2011) investigated the evolution of climate over the next 120 kyr as part of an assessment into long-term repository safety for the planned spent nuclear fuel repository at Olkiluoto, Finland. Natural and anthropogenic CO_2 scenarios were simulated using the CLIMBER-2-SICOPOLIS model, with constant atmospheric CO_2 concentrations of 280 and 400 ppmv, respectively. Ice sheet growth was projected to begin from present day for the 280 ppmv scenario, particularly over North America and large areas of Fennoscandia. This glacial period is followed by a period of interglacial conditions, before ice sheet growth occurs again at the insolation minima at ~54 kyr and 100 kyr AP, when most of Fennoscandia is covered by ice sheets. When atmospheric CO_2 is 400 ppmv, significantly less ice sheet development occurs over the next 120 kyr compared with the 280 ppmv scenario, likely linked to the significantly warmer global temperatures. During the insolation minimum at ~17 kyr AP, only a small amount of ice is projected over the Scandinavian mountains, whereas at the 54 kyr AP minimum, a limited ice sheet extends from the Scandinavian mountains to Lapland and parts of Northern Ostrobothnia.

Vettoretti and Peltier (2011) used a GCM, the National Center for Atmospheric Research Community Climate Model Version 3 (NCAR CCSM3), to produce several snapshot simulations of future climate under natural CO_2 forcing. The first simulation had orbital conditions suitable for 10 kyr AP, whilst the second had orbital conditions for 51 kyr AP, and both had atmospheric CO_2 concentrations of 260 ppmv. Glacial inceptions are produced in both simulations, with the 51 kyr AP glaciation being of a stronger magnitude.

Tzedakis et al. (2012a) proposed that the onset of bipolar-seesaw variability acts as a constraint on the time to initiation of a glacial inception. This variability is instigated when Northern Hemisphere ice sheets reach a sufficient size to produce iceberg discharges that disrupt

Meridional Ocean Circulation (MOC), resulting in warming over Antarctica and cooling over the North Atlantic. These temperature trends are then reversed once the MOC is re-established. Based on a statistical analysis of paleo ice-core and marine data, and the assumption that ice growth is mainly driven by insolation and CO_2 forcing, they suggested that the current interglacial will end within the next 1.5 kyr, on the condition that atmospheric CO_2 concentrations are less than 240 ±5 ppmv.

Ganopolski et al. (2016) performed simulations with the CLIMBER-2 EMIC, by forcing it with varying orbital values and constant CO_2 concentrations of 240 and 280 ppmv. Initially, simulations were run of several past periods and the Holocene-Future (-10–30 kyr AP), and only model configurations that simulated climate states that agreed with observations were selected, resulting in selection of four model configurations. Of these, all four model configurations predicted the end of the current interglacial several thousand years ago for CO_2 of 240 ppmv, with large ice sheets at the present day. For CO_2 of 280 ppmv, glaciation occurs at ~50 kyr AP in three of the simulations. The threshold CO_2 concentration which results in glacial inception was calculated, based on summer insolation at 65 °N and using the coldest and warmest of the four model configurations. These models were then forced by orbital variations and CO_2 for several scenarios, including natural and anthropogenic emissions, for the next 100 kyr, with a glaciation being initiated when atmospheric CO_2 falls below the critical threshold for the given insolation value. None of the scenarios projected glacial inception within the next 50 kyr, due to low eccentricity. In the simulation with no CO_2 emissions, atmospheric CO_2 gradually decreases from the starting concentration of 280 ppmv, undergoing some minor orbital-timescale variations, but the Earth system remains in an interglacial state for tens of thousands of years. For emissions of greater than 1000 Pg C, the next glacial inception is likely to be delayed for at least the next 100 kyr.

Brandefelt et al. (2013) used an EMIC and a GCM (LOVECLIM 1.2 and NCAR CCSM4) to run a selection of transient and snapshot simulations of future climate up to 61 kyr AP, for varying CO_2 forcings. The snapshot simulations were for orbital conditions at 17 kyr AP and 54 kyr AP, which coincide with minima in insolation forcing. For both models and time periods, simulations with CO_2 concentrations of 280 ppmv or lower had cooler global annual average temperatures than the pre-industrial control simulation, whilst CO_2 values of 320–400 ppmv were warmer. A general decrease in temperature at northern high latitudes was evident in LOVECLIM, particularly in the 280 ppmv simulations, due to changes in the orbital parameters at these times. The decrease in temperature in the snapshot CCSM4 simulations was significantly larger than in the equivalent LOVECLIM simulations, due to the higher equilibrium climate sensitivity (ECS) in

CCSM4. In the GCM simulations, the greatest cooling was experienced in northern high latitudes and the Southern Ocean. In the region of Central Europe, both LOVECLIM and CCSM4 appear to predict a cooling in annual average temperature of 0–2°C for both time periods with a CO_2 concentration of 280 ppmv, whilst LOVECLIM shows a warming of 0–2°C for a CO_2 concentration of 400 ppmv. Transient simulations of climate from 0–61 kyr AP with atmospheric CO_2 of 200 and 400 ppmv demonstrated global cooling at a similar time to the insolation minima, as a response to changes in orbital forcing.

1.3.4 Evolution until 1 Myr AP

Model simulations of timescales of up to a million years generally follow very similar approaches to those modelling periods of up to 100 kyr; EMICs or simple conceptual models are used for transient simulations, and GCMs for snapshot simulations. The simulations generally take into account both atmospheric CO_2 and orbital forcings.

The BIOCLIM project (Texier et al., 2003) employed two EMICs to simulate climate for the next 200 kyr. Orbital variations and three CO_2 scenarios were used to force the MoBidiC climate model (Louvain-la-Neuve), an improved and extended version of the LLN model, and CLIMBER-2.3-GREMLINS (an EMIC that includes an ice sheet). One natural CO_2 scenario was modelled, based on the simple threshold model of Paillard (1998). Additionally, two anthropogenic CO_2 scenarios were included, for which atmospheric CO_2 trajectories including a low (3160 Pg C) and high (5160 Pg C) anthropogenic CO_2 contribution calculated using the response function of Archer et al. (1997) were added to the natural CO_2 scenario (BIOCLIM, 2001). The two models produced very different future climate evolutions under the different forcing scenarios. For the natural CO_2 scenario, MoBidiC simulated that the current interglacial will last until after 100 kyr AP, when continental ice will begin to build up. On the other hand, CLIMBER-GREMLINS projected that from 50 kyr AP American ice sheets will begin to grow, experiencing almost constant growth for the remaining 150 kyr period. No ice growth is simulated over Eurasia for this simulation. For the two anthropogenic emissions scenarios, both models suggested that there will be no ice sheet cover in the Northern Hemisphere for most of the 200 kyr time span. At ~167 kyr AP, Northern Hemisphere ice sheet growth occurred in both models, at a faster rate for the scenario with a low anthropogenic CO_2 contribution. However, no ice was projected to grow over Fennoscandia within the next 200 kyr by either model. This study also suggested that atmospheric CO_2 concentrations will remain above natural values until

at least 200 kyr AP, as the CO_2 perturbation above pre-industrial values at the end of the simulation is still 60 ppmv.

Archer and Ganopolski (2005) used the CLIMBER-2 model to calculate the critical insolation threshold leading to glacial inception, under a range of orbital and CO_2 forcings. They then simulated the evolution of atmospheric CO_2 over the next 500 kyr, following anthropogenic emissions of 300, 1000 and 5000 Pg C. In the 300 Pg C emissions scenario, the next glacial inception occurs after ~50 kyr AP, whereas for emissions of 1000 Pg C, inception is delayed until ~130 kyr from present. No glacial inception was projected to occur within the next 500 kyr for anthropogenic emissions of 5000 Pg C.

1.3.5 Summary

A range of studies has addressed the evolution of future climate on both relatively short timescales of several hundred years, and longer timescales of up to a million years. A variety of model complexities and modelling approaches have been employed, depending on the length of time and aspect of climate being considered. In general, results from ensembles of models have only been obtained on timescales of hundreds of years and up to several thousand years. On longer timescales, results from single models, or a small number of models, have been reported. The simulations generally agree that mean global temperatures are likely to continue to increase for at least the remaining part of the 21st century, with the ultimate extent and timescale of warming being dependent on future anthropogenic CO_2 emissions and the natural carbon cycle. On longer timescales, the next glacial inception is generally projected to occur approximately 50 kyr AP under pre-industrial CO_2 concentrations. However, many studies suggest that atmospheric CO_2 concentrations, and thus mean global temperatures, may remain elevated above natural values due to anthropogenic CO_2 emissions for hundreds of thousands of years. This may result in the onset of the next glaciation being delayed for tens of thousands of years or longer, depending on the degree of warming, with implications for the long-term functioning of radioactive waste repositories.

1.4 Aims and objectives

This thesis aims to present a framework for addressing long-term future climate change within the context of post-closure performance assessments for disposal of radioactive wastes.

Specifically, it aims to investigate the potential evolution of long-term (>100 kyr) future climate in response to forcing from orbital variations and anthropogenic CO_2 emissions. It also aims to develop statistical tools to allow the rapid projection of future atmospheric CO_2 concentrations and the evolution of different climate variables over timescales of 1 Myr. Finally, it aims to illustrate the application of the full framework to a specific (illustrative) site, to demonstrate its potential use in a post-closure performance assessment for a radioactive waste repository.

The specific objectives of this thesis, along with their justification, are as follows:

1. Production of CO_2 scenarios that capture the long-term evolution of atmospheric CO_2 following anthropogenic emissions of a range of magnitudes and rates of release, using the *c*GENIE model.
    - For investigation of the response of atmospheric CO_2 concentration to a range of potential anthropogenic emissions pathways.
    - Used to inform GCM modelling (Objective 3).
2. Development of an impulse response function characterizing the long-term multi-component response of the carbon cycle to a range of instantaneous CO_2 emissions.
    - Provides a useful tool for rapidly projecting the response of atmospheric CO_2 to emissions across a large range of sizes and rates of release, reducing the need for long simulations using computationally expensive models.
    - Used to produce atmospheric CO_2 data used as input to the emulator (Objective 5)
    - For use in PCPAs for radioactive waste repositories.
3. Production of a set of climate simulations using the HadCM3 model, testing a range of values for atmospheric CO_2 and the three main orbital parameters (obliquity, precession and eccentricity), for two different global ice sheet extents (present-day and reduced)
    - To provide global climate data for a range of climate forcing conditions that are then used to calibrate the emulator (Objectives 4 and 5).
4. Development and validation of an emulator calibrated on data output by the GCM for a number of variables (SAT and precipitation).

- Provides a useful tool that can be used to project the possible future climate resulting from any combination of orbital and CO_2 parameter values (within the ranges sampled here), reducing the need for time and computationally expensive GCM modelling.
- For use in PCPAs for radioactive waste repositories.

5. Application of the emulator to project time series of the possible "continuous" evolution of climate over the next 1 Myr (snapshot every 1 kyr) for a number of CO_2 pathways.
    - To investigate the evolution of future climate and its possible impacts on a radioactive waste repository, and to produce long-term climate data for use in further modelling (e.g. ice sheet, landscape) as part of a PCPA.

1.5 A Framework for assessing long-term climate change

In this section, a possible framework for assessing long-term climate change in the context of radioactive waste disposal is presented. The components and workflow presented in the framework represent the main themes and approximate structure of this thesis.

The MOdelling and DAta for Radiological Impact Assessments (MODARIA) international research programme ran from 2012-2015, and was sponsored by the IAEA. The primary aim of Working Group 6 (WG6) of the programme was the "development of a common framework for addressing climate change in post-closure radiological assessment of solid radioactive waste disposal" (MODARIA Working Group 6, 2016). A flow chart was developed and presented in the final report of WG6 (MODARIA Working Group 6, 2016), which the work presented in this thesis has contributed to, which is illustrated in Figure 1.7. The flow chart shows how different climate models can be applied to investigate climate changes occurring over different timescales in the context of post-closure radiological impact assessments for nuclear waste repositories. Given that this thesis addresses climatic change on relatively long timescales of hundreds of thousands of years or more, the right branch of the chart is applicable, and the steps that have been addressed in this thesis are highlighted in red. These steps generally follow a similar methodology to previous studies of long-term climate change, by using EMICs to model a larger ensemble of simulations sampling different future conditions and/or transient simulations, before using GCMs to simulate a smaller number of particular climate states of interest.

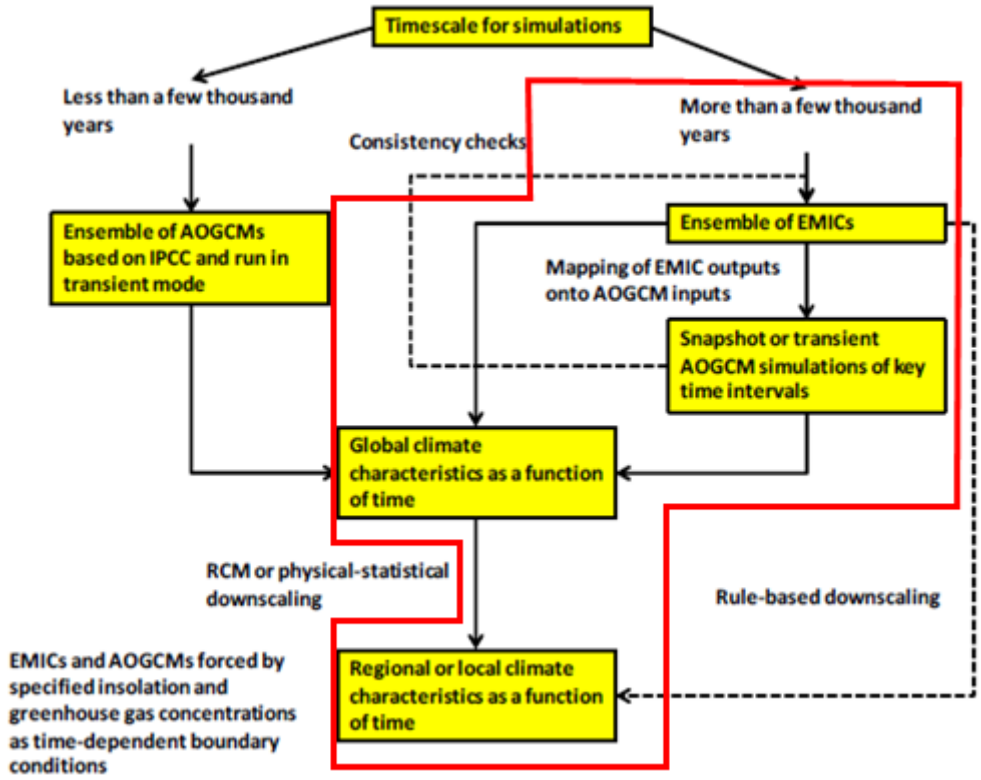

Figure 1.7. Selection of climate models for use in post-closure radiological impact assessments for nuclear waste repositories. The red box indicates the steps addressed in this thesis. Source: Modified from Figure 4.1 (p. 47) of MODARIA Working Group 6 (2016).

The flow chart shown in Figure 1.7 has been modified slightly here, and the updated framework for addressing long-term climate change, around which this thesis is based, is presented in Figure 1.8. The orange boxes represent the main forcings on climate that are relevant on the timescales of interest for the disposal of radioactive wastes (from several thousand years up to 1 Myr), which were discussed in Section 1.2.1. The blue boxes represent the tools developed and described in this thesis, being the CO_2 impulse response function, presented in Chapter 2, and the climate emulator, discussed in Chapters 3 and 4. These tools can be applied to produce the climate data required for post-closure radiological impact assessments, represented by the yellow box. Due to the modelling approach used, this can be climate data for a specific point in time, or data projecting the continuous evolution of climate over a longer time period. It can also be in the form of climate data for the whole global grid, or for a specific grid box. The advantages and limitations of each of these tools, as well as the climate data that they can produce, are discussed in detail in the relevant chapters.

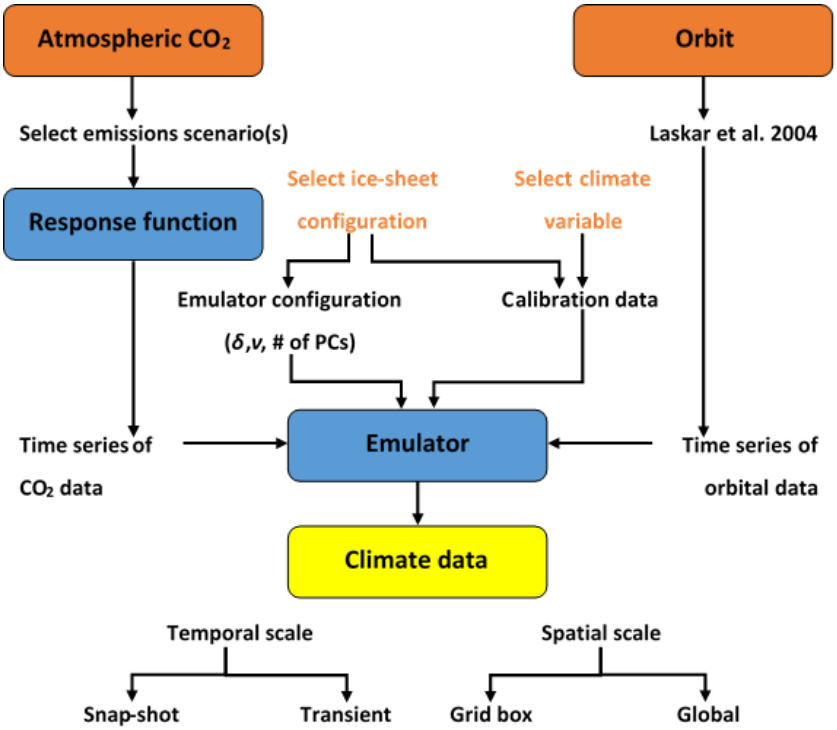

Figure 1.8. Proposed framework for addressing long-term climate change in the context of post-closure performance assessments for radioactive waste repositories.

1.6 Thesis structure

In Chapter 2, the evolution of atmospheric CO_2 over the next 1 Myr is modelled using the *c*GENIE EMIC for a range of anthropogenic CO_2 emissions scenarios, and the response of the long-term carbon cycle to different total emissions is assessed. In addition, an impulse response function is developed that can be used to rapidly project the atmospheric lifetime of CO_2 emissions of a large range of sizes and rates of release. The response function is used to produce atmospheric CO_2 data that are used as input to the emulator when modelling long-term future climate change in Chapters 3, 4 and 5.

Chapter 3 presents a statistical emulator, which is calibrated on a set of simulations with varying atmospheric CO_2 concentrations and orbital parameters run using the HadCM3 GCM. The emulator is validated using a leave-one-out approach, and used to project the long-term evolution of climate (SAT and precipitation) in the late Pliocene and over the next 200 kyr, in response to orbital variations and a range of CO_2 scenarios. The projections of late Pliocene climate are compared with paleo-proxy climate data for the same period, and the evolution of future climate at four possible sites for radioactive waste repositories is explored.

In Chapter 4, the emulator described in Chapter 3 is analysed further. Specifically, the results of the principal component analysis (PCA) used as part of the emulator methodology are examined in more detail, and the application of an emulator calibrated on precipitation (rather than SAT) is assessed. Following this, the ensemble of GCM experiments that the emulator is calibrated on is extended to cover a larger range of atmospheric CO_2 concentrations, thus increasing the maximum CO_2 concentration that the emulator can be used to model. The emulator is then recalibrated on the extended climate data, and applied to project the evolution of SAT and precipitation over the next 200 kyr.

The ideas and methods of the previous three chapters are combined in Chapter 5, in the form of a case study. This provides an illustration of the application of the full methodology for addressing long-term climate change, which is summarised in the framework (Figure 1.8) and presented in this thesis, to an example site for a potential waste repository (one that has not been studied in previous chapters).

Finally, the conclusions of this thesis are presented in Chapter 6, including the principal results, and a discussion of the different ways in which this work could be extended and improved upon.

CHAPTER 2

An impulse response function for the "long tail" of excess CO_2

As mentioned in Chapter 1, on the long timescales being considered in this thesis, the primary forcings that may be expected to have an impact on climate are atmospheric CO_2 concentration and the orbital parameters of the Earth. This chapter addresses the question of future long-term atmospheric CO_2 forcing. The evolution of atmospheric CO_2 over the next 1 Myr is modelled for a range of future CO_2 emissions scenarios. An impulse response function is also developed, which can be applied as described in the framework in Section 1.5 of Chapter 1, to rapidly project the long-term response of atmospheric CO_2 to CO_2 emissions. The atmospheric CO_2 data produced in this chapter is used as input to the emulator when modelling long-term future climate change, as described in Chapters 3, 4, and 5.

The content of this chapter has been published in Lord et al. (2016). The material here is essentially identical to that in the published paper, except that the figures and tables have been renumbered so as to be consistent with the other chapters. Regarding individual contributions to the paper, I ran the model simulations, performed the analysis of the results, and wrote the paper. A. Ridgwell, M. C. Thorne, and D. J. Lunt reviewed the draft paper and provided comments, in addition to providing discussions throughout the study, such as about the analytical methods used and the results.

2.1 Abstract

The ultimate fate of (fossil fuel) CO_2 emitted to the atmosphere is governed by a range of sedimentological and geological processes operating on timescales of up to the ca. hundred thousand year response of the silicate weathering feedback. However, how the various geological CO_2 sinks might saturate and feedbacks weaken in response to increasing total emissions is poorly known. Here the relative importance and timescales of these processes are explored using a 3-D ocean-based Earth system model. First, an ensemble of 1 Myr duration CO_2 decay curves are generated spanning cumulative emissions of up to 20,000 Pg C. To aid characterization and understanding of the model response to increasing emission size, an impulse response function description is then generated for the long-term fate of CO_2 in the model. In terms of the process of carbonate weathering and burial, this analysis is consistent with a progressively increasing fraction of total emissions that are removed from the atmosphere as emissions increase, due to the ocean carbon sink becoming saturated, together with a lengthening of the timescale of removal from the atmosphere. However, it is found that in the model used the ultimate CO_2 sink—silicate weathering feedback—is approximately invariant with respect to cumulative emissions, both in terms of its importance (it removes the remaining excess ~7% of total emissions from the atmosphere) and timescale (~270 kyr). Because a simple pulse-response description leads to initially large predictive errors for a realistic time-varying carbon release, a convolution-based description of atmospheric CO_2 decay is also developed which can be used as a simple and efficient means of making long-term carbon cycle perturbation projections.

2.2 Introduction

A variety of processes, operating on timescales ranging from years to hundreds of thousands of years, act to remove excess (i.e. direct anthropogenic) CO_2 added to the atmosphere (Figure 2.1) and hence control its atmospheric lifetime. On the shortest, approximately annual timescales (Figure 2.1a), CO_2, as a soluble gas, is transferred across the air-sea interface and reacts with seawater to increase the concentration of $CO_{2(aq)}$ and bicarbonate ions (HCO_3^-), whilst reducing the concentration of carbonate ions (CO_3^{2-}) (and decreasing pH) (Turley et al., 2010). At the same time, modelling studies have suggested that CO_2 is taken up

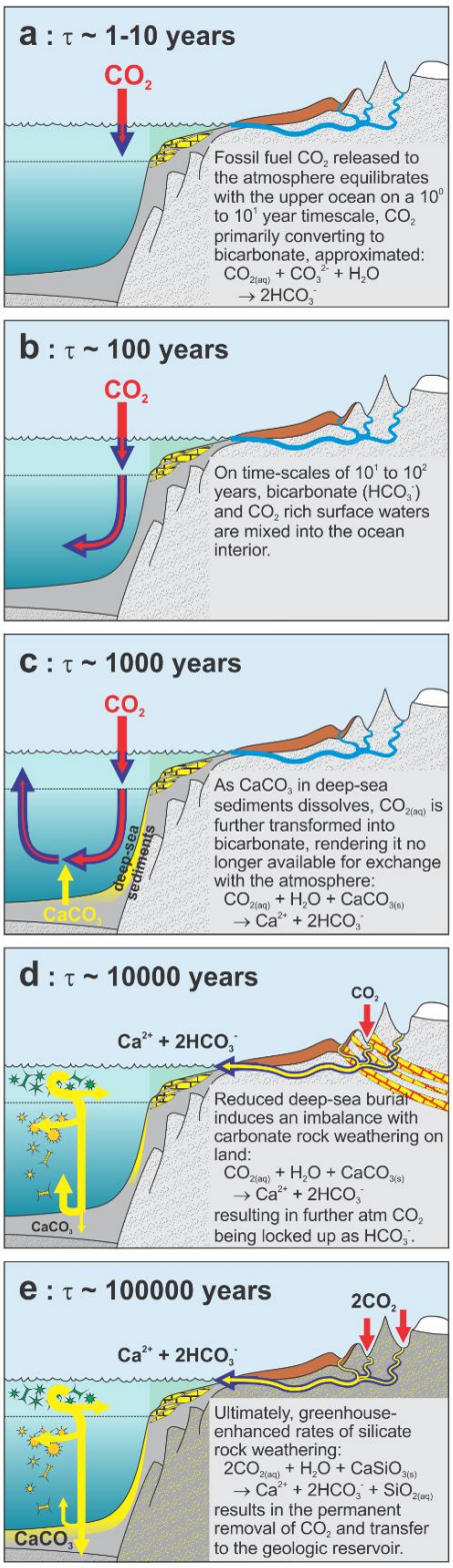

Figure 2.1. Illustration of the primary mechanisms of natural sequestration of CO_2 from the atmosphere. (a) and (b) The pathways of carbon uptake operating on timescales of years (10^0 years) to centuries (10^2 years)—Figure 1a is air-sea gas exchange and Figure 1b is ocean invasion. (c–e) The pathways of carbon uptake occurring on timescales of millennia (10^3 years) and beyond—the "geologic" carbon sinks: Figure 1c represents the operation of seafloor $CaCO_3$ neutralization, Figure 1d represents the operation of terrestrial $CaCO_3$ neutralization, and Figure 1e represents the operation of the silicate weathering carbon sink. The red arrows represent the movement of CO_2 (aq), the blue arrows are HCO_3^- , and the yellow arrows represent Ca^{2+} ions. The widths of the arrows provide an indication of the relative amounts of each dissolved species. The symbols in the ocean in Figures 1d and 1e represent marine calcifying organisms living in the surface ocean (green); a proportion of which will sink and/or dissolve once dead (yellow).

by the terrestrial biosphere through CO_2-driven fertilization of primary productivity (Sitch et al., 2008, Joos et al., 2001, Schimel et al., 2015), although this theory has recently been contested by van der Sleen et al. (2015) who found no evidence of this effect in the analysis of the width of growth rings over the past 150 years in a number of tropical regions. On decadal to century timescales (Figure 2.1b), CO_2-enriched surface waters are transported down into the ocean interior (Archer and Brovkin, 2008, Archer et al., 1998, Sarmiento et al., 1992), while soil carbon stocks will tend to approach a new quasi-equilibrium with terrestrial productivity and surface temperatures.

Out beyond about a millennium from peak carbon emissions, geological processes are expected to progressively dominate the subsequent evolution of atmospheric CO_2. Firstly, ventilation of the deep ocean with CO_2-enriched, and hence CO_3^{2-} depleted, water derived from the surface, will reduce the stability of previously deposited calcium carbonate ($CaCO_3$) in marine sediments and lead to increased rates of in-situ carbonate mineral dissolution (Figure 2.1c), a process known as seafloor $CaCO_3$ neutralization (Archer et al., 1997). This reaction regenerates carbonate ions and hence partially restores the buffering capacity of deep waters (Archer et al., 1997, Ridgwell and Hargreaves, 2007). Subsequent outcropping of these waters at the surface will then enable further CO_2 uptake from the atmosphere. Furthermore, while the rate of burial of $CaCO_3$ in marine sediments globally is reduced or even net negative with global dissolution exceeding supply to the sediment surface, weathering of carbonate rocks on land continues. CO_2 consumed from the atmosphere in the weathering reaction is hence no longer balanced (at long-term steady state) by precipitation and burial of new biogenic $CaCO_3$, allowing additional drawdown of CO_2 (Ridgwell and Hargreaves, 2007, Lenton and Britton, 2006). This process has been termed “terrestrial $CaCO_3$ neutralization” (Archer et al., 1997) (Figure 2.1d).

Finally, the residual atmospheric CO_2 perturbation is removed as a result of the response of terrestrial weathering of silicate rocks to climate (Figure 2.1e). In this process, a warmer, wetter (on average) climate resulting from elevated atmospheric CO_2 concentrations leads to increased weathering rates, drawing down more atmospheric CO_2 and so returning climate conditions and weathering rates back towards their unperturbed levels (Walker et al., 1981). In this chapter, the term “increased weathering” is used, rather than “enhanced weathering” as is often used to describe this natural climate feedback, in order to avoid confusion with the geoengineering technique of artificially increasing rates of weathering as a method of carbon capture and storage. Silicate weathering is assumed to restore atmospheric CO_2 to its original state over hundreds of thousands to millions of years (Lenton and Britton, 2006, Berner, 1999, Berner and Caldeira, 1997) and is responsible for the “long tail” of an atmospheric CO_2

perturbation (Archer and Brovkin, 2008). Increased silicate weathering is also responsible for restoring the initial pre-perturbation state of ocean chemistry as on their own, sea-floor and terrestrial $CaCO_3$ neutralization lead to an accumulation of both total dissolved carbon and alkalinity (Ca^{2+}) in the ocean (Goodwin and Ridgwell, 2010). Increased silicate weathering can thus be viewed as being entirely responsible for the removal of carbon emissions from the surficial reservoirs, but with added carbon having been almost completely partitioned away from the atmosphere by the time silicate weathering comes to dominate the atmospheric CO_2 response.

Removal of added carbon from the ocean and atmosphere need not exclusively take place via increased silicate weathering and other feedbacks may be important. Principal amongst these is organic carbon burial in marine sediments, which is thought to be enhanced under conditions of increased nutrient supply from weathering and hence marine productivity, as well as under reduced ocean oxygenation that is generally associated with a warmer climate (Zachos and Dickens, 2000, Bains et al., 2000). Quasi global-scale deoxygenation and enhanced carbon burial events occurring during the Cretaceous (145.5-65.5 Myr) Ocean Anoxic Events (Schlanger and Jenkyns, 1976, Jenkyns, 1980, Leckie et al., 2002) may well be a reflection of such a feedback response to episodic volcanism and global warming. However, in this study potential additional long-term negative feedbacks and influences involving marine organic carbon burial are ignored, as well as shorter timescale interactions with the terrestrial biosphere in order to simplify the timescale analysis.

A detailed understanding of the timescales on which different global carbon cycle processes operate is essential to correctly interpret geological events, as well as to make projections of how carbon releases, such as from the combustion of fossil fuels, will affect the Earth system in the future. The timescales of operation and CO_2 uptake capacities of these processes (summarised in Figure 2.1) will determine the length and magnitude of the atmospheric CO_2 perturbation and consequently that of the associated changes in climate. This is of particular importance for parts of the climate system that have slow response times, such as the major ice sheets (Stone et al., 2010, Winkelmann et al., 2015), permafrost (Lawrence et al., 2012), and marine hydrates (Hunter et al., 2013, Zeebe, 2013). As such, the dynamics of the long-term atmospheric CO_2 response sets the potential impact of anthropogenic emissions on future glacial-interglacial cycles (Berger and Loutre, 2002, Archer and Ganopolski, 2005).

The involvement of multiple non-linear biogeochemical processes in determining the fate of excess atmospheric CO_2 necessitates the use of numerical model simulations, simulations

which need to be of order 1 Myr in order to elucidate the complete recovery. As a consequence, box model representations of the Earth system have traditionally been developed and employed in addressing questions of long-term future (Lenton and Britton, 2006, Tyrrell et al., 2007, Zeebe and Zachos, 2013) and past (geologic) (Kohler et al., 2005, Berner, 1990, Penman et al., 2014) global carbon cycling. Yet, most box models lack representation of climate feedbacks that modulate the solubility of CO_2 and changes in ocean circulation (and hence transport of dissolved carbon and alkalinity). Off-line 3-D ocean circulation and carbon cycle models have been employed in making projections of the long-term response to carbon emissions but also lack an explicit climate feedback and hence have tended to assume the characteristics of the silicate weathering feedback (Archer et al., 1997, Archer, 2005). Even relatively computationally efficient Earth system models have generally previously only been run for a few tens of thousands of years (e.g. Archer et al., 2009, Meissner et al., 2012) and/or have not included a climate-responsive weathering feedback (e.g. Goodwin and Ridgwell, 2010, Ridgwell and Hargreaves, 2007, Ridgwell and Schmidt, 2010). In one 3-D ocean-based Earth system model study to simulate the full ~1 Myr completion timescale of this feedback (Colbourn et al., 2013), individual model experiments took ~2 months simulation time and only a limited number of emissions scenarios were explored.

Because of the challenges and computational expense of spanning a full range of mechanistically-represented CO_2 removal timescales in a single model, numerical response functions describing the decay of an atmospheric CO_2 perturbation have previously been developed by fitting multiple exponential decay curves to CO_2 data generated by a limited number of model experiments. For instance, Archer et al. (1997) derived three exponential curves from the modelled CO_2 response to a 3000 Pg C pulse emission in an off-line ocean + carbon cycle model. This analysis identified relaxation timescales of 365 years (yr), 5.5 kyr and 8.2 kyr. The Long Tail Model Intercomparison Study (LTMIP) performed by Archer et al. (2009) identified a timescale of 3-7 kyr for the process of $CaCO_3$ neutralization in a range of EMICs. A study by Maier-Reimer and Hasselmann (1987) also derived response functions for perturbation of initial atmospheric CO_2 concentrations by factors of 1.25, 2 and 4, whilst Joos et al. (2013), in a multi-model analysis of a range of models of different complexities (including comprehensive ESMs, EMICs and box-type models), fit a sum of three exponentials over the first 1000 years, detecting relaxation timescales of 4.3, 36.5 and 394.4 yr. However, because these latter studies focused on the millennium time frame, the resulting functions are most relevant in interpreting relatively short-term oceanic processes of carbon uptake such as involving atmospheric CO_2 uptake at the ocean surface and transport of dissolved carbon into the ocean interior. As part of the only explicit 1 Myr timescale analysis conducted to date, Colbourn et al. (2015) explored the

fitting of different numbers of exponential curves and found that for a 1000 Pg C instantaneous emission, an equation consisting of the sum of six exponentials, which differ in their turn-over timescale, provided the optimum fit, capturing the timescales of shorter-term oceanic processes as well as the long-term processes. However, in an initial analysis of a 5000 Pg C release, five exponentials instead provided the best fit (Colbourn, 2011), raising the question of how the relative balance and respective timescale of processes and hence overall CO_2 decay dynamics might change with total carbon emissions.

The advantage of analytical treatments such as summed exponentials is that they can be applied to simulate the overall decay of a CO_2 perturbation in lieu of running a mechanistic model. The BIOCLIM project (BIOCLIM, 2001) for example, used the response function of Archer et al. (1997) to compute long-term atmospheric CO_2 following time-dependent emissions of ~3000 and ~5000 Pg C. These potential future CO_2 trajectories were then used as an external forcing in the LLN 2-D NH climate model (Berger and Loutre, 1996, Gallee et al., 1991, Gallee et al., 1992) to simulate the possible evolution of climate over the next million years. Following this, a number of snapshot simulations were identified and modelled using the IPSL_CM4_D GCM (Marti et al., 2005), with the data then being downscaled to the regional level in order to provide, for example, input data for landscape evolution modelling. In addition, by de-convolving a series of characteristic timescales of CO_2 decay and their relative weights in the overall response, it may be possible to gain insights into carbon cycle processes such as their capacity for CO_2 uptake, the timescales over which they operate, and identify the emissions limits (if any) at which they, in effect, become saturated; the caveat in this respect being that there is no guarantee that statistically derived parameters map onto real world processes.

A limitation to the approach of representing the response of the long-term carbon cycle to a CO_2 perturbation as a pulse response function is that this type of analysis performs best when the system behaves in an approximately linear manner. However, carbon chemistry of the ocean is known to exhibit nonlinear behaviour, reducing the accuracy of this method. This issue has been addressed by Joos et al. (1996), who used a combination of two pulse response functions in order to improve the accuracy of their results; one for the ocean mixed-layer which described the surface to deep-ocean mixing, and one characterizing air-sea exchange. However, the method proposed by Joos et al. (1996) is not easily applied in this study, as the carbon cycle model used here allows ocean circulation to vary with time and includes a representation of the response of seafloor $CaCO_3$ sediments to atmospheric CO_2, which was not case for the models used in the original study.

Bearing in mind the previously employed utility of simple numerical models, the limited assessment of the importance of emissions size, but also caveats to making statistical fits, two main advances are presented here. Firstly, an ensemble of 1000-20,000 Pg C emissions experiments is created to explore how CO_2 sinks may weaken and saturate under high-end carbon releases in the *c*GENIE Earth system model. Secondly, a multi-exponential analysis is performed on this ensemble to produce an impulse response function that captures the decay of the modelled atmospheric CO_2 perturbation and aids the analysis of the total emissions dependency of carbon sink dynamics. A convoluted version of this response function is also derived that can be used for rapid prediction of the atmospheric lifetime of future anthropogenic emissions. This chapter is structured such that the *c*GENIE model and CO_2 scenarios are described in Section 2.3 and the model results are presented in Section 2.4. Section 2.5 discusses the results and their implications, and finally the conclusions of this study are presented in Section 2.6.

2.3 Methods

This work is based around the "*cGENIE*" Earth system model (Colbourn et al., 2013, Ridgwell and Hargreaves, 2007), for which a summary description is first provided (Section 2.3.1) in conjunction with the acceleration technique devised to solve the long-term geochemical mass balance (itself described and evaluated in full in Appendices A to C). The experimental setup and details of the carbon emissions experiments employed are then described (Section 2.3.2).

2.3.1 The *c*GENIE Earth system model

The carbon-centric version of the "GENIE" Earth system model (*c*GENIE) is employed. This is based on the efficient climate model of Edwards and Marsh (2005), comprising: a 2-D Energy-Moisture Balance atmosphere (EMBM), coupled to a 3-D frictional geostrophic ocean circulation model together with a dynamic-thermodynamic sea-ice component. Although lacking atmospheric dynamics and associated feedbacks, first-order estimates of the CO_2-climate feedback on ocean surface temperatures and ocean circulation can be made – both critical to projecting the millennial-scale uptake of excess CO_2 by the ocean. The version of *c*GENIE employed also includes a representation of the global carbon cycle, including ocean biogeochemical cycling of dissolved inorganic carbon (DIC), alkalinity (ALK), and a single nutrient (PO_4) (Ridgwell et al., 2007), geochemical interactions with calcium carbonate in marine

sediments (Ridgwell and Hargreaves, 2007), and terrestrial weathering (Colbourn et al., 2013). The model is configured on a 36×36 equal-area horizontal grid with 8 vertical levels in the ocean and is non-seasonally forced with insolation and wind stresses, both derived from observations. This particular configuration was selected, rather than e.g. a seasonal 36×36×16 resolution such as evaluated by Cao et al. (2009) for direct comparison with previous analyses of CO_2 decay timescales of Ridgwell and Hargreaves (2007) and Colbourn et al. (2013).

*c*GENIE allows for one of a variety of possible representations of climate-weathering feedbacks to be employed (Colbourn et al., 2013). In all schemes, the terrestrial rock weathering module calculates global fluxes of ALK and DIC from carbonate and silicate rock weathering and routes them to the coastal ocean in a pattern based on modern watersheds (Edwards and Marsh, 2005). However, each scheme differs in the assumptions regarding what environmental factors modify the value of these fluxes. In this study, the fluxes are determined by, and are in feedback with, mean annual global land surface temperature (T). In the selected parameterization used here, inputs of calcium ions (Ca^{2+}) from carbonate (F_{CaCO3}) and silicate (F_{CaSiO3}) weathering take the form:

$$F_{CaCO_3} = F_{CaCO_3,0}\left(1 + k_{Ca}\,(T - T_0)\right) \qquad (2.1)$$

$$F_{CaSiO_3} = F_{CaSiO_3,0}\, e^{\frac{1000E_a}{RT_0^2}(T-T_0)} \qquad (2.2)$$

where the 0 subscript represents an initial value of the parameter, k_{Ca} is an empirical constant (0.049), E_a is the activation energy for dissolution and R is the molar gas constant. The temperature dependence of $CaCO_3$ (Equation 2.1) follows that used by Berner (1994), derived by correlating temperatures and bicarbonate concentrations of groundwater, while the relationship between silicate weathering and temperature (Equation 2.2) is based on laboratory studies of the impact of temperature on the dissolution of calcium (Ca) and magnesium (Mg) silicates (Brady, 1991). Here, the simplest possible approach was chosen, and the one mostly likely to lead to a decomposition into a set of separate decay timescales that might have some correspondence with geological processes, and potential additional modifiers are not applied for e.g. run-off (Berner et al., 1983) or terrestrial productivity (Berner, 1991). The importance of the choice of weathering parameterization on the decay of atmospheric CO_2 on millennial timescales is analysed and discussed in Meissner et al. (2012), who found that the CO_2 response of the temperature-only dependence part of the GEOCARB II parameterization (Berner, 1994) lay approximately in the middle of the responses for the other schemes they tested. A wider-ranging

test of alternative parameterizations is provided by Colbourn et al. (2015), Colbourn et al. (2013) and Colbourn (2011).

In order to minimise the run-time of the model, an acceleration technique was employed for solving the net impact of slow changes in weathering, CO_2 out-gassing, and sedimentation. Briefly, once the relatively fast oceanic uptake processes have played out and the effect of imbalance between (increased) rates of carbonate and silicate weathering and CO_2 out-gassing and burial of $CaCO_3$ in marine sediments start to dominate the evolution of atmospheric CO_2, *c*GENIE periodically treats the ocean as a single box, solving explicitly for weathering and sedimentation on the model grid and then applying the mass difference uniformly throughout the ocean (preserving the tracer gradients). The underlying reasoning for this approach, as well as details regarding its detailed methodology, and an analysis of its fidelity in capturing projections of atmospheric CO_2 decay made using the full model, is provided in Appendices A to C.

2.3.2 Model spin-up and CO_2 scenarios

The *c*GENIE Earth system model was spun up in two stages following Ridgwell and Hargreaves (2007): firstly for 20 kyr with a "closed" $CaCO_3$ cycle where the flux of solutes to the ocean from terrestrial carbonate weathering is forced to equal the $CaCO_3$ burial rate, meaning that there is no gain or loss in ocean solutes. The second, 50 kyr spin-up, was with an "open" system configuration, meaning that ocean chemistry would adjust to any imbalance between inputs of solutes from weathering and losses from sediment burial, until the system came into balance. Total initial (pre-industrial) weathering was split 50:50 between carbonate (5.59 teramoles per year; Tmol yr^{-1}) and silicate weathering (5.59 Tmol yr^{-1}). To initially balance the silicate weathering component, a fixed volcanic CO_2 outgassing flux of (5.59 Tmol yr^{-1}) was specified. The annual mean land surface reference temperature (T_0 in Equations 2.1 and 2.2) was 8.5°C. This configuration is essentially the same as examined by Colbourn et al. (2013) and contrasted against alternative possible representations of long-term carbon cycle feedback, as well as by Archer et al. (2009) as part of a model inter-comparison exercise.

Following on from this equilibrium state of global carbon cycling, two different series of emissions scenarios were carried out as summarised in Table 2.1. The first set consisted of an ensemble of 20 idealised pulse emissions experiments, in which the CO_2 release to the atmosphere occurred instantaneously at the start of year 0. Pulse emissions, as used previously

by Archer et al. (2009), have been adopted here as it has been shown that the dominant control on the long-term response of atmospheric CO_2 is the total emissions rather than the rate of release (Eby et al., 2009). The carbon emissions range is 1000-20,000 Pg C (Table 2.1). Whilst remaining fossil fuel reserves that are currently potentially technically and economically viable have been estimated to be approximately 1000 Pg C, fossil fuel resources (where economic extraction may be feasible in the future) are estimated at ~4000 Pg C (McGlade and Ekins, 2015). The higher upper limit hence assumes future techno-economic advances which make additional non-conventional resources such as methane clathrates (as high as 20-25,000 Pg C (Rogner, 1997)) available for extraction. Natural positive carbon cycle feedbacks involving for example permafrost would further amplify the effective total emissions. A broad range of emissions are also deliberately adopted so as to encompass geologically relevant carbon release estimates that run as high as ~13,000 Pg C or more for the transient Cenozoic global warming event, the PETM (Cui et al., 2011). All ensemble members, including a zero-emission experiment as a control, were

Table 2.1. Summary of accelerated cGENIE model experiments[a]

Set	Experiment	Total emissions (Pg C)	Release period (year)
Pulse series	1000	1000	0
	2000	2000	0
	3000	3000	0
	*	*	*
	*	*	*
	*	*	*
	20,000	20,000	0
Logistics series	1000	1000	2010-2810 CE
	2000	2000	2010-2972 CE
	3000	3000	2010-3050 CE
	4000	4000	2010-3098 CE
	5000	5000	2010-3132 CE
	6000	6000	2010-3158 CE
	8000	8000	2010-3196 CE
	10,000	10,000	2010-3223 CE

[a](See Appendices A to C for details and evaluation of the acceleration methodology).

run for 1 Myr and used the accelerated version of *c*GENIE (see Appendices A to C).

The second set of 1 Myr long experiments (Table 2.1) comprise emissions scenarios which follow observed historical atmospheric CO_2 concentrations from 1750 to year 2010 (Meinshausen et al., 2011). Emissions thereafter follow a logistic trajectory (Winkelmann et al., 2015) to achieve cumulative emissions of 1000-10,000 Pg C between the years 2010 CE and ~3200 CE (Figure A1a; Appendix C). These experiments were also run out to 1 Myr and used the accelerated version of *c*GENIE.

2.4 Results

2.4.1 Atmospheric lifetime of fossil fuel CO_2

As expected, the atmospheric CO_2 perturbation in the model caused by each of the pulse emissions of 1000-20,000 Pg C is long-lived, taking hundreds of thousands of years to subside (Figures 2.2 and 2.3a). Even after 500 kyr, atmospheric pCO_2 (partial pressure) has not yet returned to its pre-industrial value, being 359.8 ppmv in the 20,000 Pg C scenario and 282.9 ppmv in the 1000 Pg C scenario, and is still gradually decreasing at a rate of 0.02 and 0.35 ppmv kyr^{-1}, respectively. This finding is consistent with previous studies which have found that an effectively complete recovery of atmospheric CO_2 takes more than 1 Myr for similar-sized emissions (Walker and Kasting, 1992, Colbourn et al., 2013, Lenton and Britton, 2006). Associated impacts such as warming (Figure 2.3b), ocean acidification (Figure 2.3c), and increased terrestrial carbonate and silicate weathering rates (Figure 2.3e), also last for hundreds of thousands of years. However, not all facets of the climate and carbon cycling recover at the same rates or even behave monotonically in post peak emissions recovery (Figure 2.3).

These results show that the lag between the peak atmospheric CO_2 concentration and the peak increase in mean surface air temperature increases with total emissions, ranging from ~60 years for the 1000 Pg C scenario up to ~700 years for the 20,000 Pg C release. The same pattern over time is also evident in the supply of Ca^{2+} to the ocean from terrestrial weathering (Figure 2.3e), due to its direct although non-linear dependence on temperature in the chosen model configuration. As with atmospheric CO_2 concentration, surface air temperature, mean surface ocean pH and weathering rate experience an initial perturbation following CO_2 emissions,

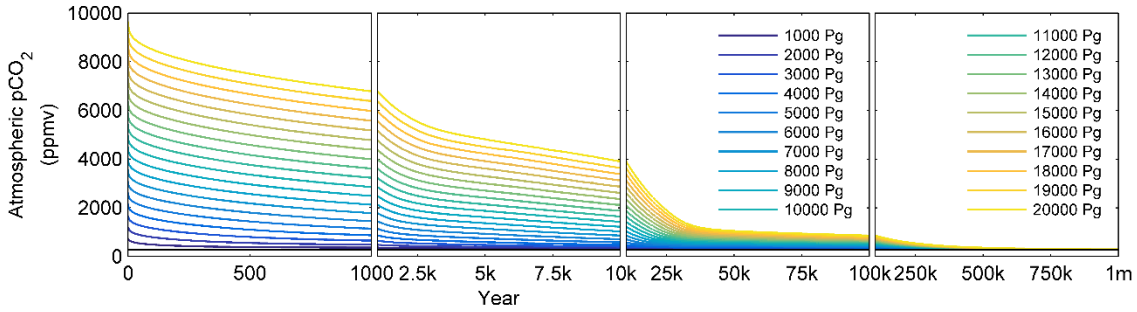

Figure 2.2 Atmospheric pCO_2 predicted by cGENIE for the pulse series scenarios (1000–20,000 Pg C). Pre-industrial CO_2 concentrations are shown in black.

which then subsides slowly over time. In contrast, mean global ocean surface calcite saturation exhibits a more complex evolution with time. Initially, a period of reduced surface ocean calcite saturation state occurs (Figure 2.3d), which for the 6000-20,000 Pg C scenarios results in an interval of surface undersaturation on a global mean basis and which lasts for up to 3000 years under the highest emissions scenario. Subsequent to this, an overshoot in saturation state, caused by the imbalance between the input of solutes to the ocean from terrestrial weathering and marine sedimentation rates, occurs. Associated with the surface saturation changes is an overshoot in the $CaCO_3$ content of marine sediments (Figure 2.3f) caused by enhanced (above pre-industrial levels) preservation of carbonate delivered to the sea floor. Conditions then relax towards their pre-industrial states over several hundred thousand years but now from the opposite direction (of overshoot). The recovery of different elements of the carbonate system hence fundamentally diverges, with saturation state decoupled from pH (Figure 2.3d vs. 2.3c). This phenomena is important in understanding the nature and biotic impacts of past ocean acidification (Honisch et al., 2012) as well as future impacts on e.g. tropical coral reefs (Meissner et al., 2012).

Figure 2.4 shows the fraction of total emissions remaining in the atmosphere at various years as a cubic function of the total CO_2 emissions released. Appendix D provides full details of the analysis performed, as well as the cubic function (Equation A1) and the coefficient values for the curves (Table A2). It was found that the fraction of emissions remaining in the atmosphere is dependent on the amount of CO_2 released, with the fraction remaining on shorter timescales (10^3 and 10^4 years) being particularly sensitive. For these two timescales, this fraction increases with total emissions, due to the responses of a number of feedbacks in the system to the atmospheric CO_2 perturbation, which is discussed in more detail in Section 2.5. As total emissions increase, the fraction remaining at 10^5 years increases slightly, whilst at the longest timescale of 10^6 years the fraction generally decreases. However, the relative change in the amount of CO_2

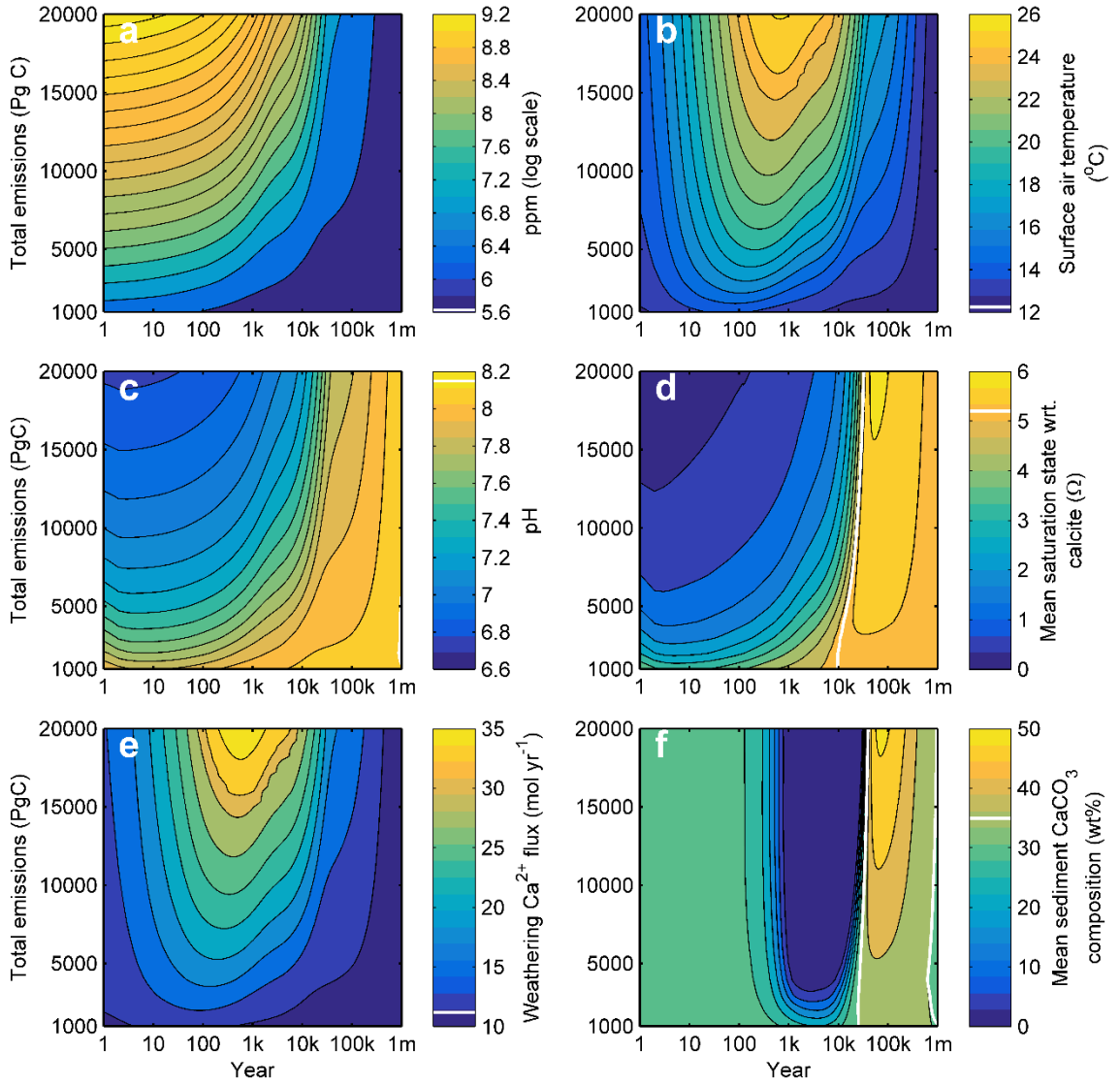

Figure 2.3. Response of climate to anthropogenic emissions for pulse series scenarios. Pre-industrial state is shown as a white contour. (a) Atmospheric pCO_2 (ppmv), (b) mean global surface air temperature (°C), (c) ocean surface pH, (d) ocean surface calcite saturation state (Ω), (e) global flux of Ca^{2+} to the ocean from terrestrial carbonate and silicate weathering (moles per year; mol yr^{-1}), and (f) mean seafloor sediment $CaCO_3$ composition (weight percent; wt%).

remaining in the atmosphere in response to emissions on the two longest timescales is trivial when compared to that of the shorter timescales.

2.4.2 Multi-exponential analysis of atmospheric CO_2 decay

A multi-exponential function was fitted to the ensemble of atmospheric CO_2 decay curves generated in the pulse experiments (Figure 2.2), using the Matlab function `NonLinearModel.fit`, which took the form:

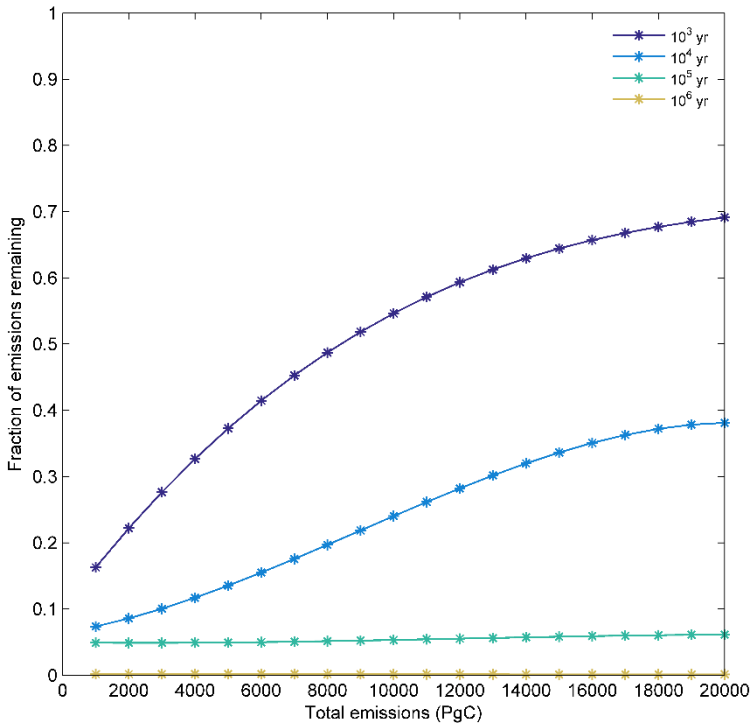

Figure 2.4. Fraction of emissions remaining in the atmosphere at 10^3, 10^4, 10^5, and 10^6 years as a function of total CO_2 emissions in Pg C for pulse series experiments. See Appendix D (Table A2) for cubic coefficient values.

$$CO_2(t) = B + E\sum_{i=1}^{n} A_i exp^{-(t-t_0)/\tau_i} \qquad (2.3)$$

where $CO_2(t)$ is the atmospheric CO_2 concentration in ppmv at a given time (t) after the start of the decay curve t_0 (time 0 at the start of year 1), B is the pre-industrial atmospheric CO_2 concentration (278 ppmv), and E is the total emissions released to the atmosphere in ppmv. Multiple numbers of exponentials were tested, with n ranging from 3 to 6. Each exponential term has two free parameters; τ_i is the timescale of decay and A_i represents the fraction of total emissions removed from the atmosphere over this timescale. Each curve fitting exercise was repeated 1000 times using different sets of randomly sampled initial coefficient values, establishing that the values identified for the coefficients are robust across a wide range of starting points. The curves were ranked using the Akaike Information Criterion (AIC), which measures the relative quality of the fit while favouring models with fewer parameters (the lowest score represents the best fit).

It was found that five exponentials gave the optimal fit, having a lower AIC value and higher R-squared value (R^2) for all emissions scenarios compared with the 3- and 4-exponential fits. A number of previous studies have sought to capture the timescales of CO_2 decay by fitting four exponentials (Archer et al., 1997, Maier-Reimer and Hasselmann, 1987). In contrast, (Colbourn, 2011) tested fits of up to n=10 on emissions of 1000 and 5000 Pg C. For the lower

emissions scenario, he found that *n*=7 was the optimal fit, whereas fewer curves (*n=5*) gave the optimal fit for the scenario with higher emissions. In a recently published extension to this analysis, Colbourn et al. (2015) found that the sum of six exponential curves provided the best fit for a 1000 Pg C pulse emission. The results of the analysis presented here are more in keeping with earlier studies as well as the higher-end emissions of Colbourn (2011), and for the remainder of the results in this chapter, *n*=5 was used.

The median values and range (minimum to maximum) for the five lifetimes (quoted as the *e*-folding time) across the full range of emissions scenarios, are: 1.2 yr (1 to 5.1 yr), 36 yr (34 to 60 yr), 730 yr (230 to 880 yr), 11 kyr (4 to 16 kyr) and 268 kyr (245 to 281 kyr). The exponentials represent the action of different processes or combinations of processes in the global carbon cycle that act to reduce the atmospheric CO_2 perturbation in the model (Figure 2.1). However, processes are unlikely to be individually captured by different terms due to overlaps in the timescales of their operation, an issue which is more likely to be a problem in interpreting the shorter timescale responses. Never-the-less, some possible interpretations are provided later (Section 2.5) of the processes that may in some way be associated with each of the terms.

It was found that the fitting parameters (A_i, τ_i) generally change in a non-linear manner and some of them demonstrate covariance in their relationship with total emissions, as evident in Figure 2.5. The first two exponentials decrease in efficiency (A_1 and A_2) as emissions increase, with a comparatively larger step decrease for the scenarios with total emissions of up to 5000 Pg C. The timescales of these terms (τ_1 and τ_2) increase up to emissions of 2000 Pg C, before decreasing, with the lifetimes captured by the 2nd term beginning to increase again for a 16,000 Pg C release.

The timescales of both the 3rd and 4th exponentials (τ_3 and τ_4) monotonically increase with total emissions, but the responses of their efficiencies differ. For the 3rd term (A_3), the efficiency increases up to emissions of 4000 Pg C, and then decreases as emissions increase further, potentially highlighting a threshold in the modelled carbon cycle response. In contrast, the fraction of CO_2 removed by the 4th exponential (A_4) monotonically increases with increasing emissions. As with the earlier terms, a relatively larger change in the uptake fraction is seen for the lower emissions scenarios and as the emissions increase, the change in fractional uptake per Pg C increase declines.

Finally, and perhaps a little surprisingly, it was found that A_5 varies only very little with total emissions. The timescale of CO_2 removal (τ_5) also only increases very slightly as emissions increase and the relative change is trivial compared to the shorter timescale terms.

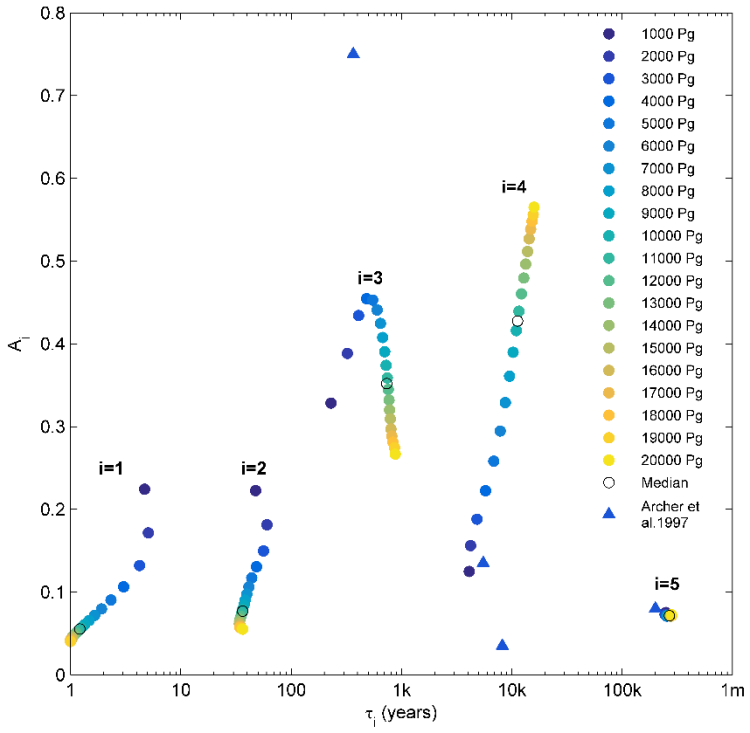

Figure 2.5. Change in fitting coefficient values (A_i and τ_i) for the five exponentials with total CO_2 emissions in Pg C for pulse series experiments. Also shown are the median values and the parameter values of Archer et al. (1997).

2.4.3 Convolution analysis of atmospheric CO_2 decay

In order to create a single numerical description of CO_2 decay applicable across a range of total CO_2 emissions, a regression analysis was performed on the relationship between each fitting coefficient and total emissions. In this, Equation 2.3 was extended and tested coefficients represented as linear, quadratic and cubic functions of the total amount of carbon released. The projected decays of atmospheric CO_2 following pulse emissions of 1000-20,000 Pg C calculated using each possible variant (linear, quadratic or cubic) of the response function were then contrasted to the equivalent atmospheric CO_2 response in *c*GENIE (pulse series experiments; Table 2.1). An F-test was performed to assess which version of the regression model provided the best fit. For all the fitting coefficients except A_5 and τ_2, increasing the number of terms improved the model fit each time, significant at the 0.05 level. Use of cubic regression scaling factors for the fitting coefficients also decreased the RMSE to 44 ppmv, from 53 ppmv for a quadratic fit and from 136 ppmv for a linear fit. The cubic coefficient description was therefore adopted in the remainder of this chapter, with the parameters listed in Table A3 in Appendix E. The full numerical function took the form:

$$CO_2(t) = B + E\sum_{i=1}^{n}(\alpha_i + \beta 1_i\mu + \beta 2_i\mu^2 + \beta 3_i\mu^3)exp^{-(t-t_0)/(\gamma_i + \delta 1_i\mu + \delta 2_i\mu^2 + \delta 3_i\mu^3)} \quad (2.4)$$

where μ is the carbon released at time 0 at the start of year 1 (Pg C).

This empirical form was also applied in a convolution analysis approach in order to improve the predictive capability of the response function for time-dependent emissions releases (logistics series experiments; Table 2.1). This is because the original response function (Equation 2.3) is based on the decay curve of an instantaneous pulse emission rather than a more drawn-out time-varying history of emissions as is occurring now and would characterise emissions across a geological event. To simulate the atmospheric response to the time-dependent emissions of the logistics series scenarios, CO_2 decay was modelled as a series of yearly pulse emissions using the response function. The CO_2 perturbations above pre-industrial were then summed to give the progressive increase in atmospheric CO_2 over the emissions period:

$$CO_2(t) = B + \int_{t_0}^{t} q(x) \left(\sum_{i=1}^{n} A_i(\mu) exp^{-(t-x)/\tau_i(\mu)} \right) dx \qquad (2.5)$$

where $q(x)$ is the release rate in ppmv yr^{-1}. The integral is over the period t_0 to t and the fitting coefficients are a cubic function of the total amount of carbon released (μ Pg C).

Depending on the emissions scenarios being used, both the pulse (Equation 2.4) and convoluted (Equation 2.5) response functions can be employed to predict the atmospheric CO_2 perturbation starting from initial pre-industrial conditions (278 ppmv), or from already perturbed conditions, for example following historical CO_2 emissions. For the latter, an additional step is required in which the decay of historical fossil fuel emissions to date is calculated and added to the projected CO_2 following future emissions, improving the prediction of the start of the curve for scenarios which include historical emissions. This approach was used in the following evaluation of the ability of the two impulse response functions to reproduce atmospheric pCO_2 for the logistics emissions scenarios. For the basic pulse response function, large residuals occur over the emissions period (the emissions occur from year 1750 to year 2810 CE for the 1000 Pg C emissions scenario and to year 3223 CE for the 10,000 Pg C scenario) due to the response function only being able to capture the decay of a pulse (Figure 2.6, and Figure A3; Appendix E.). Response function and original model projections progressively converge after this, agreeing with the conclusion of Eby et al. (2009) that the long-term response of atmospheric CO_2 is dependent on the total emissions rather than the rate of release. Overall, from the end of the respective emissions period (see Table 2.1 for years) onwards percentage errors decline and are less than ±9% of *c*GENIE-modelled atmospheric pCO_2 in all scenarios (Figure 2.6c). The maximum

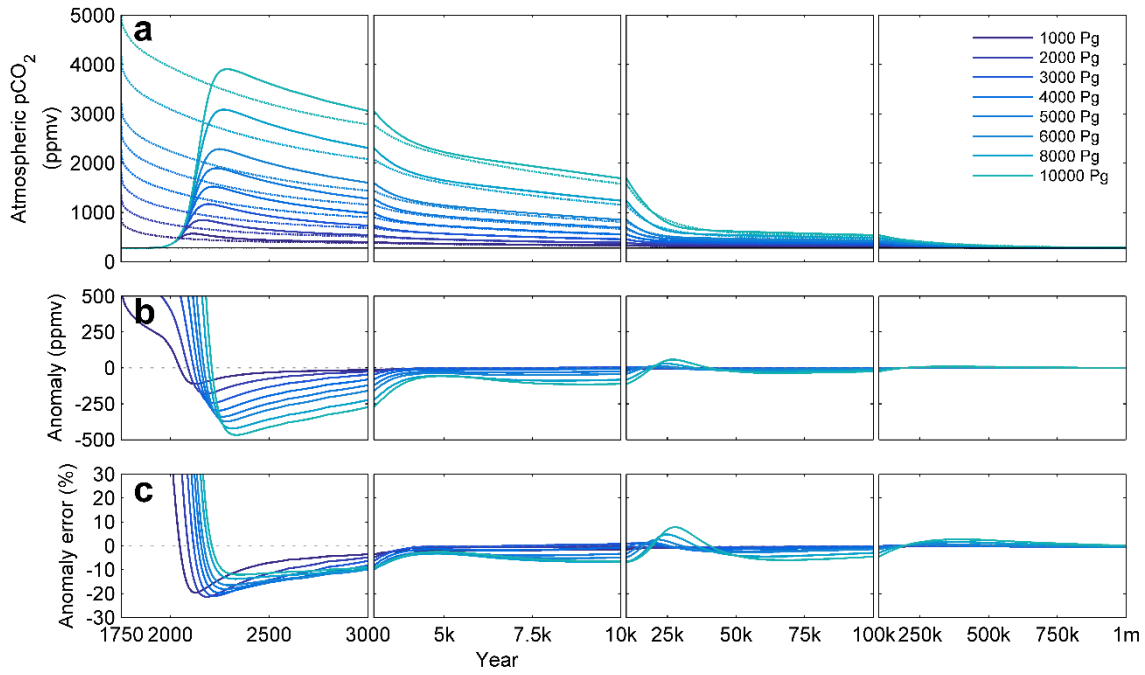

Figure 2.6. Logistics series scenarios for 1000–10,000 Pg C total emissions reproduced using the pulse response function (Equation 2.4). (a) Atmospheric pCO_2 predicted by cGENIE (solid line) and the pulse response function (dashed line). Pre-industrial CO_2 concentrations are shown in black. (b) pCO_2 anomaly. (c) pCO_2 anomaly error. For initial residuals see Appendix E (Figure A3).

percentage errors for this period for the 1000 and 10,000 Pg C scenarios are equivalent to 17.7 and 57.2 ppmv, respectively.

It was found that the convoluted response function (Equation 2.5) much more closely reproduces the modelled atmospheric pCO_2 trajectories in the case of time-dependent emissions (Figure 2.7a), with the initial large residuals that occurred when using a single pulse response function (Figure A3; Appendix E) now significantly reduced. CO_2 is still over-predicted during the interval of CO_2 release compared to the explicitly modelling (*c*GENIE) results (Figure 2.7) – a consequence of the cubic scaling coefficients being derived from an ensemble of experiments run with total instantaneous emissions starting at 1000 Pg C, which represents a release rate averaged over one year some two orders of magnitude larger than current emissions. Nevertheless, maximum percentage errors in all scenarios are less than ±26% of atmospheric pCO_2, equivalent to 179.9 ppmv for the highest emissions scenario, and fall below ±9% by year 2200 CE (Figure 2.7c). For the 1000 and 10,000 Pg C scenarios, the maximum percentage errors beyond year 2200 are equivalent to 14.6 and 64.5 ppmv, respectively.

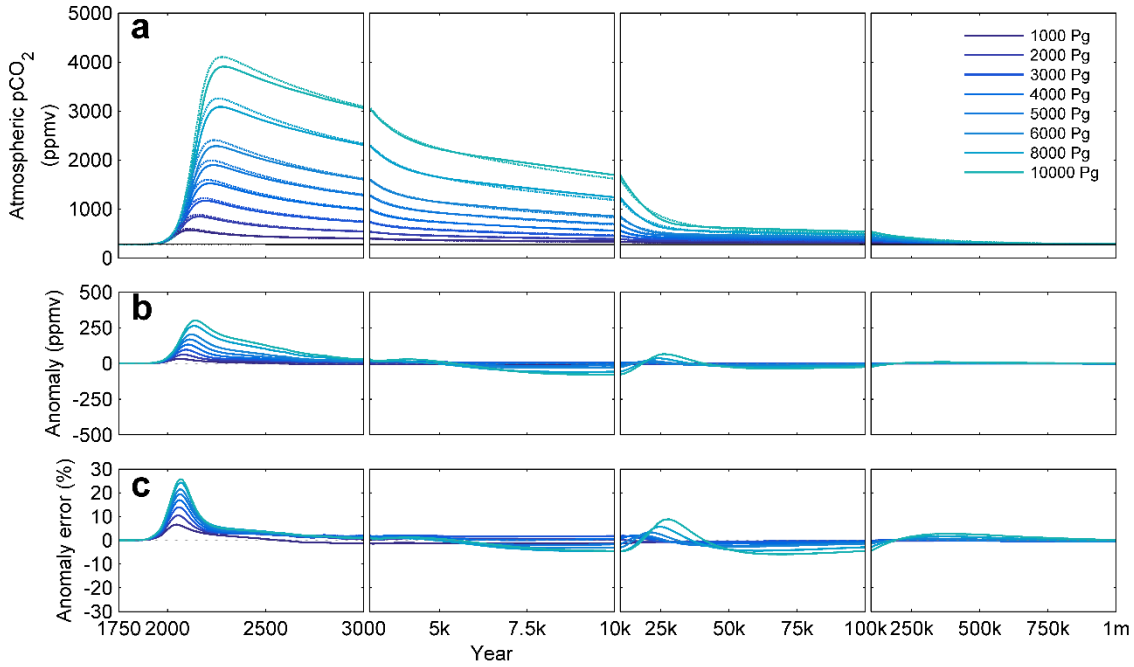

Figure 2.7. Logistics series scenarios for 1000–10,000 Pg C total emissions reproduced using the convoluted response function (Equation 2.5). (a) Atmospheric pCO_2 predicted by cGENIE (solid line) and the convoluted response function (dashed line). Pre-industrial CO_2 concentrations are shown in black. (b) pCO_2 anomaly. (c) pCO_2 anomaly error.

2.5 Discussion

By fitting a series of exponential decay curves to atmospheric pCO_2 data predicted using the *c*GENIE Earth system model, one can explore how the dynamics of removal of excess CO_2 from the atmosphere changes with cumulative CO_2 emissions. In theory, the principal carbon cycle process(es) most likely to be influencing the parameter values of each of the exponentials can be identified on the basis of *a priori* known timescales of these processes as well as the results of previous studies. However, in practice the exponentials will tend to represent the action of more than one process. In addition, changes in fitted parameter values with increasing emissions may reflect a change in the balance of processes encapsulated by a term, rather than a process(es) necessarily responding itself to emissions size. As in Section 2.4, the values presented below are the median values for the fitting coefficients, and the range of values (minimum to maximum) across the full range of emissions of 1000-20,000 Pg C.

2.5.1 Timescales and magnitude of CO_2 removal

The two exponentials with the shortest timescales of years to decades (1.2, 36 yr) likely reflect a range of processes involving air-sea gas transfer, reaction of CO_2 with seawater, and

invasion of CO_2 into the upper water column. Particularly in light of their very similar response to increasing total emissions in τ_i vs. A_i space (Figure 2.5), they are here regarded as inseparable with respect to their interpretation. While the 3rd exponential is separated by an order of magnitude in timescale from the 2nd, the existence of a common inflection point around 4000-5000 Pg C in all first three terms suggests that again, distinct or independent processes are not being separated by the exponential deconvolution. The 730 yr timescale of the 3rd term suggests that ocean circulation and CO_2 transport away from the surface is involved, but the nature of this may not be separable from the shorter timescale terms.

One might more usefully then combine terms 1-3 and ascribe this sink to "ocean" (primarily physical transport) processes and the carbonate buffering capacity of ocean waters. Across the range of pulse emissions (1000-20,000 Pg C), the equilibrium partitioning of CO_2 between ocean and atmosphere is such that approximately 50% (6%+8%+35%) is removed (range: 36-80%), leaving ~50% (20-64%) in the atmosphere. This estimated value for the CO_2 sink capacity of the ocean is lower than some previous estimates, which have estimated that the ocean may be able to store ~60-80% of fossil fuel emissions (Ridgwell and Hargreaves, 2007, Archer and Brovkin, 2008, Archer et al., 1997). However, as identified previously (Archer, 2005, Archer et al., 2009, Archer et al., 1998) the fraction removed by the ocean depends on total emissions, and the value quoted here is an average across a wide range of emissions. The findings of this chapter can be reconciled with previous studies by considering how the life-times and values of fractional uptake depend on emissions, as discussed in Section 2.5.2.

Rather more confidence is had that the final two terms represent relatively distinct (geological) processes. Firstly, the behaviour of the 4th and 5th exponentials is very different both from each other as well as from the first three exponentials (Figure 2.5), i.e. their behaviour with increasing emissions size is unlikely to be a statistical artefact of the CO_2 decay curve fitting. The characteristics of both the final two terms are also broadly consistent with previous studies carried out with different analysis methods and often using very different ocean model components.

Across the range of modelled emissions, the 4th exponential has a median timescale of 11 kyr and accounts for the removal of 43% (12-57%) of the excess CO_2 added to the atmosphere. A study by Ridgwell and Hargreaves (2007) characterised the individual operating timescales of seafloor neutralization and terrestrial neutralization for a 4000 Pg C release, obtaining values of 1.7 kyr and 8.3 kyr, respectively. It is therefore inferred that the 4th timescale in this study is likely

to, at least partially, represent the combined action of these processes, as a response time (τ_4) of 5.8 kyr for an equivalent total CO_2 release is obtained.

The 5th and final exponential represents increased silicate weathering. Previous studies have often not modelled long-term silicate weathering explicitly but instead assume a relaxation timescale for this process of, for example, 200 kyr (Archer et al., 1997, Archer et al., 1998) or 400 kyr (Archer, 2005). However, using a box model, Lenton and Britton (2006) made a half-life estimate of ~200 kyr for silicate weathering following emissions of ~1100-15,000 Pg C in model simulations run for 1 Myr. This value is broadly similar to the timescale for the 5th and final exponential in this chapter of 245-278 kyr for the same range of emissions. The modelled fraction of CO_2 that is neutralised on this timescale was found to be 7% (7-8%), in good agreement with previous estimates of 7-8% deduced from the CO_2 residual in experiments lacking an explicit representation of the feedback (Archer et al., 1997, Archer et al., 1998, Ridgwell and Hargreaves, 2007).

2.5.2 The importance of CO_2 emissions size and buffer depletion

The values of the fractions and timescales of CO_2 uptake in the model captured by the five exponentials vary with total emissions. These trends are related to the marine carbon feedbacks in the Earth system that are included in the *c*GENIE model. For example, a range of modelling studies have recognised that the proportional uptake by the ocean of an atmospheric CO_2 anomaly is a function of the size of that anomaly (magnitude of total emissions) (Lenton and Britton, 2006, Archer, 2005, Archer et al., 1998, Eby et al., 2009). One reason for this is that the efficiency of ocean invasion decreases as emissions increase due to a series of well-established carbon feedbacks. The first feedback links CO_2 uptake and temperature as a result of the reduction of the solubility of gaseous CO_2 in sea water with increasing temperature (Zeebe and Wolf-Gladrow, 2001). The second feedback relates to the decline in the strength of carbonate ion buffering of seawater and an increasing "Revelle factor" (Zeebe and Wolf-Gladrow, 2001) as atmospheric CO_2 concentrations increase. In other words, the proportional uptake by the ocean of a unit excess of atmospheric CO_2 declines as atmospheric CO_2 (and total emissions) increases (Sarmiento et al., 1995). Thirdly, differential warming of the surface versus depth will increase stratification and tend to decrease the strength of ocean overturning circulation and hence CO_2 transport to depth. The general decline in the fractional importance of all three initial terms (A_1, A_2, A_3) is consistent with these processes. The initial strengthening of importance of the 3rd term and increase in value of A_3 for total emissions up to ~4000 Pg C in size may perhaps paradoxically,

be related to the progressive collapse of the AMOC. Although collapse of AMOC in the model would inhibit transport of dissolved CO_2 into the deep ocean from the North Atlantic surface, a small positive feedback arises from reduced CO_2 uptake associated with a weakening of the AMOC as carbon delivered to depth via the biological pump becomes more effectively isolated in the deep North Atlantic (Zickfeld et al., 2008, Montenegro et al., 2007). In other words, high carbon storage due to a more efficient biological pump in the North Atlantic may at least temporarily, outweigh a weaker solubility pump (e.g. see Chikamoto et al., 2008). The timescales of the first two terms (τ_1, τ_2) generally decrease with total emissions, whilst those of the 3rd term (τ_3) increase with total emissions, although the inflection following the initial increase in timescale of τ_1 and τ_2 is not readily ascribed any physical reason and may reflect a shift in the statistical fit associated with the more pronounced inflection in A_3. Overall, analysis of the first three terms is a good illustration of the difficulties in ascribing specific process to statistical terms. However, the inflection in the parameter space trajectories of all three terms around 4000 Pg C (Figure 2.5) may well be driven by a real physical phenomenon (AMOC collapse in the model).

Previous studies have estimated that the ocean removes 60-80% of total emissions of 1000-5000 Pg C (higher for higher emissions) (Archer et al., 1997, Archer, 2005), a fraction that declines to ~30% for 15,000 Pg C (Lenton, 2006). This is in broadly good agreement with the range of values for the estimated ocean fraction (sum of A_1, A_2 and A_3) derived here, which vary from 80% to 42% for 1000 and 15,000 Pg C respectively. The approximate timescale of ocean uptake of up to ~550 years for emissions of 1000-5000 Pg C (longer for higher emissions) is also close to previous estimates of 200-450 years (Archer et al., 1997, Archer et al., 1998). The difference here and the reason for this slightly longer estimate may simply reflect the lack of a climate feedback and hence of a circulation slow-down in the analysis of Archer et al. (1997), Archer et al. (1998).

The values of A_4 and τ_4 increase with emissions size, as they are likely affected by the combined responses of sea-floor and terrestrial $CaCO_3$ neutralization to the modelled atmospheric CO_2 perturbation. This is partly a consequence of the fact that the erodable deep-sea sediment $CaCO_3$ reservoir becomes depleted in the higher emissions scenarios (≥ 5000 Pg C) as first recognised by Archer et al. (1997), Archer et al. (1998) and further elucidated by Goodwin and Ridgwell (2010). Once the available surface and near-surface sediment $CaCO_3$ is depleted, the further uptake of atmospheric CO_2 by the process of seafloor $CaCO_3$ neutralization ceases. However, at the same time, with increasing total emissions, the imbalance between terrestrial weathering rates and deep-sea carbonate burial also increases with a more rapid supply of weathering solutes to the ocean. The result is that the characteristic fraction (A_4) and timescale

(τ_4) both progressively increase with total emissions, but do not exhibit any obvious threshold behaviour in the region of 5000 Pg C emissions, which is the point at which the erodible deep-sea $CaCO_3$ is projected to become exhausted (Archer et al., 1997, Goodwin and Ridgwell, 2010). The lack of an identifiable statistically-recoverable transition as the seafloor $CaCO_3$ neutralization sink is exhausted cautions against separating seafloor and terrestrial neutralization processes (e.g. as per Ridgwell and Hargreaves, 2007), or at least, cautions against over-interpreting the importance of exhausting the former.

Combining the two processes of seafloor and terrestrial $CaCO_3$ neutralization, Ridgwell and Hargreaves (2007) estimated the total CO_2 uptake to be ~26%, which aligns well with the results here when taking into account emissions size, with the 4000 Pg C scenario value for A_3 in this chapter being 22%. Archer et al. (1997) projected that, for emissions of 900-4500 Pg C, these two processes account for the removal of 13-23% of total emissions from the atmosphere over periods of 5.5-6.8 kyr and 8.2 kyr. Here, the comparable range for total emissions of 1000-5000 Pg C is somewhat higher at 12-26%, but with a combined *e*-folding timescale ranging from 4-6.9 kyr, i.e. slightly shorter than found by Archer et al. (1997). These differences can be explained because the modelling approach used by Archer et al. (1997) did not include the feedbacks that result from increased atmospheric CO_2 on ocean circulation, meaning that ocean invasion will tend to proceed more rapidly and hence interactions with deep-sea sediments occur sooner. The findings here are also consistent with the work of Goodwin and Ridgwell (2010), who compared the ocean-atmosphere partitioning of CO_2 emissions following $CaCO_3$ sediment equilibration as calculated by an analytical method and found that ~7-33% of total emissions were removed from the atmosphere by the equilibrated $CaCO_3$ sediment feedback, and that this fraction increases as total emissions increase.

Finally, and perhaps a little surprisingly, it is found that A_5 varies only very little with total emissions, as the relative efficiency of CO_2 removal by the four faster mechanisms in the model tend to compensate for each other, meaning that the atmospheric fraction of total emissions that remains to be neutralised by increased weathering is approximately the same in all scenarios. This is consistent with previous work that found that the fraction of emissions remaining in the atmosphere beyond 100 kyr (and hence that left to be neutralised by silicate weathering) to be relatively unaffected by total emissions (Lenton and Britton, 2006). The timescale of CO_2 removal (τ_5) can be seen to increase slightly with total emissions, but again the relative change is small particularly compared to that of e.g. τ_3 and τ_4 (Figure 2.5).

2.6 Summary and Conclusions

A series of instantaneous pulse emissions of 1000-20,000 Pg C have been carried out in an Earth system model to highlight the long-term decay dynamics of a CO_2 perturbation. In a multi-exponential analysis of this model ensemble, how the characteristics of the CO_2 decay change with total emissions has been assessed. It is found that for the shorter (<1000 year) timescales of decay, which likely reflect a range of ocean circulation, carbonate chemistry, and air-sea gas exchange processes, the fractional removal of excess CO_2 from the atmosphere depends strongly and non-linearly on total emissions. This illustrates how the buffering and CO_2 uptake by the ocean on anthropogenic timescales progressively saturates with increasing total emissions. To compensate, excess CO_2 removal from the atmosphere due to carbonate weathering and burial progressively increases in importance with increasing emissions, but at a progressively slower rate for higher total emissions. In contrast to the ocean dynamics and carbonate weathering processes, it was found that the e-folding timescale for the silicate feedback as well as its relative importance in removal of excess CO_2 from the atmosphere, is almost independent of emissions size.

An impulse response function (pulse emissions - Equation 2.4, and time-dependent emissions – Equation 2.5, both using coefficient values in Table A3 in Appendix E) is created which is able to reproduce model-predicted atmospheric CO_2 data following pulse emissions of up to 20,000 Pg C. The function provides a simple and practical tool for rapidly projecting the atmospheric lifetime of a CO_2 emission. Its primary advantage is that it can be used across a large range of emissions sizes and rates of release and removes the need for long simulations using computationally expensive models.

However, the role of the terrestrial biosphere has been emitted from this analysis and furthermore, focused on a relatively simple and global mean function linking weathering rates and climate. Future work should explore uncertainties in the strength and dynamical characteristics of the silicate weathering feedback, as well as accounting for the role of the organic carbon cycle.

The impulse response function developed in this chapter allows the long-term response of atmospheric CO_2 concentration to a variety of future CO_2 emissions to be projected. In the following chapters, this data is applied as a climate forcing to a statistical emulator, along with orbital variations, allowing projections of the possible evolution of climate over the next 200 kyr or more to be produced.

CHAPTER 3

Emulation of long-term changes in global climate – Application to the late Pliocene and future

In the previous chapter, an EMIC with a representation of the long-term carbon cycle was used to model the response of atmospheric CO_2 concentration over the next 1 Myr to anthropogenic CO_2 emissions ranging from 1000 Pg C to 20,000 Pg C. An impulse response function was also developed, which can be used to rapidly estimate the atmospheric lifetime of a large range of CO_2 emissions, in place of a mechanistic model. In this chapter, a statistical emulator is presented, which can be used to project the long-term evolution of climate in response to atmospheric CO_2 concentration (results used from Chapter 2) and orbital forcing, following the steps described in the framework in Section 1.5 of Chapter 1. Various CO_2 emissions scenarios are simulated, and the climate data produced by the emulator can be used in further modelling as part of post-closure radiological impact assessments.

The content of this chapter has been published in Lord et al. (2017). The material here is essentially identical to that in the published paper, except that the figures and tables have been renumbered so as to be consistent with the other chapters. Regarding individual contributions to the paper, I ran the GCM simulations and the emulator, performed the analysis of the results, and wrote the paper. M. Crucifix wrote the emulator package, and provided training and instruction for me in its application, and advice on the interpretation of its results. The paper was reviewed and commented on by M. Crucifix, D. J. Lunt, M. C. Thorne, N. Bounceur, H. Dowsett, C. L. O'Brien, and A. Ridgwell. In addition, M. Crucifix, D. J. Lunt, M. C. Thorne, and A. Ridgwell

provided discussions throughout the study, such as about the experimental design, analytical methods used and the results. Details of the review process, including the comments from the reviewers and the authors' revisions, are available from: www.clim-past-discuss.net/cp-2017-57.

3.1 Abstract

Multi-millennial transient simulations of climate changes have a range of important applications, such as for investigating key geologic events and transitions for which high resolution palaeoenvironmental proxy data are available, or for projecting the long-term impacts of future climate evolution on the performance of geological repositories for the disposal of radioactive wastes. However, due to the high computational requirements of current fully coupled General Circulation Models (GCMs), long-term simulations can generally only be performed with less complex models and/or at lower spatial resolution. In this study, novel long-term "continuous" projections of climate evolution are presented based on the output from GCMs, via the use of a statistical emulator. The emulator is calibrated using ensembles of GCM simulations which have varying orbital configurations and atmospheric CO_2 concentrations and enables a variety of investigations of long-term climate change to be conducted which would not be possible with other modelling techniques at the same temporal and spatial scales. To illustrate the potential applications, the emulator is applied to the late Pliocene (by modelling surface air temperature (SAT)), comparing its results with palaeo-proxy data for a number of global sites, and to the next 200 thousand years (kyr) (by modelling SAT and precipitation). A range of CO_2 scenarios are prescribed for each period. During the late Pliocene, it is found that emulated SAT varies on an approximately precessional timescale, with evidence of increased obliquity response at times. A comparison of atmospheric CO_2 concentration for this period, estimated using the proxy sea surface temperature (SST) data from different sites and emulator results, finds that relatively similar CO_2 concentrations are estimated based on sites at lower latitudes, whereas higher latitude sites show larger discrepancies. In the second illustrative application, spanning the next 200 kyr into the future, it is found that SAT oscillations appear to be primarily influenced by obliquity for the first ~120 kyr, whilst eccentricity is relatively low, after which precession plays a more dominant role. Conversely, variations in precipitation over the entire period demonstrate a strong precessional signal. Overall, it is found that the emulator provides a useful and powerful tool for rapidly simulating the long-term evolution of climate, both past and future, due to its relatively high spatial resolution and relatively low computational cost. However, there are

uncertainties associated with the approach used, including the inability of the emulator to capture deviations from a quasi-stationary response to the forcing, such as transient adjustments of deep ocean temperature and circulation, in addition to its limited range of fixed ice sheet configurations and its requirement for prescribed atmospheric CO_2 concentrations.

3.2 Introduction

Palaeoclimate natural archives reveal how the Earth's past climate has fluctuated between warmer and cooler intervals. Glacial periods, such as the Last Glacial Maximum (Yokoyama et al., 2000, e.g. Lambeck et al., 2001), exhibit relatively lower temperatures associated with extensive ice sheets at high northern latitudes (Lisiecki and Raymo, 2005, Jouzel et al., 2007, Herbert et al., 2010), whilst interglacials are characterised by much milder temperatures in global mean. Even warmer and sometimes transient ("hyperthermal") intervals, such as occurred during the Palaeocene-Eocene Thermal Maximum (e.g. Kennett and Stott, 1991), are characterised by even higher global mean temperatures. Assuming that on glacial-interglacial timescales and across transient warmings and climatic transitions, tectonic effects can be neglected, the timing and rate of climatic change is at least partly controlled by the three main orbital parameters – precession, obliquity and eccentricity – which have cycle durations of approximately 23, 41, and both 96 and ~400 thousand years (kyr), respectively (Milankovitch, 1941, Hays et al., 1976, Berger, 1978, Kawamura et al., 2007, Lisiecki and Raymo, 2007). Further key drivers of past climate dynamics include changes in atmospheric CO_2 concentration and in respect of the glacial-interglacial cycles, changes in the extent and thickness of ice sheets.

In order to investigate the dynamics, impacts and feedbacks associated with the response of the climate system to orbital forcing and CO_2, long-term (>10^3 years (yr)) projections of changing climate are required. Transient simulations such as these are useful for investigating key past episodes of extended duration for which detailed palaeoenvironmental proxy data are available, such as through the Quaternary and Pliocene, allowing data-model comparisons. Simulations of long-term future climate change also have a number of applications, such as in assessments of the safety of geological disposal of radioactive wastes. Due to the long half-lives of potentially harmful radionuclides in these wastes, geological disposal facilities must remain functional for up to 100 kyr in the case of low- and intermediate-level wastes (e.g. Low Level Waste Repository, UK (LLWR, 2011)), and up to 1 Myr in the case of high-level wastes and spent nuclear fuel (e.g. proposed KBS-3 facility, Sweden (SKB, 2011)). Projections of possible long-term

future climate evolution are therefore required in order for the impact of potential climatic changes on the performance and safety of a repository to be assessed (NDA, 2010, Texier et al., 2003). Indeed, while the glacial-interglacial cycles are expected to continue into the future, the timing of onset of the next glacial episode is currently uncertain and will be fundamentally impacted by the increased radiative forcing from anthropogenic CO_2 emissions (Loutre and Berger, 2000b, Archer and Ganopolski, 2005, Ganopolski et al., 2016).

Making spatially-resolved past or future projections of changes in surface climate generally involves the use of fully coupled General Circulation Models (GCMs). However, a consequence of their high spatial and temporal resolution and structural complexity (and attendant computational resources) is that it is not usually practical to run them for simulations of more than a few millennia, and invariably, rather less than a single precessional cycle. Even when run for several thousand years, only a limited number of runs can be performed. Previously, therefore, lower complexity models such as Earth system Models of Intermediate Complexity (EMICs) have been used to simulate long-term transient past (e.g. Loutre and Berger, 2000a, Stap et al., 2014) and future (e.g. Archer and Ganopolski, 2005, Lenton et al., 2006, Eby et al., 2009, Ganopolski et al., 2016, Loutre and Berger, 2000b) climate development. Where GCMs have been employed, generally only a relatively small number of snapshot simulations of particular climate states or time slices of interest have been modelled (Braconnot et al., 2007, Masson-Delmotte et al., 2011, Haywood et al., 2013, Prescott et al., 2014, Marzocchi et al., 2015).

In this study, long-term continuous projections of climate evolution are presented based on the output from a GCM, via the use of a statistical emulator. Emulators have been utilised in previous studies for a range of applications, including sensitivity analyses of climate to orbital, atmospheric CO_2 and ice sheet configurations (Araya-Melo et al., 2015, Bounceur et al., 2015) and model parameterizations (Holden et al., 2010). However, to the best of our knowledge, this is the first time that an emulator has been trained on data from a GCM and then used to simulate long-term future transient climate change. It should be noted that, whilst other research communities may use different terms, the groups of climate model experiments are referred to as “ensembles”, and the GCM is referred to directly when discussing calibration of the emulator, rather than using the term “simulator” as has been used in a number of previous studies.

An emulator was calibrated using SAT data produced using the HadCM3 GCM (Gordon et al., 2000). Two ensembles of simulations were run, with varying orbital configurations and atmospheric CO_2 concentrations. Each ensemble was run twice, once with modern-day continental ice sheets and once (for a reduced number of members) with reduced-extent ice

sheets. This approach was adopted because in at least two of the intended uses for the emulator (Pliocene, and long-term future climate for application to performance assessments for potential radioactive waste repositories), it is thought that the Greenland and West Antarctic ice sheets (WAIS) could be reduced relative to their current size. The implications and uncertainties associated with this approach are discussed in Section 3.7. The ensembles thus cover a range of possible future conditions, including the high atmospheric CO_2 concentrations expected in the near-term due to anthropogenic CO_2 emissions, and the gradual reduction of this CO_2 perturbation over timescales of hundreds of thousands of years by the long-term carbon cycle (Lord et al., 2015, 2016).

This study goes on to illustrate a number of different ways in which the emulator can be applied to investigate long-term climate evolution over hundreds of thousands to millions of years. Firstly, the emulator is used to simulate SAT changes for the late Pliocene for the period 3300-2800 kyr before present (BP) for a range of CO_2 concentrations. This interval occurs in the middle part of the Piacenzian Age, and was previously referred to as the "mid-Pliocene" (e.g. Dowsett and Robinson, 2009). During this time, global temperatures were warmer than pre-industrial (e.g. Dowsett et al., 2011, Haywood and Valdes, 2004, Lunt et al., 2010), before the transition to the intensified glacial-interglacial cycles that are associated with Quaternary climate (Lisiecki and Raymo, 2007). The emulator is then applied to future climate, simulating temperature and precipitation data for the next 200 kyr AP for a range of anthropogenic CO_2 emissions scenarios. Regional changes in climate at a number of European sites (grid boxes) are presented, selected either because they have been identified as adopted or proposed locations for the geological disposal of solid radioactive wastes, as in the cases of Forsmark, Sweden and El Cabril, Spain, or simply as reference locations where a suitable site has not yet been identified, as in the cases of Switzerland and the UK.

The paper is structured such that the theoretical basis of the emulator is described in Section 3.3, the GCM model description and simulations are presented in Section 3.4 and an account of how the emulator is trained and evaluated is given in Section 3.5. Section 3.6 presents illustrative examples of a number of potential applications of the emulator for the late Pliocene. Further examples of the application of the emulator to the next 200 kyr are described in Section 3.7. Section 3.8 includes a description and discussion of uncertainties associated with the methodology and tools, and the conclusions of this study are presented in Section 3.9.

3.3 Theoretical basis of the emulator

The emulator is a statistical representation of a more complex model, in this case a GCM. It works on the principle that a relatively small number of experiments are carried out using the GCM, which fill the entire multidimensional input space (in this case, four dimensions consisting of three orbital dimensions and a CO_2 dimension), albeit rather sparsely, are carried out using the GCM. The statistical model is calibrated on these experiments, with the aim of being able to interpolate the GCM results such that it can provide a prediction of the output that the GCM would produce if it were run using any particular input configuration (i.e. any set of orbital and CO_2 conditions). If successful (as can be tested by comparing emulator results with additional GCM results not included in the calibration), no further experiments are required using the GCM; the emulator can then be used to produce results for any set of conditions or sequence of sets of conditions within the range of conditions on which it has been calibrated. It should not, of course, be used to extrapolate to conditions outside that range.

In this study, a principal component analysis (PCA) Gaussian Process (GP) emulator is used based on Sacks et al. (1989), with the subsequent Bayesian treatment of Kennedy and O'Hagan (2000) and Oakley and O'Hagan (2002), and a principal component analysis approach associated with Wilkinson (2010). All code for the GP package is available online at https://github.com/mcrucifix/GP. This principal component (PC) emulator is based on climate data for the entire global grid, as opposed to calibrating separate emulators based on data for individual grid boxes. This approach is taken because, for past climate, the global response overall is of interest, rather than just the response at specific locations individually. It also means that the results are consistent across all locations. For future climate, and in particular for application to nuclear waste, recommendations and results should be consistent across all sites, which would be especially relevant to a large country such as the US. Alternatively, for some countries and locations, it may be more appropriate to emulate specific grid boxes. The theoretical basis for the emulator and its calibration, is as follows.

Let $\boldsymbol{D}$ represent the design matrix of input data with n rows, where n is the total number of experiments performed with the GCM, here 60 (sum of the two ensembles). The number of columns, p, is defined by the number of dimensions in input parameter space. In this case, $p = 4$ representing the three orbital parameters and atmospheric CO_2 concentration. A more detailed explanation of the orbital input parameters is included in Section 3.4; however, briefly, they are longitude of perihelion (ϖ), obliquity (ε) and eccentricity (e), with longitude of perihelion and

eccentricity being combined under the form $e\sin\varpi$ and $e\cos\varpi$. For a set of i=1,n simulations, each simulation represents a point in input space, and is characterised by the input vector $\boldsymbol{x}_i$, i.e. a row of $\boldsymbol{D}$.

The corresponding GCM climate data output is denoted $f(\boldsymbol{x}_i)$, where the function f represents the GCM model. This output for all n experiments is contained in the matrix $\boldsymbol{Y}$. The raw output from the GCM is in the form of gridded data covering the Earth's surface, with 96 longitude by 73 latitude grid boxes. A principal component analysis is performed, to reduce the dimension of the output data before it is used to calibrate the emulator. Each column of $\boldsymbol{Y}$ contains the results for one experiment, i.e. $\boldsymbol{Y} = [y(x_1), \ldots, y(x_n)]$. Furthermore, the centred matrix $\boldsymbol{Y}^*$ can be defined as $\boldsymbol{Y} - \boldsymbol{Y}_{mean}$, where $\boldsymbol{Y}_{mean}$ is a matrix in which each row comprises a set of identical elements that are the row averages of $\boldsymbol{Y}$. The singular value decomposition (SVD) of $\boldsymbol{Y}^*$ is:

$$\boldsymbol{Y}^* = \boldsymbol{USV}^{T*} \qquad (3.1)$$

where $\boldsymbol{S}$ is the diagonal matrix containing the corresponding eigenvalues of $\boldsymbol{V}$, $\boldsymbol{V}$ is a matrix of the right singular vectors of $\boldsymbol{Y}$, and $\boldsymbol{U}$ is a matrix of the left singular vectors. $\boldsymbol{U}$ and $\boldsymbol{V}$ are orthonormal, and V^{T^*} denotes the conjugate transpose of the unitary matrix $\boldsymbol{V}$. The columns of $\boldsymbol{US}$ represent the principal components, and the columns of $\boldsymbol{V}$ the principal directions/axes. Each column of $\boldsymbol{U}$ represents an eigenvector, $\boldsymbol{u}_k$, and $\boldsymbol{VS}$ provides the projection coefficients $\boldsymbol{\theta}_k$. Specifically, for experiment i, $a_k(\boldsymbol{x}_i) = \sum_k \boldsymbol{V}_{ik}\boldsymbol{S}_{kk}$ gives the projection coefficient for the kth eigenvector. The eigenvectors are ordered by decreasing eigenvalue, and in practice only a relatively small number of the eigenvectors will be retained (n'), typically selected on the basis of the largest values of $a_k(\boldsymbol{x})$. Thus:

$$y(\boldsymbol{x}) = \sum_{k=1}^{n'} a_k(\boldsymbol{x})\boldsymbol{u}_k \qquad (3.2)$$

The emulator is calibrated using the reduced dimension output data rather than the raw spatial climate data. However, for simplicity, a simple GP emulator will first be considered. For this, the model output $f(\boldsymbol{x})$ for the input conditions $\boldsymbol{x}$ is modelled as a stochastic quantity that is defined by a Gaussian process. Its distribution is fully specified by its mean function, $m(\boldsymbol{x})$, and its covariance function, $V(\boldsymbol{x}, \boldsymbol{x}')$, which may be written:

$$f(\boldsymbol{x}) = GP[m(\boldsymbol{x}), V(\boldsymbol{x}, \boldsymbol{x}')] \qquad (3.3)$$

The mean and covariance functions take the form:

$$m(\boldsymbol{x}) = \boldsymbol{h}(\boldsymbol{x})^T \boldsymbol{\beta} \quad (3.4)$$

$$V(\boldsymbol{x}, \boldsymbol{x}') = \sigma^2 [c(\boldsymbol{x}, \boldsymbol{x}')] \quad (3.5)$$

where $\boldsymbol{h}(\boldsymbol{x})$ is a vector of known regression functions of the inputs, $\boldsymbol{\beta}$ is a column vector of regression coefficients corresponding to the mean function, $c(\boldsymbol{x}, \boldsymbol{x}')$ is the GP correlation function and σ^2 is a scaling value for the covariance function. $\boldsymbol{h}(\boldsymbol{x})$ and $\boldsymbol{\beta}$ both have q components and, as before, ^{T} denotes the transpose operation.

A range of options are available for the regression functions $\boldsymbol{h}(\boldsymbol{x})$ and the GP correlation function c, the most suitable of which depends on the application of the emulator. Any existing knowledge that the user may have about the expected response of the GCM to the input parameters can be used to inform their function choices. However, if the emulator performs poorly, an alternative function can be selected which may prove to be more suitable.

A linear model is assumed, $\boldsymbol{h}(\boldsymbol{x})^T = (1, \boldsymbol{x}^T)$, with any non-linearities in the GCM response being absorbed by the stochastic component of the GP. The correlation function is exponential decay with a nugget, a detailed discussion of which can be found in Andrianakis and Challenor (2012). Hence, for the input parameters a=1, p, the correlation function can be written as:

$$c(\boldsymbol{x}, \boldsymbol{x}') = exp\left[-\sum_{a=1}^{p} \left\{ \frac{(x_a - x_a')}{\delta_a} \right\}^2 \right] + \nu I_{x=x'} \quad (3.6)$$

where δ is the correlation length hyperparameter for each input, v is the nugget term, and I is an operator which is equal to 1 when $\boldsymbol{x} = \boldsymbol{x}'$, and 0 otherwise. The nugget term has a number of functions in this application, including accounting for any non-linearity in the output response to the inputs and for non-explicitly specified inactive inputs, such as initial conditions and experiment, and averaging length. It also represents the effects of lower-order PCs that are excluded from the emulator.

Now consider run i, which has inputs characterised by $\boldsymbol{x}_i$ and outputs by $\boldsymbol{y}_i$. Let $\boldsymbol{H}$ be the design matrix relating to the GCM output, where row i represents the regressors $\boldsymbol{h}(\boldsymbol{x}_i)$, making $\boldsymbol{H}$ an n by q matrix. The adopted modelling approach states that the prior distribution of $\boldsymbol{y}$ is Gaussian, characterised by $\boldsymbol{y} \sim N(\boldsymbol{H\beta}, \sigma^2 \boldsymbol{A})$, with $\boldsymbol{A}_{ij} = c(\boldsymbol{x}_i, \boldsymbol{x}_j)$.

Following the specification of the prior model above, a Bayesian approach is now used to update the prior distribution. The posterior estimate of the GCM output is described by:

$$m^*(\boldsymbol{x}) = \boldsymbol{h}(\boldsymbol{x})^T\widehat{\boldsymbol{\beta}} + t(\boldsymbol{x})\boldsymbol{A}^{-1}(\boldsymbol{y} - \boldsymbol{H}\widehat{\boldsymbol{\beta}}) \quad (3.7)$$

$$V^*(\boldsymbol{x}, \boldsymbol{x}') = \sigma^2[c(\boldsymbol{x}, \boldsymbol{x}') - t(\boldsymbol{x})^T\boldsymbol{A}^{-1}t(\boldsymbol{x}') + \boldsymbol{P}(\boldsymbol{x})(\boldsymbol{H}^T\boldsymbol{A}^{-1}\boldsymbol{H})^{-1}\boldsymbol{P}(\boldsymbol{x}')^T] \quad (3.8)$$

where

$$\sigma^2 = (n - q - 2)^{-1}(\boldsymbol{y} - \boldsymbol{H}\widehat{\boldsymbol{\beta}})^T\boldsymbol{A}^{-1}(\boldsymbol{y} - \boldsymbol{H}\widehat{\boldsymbol{\beta}}) \quad (3.9)$$

$$\widehat{\boldsymbol{\beta}} = (\boldsymbol{H}^T\boldsymbol{A}^{-1}\boldsymbol{H})^{-1}\boldsymbol{H}^T\boldsymbol{A}^{-1}\boldsymbol{y} \quad (3.10)$$

and $t(\boldsymbol{x})_i = c(\boldsymbol{x}, \boldsymbol{x}_i)$ and $\boldsymbol{P}(\boldsymbol{x}) = h(\boldsymbol{x})^T - t(\boldsymbol{x})^T\boldsymbol{A}^{-1}\boldsymbol{H}$.

The suggestion of Berger et al. (2001) is followed and a vague prior ($\boldsymbol{\beta}$,σ^2) is assumed which is proportional to σ^2, an approach that has been adopted by several other studies, including Oakley and O'Hagan (2002), Bastos and O'Hagan (2009), Araya-Melo et al. (2015) and Bounceur et al. (2015). The posterior distribution of the GCM output is a student-t distribution with $n - q$ degrees of freedom, but is sufficiently close to being Gaussian for this application.

Now, taking the output from the PCA performed earlier, the GP model is applied to each basis vector ($a_k(\boldsymbol{x})$), which has been updated according to Eq. 7 and 8, in turn. Thus:

$$a_k(\boldsymbol{x}) = GP[m_k(\boldsymbol{x}), V_k(\boldsymbol{x}, \boldsymbol{x}')] \quad (3.11)$$

where mean and covariance functions take the form:

$$\boldsymbol{m}(\boldsymbol{x}) = \sum_{k=1}^{n'} m_k(\boldsymbol{x})\boldsymbol{u}_k \quad (3.12)$$

$$\boldsymbol{V}(\boldsymbol{x}, \boldsymbol{x}') = \sum_{k=1}^{n'} V_k(\boldsymbol{x}, \boldsymbol{x}')\boldsymbol{u}_k\boldsymbol{u}_k^T + \sum_{k=n'+1}^{n} \frac{\boldsymbol{s}_{kk}^2}{n}\boldsymbol{u}_k\boldsymbol{u}_k^T \quad (3.13)$$

The values of the hyperparameters are chosen by maximising the likelihood of the emulator, following Kennedy and O'Hagan (2000), and based on the following expression from Andrianakis and Challenor (2012):

$$logL(\nu, \delta) = -\frac{1}{2}(log(|\boldsymbol{A}||\boldsymbol{H}^T\boldsymbol{A}^{-1}\boldsymbol{H}|) + (n - q)\, log(\hat{\sigma}^2)) + K \quad (3.14)$$

where K is an unspecified constant. On the recommendation of Andrianakis and Challenor (2012), a penalised likelihood is used, which limits the amplitude of the nugget:

$$logL^P(\nu, \delta) = logL(\nu, \delta) - 2\frac{\bar{M}(\nu, \delta)}{\epsilon\bar{M}(\infty)} \quad (3.15)$$

where $\bar{M}(\nu,\delta)$ is the Mean Squared Error between the GCM's output data and the emulator's posterior mean at the design points, defined by $\bar{M}(\nu,\delta) = \nu^2/n(\boldsymbol{y}-\boldsymbol{H\beta})^T\boldsymbol{A}^{-2}(\boldsymbol{y}-\boldsymbol{H\beta})$. $\bar{M}(\infty)$ is its asymptotic value at $\delta_i \rightarrow \infty$, given by $\bar{M}(\infty) = 1/n(\boldsymbol{y}-\boldsymbol{H\beta})^T(\boldsymbol{y}-\boldsymbol{H\beta})$. ϵ is assigned a value of 1.

To summarise, in this study ***D*** is a 60 x 4 matrix (*n* x *p*) of input data, consisting of 60 GCM simulations and four input factors (ε, $e\sin\varpi$, $e\cos\varpi$, and CO_2). The matrix ***Y*** contains the output data from the GCM, with dimensions of 96 x 73 x 60 (longitude x latitude x *n*). A PC analysis is performed on this output data, which is then used to calibrate the emulator. Four hyperparameters (δ) are used, due to there being four input factors, along with a nugget term (ν). The optimal values for these hyperparameters and the number of PCs retained are calculated during calibration and evaluation of the emulator, discussed in Section 3.5. The GCM data used in this study are mean annual SAT and mean annual precipitation, although these are each emulated separately using different emulators.

3.4 AOGCM simulations

3.4.1 Model description

To run the GCM simulations, the HadCM3 climate model (Gordon et al., 2000, Pope et al., 2000) was used – a coupled atmosphere-ocean general circulation model (AOGCM) developed by the UK Met Office. Although HadCM3 can no longer be considered as state-of-the-art when compared with the latest generation of GCMs, such as those used in the most recent IPCC Fifth Assessment Report (IPCC, 2013), its relative computational efficiency makes it ideal for running experiments for comparatively long periods of time (of several centuries) and for running large ensembles of simulations, as performed in this study. As a result, this model is still widely used in climate research, both in palaeoclimatic studies (e.g. Prescott et al., 2014) and in projections of future climate (Armstrong et al., 2016). In addition, it has previously been employed in research into climate sensitivity using a statistical emulator (Araya-Melo et al., 2015). The horizontal resolution of the atmosphere component is 2.5° latitude by 3.75° longitude with 19 vertical levels, whilst the ocean has a resolution of 1.25° by 1.25° and 20 vertical levels.

HadCM3 is coupled to the land surface scheme MOSES2.1 (Met Office Surface Exchange Scheme), which was developed from MOSES1 (Cox et al., 1999). It has been used in a wide range

of studies (Cox et al., 2000, Crucifix et al., 2005), and a comparison to MOSES1 and to observations is provided by Valdes et al. (2017). MOSES2.1 in turn is coupled to the dynamic vegetation model TRIFFID (Top-down Representation of Interactive Foliage and Flora Including Dynamics) (Cox et al., 2002). TRIFFID calculates the global distribution of vegetation based on five plant functional types: broadleaf trees, needleleaf trees, C3 grasses, C4 grasses and shrubs. Further details of the overall model setup, denoted HadCM3B-M2.1aE, can be found in Valdes et al. (2017).

3.4.2 Experimental design

In the simulations, four input parameters are varied: atmospheric CO_2 concentration and the three main orbital parameters of longitude of perihelion (ϖ), obliquity (ε) and eccentricity (e). The extents of the GrIS and WAIS are also modified, although only between two modes – their present-day configurations and their reduced-extent Pliocene configurations (Haywood et al., 2016). The extent and thickness of the East Antarctic Ice Sheet (EAIS) was not modified. A more detailed description of the continental ice sheet configurations is provided in Section 3.45.

Eccentricity and longitude of perihelion were combined under the forms $e\sin\varpi$ and $e\cos\varpi$ given that, in general at any point in the year, insolation can be approximated as a linear combination of these two terms and obliquity (ε) (Loutre, 1993). The ranges of orbital and CO_2 values considered are appropriate for the next 1 Myr and a range of anthropogenic emissions scenarios. For the astronomical parameters, calculated using the Laskar et al. (2004) solution, this essentially equates to their full ranges of -0.055 to 0.055 for $e\sin\varpi$ and $e\cos\varpi$, and 22.2^o to 24.4^o for ε.

For CO_2, an emissions scenario is selected from Lord et al. (2016) in which atmospheric CO_2 follows observed historical concentrations from 1750 CE (Common Era) to 2010 CE (Meinshausen et al., 2011), after which emissions follow a logistic trajectory, resulting in cumulative total emissions of 10,000 Pg C by year ~3200 CE. This experiment was run for 1 Myr using the cGENIE Earth system model, and aims to represent a maximum total future CO_2 release. To put this into perspective: current estimates of fossil fuel reserves are approximately 1000 Pg C, with an estimated ~4000 Pg C in fossil fuel resources that may be extractable in the future (McGlade and Ekins, 2015), and up to 20-25,000 Pg C in nonconventional resources such as

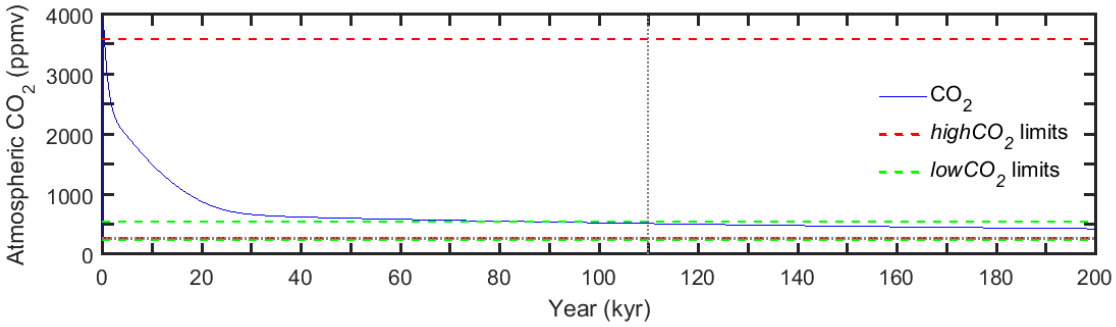

Figure 3.1. Time series of atmospheric CO_2 concentration (ppmv) for the next 200 kyr following logistic CO_2 emissions of 10,000 PgC, run using the cGENIE model (Lord et al., 2016). Also shown are the upper and lower CO_2 limits of the highCO_2 (red dashed lines) and lowCO_2 (green dashed lines) ensembles. The pre-industrial CO_2 concentration of 280 ppmv (horizontal grey dotted line), and the 110 kyr cut-off for the highCO_2 ensemble (vertical grey dotted line) are included for reference.

methane clathrates (Rogner, 1997). The evolution of atmospheric CO_2 concentration over the next 200 kyr for this emissions scenario is show in Figure 3.1. Although in the *c*GENIE simulation, atmospheric CO_2 reaches a maximum of 3900 parts per million (ppmv) within the first few hundred years, this concentration is not at equilibrium and only lasts for a couple of decades before decreasing. As a result, the concentration at 500 years into the experiment, 3600 ppmv, is chosen as the upper CO_2 limit, which means that the climatic effects of emissions of more than 10,000 Pg C cannot be estimated with the emulator.

By the end of the 1 Myr emissions scenario, atmospheric CO_2 concentrations have nearly declined to pre-industrial levels, reaching 285 ppmv. However, this experiment does not account for natural variations in the carbon cycle, which result in periodic fluctuations in CO_2. For example, during the Holocene (11 kyr BP to ~1750 CE) atmospheric CO_2 varied between 260 and 280 ppmv (Monnin et al., 2004). A value of 250 ppmv is therefore deemed to be appropriate to account for these natural variations in an unglaciated world, in addition to possible uncertainties in the model and hence is assumed as the value of the lower CO_2 limit in the ensemble.

The orbital and CO_2 parameter ranges that have been selected are also applicable to unglaciated periods during the late Pliocene, when atmospheric CO_2 was estimated to be higher than pre-industrial values (Raymo et al., 1996, Martinez-Boti et al., 2015). This study does not consider or attempt to simulate past or future glacial episodes, which may be accompanied by larger continental ice sheets (see Section 3.8 for more discussion), although the conditions required to initiate the next glaciation, and extending the ensemble of GCM simulations to represent glacial states, are being investigated in a forthcoming study. The underlying

assumption of this ensemble is that it is suitable for simulating periods for which the CO_2 concentration is high enough to prevent entry into a glacial state.

Two ensembles were generated, each made up of 40 simulations, meeting the recommended 10 experiments per input parameter (Loeppky et al., 2009). One ensemble includes orbital values suitable for the next 1 Myr and a relatively small range of lower CO_2 values, whereas the other ensemble represents the shorter-term future with a reduced range of orbital values and a larger range of higher CO_2 concentrations. This approach was adopted because various studies have shown that on geological timescales of thousands to hundreds of thousands of years, an emission of anthropogenic CO_2 to the atmosphere is taken up by natural carbon cycle processes over different timescales (Archer et al., 1997, Lord et al., 2016). A relatively large fraction of the CO_2 perturbation is neutralised on shorter timescales of 10^3-10^4 years, but it takes 10^5-10^6 years for atmospheric CO_2 concentrations to very slowly return to pre-industrial levels (Lenton and Britton, 2006, Colbourn et al., 2015, Lord et al., 2016), if the effects of glacial-interglacial cycles and other natural variations, such as those due to imbalances between volcanic outgassing and weathering, are excluded. Hence, only a relatively short portion of the full million years has very high CO_2 concentrations under any emissions scenario, with the major part of the time having a CO_2 concentration no more than several hundred ppmv above pre-industrial, as demonstrated in Figure 3.1.

The parameter ranges for the two ensembles, which are referred to as "*highCO_2*" and "*lowCO_2*", are given in Table 3.1. The cut-off point for the *highCO_2* ensemble is set at 110 kyr AP, as after this time eccentricity, which remained relatively low prior to this time, starts to increase more rapidly, and variability in $e\sin\varpi$ and $e\cos\varpi$ increases. This first ensemble therefore has CO_2 sampled up to 3600 ppmv, and the orbital parameters are sampled within the reduced range of values that will occur over the next 110 kyr. The *lowCO_2* ensemble samples the full range of orbital values and the upper CO_2 limit is set to 560 ppmv. This upper limit also covers the range of CO_2 concentrations that have been estimated for the late Pliocene (Seki et al., 2010, e.g. Martinez-Boti et al., 2015). At 110 kyr in the 10,000 Pg C emissions scenario, the atmospheric CO_2 concentration is 542 ppmv, which is rounded up to twice the pre-industrial atmospheric CO_2 concentration (560 ppmv = 2*280 ppmv), a common scenario used in future climate-change modelling studies.

The benefits of the approach of having separate ensembles for high and low CO_2 mean that both parameter ranges have sufficient sampling density, whilst also reducing the chance of unrealistic sets of parameters, in particular for the period of the next 110 kyr. During this time,

Table 3.1. Ensembles setup: sampling ranges for input parameters (obliquity, esinϖ, ecosϖ and CO_2) for the highCO_2 and lowCO_2 ensembles.

Ensemble	Time covered from present day (AP)	Parameter	Sampling range	
			Minimum	Maximum
highCO_2	110 kyr	ε (°)	22.3	24.3
		*e*sinϖ	-0.016	0.016
		*e*cosϖ	-0.016	0.015
		CO_2 (ppmv)	280	3600
lowCO_2	1 Myr	ε (°)	22.2	24.4
		*e*sinϖ	-0.055	0.055
		*e*cosϖ	-0.055	0.055
		CO_2 (ppmv)	250	560

CO_2 is likely to be comparatively high, while eccentricity remains relatively low, and *e*sinϖ and *e*cosϖ exhibit relatively low variability. Having a separate ensemble in which CO_2 and the orbital parameters are only sampled within the ranges experienced within the next 110 kyr avoids wasting computing time on parameter combinations that are highly unlikely to occur, such as very high CO_2 and very high eccentricity. This methodology also provides the additional benefit of the low CO_2 emulator being applicable to palaeo-modelling studies, as the ensemble encompasses an appropriate range of CO_2 and orbital values for many past periods of interest, such as the Pliocene.

3.4.3 Generation of experiment ensembles

The Latin hypercube sampling function from the MATLAB Statistics and Machine Learning Toolbox (LHC; (MATLAB, 2012b)) was used to generate the two ensembles, thereby efficiently sampling the four-dimensional input parameter space (Mckay et al., 1979). Briefly, this method divides the parameter space within the prescribed ranges into *n* equally probable intervals, *n* being the number of experiments required, which in this case is 40 per ensemble. *n* points are then selected for each input variable, one from each interval, without replacement. The sample points for the four variables are then randomly combined. The LHC sampling function also includes an option to maximise the minimum distance between all pairs of points (the maxi-min criterion), which is utilised here to ensure the set of experiments is optimally space filling.

For each ensemble, 3000 sample sets were created, with each set consisting of an *n* by *p* matrix, ***X***, containing the four sampled input parameter values for each of the 40 experiments, and then the optimal sample set was selected as the final ensemble based on a number of criteria. Following Joseph and Hung (2008), it is sought, in addition to the maxi-min criterion, to maximise $det(\boldsymbol{X}^T\boldsymbol{X})$. Here, this determinant will be termed the "orthogonality", because the columns of the design matrix will approach orthogonality as this determinant is maximised (assuming that input factors are normalised). However, a limitation of the method of sampling the parameters $e\sin\varpi$ and $e\cos\varpi$, rather than eccentricity and longitude of perihelion directly, is that due to the nature of the $e\sin\varpi$ and $e\cos\varpi$ parameter space, the sampling process favours higher values of eccentricity over lower ones. This is not an issue for the longitude of perihelion, because when eccentricity is low the value of this parameter has little effect on insolation. However, the value of obliquity selected for a given eccentricity value could have a significant impact on climate, meaning that it is desirable to have a relatively large range of obliquity values for low (<0.01) and high (>0.05) eccentricity values, in order to sample the boundaries sufficiently. It was observed that the sample sets with the highest orthogonality had comparatively few, if any, values of low eccentricity, also meaning that a very limited number of obliquity values were sampled for low eccentricity. Therefore, the approach was adopted whereby all sample sets that demonstrated normalised orthogonality values that were more than 1 standard deviation above the mean orthogonality were selected. From these, the single sample set with the greatest range of obliquity values for low eccentricity, hence with maximal sampling coverage of the low eccentricity boundary, was selected as the final ensemble design. The input parameter values for the *highCO_2* and *lowCO_2* ensembles are given in Table 3.2, and the distributions in parameter space illustrated in Figure 3.2.

3.4.4 AOGCM simulations

The two CO_2 ensembles were initially run with constant modern-day GrIS and WAIS configurations (*modice*). All experiments were initiated from a pre-industrial spin-up experiment, with an atmospheric CO_2 concentration of 280 ppmv, and pre-industrial ice sheet extents and orbital conditions. Atmospheric CO_2 and the orbital parameters were kept constant throughout each simulation, and each experiment was run for a total of 500 model years. This simulation length allows the experiments with lower CO_2 to reach near-equilibrium at the surface. Experiments with higher CO_2 have not yet equilibrated by the end of this period; the significance of this is addressed in Section 3.4.6. A number of the very high CO_2 experiments caused the model

Table 3.2. Experiment setup: Orbital parameters (obliquity, eccentricity and longitude of perihelion) and atmospheric CO_2 concentration for simulations in the highCO_2 and lowCO_2 ensembles. All experiments in both ensembles were run with modern ice sheet (modice) configurations. Experiments shown in bold were also run with reduced ice sheet (lowice) configurations. The experiment number is given, and the experiment name is constructed using the ice sheet configuration, the ensemble name and the experiment number, for example: modice_lowCO2_1.

Ensemble	#	ε (°)	e -	ϖ (°)	CO_2 (ppmv)	Ensemble	#	ε (°)	e -	ϖ (°)	CO_2 (ppmv)
highCO_2	1	23.53	0.0093	240.3	3348.2	*lowCO_2*	1	22.99	0.0481	320.1	375.7
	2	24.24	0.0135	212.6	2159.3		2	23.02	0.0323	63.7	516.9
	3	22.38	0.0110	260.0	1645.0		3	22.81	0.0481	334.2	470.4
	4	24.07	0.0044	101.8	800.8		4	24.03	0.0537	84.9	390.3
	5	23.07	0.0203	313.0	1999.9		5	23.09	0.0294	293.8	325.3
	6	24.03	0.0087	184.9	3049.0		6	23.58	0.0098	325.1	337.5
	7	22.53	0.0163	162.0	900.9		7	23.72	0.0133	74.3	489.2
	8	23.57	0.0158	21.0	1746.3		**8**	**24.17**	**0.0066**	**174.1**	**346.0**
	9	23.34	0.0131	113.5	996.8		9	23.82	0.0400	48.2	260.6
	10	23.37	0.0198	220.2	3139.3		10	23.39	0.0412	53.8	409.5
	11	22.73	0.0187	236.1	1081.9		11	22.89	0.0531	115.2	436.6
	12	22.63	0.0121	184.8	2451.5		12	23.34	0.0281	133.9	504.4
	13	22.41	0.0131	192.8	3372.4		13	22.65	0.0473	102.6	555.6
	14	22.78	0.0137	299.3	448.2		14	23.20	0.0368	180.9	385.1
	15	22.97	0.0111	14.1	1225.7		15	23.96	0.0232	40.0	403.4
	16	22.90	0.0087	62.2	1841.9		16	24.27	0.0460	298.1	341.1
	17	23.63	0.0151	200.6	1151.6		17	22.35	0.0391	265.9	522.1
	18	23.77	0.0134	78.7	2101.7		18	23.91	0.0361	343.2	318.6
	19	23.73	0.0159	323.7	1526.6		**19**	**22.33**	**0.0484**	**324.2**	**264.5**
	20	24.29	0.0082	164.6	2890.4		20	22.94	0.0350	268.7	540.8
	21	**22.31**	**0.0038**	**299.1**	**1389.5**		21	22.68	0.0323	332.4	531.5
	22	23.42	0.0117	122.5	397.3		22	24.28	0.0387	118.7	446.7
	23	24.00	0.0101	206.6	303.4		23	23.60	0.0484	282.0	310.5
	24	22.48	0.0146	294.9	2845.7		24	24.19	0.0337	346.3	548.3
	25	22.57	0.0067	81.2	1341.2		25	24.14	0.0423	11.6	425.4
	26	22.93	0.0171	114.4	3516.0		26	22.20	0.0035	85.2	303.0
	27	24.13	0.0143	257.3	2951.8		27	22.78	0.0070	212.1	480.4
	28	23.00	0.0062	272.2	2274.6		28	22.72	0.0526	239.9	280.0
	29	23.95	0.0103	114.7	564.7		**29**	**23.65**	**0.0543**	**30.3**	**362.0**
	30	23.17	0.0169	56.7	1900.9		30	23.24	0.0351	200.4	411.9
	31	23.70	0.0122	1.4	773.0		31	23.87	0.0276	156.5	287.5
	32	23.24	0.0021	310.2	2582.1		32	22.25	0.0499	208.9	365.3
	33	22.81	0.0121	66.3	2386.5		33	22.54	0.0510	103.4	471.1
	34	**24.18**	**0.0145**	**36.6**	**668.2**		34	22.58	0.0404	292.2	544.5
	35	23.82	0.0075	10.8	2244.8		35	22.87	0.0530	20.9	498.2
	36	23.14	0.0141	314.1	3588.9		36	23.53	0.0414	147.0	507.0

37	23.49	0.0121	101.5	2760.4	37	22.39	0.0165	149.1	393.9
38	22.66	0.0162	69.5	2623.9	38	22.43	0.0537	175.0	484.8
39	23.28	0.0146	207.5	1484.8	39	24.38	0.0482	342.9	418.3
40	23.89	0.0092	21.1	3188.8	40	23.76	0.0504	127.0	528.1

to become unstable and the interpretation of these experiments is discussed in Section 3.4.4.1. A control simulation was also run for 500 years, with the atmospheric CO_2 concentration and the orbital parameters set at pre-industrial values. All climate variable results for the model, unless specified, are an average of the final 50 years of the simulation. Anomalies compared with the pre-industrial control (i.e. emulated minus pre-industrial) are discussed and used in the emulator, rather than absolute values, to account for biases in the control climate of the model.

3.4.4.1 Very high CO_2 simulations

As mentioned previously, experiments in the *highCO_2* ensemble with CO_2 concentrations of greater than 3100 ppmv become unstable. These experiments exhibit accelerating warming trends several hundred years into the simulation, which eventually cause the model to crash before completion. This is the result of a runaway positive feedback in the GCM caused, at least in part, by the vertical distribution of ozone in the model being prescribed for modern-day climate conditions. Consequently, the ozone distribution is not able to respond to changes in climate, meaning that when increased mean global temperatures result in an increase in altitude of the tropopause and hence an extension of the troposphere, relatively high concentrations of ozone, which were previously located in the stratosphere, enter the troposphere, resulting in runaway warming.

All other experiments ran for the full 500 years. However, those with a CO_2 concentration of 2000 ppmv or higher also exhibited accelerating warming trends before the end of the simulation. Consequently, only simulations with CO_2 concentrations of less than 2000 ppmv (equivalent to a total CO_2 release of up to 6000 Pg C) are included in the rest of this study, meaning the methodology is not appropriate for CO_2 values greater than this. This equates to 20 experiments in total from the *highCO_2* ensemble, with CO_2 concentrations ranging from 303 to 1901 ppmv. All 40 of the *lowCO_2* experiments were used.

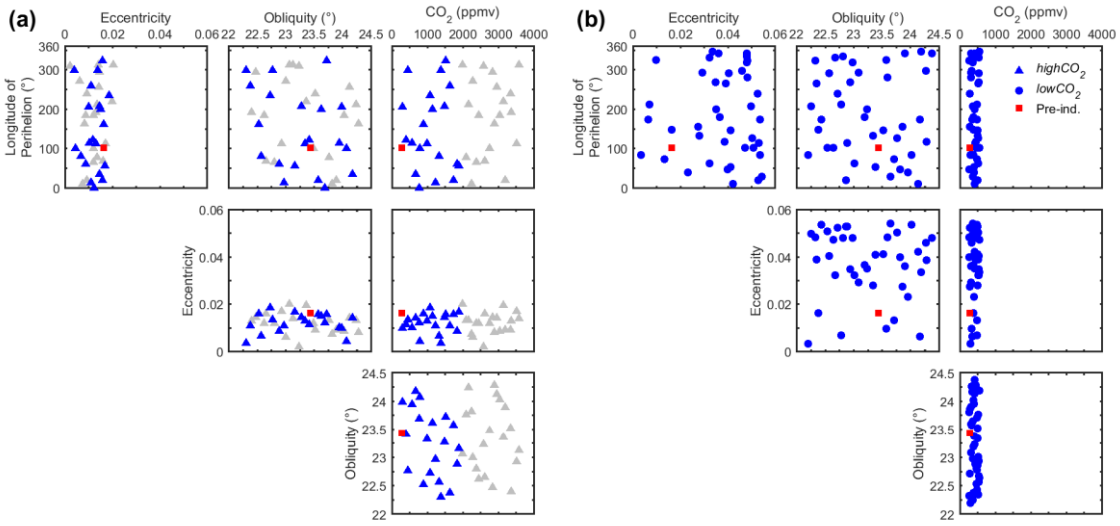

Figure 3.2. Distribution of 40 experiments produced by Latin hypercube sampling, displayed as two-dimensional projections through four-dimensional space. (a) highCO_2 ensemble, (b) lowCO_2 ensemble. The variables are eccentricity (e), longitude of perihelion (ϖ; degrees), obliquity (ε; degrees), and atmospheric CO_2 concentration (ppmv). A pre-industrial control simulation is shown in red. In the highCO_2 ensemble, experiments with CO_2 concentrations of more than 2000 ppmv, shown in grey, were excluded from the emulator.

3.4.5 Sensitivity to ice sheets

In addition to running the two ensembles with modern-day GrIS and WAIS configurations, the climatic impact of reducing the sizes of the ice sheets was also investigated. Many of the CO_2 values sampled, particularly in the *highCO_2* ensemble, are significantly higher than pre-industrial levels, and if the resulting climate were to persist for a long period of time it could result in significant melting of the continental ice sheets over timescales of 10^3-10^4 years (Charbit et al., 2008, Stone et al., 2010, Winkelmann et al., 2015).

Therefore, the *highCO_2* and *lowCO_2* ensembles were set up with reduced GrIS and WAIS extents (*lowice*), using the PRISM4 Pliocene reconstruction of the ice sheets (Dowsett et al., 2016). In this reconstruction, the GrIS is limited to high elevations in the Eastern Greenland Mountains, and no ice is present over Western Antarctica. Similar patterns of ice retreat have been simulated in response to future warming scenarios for the GrIS (Huybrechts and de Wolde, 1999, Greve, 2000, Ridley et al., 2005, Stone et al., 2010) and WAIS (Huybrechts and de Wolde, 1999, Winkelmann et al., 2015), equivalent to ~7 m (Ridley et al., 2005) and ~3 m (Bamber et al., 2009, Feldmann and Levermann, 2015) of global sea level rise, respectively. Large regions of the EAIS show minimal changes or slightly increased surface elevation, although there is substantial loss of ice in the Wilkes and Aurora subglacial basins (Haywood et al., 2016).

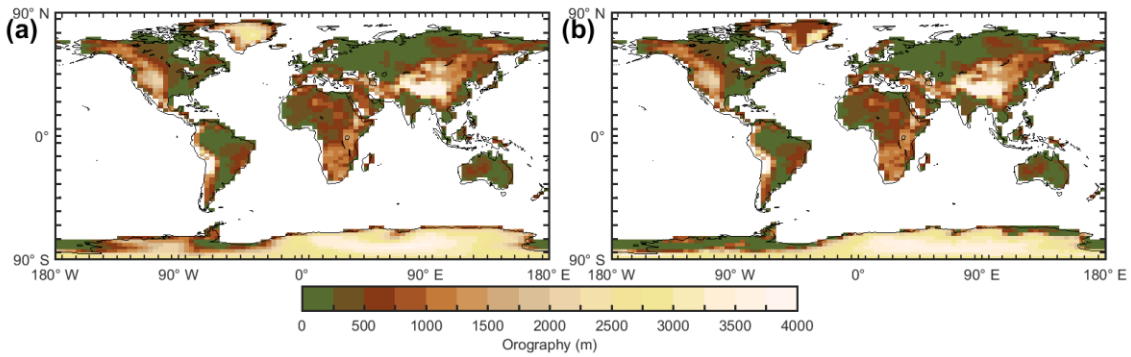

Figure 3.3. Orography (m) in the two ice sheet configuration ensembles. (a) modice ensemble, (b) lowice ensemble. Differences only occur over Greenland and Antarctica.

The same CO_2 and orbital parameter sample sets were used for both ice configuration ensembles to allow the impact of varying the ice sheet extents on climate to be directly compared. Only the Greenland and Antarctic grid boxes were modified; the boundary conditions for all other grid boxes, as well as the land/sea mask, were the same as in the modern-day ice sheet simulations. For Greenland and Antarctica, the extent and orography of the ice sheets was updated with the PRISM4 data, as well as the orography of any grid boxes that are projected to be ice-free. Soil properties, land surface type and snow cover were also updated for these grid boxes. Figure 3.3 compares the orography for the *modice* and *lowice* ensembles, clearly showing the reduced extents for the ice sheets.

3.4.5.1 Pattern scaling of reduced ice simulations

It was expected that reducing the size of the continental ice sheets would have a relatively localised impact on climate (Lunt et al., 2004), and that the effect would be of a linear nature. Therefore, a subset of five simulations from the two ensembles were selected as reduced ice sheet simulations (*lowCO_2* – experiments 8, 19 and 29; *highCO_2* – experiments 21, and 34; see Table 3.2), covering a range of orbital and CO_2 values.

A comparison of the mean annual SAT anomaly for the five experiments showed that the largest temperature changes occur over Greenland and Antarctica, particularly in regions where there is ice in the *modice* ensemble but that are ice free in *lowice*. The spatial pattern of the change is also fairly similar across the simulations, suggesting that the response of climate to the extents of the ice sheets is largely independent of orbital variations or CO_2 concentration. The SAT anomaly for the five *lowice* experiments compared with their *modice* equivalents was calculated, and then averaged across the experiments, shown in Figure 3.4a. The largest SAT

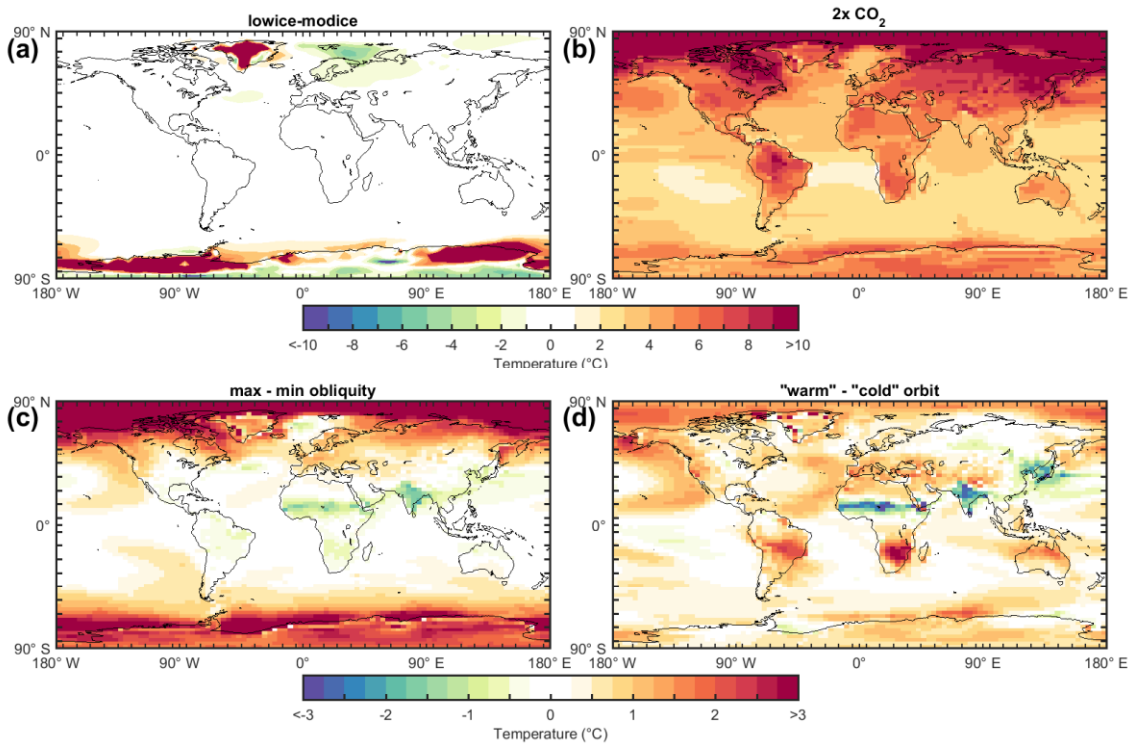

Figure 3.4. Mean annual SAT (°C) anomalies produced by the various climate forcings. (a) The lowice experiments compared with their modice equivalents, averaged across the five lowice experiments. (b):(d) Idealised experiments performed using the modice emulator. All orbital and CO_2 conditions are set to pre-industrial values unless specified: (b) 2x pre-industrial CO_2, (c) maximum obliquity compared to minimum obliquity, (d) "warm" orbital conditions (high eccentricity, NH summer at perihelion) compared to "cold" orbital conditions (low eccentricity, NH summer at aphelion). The different forcings result in global mean SAT anomalies of: (b) 4.2°C, (c) 0.4°C, and (d) 0.4°C.

anomalies occur locally to the GrIS and AIS, accompanied by smaller anomalies in some of the surrounding ocean regions (e.g. Barents and Ross Seas), with no significant changes in SAT elsewhere, in line with the results of Lunt et al. (2004), Toniazzo et al. (2004) and (Ridley et al., 2005). This SAT anomaly, caused by the reduced extents of the GrIS and WAIS, was then applied (added) to the mean annual SAT anomaly data for all other *highCO_2* and *lowCO_2 modice* experiments, to generate the SAT data for two *lowice* ensembles.

Also shown in Figure 3.4, for comparison, are mean annual SAT anomalies produced by the other forcings, including a doubling of CO_2, the difference between maximum and minimum obliquity and the difference between "warm" orbital conditions and "cold" orbital conditions. The warming caused by increased CO_2 is more widespread (Figure 3.4b), with the largest warming occurring at high latitudes and for land regions, in agreement with typical future-climate simulations (IPCC, 2013, p. 1059). The temperature change due to obliquity and "warm" versus "cold" orbital conditions is less than that for either reduced ice (compared to pre-industrial) or increased CO_2. Changes in obliquity have the largest impact on temperatures in high latitude regions, since the exposure of these regions to the sun's radiation is most affected by changes in

obliquity. Smaller temperature anomalies are observed over northern Africa and India and, since an increase in obliquity is indeed known to boost monsoon dynamics (e.g. Bosmans et al., 2015, Araya-Melo et al., 2015), changes in soil latent heat exchanges are therefore expected to contribute negatively to the temperature response. The comparison of "warm" versus "cold" orbital conditions, which highlights (annual mean) temperature changes primarily caused by precession, generally shows a warming trend, with the largest temperature changes occurring in monsoonal regions. Lower temperatures are observed in the Northern Hemisphere over northern Africa, India and, East Asia, whilst warmer temperatures occur in the Southern Hemisphere over South America, southern Africa and Australia. Figure 3.4 demonstrates that the temperature forcing caused by CO_2 affects mean annual temperatures on a global scale, whilst the forcing due to ice sheet and orbital changes affects mean annual temperatures in specific regions, having a limited impact on global mean temperatures. This is supported by the relatively high global mean SAT anomaly for the $2xCO_2$ scenario of 4.2°C, compared with the lower SAT anomalies that result from the obliquity and precession forcing of 0.4°C each (see caption of Figure 3.4).

3.4.6 Calculation of equilibrated climate

Given the high values of CO_2 concentration in many of the experiments, particularly in the *highCO_2* ensemble, even by the end of the 500 yr running period the climate has not yet reached steady state. The fully equilibrated climate response was therefore estimated using the methods described below.

3.4.6.1 Gregory plots

In order to estimate the equilibrated response, the method of Gregory et al. (2004) was applied to the model results, regressing the net radiative flux at the top of the atmosphere (TOA) against the global average SAT change, as displayed in figures termed Gregory plots (Andrews et al., 2012, Andrews et al., 2015, Gregory et al., 2015). In this method, for an experiment which has a constant forcing applied (i.e. with no inter-annual variation) it can be assumed that:

$$N = F - \alpha \Delta T \qquad (3.16)$$

where N is the change in the global mean net TOA radiative flux (W m^{-2}), F is the effective radiative forcing (W m^{-2}; positive downwards), α is the climate feedback parameter (W m^{-2} °C^{-1}),

and ΔT is the global mean annual SAT change compared with the control simulation (°C). This method works on the assumption that if F and α are constant, N is an approximately linear function of ΔT. By linearly regressing ΔT against N, both F (intercept of the line at $\Delta T = 0$) and -α (slope of the line) can be diagnosed. The intercept of the line at $N = 0$ provides an estimate of the equilibrium SAT change (relative to the pre-industrial SAT) for the experiment, denoted $\Delta T_{eq}{}^{g}$ to indicate it was calculated from the Gregory plots, and is equal to F/α. This is in contrast to the SAT change calculated directly from the GCM model data by averaging the final 50 years of the experiment (ΔT_{500}).

The Gregory plots for two *modice* experiments, *modice_lowCO2_13* (CO_2 555.6 ppmv) and *modice_highCO2_17* (CO_2 1151.6 ppmv), are shown in Figure 3.5. These experiments were selected as they have CO_2 values nearest to the 2x and 4x pre-industrial CO_2 scenarios that are commonly used in idealised future climate experiments. For each experiment, mean annual data are plotted for years 1-20 of the simulation, and mean decadal data for years 21-500. The regression fits are to mean annual data in each case, and years 1-20 and 21-500 were fitted separately. The values for F and α estimated from Figure 3.5 are presented in Table 3.3. These values are slightly lower than those identified in other studies using the same method. For example, Gregory et al. (2004) used HadCM3 to run experiments with 2x and 4xCO_2, obtaining values for years 1-90 of 3.9 ± 0.2 and 7.5 ± 0.3 W m^{-2} for F, and -1.26 ± 0.09 and -1.19 ± 0.07 W m^{-2} °C^{-1} for α, respectively. Andrews et al. (2015) calculated F to be 7.73 ± 0.26 W m^{-2} and α to be -1.25 W m^{-2} °C^{-1} for years 1-20 and -0.74 W m^{-2} °C^{-1} for years 21-100 for 4xCO_2 simulations using HadCM3. The differences between the results here and theirs may be due to the fact that MOSES2.1 and the TRIFFID vegetation model was used, whereas they used MOSES1, which is a different land-surface scheme and does not account for vegetation feedbacks.

The decrease in the climate response parameter (α) as the experiment progresses suggests that the strength of the climate feedbacks changes as the climate evolves over time. Consequently, the ΔT intercept ($N = 0$) for the first 20 years of the simulation underestimates the actual warming of the model. Over longer timescales, the slope of the regression line becomes less negative, implying that the sensitivity of the climate system to the forcing increases (Gregory et al., 2004, Andrews et al., 2015, Knutti and Rugenstein, 2015). This non-linearity has been found to be particularly apparent in cloud feedback parameters, in particular shortwave cloud feedback processes (Andrews et al., 2012, Andrews et al., 2015). A number of studies have attributed this strengthening of the feedbacks to changes in the pattern of surface warming

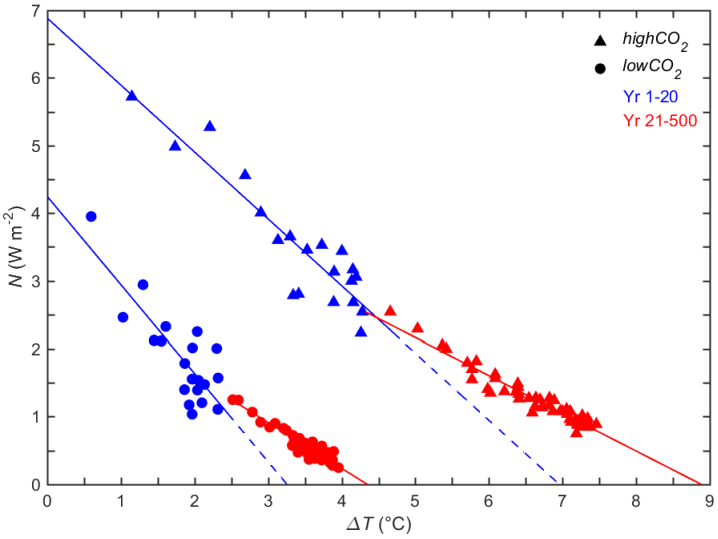

Figure 3.5. Gregory plot showing change in TOA net downward radiation flux (N; W m^{-2}) as a function of change in global mean annual SAT (ΔT; °C) for approximate 2xCO_2 (modice_lowCO2_13; circles) and 4xCO_2 (modice_highCO2_17; triangles) experiments. Lines show regression fits to the global mean annual data points for years 1-20 (blue) and years 21-500 (red). Data points are mean annual data for years 1-20 (blue) and mean decadal data for years 21-500 (red). The ΔT intercepts (N=0) of the red lines give the estimated equilibrated SAT (ΔT_{eq}^{g}) for the two experiments. The ΔT intercepts of the dashed blue lines represent the equilibrium that the experiment would have reached if the feedback strengths in the first 20 years had been maintained. SAT is shown as an anomaly compared with the pre-industrial control simulation.

(Williams et al., 2008), mainly in the eastern tropical Pacific where an intensification of warming can occur after a few decades, but also in other regions such as the Southern Ocean (Andrews et al., 2015). The impact of variations in ocean heat uptake has also been suggested to be a contributing factor (Held et al., 2010, Winton et al., 2010, Geoffroy et al., 2013).

The ΔT intercept ($N = 0$) for years 21-500 is taken to give the equilibrium temperature change (ΔT_{eq}^{g}) for the experiments, equating to values of 4.3°C and 8.9°C for the 2x and 4xCO_2 scenarios in Figure 3.5. A limitation of this approach is that it assumes that the response of

Table 3.3. Parameter values estimated from Gregory plots for the 2x and 4x pre-industrial CO_2 simulations. Shown are the effective radiative forcing (F; W m^{-2}) and the climate feedback parameter (α; W m^{-2} °C^{-1}) for years 1-20 and years 21-100. The uncertainties are the standard error from the linear regression.

Simulation		*F* (W m^{-2})		*α* (W m^{-2} °C^{-1})	
		yr 1-20	yr 21-100	yr 1-20	yr 21-100
2xCO_2	*modice_lowCO2_13*	4.24 ± 0.4	-	-1.30 ± 0.2	-0.68 ± 0.05
4xCO_2	*modice_highCO2_17*	6.88 ± 0.3	-	-0.99 ± 0.1	-0.56 ± 0.02

climate to a forcing is linear after the first 20 years, which has been shown to be unlikely in longer simulations of several decades or centuries (Winton et al., 2010, Armour et al., 2013, Andrews et al., 2015). However, a comparison of the difference in temperature response to upper- and deep-ocean heat uptake and its contribution to the relationship between net radiative flux change (N) and global temperature change (ΔT) in Geoffroy et al. (2013) indicated that the method of Gregory et al. (2004) of fitting two separate linear models to the early and subsequent (N, ΔT) data gives a good approximation of $\Delta T_{eq}{}^{g}$, F and α as they have been calculated here. A study by Li et al. (2013) also found that, using the Gregory plot methodology, $\Delta T_{eq}{}^{g}$ was estimated to within 10% of its actual value, obtained by running the simulation very close to equilibrium (~6000 yr). However, this was using the ECHAM5/MPIOM model, meaning that it is not necessarily also true for HadCM3.

Given that the slope of the 21-500 yr regression line appears to become shallower with time, the estimates of $\Delta T_{eq}{}^{g}$ should be taken as a lower limit of the actual equilibrated SAT anomaly. However, this tendency to flatten, particularly as the CO_2 concentration is increased, further justifies the use of the Gregory methodology; by the end of 500 years the high CO_2 experiments have not yet reached steady state, and even in the lower CO_2 experiments SAT is increasing very slowly, so will likely take a long time to reach equilibrium. It would therefore not be feasible to run most of these experiments to steady state using a GCM, due to the associated computational and time requirements. Furthermore, on longer timescales the boundary conditions (orbital characteristics and, more importantly, atmospheric CO_2 concentrations) would have changed, such that, in reality, equilibrium would never be attained.

3.4.6.2 Equilibrated climate

The final estimates of $\Delta T_{eq}{}^{g}$ for the *lowCO_2* and *highCO_2 modice* ensembles range from a minimum of -0.4°C (CO_2 264.5 ppmv) to a maximum of 12.5°C (CO_2 1900.9 ppmv). Figure 3.6 illustrates the difference between global mean annual SAT anomaly calculated from the GCM model data (ΔT_{500}) and calculated using the Gregory plot ($\Delta T_{eq}{}^{g}$). Experiments with CO_2 below or near to pre-industrial levels tended to reach equilibrium by the end of the 500 years making a Gregory plot unnecessary, hence $\Delta T_{eq}{}^{g}$ is taken to be the same as ΔT_{500} in these cases. As CO_2 increases, the data points in Figure 3.6 deviate further from the 1:1 line. This is the result of the ratio between $\Delta T_{eq}{}^{g}$ and ΔT_{500} increasing, as the experiments grow increasingly far from equilibrium by the end of the GCM run with increasing CO_2.

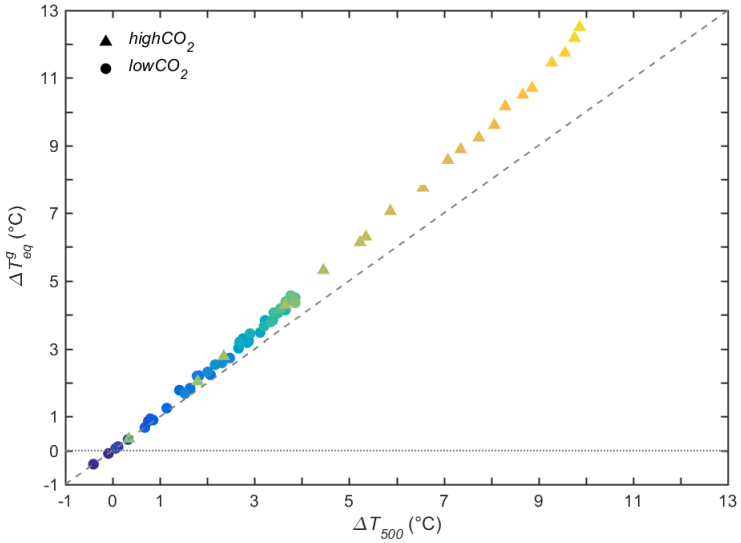

Figure 3.6. Equilibrated global mean annual change in SAT (ΔT_{eq}^{g}; °C) estimated using the methodology of Gregory et al. (2004) against global mean annual change in SAT (ΔT_{500}; °C) at year 500 (average of final 50 years) for the lowCO_2 (circles) and highCO_2 (triangles) modice ensembles. The colours of the points indicate the CO_2 concentration of the experiment, from low (blue) to high (yellow). The 1:1 line (dashed) is included for reference. SAT is shown as an anomaly compared with the pre-industrial control simulation.

Next the ratio between ΔT_{eq}^{g} and ΔT_{500} was calculated for each experiment ($\Delta T_{eq}^{g}/\Delta T_{500}$), which represents the fractional increase in climate change still due to occur after the end of the 500-year model run in order for steady state to be reached. To estimate the fully equilibrated climate anomaly, the spatial distribution of mean annual SAT anomaly was multiplied by the $\Delta T_{eq}^{g}/\Delta T_{500}$ ratio. The ratio identified for each experiment is assumed to be equally applicable to all grid boxes. The same scaling ratio was also applied to the precipitation anomaly data to estimate the equilibrated mean annual precipitation.

The equilibrated global mean annual SAT anomaly (ΔT_{eq}) for the *highCO_2* and *lowCO_2 modice* ensembles is plotted against ln(CO_2) in Figure 3.7, along with ΔT_{500} for reference.. Also plotted on Figure 3.7 are a number of lines illustrating idealised relationships between ΔT_{eq} and CO_2 based on a range of climate sensitivities. The most recent IPCC report suggested that the likely range for equilibrium climate sensitivity is 1.5°C to 4.5°C (IPCC, 2013), hence sensitivities of 1.5°C, 3°C and 4.5°C have been plotted. The size of the correction required to calculate ΔT_{eq} from ΔT_{500} increases with increasing CO_2, and brings the final temperature estimates in line with the expected response (red lines), resulting in further increased confidence. The ΔT_{eq} estimated for the experiments generally follows the upper line, equivalent to an equilibrium climate sensitivity of 4.5°C, which is higher than a previous estimate of 3.3°C for HadCM3 (Williams et al., 2001). This difference may be due to the simulations here being "fully equilibrated" following the

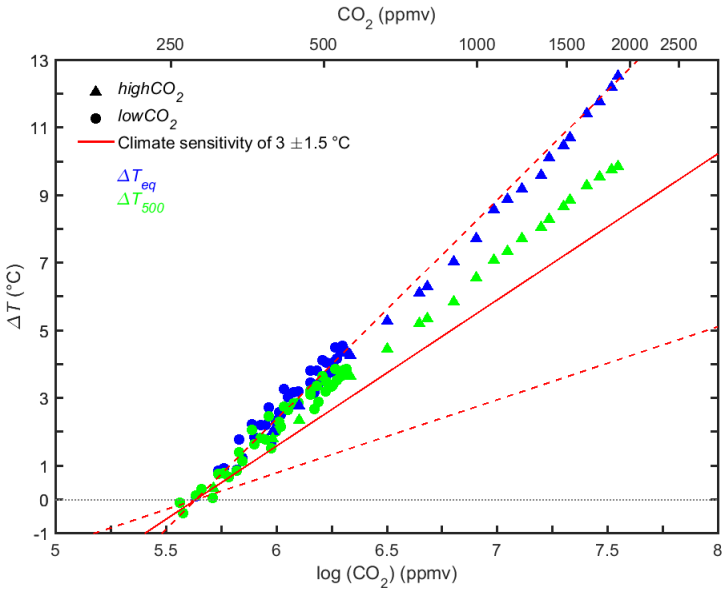

Figure 3.7. Equilibrated global mean annual change in SAT (ΔT_{eq}; °C; blue), estimated by applying the $\Delta T_{eq}{}^{g}/\Delta T_{500}$ ratio identified using the Gregory methodology to the GCM data, against atmospheric CO_2 (ppmv) for the lowCO_2 (circles) and highCO_2 (triangles) modice ensembles. Also shown is ΔT_{500} (green), along with the idealised relationship between ln(CO_2) and ΔT (red lines) for a climate sensitivity of 3°C (solid), 1.5°C (lower dashed) and 4.5°C (upper dashed) (IPCC, 2013). SAT is shown as an anomaly compared with the pre-industrial control simulation.

application of the Gregory plot methodology. In addition, Williams et al. (2001) used an older version of HadCM3 and prescribed vegetation (MOSES1), whilst in this study interactive vegetation is used (MOSES2.1 with TRIFFID).

3.5 Calibration and evaluation of the emulator

By considering different contributions of modern and low ice, high and low CO_2, different number of PCs, and different values for the correlation length hyperparameters, an ensemble of emulators was generated, in order to test their relative performance. The *modice* and *lowice* ensembles were treated as independent data sets that were used separately when calibrating the emulator, since ice extent is not defined explicitly as an input parameter in the emulator code. This approach was adopted, rather than including the ice sheet extent as an active input parameter to the emulator, because only two ice sheet configurations have been simulated, which are not sufficient for an interpolation. One of the main benefits of including ice sheet extent as an active input parameter would be to emulate changing ice sheets over time, but this was beyond the scope of this study. ln(CO_2) was used as one of the four input parameters, along with obliquity, $e\sin\varpi$ and $e\cos\varpi$. The performance of each emulator was assessed using a leave-

one-out cross-validation approach, where a series of emulators is constructed, and used to predict one left-out experiment each time. For example, for the *lowCO₂ modice* ensemble (40 experiments), 40 emulators were calibrated with one experiment left out of each. This left-out experiment was then reproduced using the corresponding emulator, and the results compared with the actual experiment results. The number of grid boxes for each experiment calculated to lie within different standard deviation bands, and the root mean squared error (RMSE) averaged across all the emulators were used as performance indicators to compare the different input configurations and hyperparameter value selections. The results in this section are applicable to the *modice* emulator, unless otherwise specified, however the calibration and evaluation for the *lowice* emulator yielded similar trends and results.

3.5.1 Sensitivity to input data

The impact on performance was investigated of calibrating the emulator on the *highCO₂* and *lowCO₂ modice* ensembles separately, and combined. The *lowCO₂ modice* emulator generally performs slightly better in the leave-one-out cross-validation exercise than the *highCO₂ modice* version, with a lower RMSE and fewer grid boxes with an error of more than 2 standard deviations. Combining the two ensembles into one emulator results in a similar RMSE to the *lowCO₂*-only *modice* emulator but decreases the RMSE compared with the *highCO₂*-only *modice* emulator. As a consequence, the approach was taken of calibrating the emulator on the combined ensembles for the rest of the study. This has the advantage that continuous simulations of climate with CO_2 levels that cross the boundary between the high and low CO_2 ensembles (~560 ppmv), such as may be appropriate for emulation of future climate, can be performed using one emulator, rather than having to calibrate separate emulators for different time periods based on CO_2 concentration. There is also no loss of performance in the emulator for either set of CO_2 ranges, but rather a slight improvement for the *highCO₂* ensemble.

3.5.2 Optimisation of hyperparameters

Two separate emulators were calibrated, the first using the *modice* data and the second using the *lowice* data, both with 60 experiments each (combined *highCO₂* and *lowCO₂*). The input factors (ε, $e\sin\varpi$, $e\cos\varpi$ and $\ln(CO_2)$) were standardised prior to the calibration being performed; each was centred in relation to its column mean, and then scaled based on the standard deviation of the column. Different emulator configurations were tested by varying the number of principal

components retained, ranging from 5 to 20, and for each emulator configuration, the correlation length scales δ and nugget v were optimised by maximization of the penalised likelihood. This optimisation was carried out in log-space, ensuring that the optimised hyperparameters would be positive. A leave-one-out validation was performed each time, and the *modice* and *lowice* configurations that performed best were selected as the final two optimised emulators. It was found that a *modice* emulator retaining 13 principal components has the lowest RMSE and a relatively low percentage of grid boxes with errors of more than 2 standard deviations. The scales δ for the *modice* emulator are 7.509 (ε), 3.361 ($e\sin\varpi$), 3.799 ($e\cos\varpi$), 0.881 (CO_2), and the nugget is 0.0631. In contrast, a *lowice* emulator using 15 principal components exhibits the best performance, with length scales δ of 5.597 (ε), 2.887 ($e\sin\varpi$), 3.273 ($e\cos\varpi$), 0.846 (CO_2), and a nugget of 0.0925. In both cases, the scales for the three orbital parameters are larger than the range associated with the input factors, indicating that the response is relatively linear with respect to these terms.

The *modice* emulator was evaluated using the leave-one-out methodology and results are shown in Figure 3.8. The results suggest that the emulator performs well. Figure 3.8a shows the percentage of grid boxes for each left-out experiment estimated by the corresponding emulator within different standard deviation bands, along with the RMSE. The mean percentage of grid boxes within 1 and 2 standard deviations is 80% and 97%, which roughly corresponds to the 68% and 95% ratios expected for a normal distribution, suggesting that the uncertainty in the prediction is being correctly captured.

Several of the experiments performed considerably worse than others, exhibiting below the expected number of grid boxes with errors within 1 standard deviation (for reference, the mean value for 1 standard deviation across the left-out experiments is 0.3°C), and/or higher than the expected number of grid boxes with errors of greater than 2 standard deviations, which is generally accompanied by a higher RMSE. However, the input conditions for these experiments are not particularly similar or unique. Experiments *modice_highCO2_43*, *modice_highCO2_45* and *modice_highCO2_46* all have a fairly low eccentricity and obliquity, and a CO_2 concentration of ~1000 ppmv, but there are multiple experiments with similar values that have lower RMSE values. A spatial map of the errors (not shown) indicates that the grid boxes with errors of 3 or more standard deviations are at high northern latitudes in these experiments. However, the signs of the anomalies are not the same across these experiments, as the emulator overestimates the Arctic SAT anomaly in *modice_highCO2_43* and underestimates it in *modice_highCO2_45* and *modice_highCO2_46*. This suggests that the emulator is perhaps not quite capturing the full model behaviour in high northern latitudes, particularly for low eccentricity values, but this is

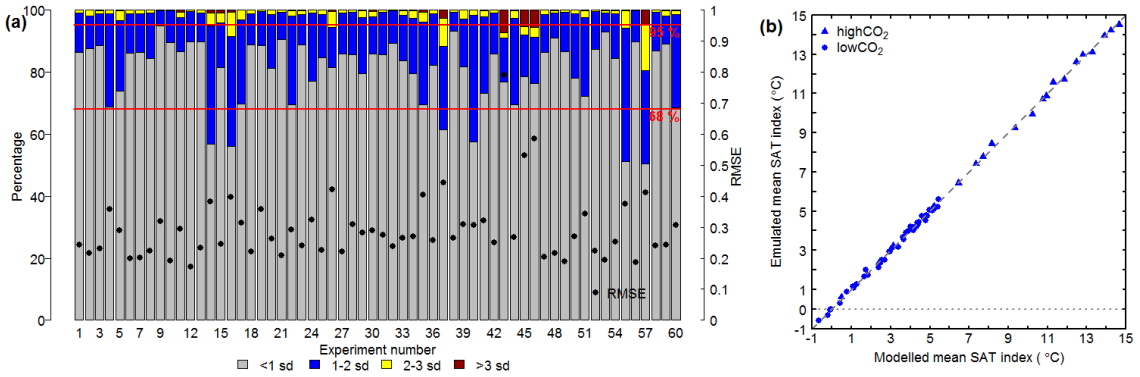

Figure 3.8. Evaluation of emulator performance. (a) Bars give the percentage of grid boxes for which the emulator predicts the SAT of the left-out experiment to within 1, 2, 3 and more than 3 standard deviations (sd). Also shown is the RMSE for the experiments (black circles). Red lines indicate 68% and 95%. (b) Global mean annual SAT index (°C) calculated by the emulator and the GCM for the lowCO_2 (circles) and highCO_2 (triangles) modice ensembles. The 1:1 line (dashed) is included for reference. Note: this is the mean value for the GCM output data grid assuming all grid boxes are of equal size, hence not taking into account variations in grid box area: it is therefore referred to it as a SAT index. SAT is shown as an anomaly compared with the pre-industrial control simulation.

certainly not true for all experiments. The errors in the experiments are generally less than ±4°C, and for most of the Arctic much lower than that. Note that the Arctic is a region in the model with high inter-annual variability, so one factor may be that the model simulations which are used to calibrate the emulator are not representative of the true stationary mean. There does not appear to be any obvious systematic error associated with the input parameters, suggesting that errors are less likely to be an issue resulting from the design of the emulator and more likely to arise from run-to-run variability in the behaviour of the underlying GCM.

Figure 3.8b compares the mean annual "SAT index" for each left-out experiment calculated by the GCM and the corresponding emulator (Note: this is the mean value for the GCM output data grid assuming all grid boxes are of equal size, hence not taking into account grid box area). There are no obvious outliers, and the emulated means are relatively close to their modelled equivalents. There also does not appear to be any significant loss of performance at very low or very high temperature, and therefore at very low or very high CO_2.

In summary, the calibration and evaluation shows that the emulator is able to reproduce the left-out ensemble simulations reasonably well, with no obvious systematic errors in its predictions. Using the emulator, calibrated on the full set of 60 simulations (*modice* or *lowice*), one can simulate global climate development over long periods of time (several hundred thousand years or longer), provided that the atmospheric CO_2 levels for the period are known, and are within the limits of those used to calibrate the emulator, ice sheets do not change outside of the two configurations considered in the two ensembles, and the topography and land-sea mask are unchanged.

In the next two sections, illustrative examples of a number of potential applications of the emulator are presented, by applying it to the late Pliocene in Section 3.6, and the next 200 kyr in Section 3.7.

3.6 Application of the emulator to the late Pliocene

In addition to being able to rapidly project long-term climate evolution, the emulator also allows climatic changes to be examined and analysed using a range of different methods that may not be possible using other modelling approaches. To illustrate this, the *lowice* emulator was applied to the late Pliocene and compared the results to palaeo-proxy data for the period. The *lowice* emulator was used because the ice sheets in this configuration are the PRISM4 Pliocene ice sheets (Dowsett et al., 2016). It should be noted, however, that this approach is only appropriate for periods of the Pliocene with equivalent or less than modern ice sheet extents (i.e. not glacial conditions), and that palaeogeographic changes for the Pliocene are not included here (see Section 3.8 for further discussion). The *modice* emulator was also tested which, in agreement with the findings in Section 3.5, had a limited impact on the long-term evolution of global SSTs outside the immediate region of the ice sheets themselves. Potential applications of the emulator for palaeoclimate are described below.

3.6.1 Time series data

One application of the emulator is to produce a time series of the continuous evolution of climate for a particular time period, as is illustrated here where climate is simulated at 1 kyr intervals over the period 3300 – 2800 kyr BP. This period of the late Pliocene was selected because it has been extensively studied as part of a number of projects (e.g. PRISM (Dowsett, 2007, Dowsett et al., 2016), PlioMIP (Haywood et al., 2010, Haywood et al., 2016)), represents the warm phase of climate (interglacial conditions), and does not include major glaciations (though the M2 cooling event may persist to the very start of the simulation at 3300 kyr BP, and the simulated period does include periods of likely glaciation, such as KM2 (~3100 kyr BP) and G20 (~3000 kyr BP)). The emulator would not be appropriate to periods of extensive glaciation and may not be well-matched to the periods of lesser glaciation included within the simulated interval. Orbital data for each 1 kyr (Laskar et al., 2004) were provided as input to the calibrated emulator, along with three representative CO_2 concentrations. Three CO_2 reference scenarios

were initially emulated, with constant concentrations of 280, 350 and 400 ppmv (although note that in reality, CO_2 varied during this period on orbital timescales (Martinez-Boti et al., 2015)).

To illustrate the comparison of the emulator results to palaeo-proxy data, SST data for various locations were compared with the emulated SAT for the equivalent grid box. Specifically, alkenone-derived palaeo-SST estimates from four (Integrated) Ocean Drilling Program (IODP/ODP) sites were used: ODP Site 982 (North Atlantic; (Lawrence et al., 2009)), IODP Site U1313 (North Atlantic; (Naafs et al., 2010)), ODP Site 722 (Arabian Sea; (Herbert et al., 2010)) and ODP Site 662 (tropical Atlantic; (Herbert et al., 2010)). The locations of the sites are shown in Figure 3.9a and detailed in Table 3.4. These Pliocene datasets were selected because they are all of sufficiently high resolution (≤4 kyr) for the impacts of individual orbital cycles on climate to be captured, whilst covering a range of locations and climatic conditions. Alkenone data are shown converted to SST using two commonly applied calibrations: Prahl et al. (1988) and Muller et al. (1998). All temperatures are presented as an anomaly compared with pre-industrial. The emulator results are compared with the SAT for the relevant grid box in the pre-industrial control experiment, whilst the proxy data are compared with SST observations for the relevant location taken from the Hadley Centre sea-ice and sea surface temperature (HadISST) data set (Rayner et al., 2003). Observations are annual means and are averaged over the period 1870-1900.

Table 3.4. Mean temperature anomalies and uncertainties (1 standard deviation) for the period 3300-2800 kyr BP estimated by the emulator and alkenone proxy data for the four ODP/IODP sites.

ODP/IODP Site	Location			Emulated SAT anomaly (°C)			Proxy data SST anomaly (°C)	
		Lat	Lon	280 ppmv	350 ppmv	400 ppmv	Prahl et al. (1988)	Muller et al. (1998)
982[1]	North Atlantic	57.5° N	15.9° W	0.6 ±0.4	2.4 ±0.3	3.3 ±0.3	5.4	5.7
U1313[2]	North Atlantic	41.0° N	33.0° W	-0.8 ±0.3	0.0 ±0.2	0.8 ±0.2	1.6	2.0
722[3]	Arabian Sea	16.6° N	59.8° E	0.0 ±0.2	1.0 ±0.2	1.7 ±0.2	1.0	1.7
662[3]	Tropical Atlantic	1.4° S	11.7° W	0.2 ±0.2	0.9 ±0.2	1.3 ±0.2	1.3	1.9

[1]Lawrence et al. (2009); [2]Naafs et al. (2010); [3]Herbert et al. (2010).

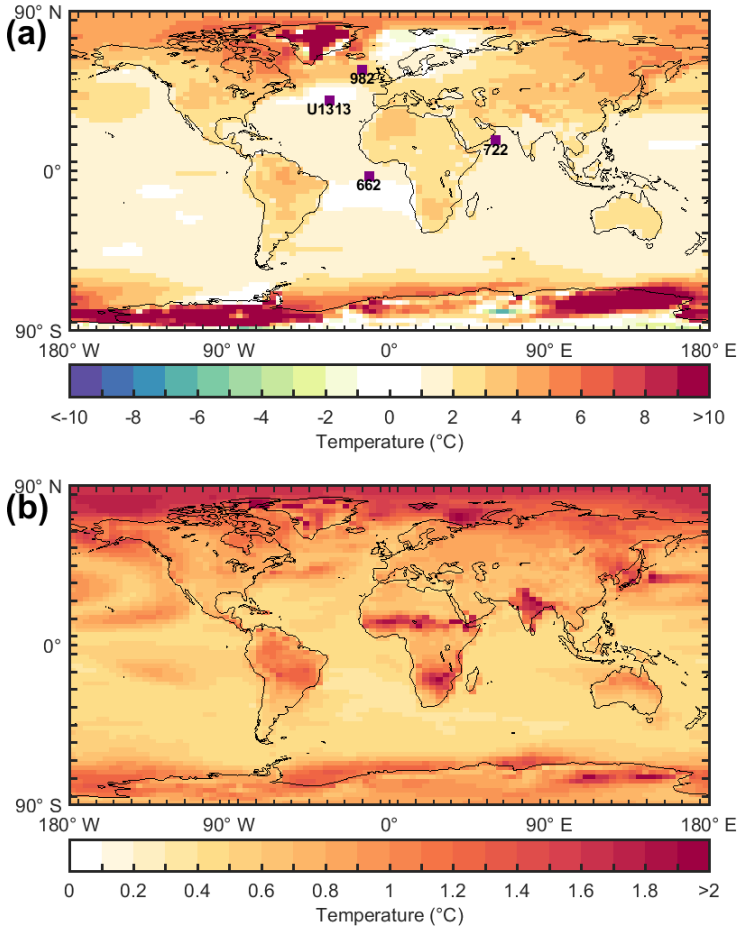

Figure 3.9. Emulated mean annual SAT (°C) for the 400 ppmv CO_2 scenario, modelled using the lowice emulator. SAT is shown as an anomaly compared with the pre-industrial control simulation. (a) Mean annual SAT for modern-day orbital conditions. Also shown are the locations of the four ODP/IODP sites (purple squares): Site 982 (North Atlantic; (Lawrence et al., 2009)), Site U1313 (North Atlantic; (Naafs et al., 2010)), Site 722 (Arabian Sea; (Herbert et al., 2010)) and Site 662 (tropical Atlantic; (Herbert et al., 2010)). (b) Standard deviation of mean annual SAT for the period 3300-2800 kyr BP (late Pliocene), also taking into account the emulator posterior variance.

Table 3.4 presents the mean SAT anomaly (compared with pre-industrial) for the modelled period as estimated by the emulator for the 280 ppmv scenario for each of the four grid boxes. The mean increases with increasing CO_2, by ~1°C at low latitudes to 2-3°C at high latitudes for atmospheric CO_2 of 400 ppmv. Figure 3.10 illustrates the evolution of annual mean temperature variations through the late Pliocene as calculated using the various methods. For the equatorial and Arabian Sea sites (662 and 722), the SAT and SST estimates are relatively similar to each other in terms of the general estimated temperature, particularly for the higher CO_2 scenarios of 350 and 400 ppmv. However, the comparison of timings and variations between the SAT and SST data is fairly poor, and there was not found to be a significant correlation between the emulated and proxy data temperatures at these sites when correlation coefficients were calculated. In fact, Site 982 was the only location for which significant (negative) correlations were found for a confidence interval of 95%, although the correlation coefficient is

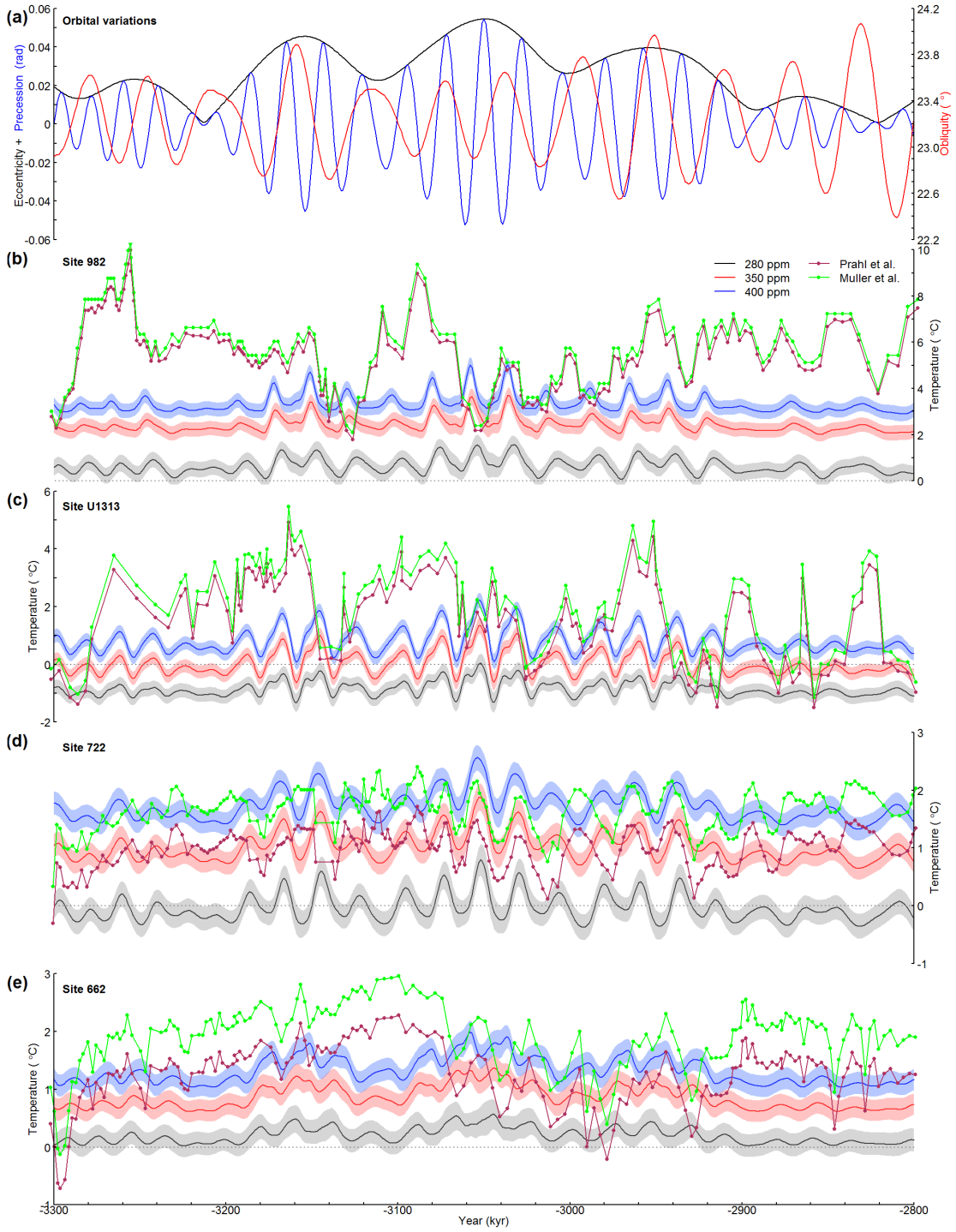

Figure 3.10. Data-model comparison of temperature anomaly for the period 3300-2800 kyr BP (late Pliocene). (a) Time series of orbital variations (Laskar et al., 2004), showing eccentricity (black) and precession (radians; blue) on the left axis, and obliquity (degrees; red) on the right axis. (b):(e) Time series of emulated grid box mean annual SAT (°C; plain lines), modelled every 1 kyr, for three constant CO_2 scenarios; 280 ppmv (black), 350 ppmv (red) and 400 ppmv (blue). Modelled using the lowice emulator. Error bands represent the emulated grid box posterior variance (1 standard deviation). Also shown is SST proxy data (°C; dotted lines) calibrated using the method of Prahl et al. (1988) (maroon), and the method of Muller et al. (1998) (green). SSTs for four ODP/IODP sites are compared: Site 982 (North Atlantic; (Lawrence et al., 2009)), Site U1313 (North Atlantic; (Naafs et al., 2010)), Site 722 (Arabian Sea; (Herbert et al., 2010)) and Site 662 (tropical Atlantic; (Herbert et al., 2010)). SAT is shown as an anomaly compared with the pre-industrial control simulation, SST is shown as an anomaly compared with SST observations for the period 1870-1900 taken from the HadISST data set (Rayner et al., 2003). Note the different vertical axis scales.

still relatively low. These correlation coefficients were -0.22 (p-value 0.004) for the Prahl et al. (1988) proxy SST data compared with the emulated SAT for the 280 ppmv scenario, and -0.2 (p-value 0.007) for the same SST data compared with the emulated SAT for the 350 ppmv scenario. The Muller et al. (1998) SST data demonstrated correlation coefficients that were essentially identical to those above when compared with the same emulated SATs.

At the higher latitudes, the simulated SAT estimate is generally lower than the proxy data SST. This is a common issue in GCM simulations of the late Pliocene, where temperatures at high latitudes under increased CO_2-induced radiative forcing are often underestimated (Haywood et al., 2013). It could also be that the alkenones are not recording mean annual temperature, and instead are being produced during peak warmth (e.g. during the summer months), especially at higher latitudes (Lawrence et al., 2009). This issue could be explored further by extending the methodology presented here to other variables. This seasonal bias could explain the large offset in temperature at the northernmost site (982), which exhibits a maximum difference in mean temperature anomaly for the period of 5.1°C between data sets, and possibly also at Site U1313. The emulated uncertainty in SAT (defined as 1 standard deviation of the emulated grid box posterior variance) is also shown in Figure 3.10, and average values for the period given in Table 3.4. This is slightly higher at the northernmost North Atlantic site (982) compared to the lower latitude sites, but overall the uncertainty is relatively small when compared with the effects of variations in the orbital parameters and atmospheric CO_2 concentration.

3.6.2 Orbital variability and spectral analysis

The emulator can also be used to identify the influence of orbital variations on long-term climate change. One approach is to assess the spatial distribution of orbital timescale variability, by plotting the standard deviation for a climate variable for each grid box, as illustrated for SAT in Figure 3.9 for the 400 ppmv CO_2 scenario (blue lines in Figure 3.10). Figure 3.9a shows mean annual SAT (compared with pre-industrial) produced by the emulator under modern-day orbital conditions. Anomalies over the majority of the Earth's surface are positive, due to the relatively high atmospheric CO_2 concentration of 400 ppmv. Warming is larger at high latitudes, primarily due to a number of positive feedbacks operating in these regions (known as polar amplification). The greatest warming is centred over parts of the GrIS and WAIS, showing a similar spatial pattern to that in Figure 3.4, and is a result of the reduced ice sheet extents in the emulated experiments compared with the pre-industrial simulation. Figure 3.9b shows the standard deviation of mean annual SAT for the late Pliocene, with spatial variations primarily illustrating

differences in the impact of orbital forcing on climate. For example, the relatively higher values at high latitudes compared with low latitudes in Figure 3.9b suggest that changes in the orbital parameters have a relatively large impact on SAT in these regions. This is consistent with astronomical theory, as changes in both obliquity and precession affect the distribution of insolation in space and time, with this effect being particularly significant at high latitudes. Monsoonal regions also demonstrate relatively large variations (Figure 3.9b), including Africa, India, and South America, in agreement with previous studies which suggest a link between orbital changes and monsoon variability (Prell and Kutzbach, 1987, Tuenter et al., 2003, Caley et al., 2011).

In order to visualise the effects of orbital forcing over time, a spectral wavelet analysis was performed on the SAT time series data produced by the emulator, for the scenario with constant CO_2 at 400 ppmv, shown in Figure 3.10 (blue line). The standard MATLAB wavelet software of Torrence and Compo (1998) (available online at http://atoc.colorado.edu/research/wavelets) was used. The wavelet power spectra for the four ODP/IODP sites are presented in Figure 3.11, from which the dominant orbital frequencies influencing climate can be identified. For the late Pliocene up to ~2900 kyr, Figure 3.11 suggests that changes in emulated SAT are paced by a combination of precession (longitude of perihelion) and eccentricity, with periodicities of approximately 21 and 96 kyr, respectively. The influence of precession is also supported by Figure 3.4c, which demonstrates precessional forcing in the regions where the sites are located, as well as by the frequency of the SAT oscillations for this period shown in Figure 3.10, and the observation that it appears to have a larger impact on SAT at higher latitudes (Figures 3.10 and 3.11). After ~2900 kyr, obliquity appears to have an increased impact at the high latitude site 982, superimposing the precession-driven temperature variations with a periodicity of ~41 kyr (Figures 3.10 and 3.11). This signal is also apparent to a lesser extent at Site 722, but not at Site U1313. Spectral analysis of palaeo-proxy data and June insolation at 65^{o} N also finds a reduction in the influence of precession and an increase in 41 kyr obliquity forcing around this time (Lawrence et al., 2009, Herbert et al., 2010). SAT changes at the lower latitude sites generally continue to be dominated by variations in precession and eccentricity, although the relatively low eccentricity during this period is likely to reduce the impact that precession has on climate. It also significantly reduces the variability in temperature, which is also observed during the period of low eccentricity between approximately 3240 and 3200 kyr in both Figures 3.10 and 3.11. The slightly higher amplitudes of the peaks in temperature around 3150 kyr, 3050 kyr and 2950 kyr in Figure 3.10 coincide with periods of high eccentricity, when its impact on climate is increased (Figure 3.11). It is more difficult to identify orbital trends

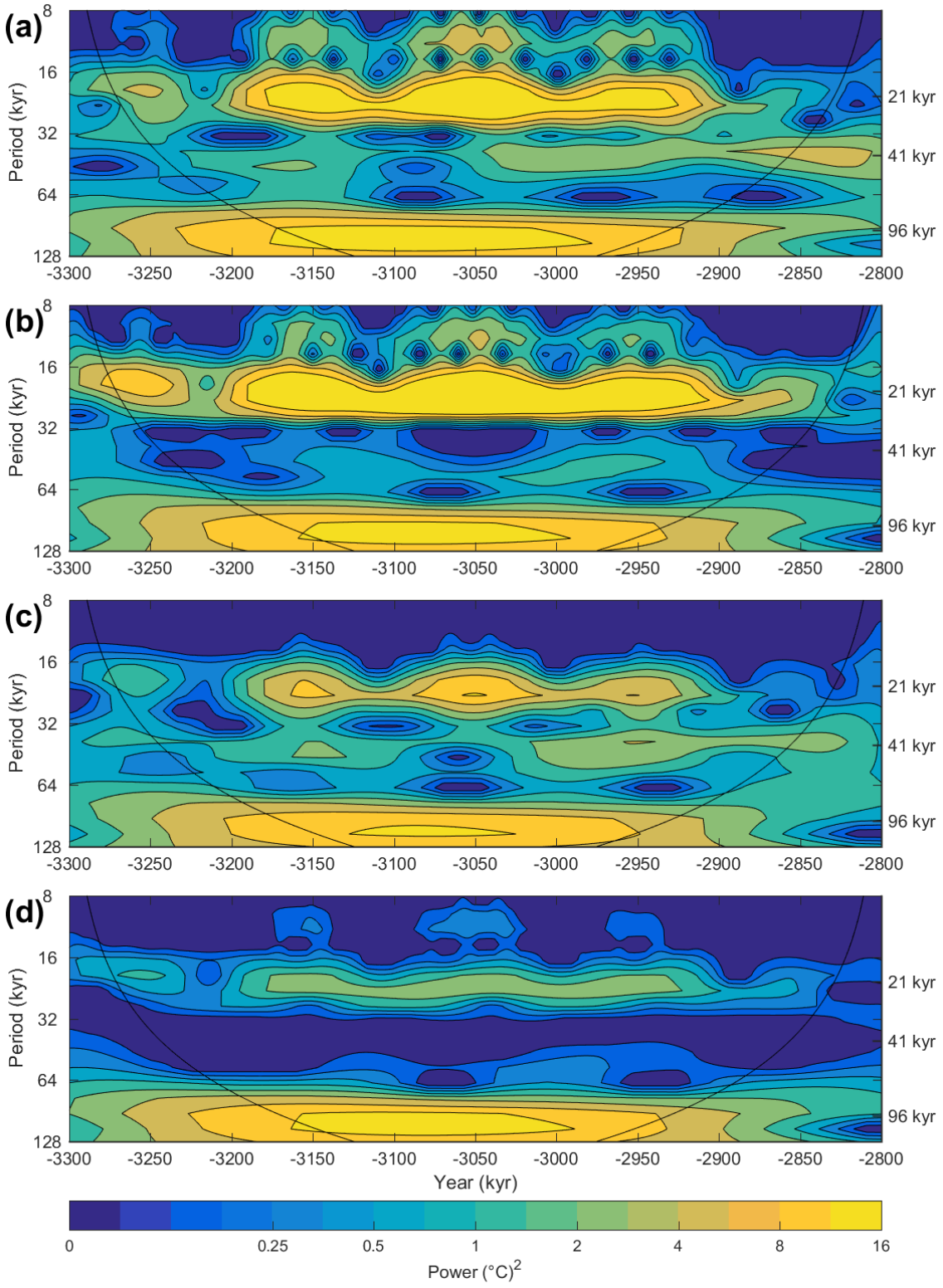

Figure 3.11. The wavelet power spectrum for 3300-2800 kyr BP (late Pliocene). Wavelet analysis was performed on emulated grid box mean annual SAT (°C), modelled every 1 kyr using the lowice emulator, for constant CO_2 of 400 ppmv (blue line in Figures 3.10b to 3.10e). The data are normalised by the mean variance for the analysed SAT data (σ^2 = 0.14°C). Four ODP/IODP sites are compared: (a) Site 982 (North Atlantic; (Lawrence et al., 2009)), (b) Site U1313 (North Atlantic; (Naafs et al., 2010)), (c) Site 722 (Arabian Sea; (Herbert et al., 2010)) and (d) Site 662 (tropical Atlantic; (Herbert et al., 2010)).

in the proxy data, particularly in sections with lower resolution. This is due to there being significantly more variation, both on shorter timescales of several tens of thousands of years, and longer timescales of hundreds of thousands of years, likely caused in part by changes in atmospheric CO_2. However, the amplitude of variations in the palaeo data at all four sites is generally, though not always, lower during periods of low eccentricity, particularly for the period ~3225-3200 kyr.

3.6.3 Calculation of atmospheric CO_2

The use of the emulator for calculating a simple estimate of atmospheric CO_2 concentration during the late Pliocene is also illustrated, and its comparison to published palaeo CO_2 records obtained from proxy data. CO_2 is estimated from the four alkenone SST records presented in Table 3.4 and Figure 3.10: Herbert et al. (2010) (Sites 662 and 722), Naafs et al. (2010) (Site U1313) and Lawrence et al. (2009) (Site 982). Individual records of SST, rather than stacked benthic data, were used because the GCM experiments that the emulator is calibrated on were only run for 500 years, meaning that deep ocean conditions would not yet have spun-up sufficiently, particularly in the experiments with high CO_2. Thus, it would not be appropriate to compare deep ocean temperatures from the experiments with those from the proxy data.

A linear regression is performed on the emulated grid box mean annual SAT data versus prescribed atmospheric CO_2 concentration, for constant CO_2 scenarios ranging from 260 ppmv up to 800 ppmv. The CO_2 concentration is then estimated from the palaeo SST data based on this linear relationship, and is presented in Figure 3.12, along with the uncertainty. A number of CO_2 proxy records are also compared, derived from alkenone data at ODP Site 1241 in the east tropical Pacific (Seki et al., 2010) and Site 999 in the Caribbean (Seki et al., 2010, Badger et al., 2013), and from boron ($\delta^{11}B$) data at Site 662 (Martinez-Boti et al., 2015) and Site 999 (Seki et al., 2010, Bartoli et al., 2011, Martinez-Boti et al., 2015).

The new model-based CO_2 estimates suggest a mean atmospheric CO_2 concentration for the period of between approximately 350 ± 15 and 629 ± 37 ppmv (error represents the uncertainty taking into account the emulated gird box posterior variance for SAT), indicated at Sites 722 and 982, respectively. The new CO_2 estimates are generally higher than the CO_2 proxy records, particularly using data from the two North Atlantic sites (982 and U1313), where palaeo SST anomalies were also estimated to be high, compared with tropical anomalies, by the proxy data (Figure 3.10). However, CO_2 concentrations derived from SST data calibrated using

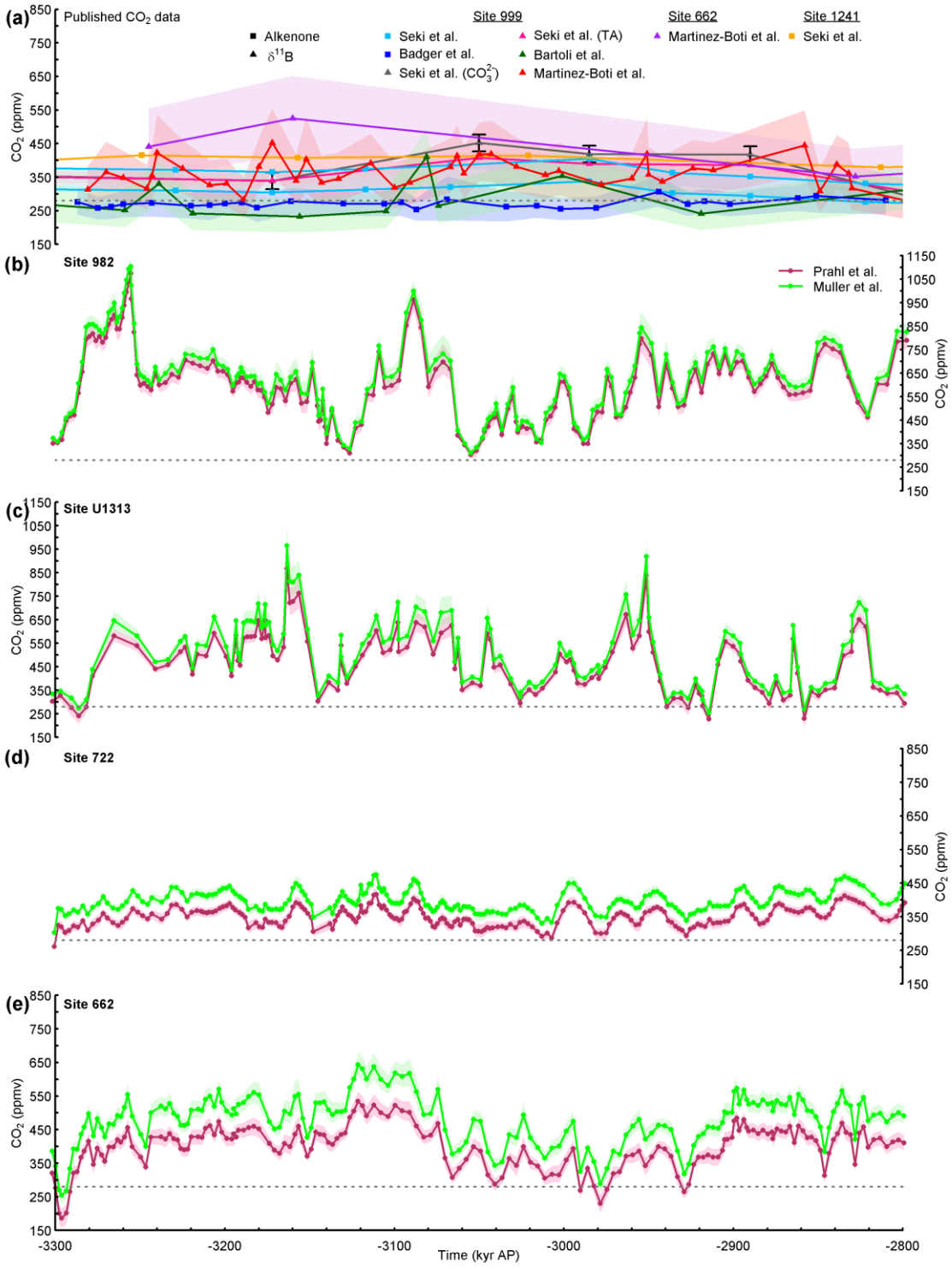

Figure 3.12. Data-model comparison of atmospheric CO_2 concentration (ppmv) for the period 3300-2800 kyr BP (late Pliocene) for six ODP/IODP sites: Site 982 (North Atlantic), Site U1313 (North Atlantic), Site 722 (Arabian Sea), Site 999 (Caribbean), Site 662 (tropical Atlantic), and Site 1241 (east tropical Pacific). (a) Time series of atmospheric CO_2 concentration from selected proxy data records. Shown is CO_2 estimated from alkenone (squares) for Site 999 by Seki et al. (2010) (light blue), Badger et al. (2013) (dark blue) and for Site 1241 by Seki et al. (2010) (orange), and estimated from $\delta^{11}B$ (triangles) for Site 999 by Seki et al. (2010) based on modelled carbonate concentration ($[CO_3^{2-}]$) (grey) and assuming modern total alkalinity (TA; pink), Bartoli et al. (2011) (dark green), Martinez-Boti et al. (2015) (red) and for Site 662 by Martinez-Boti et al. (2015) (purple). For the Seki et al. (2010) $\delta^{11}B$ records, error bars are ±25 ppmv and the error band is the result of varying the modern TA by ±5%, whilst for Martinez-Boti et al. (2015) the error band represents the 95% confidence interval for a 10,000 member Monte Carlo analysis. (b):(e) Time series of atmospheric CO_2 concentration estimated from SST proxy data (circles; Herbert et al. (2010) – Sites 662 and 722, Naafs et al. (2010) – Site U1313, Lawrence et al. (2009) – Site 982) calibrated using the method of Prahl et al. (1988) (maroon), and the

method of Muller et al. (1998) (light green). CO_2 is calculated based on a linear relationship between emulated grid box mean annual SAT (modelled using the lowice emulator) and CO_2, for three constant CO_2 scenarios of 280, 350 and 400 ppmv. Error bands represent estimated atmospheric CO_2 concentration taking into account the emulated grid box posterior variance (1 standard deviation). Where the error appears to be very low, this is generally an artefact of the way that the data has been plotted. The pre-industrial CO_2 concentration of 280 ppmv (grey dotted line) is included for reference.

the approach of Prahl et al. (1988) at the tropical sites of 722 and 662 shows greater similarity to the CO_2 proxy data, both in terms of mean concentration and variance (not shown). It is difficult to identify temporal similarities between the new CO_2 estimates and the palaeo records. This is partly due to the high level of variability in the new CO_2 time series, resulting from the variability in the SST records that they were derived from. In addition, the CO_2 proxy records have comparatively low resolutions, generally with intervals of 10 kyr or greater, and there is also considerable variation between them.

There is substantial variation between the new CO_2 estimates at different sites, and this may be attributed to a number of causes. It could be that there are errors in the GCM model used, in particular in its representation of the response of climate to CO_2 and/or orbital forcing. There could be errors in the SST data at one or more locations as, if the model was assumed to be correct, the estimated CO_2 should be similar across the four locations. The fact that they are not may indicate that the temperature records are not consistent with each other, which may not have been obvious by just comparing the records visually. This is one of the potential advantages to using individual temperature records rather than stacked records. It may also be that there is an issue with the dating of some of the proxy records; the data may be correct but the time data associated with them may be wrong. Alternatively, the emulator may be wrong; for example, there may be non-linearities in the climate response simulated by the GCM that it is not capturing. Finally, there may be errors related to the modelled representation of the ice sheets, which are fixed at a constant configuration. In reality, the variations are less likely to be the result of errors in the emulator's estimates of the GCM output because the validation diagnostics did not seem to suggest systematic failures, or of unrepresented changes in climate due to the ice sheets. Whilst some of the variation at the high latitude sites (982 and U1313) may be attributed to some regional climate processes not fully accounted for, e.g. involving the ice sheets and sea-ice, two of the sites (722 and 662) are in tropical regions. Thus, SSTs at these sites would not be expected to be affected by changes in the ice sheets, and yet they show significant variations to each other. Therefore, the inconsistencies are likely to be due to a combination of errors in the GCM model and in the SST data.

3.7 Application of the emulator to future climate

In addition to using the emulator to model past climates, it can also be applied to future climate, and in particular on the long timescales (>10^3 yr) that are of interest for the disposal of solid radioactive wastes. Previous modelling of long-term future climate has involved the use of lower complexity models such as EMICs for transient simulations (Archer and Ganopolski, 2005, Eby et al., 2009, Ganopolski et al., 2016, Loutre and Berger, 2000b), or of GCMs to model a relatively small number of snapshot simulations of particular reference climate states of interest. The BIOCLIM (Modelling Sequential Biosphere Systems under Climate Change for Radioactive Waste Disposal) research programme (BIOCLIM, 2001, 2003a), for example, utilised both of these approaches to investigate climatic and vegetation changes for the next 200 kyr, for use in performance assessments for radioactive waste disposal facilities.

Here, for the first time, a GCM has been used to project future long-term transient climate evolution, via use of the emulator. Illustrations of two possible applications of the emulator are provided, including production of a time series of climatic data and assessing the impact of orbital variations on climate. This work has input to the International Atomic Energy Agency (IAEA) MOdelling and DAta for Radiological Impact Assessments (MODARIA) collaborative research programme (http://www-ns.iaea.org/projects/modaria).

3.7.1 Time series data

Similarly to the late Pliocene, snapshots of SAT and precipitation at 1 kyr intervals were produced using the *modice* emulator for the next 200 kyr, assuming modern day ice sheet configurations. The projected evolution of climate is a result of future variations in the orbital parameters and atmospheric CO_2 concentrations, which were provided as input data to the emulator (again, at 1 kyr intervals). Four CO_2 emissions scenarios were modelled, with the response of atmospheric CO_2 concentration to emissions and its long-term evolution calculated using the impulse response function of Lord et al. (2016). The scenarios adopted logistic CO_2 emissions of 500, 1000, 2000 and 5000 Pg C released over the first few hundred years, followed by a gradual reduction of atmospheric CO_2 concentrations by the long-term carbon cycle. These four scenarios cover the range of emissions that might occur given currently economic and potentially economic fossil fuel reserves, but not including other potentially exploitable reserves, such as clathrates.

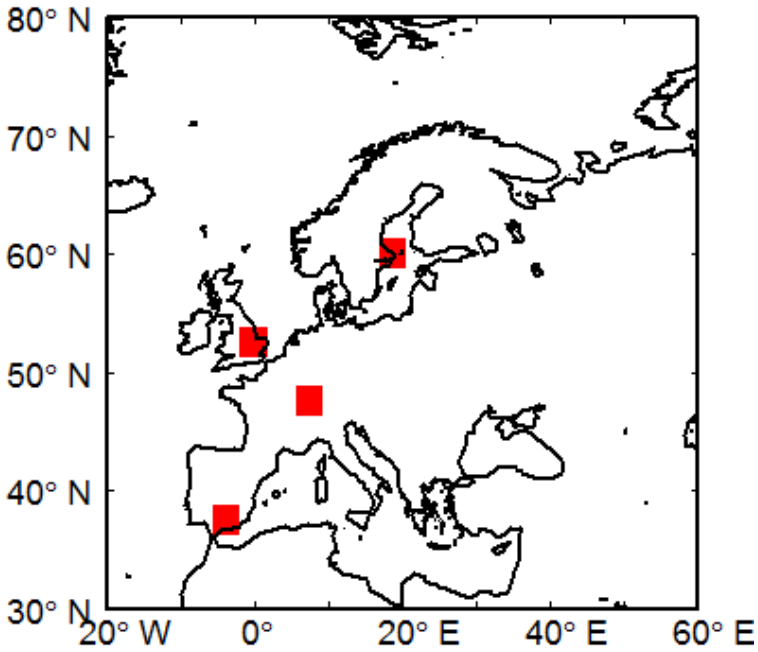

Figure 3.13. Map of Europe highlighting the grid boxes that represent the four case study sites. From north to south: Sweden, Central England, Switzerland and Spain.

Four single grid boxes are selected, shown in Figure 3.13, which represent example locations that could potentially be relevant for nuclear waste disposal: Forsmark, Sweden (60.4° N latitude, 18.2° E longitude), Central England, UK (52.0° N latitude, 0° W longitude), Switzerland (47.6° N latitude, 8.7° E longitude) and El Cabril, Spain (38° N latitude, 5.4° W longitude). The evolution of SAT at these grid boxes is presented in Figure 3.14, along with the emulated uncertainty (1 standard deviation of the emulated grid box posterior variance)). In the 500 Pg C scenario, the largest SAT increase of 4.1 ± 0.2°C occurs at the Switzerland grid box, whilst the Spain grid box exhibits the largest warming in the 5000 Pg C scenario, of 12.3 ± 0.3°C. For comparison, when the *lowice* emulator is utilised, these values are reduced slightly to 3.9 ± 0.3°C (Spain grid box) and 12.2 ± 0.3°C (Spain grid box) in the 500 Pg C and 5000 Pg C scenarios, respectively. This peak in temperature occurs up to the first thousand years, when atmospheric CO_2 is at its highest following the emissions period, after which it decreases relatively rapidly with declining atmospheric CO_2 until around 20 kyr AP. By 200 kyr AP, SAT at all sites is within 2.6°C (2.2°C using the *lowice* emulator) of pre-industrial values, calculated by averaging the final 10 kyr of the 5000 Pg C scenarios. The emulated uncertainty for the next 200 kyr is of a similar magnitude to that for the late Pliocene and, similarly, is relatively small when compared with the fluctuations in SAT that result from orbital variations and changing atmospheric CO_2 concentration.

Until ~20 kyr AP, the behaviour of the climate is primarily driven by the high levels of CO_2

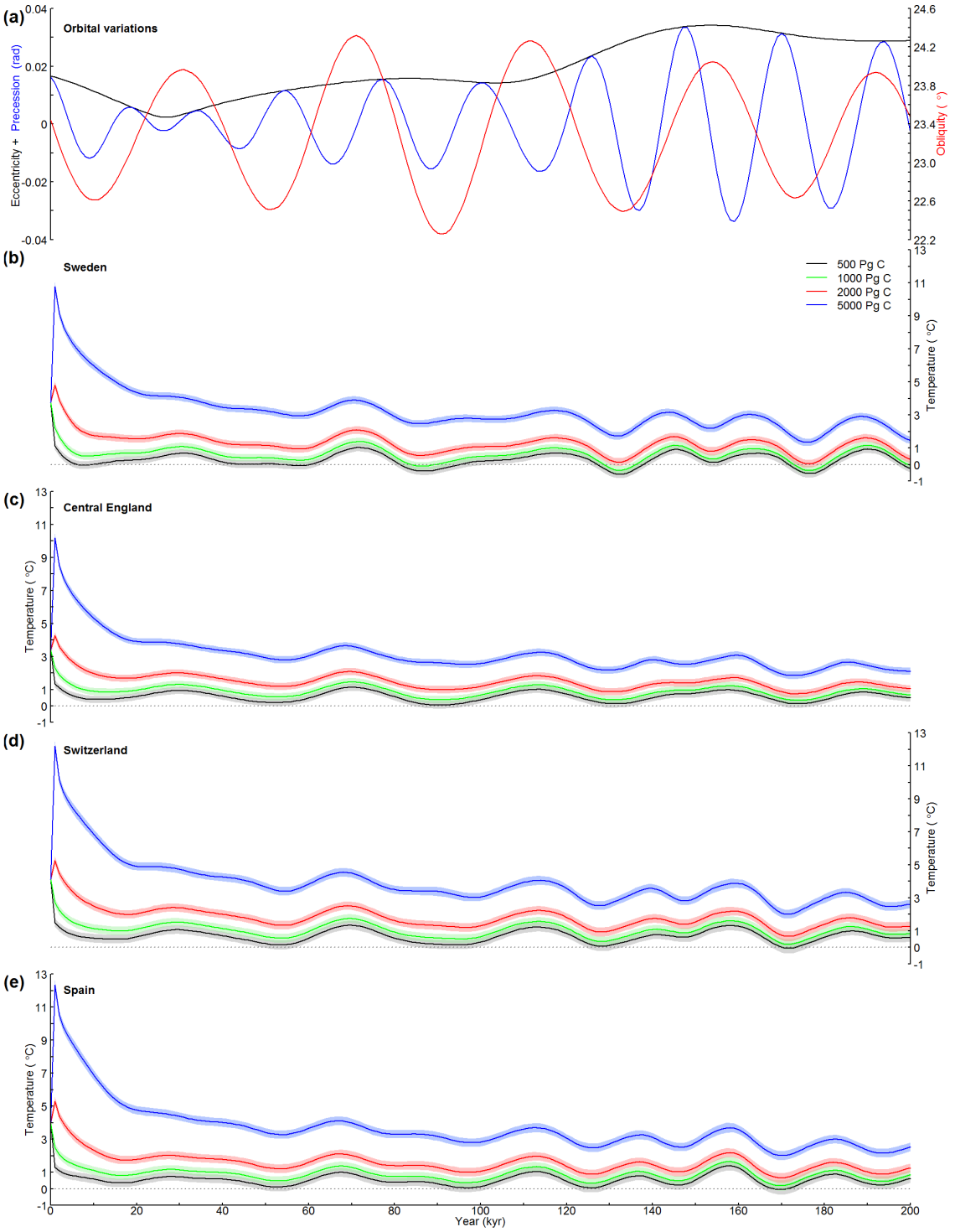

Figure 3.14. Emulation of SAT anomaly for the next 200 kyr. (a) Time series of orbital variations (Laskar et al., 2004), showing eccentricity (black) and precession (radians; blue) on the left axis, and obliquity (degrees; red) on the right axis. (b):(e) Time series of emulated grid box mean annual SAT (°C), modelled every 1 kyr, for four CO_2 emissions scenarios; 500 Pg C (black), 1000 Pg C (green), 2000 Pg C (red) and 5000 Pg C (blue). Modelled using the modice emulator. Error bands represent the emulated grid box posterior variance (1 standard deviation). Four sites are presented, representing grid boxes in Sweden, Central England, Switzerland and Spain. SAT is shown as an anomaly compared with the pre-industrial control simulation.

in the atmosphere as a result of anthropogenic CO_2 emissions from a range of sources, including combustion of fossil fuels, land-use change and cement production. However, after this time, changes in orbital conditions begin to exert a relatively greater influence on climate, as the periodic fluctuations in SAT at all locations appear to be paced by the orbital cycles, which are shown in Figure 3.14a.

The timing and relative amplitudes of the oscillations in future SAT are in good agreement with a number of previous studies. Paillard (2006) applied the conceptual model of Paillard and Parrenin (2004), previously mentioned in Section 3.6, to the next 1 Myr. The development of atmospheric CO_2 over the next 200 kyr, simulated by the model following emissions of 450 to 5000 Pg C and accounting for natural variations, shows a similar pattern of response to that of SAT presented here. Estimates of global mean temperature in Archer and Ganopolski (2005), derived by scaling changes in modelled ice volume to temperature, before applying anthropogenic CO_2 temperature forcing for a number of emissions scenarios, also demonstrate fluctuations in global mean annual SAT (not shown) of a similar timing and relative scale. The influence of declining CO_2 is still evident after 20 kyr, particularly for the higher emissions scenarios, in the slightly negative gradient of the general evolution of SAT. This is due to the long atmospheric lifetime of CO_2 emissions (Archer, 2005), and is also demonstrated in other studies (Archer and Ganopolski, 2005, Paillard, 2006, Archer et al., 2009, Lord et al., 2016). The impact of excess atmospheric CO_2 on the long-term evolution of SAT appears to be fairly linear, with only minor differences between the scenarios and sites, discounting the overall offset of SAT for different total emissions.

One of the key uncertainties associated with future climate change, which is of particular relevance to radioactive waste repositories located at high northern latitudes, is the timing of the next glacial inception. This is expected to occur during a period of relatively low incoming solar radiation at high northern latitudes, which, for the next 100 kyr, occurs at 0 kyr, 54 kyr and 100 kyr. A number of studies have investigated the possible timing of the next glaciation under pre-industrial atmospheric CO_2 concentrations (280 ppmv), finding that it is unlikely to occur until after 50 kyr AP (Archer and Ganopolski, 2005, Paillard, 2001, Berger and Loutre, 2002).

When anthropogenic CO_2 emissions are taken into account, the current interglacial is likely to last significantly longer, until ~130 kyr AP following emissions of 1000 Pg C and beyond 500 kyr AP for emissions of 5000 Pg C (Archer and Ganopolski, 2005). A recent study by Ganopolski et al. (2016) using the CLIMBER-2 model found that emissions of 1000 Pg C

significantly reduced the probability of a glaciation in the next 100 kyr, and that a glacial inception within the next 100 kyr is very unlikely for CO_2 emissions of 1500 Pg C or higher.

The CO_2 emissions scenarios, modelled using the response function of Lord et al. (2016), suggest that atmospheric CO_2 will not have returned to pre-industrial levels by 100 kyr AP, equalling 298 and 400 ppmv for the 500 and 5000 Pg C emissions scenarios, respectively. The critical summer insolation threshold at 65° N was calculated using the logarithmic relationship identified between maximum summer insolation at 65° N and atmospheric CO_2 by Ganopolski et al. (2016). The evolution of atmospheric CO_2 concentration over the course of the emissions scenarios suggests that, for emissions of 1000 Pg C or less, Northern Hemisphere summer insolation will next fall below the critical insolation threshold in approximately 50 kyr, and in ~100 kyr for emissions of 2000 Pg C. For the highest emissions scenario of 5000 Pg C, the threshold is not passed for considerably longer, until ~160 kyr. However, the uncertainty of the critical insolation value is ±4 W m^{-2} (1 standard deviation), and often the difference between summer insolation at 65° N and the insolation threshold is less than this, potentially impacting whether the threshold has in fact been passed and therefore whether glacial inception is likely. For example, for the 1000 Pg C scenario, whilst insolation first falls below the critical threshold at ~50 kyr, it does not fall below by more than the uncertainty value until ~130 kyr.

A limitation of this study relates to the continental ice sheets in HadCM3 being prescribed rather than responsive to changes in climate. A consequence of this is that an increase in the extent or thickness of the ice sheets, and hence the onset of glaciation, cannot be explicitly projected, but this also means that a regime shift of the ice sheets to one of negative mass balance, which may be expected to occur under high CO_2 emissions scenarios (Ridley et al., 2005, Swingedouw et al., 2008, Stone et al., 2010, Winkelmann et al., 2015), cannot be modelled. However, the results of the sensitivity analysis to ice sheets described in Section 3.4.5, for which a number of simulations were run again with reduced GrIS and WAIS extents, suggest that the reduction in continental ice results in relatively localised increases in SAT in regions that are ice free, in addition to some regional cooling at high latitudes. Consequently, this does not act as a significant restriction on the glaciation timings put forward in this study considering their radioactive waste disposal application; given that the earliest timing of the next glaciation is of significant interest, smaller continental ice sheets and therefore higher local SATs would likely inhibit the build-up of snow and ice, delaying glacial inception further. As such, the estimates presented here should be viewed as conservative. As will be discussed in Section 3.8, however, the emulator was not designed and calibrated to predict changes in ice sheets. This is a limitation that should be addressed when modelling future climate on timescales of tens of thousands of

years or more (depending on the CO_2 scenario(s) being modelled). Another caveat is that the carbon cycle in the emulator is also essentially prescribed, and thus not interactive. This means that the atmospheric CO_2 trajectory follows a smooth decline, as was projected using an impulse response function based on experiments using the *c*GENIE model (Lord et al., 2016), with long-term future climate being modelled as a series of snapshot simulations with the emulator. This smooth decline in CO_2 assumes that no non-linear or unexpected behaviour will be demonstrated by the long-term carbon cycle, and that the silicate weathering mechanism, which is associated with a substantial degree of uncertainty, is correct.

The emulator can also be used to project the evolution of a range of other climate variables, providing that they were modelled as part of the initial GCM ensembles. Figure 3.15 illustrates the development of mean annual precipitation and emulated uncertainty over the next 200 kyr at the four sites. The maximum increase in precipitation is between 0.3 ± 0.1 millimetres per day (mm day^{-1}; Switzerland grid box) and 0.6 ± 0.1 mm day^{-1} (Sweden grid box) in the 500 Pg C and 5000 Pg C scenarios, respectively. Precipitation increases with increasing atmospheric CO_2 at all sites apart from the Spain grid box, where it decreases by up to 0.9 ± 0.1 mm day^{-1}. Regional differences in the sign of changes in precipitation, including an increase at high latitudes and a decrease in the Mediterranean, are consistent with modelling results included in the International Panel on Climate Change (IPCC) Fifth Assessment Report, for simulations forced with the Representative Concentration Pathway (RCP) 8.5 scenario (Collins et al., 2013). In contrast to SAT, precipitation appears to be more closely influenced by precession, illustrated by its periodicity of slightly less than 25 kyr. There appears to be an increase in the intensity of precipitation fluctuations from approximately 140 kyr onwards, implying that the modulation of precession by eccentricity also has an impact.

3.7.2 Orbital variability and spectral analysis

The impact of orbital forcing was assessed by performing a spectral wavelet analysis on the SAT and precipitation time series data produced by the emulator for the Central England grid box for the 5000 Pg C emissions scenario, represented by blue lines in Figures 3.14c and 3.15c, respectively. As for the late Pliocene, the wavelet software of Torrence and Compo (1998) was utilised. The analysis was performed on the data for 20-200 kyr AP, because the climate response up until ~20 kyr AP is dominated by the impact of elevated atmospheric CO_2 concentrations, which masks the orbital signal and affects the results of the wavelet analysis.

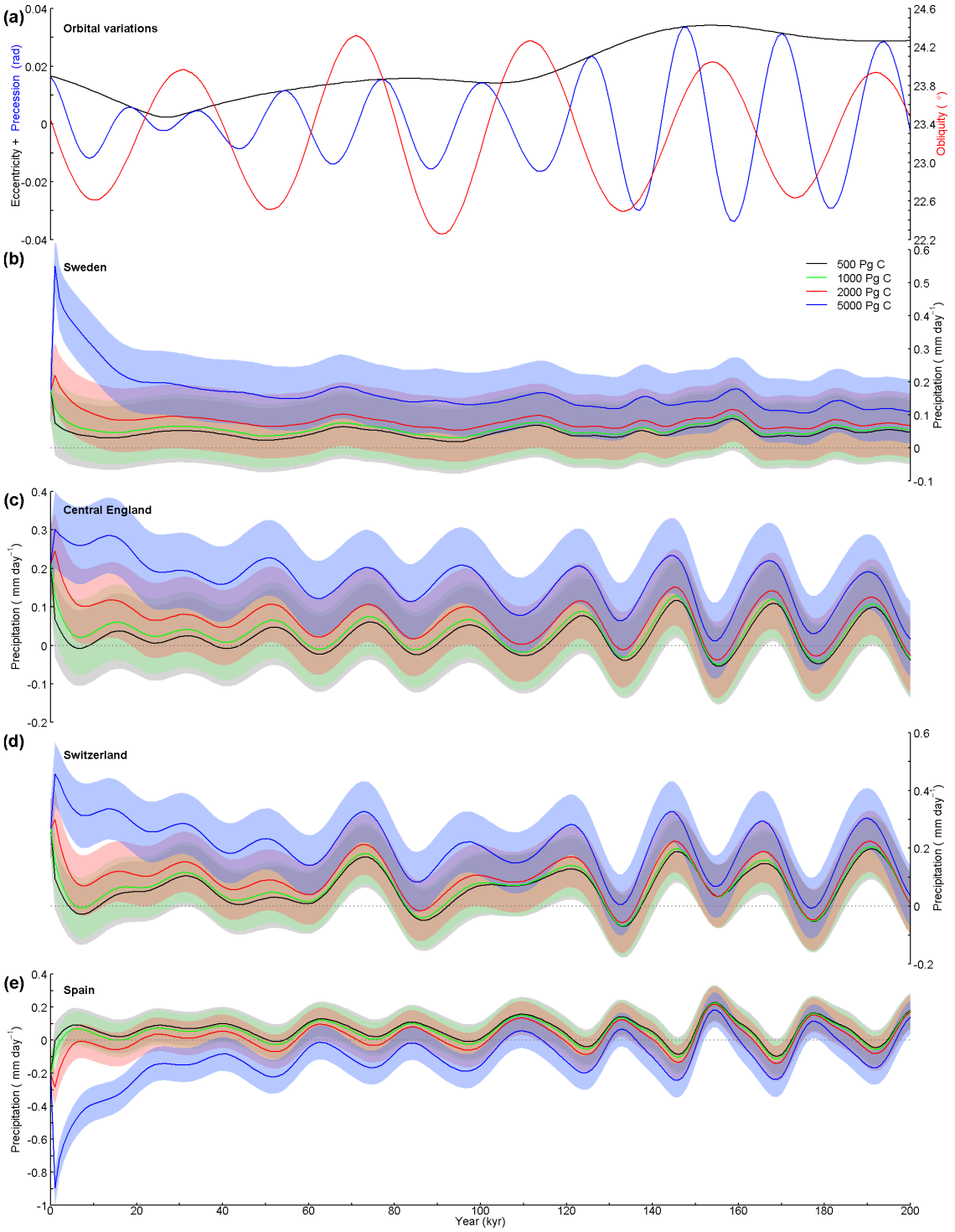

Figure 3.15. Emulation of precipitation anomaly for the next 200 kyr. (a) Time series of orbital variations (Laskar et al., 2004), showing eccentricity (black) and precession (radians; blue) on the left axis, and obliquity (degrees; red) on the right axis. (b):(e) Time series of emulated grid box mean annual precipitation (mm day^{-1}), modelled every 1 kyr, for four CO_2 emissions scenarios; 500 Pg C (black), 1000 Pg C (green), 2000 Pg C (red) and 5000 Pg C (blue). Modelled using the modice emulator. Error bands represent the emulated grid box posterior variance (1 standard deviation). Four sites are presented, representing grid boxes in Sweden, Central England, Switzerland and Spain. Precipitation is shown as an anomaly compared with the pre-industrial control simulation. Note the different vertical axis scales.

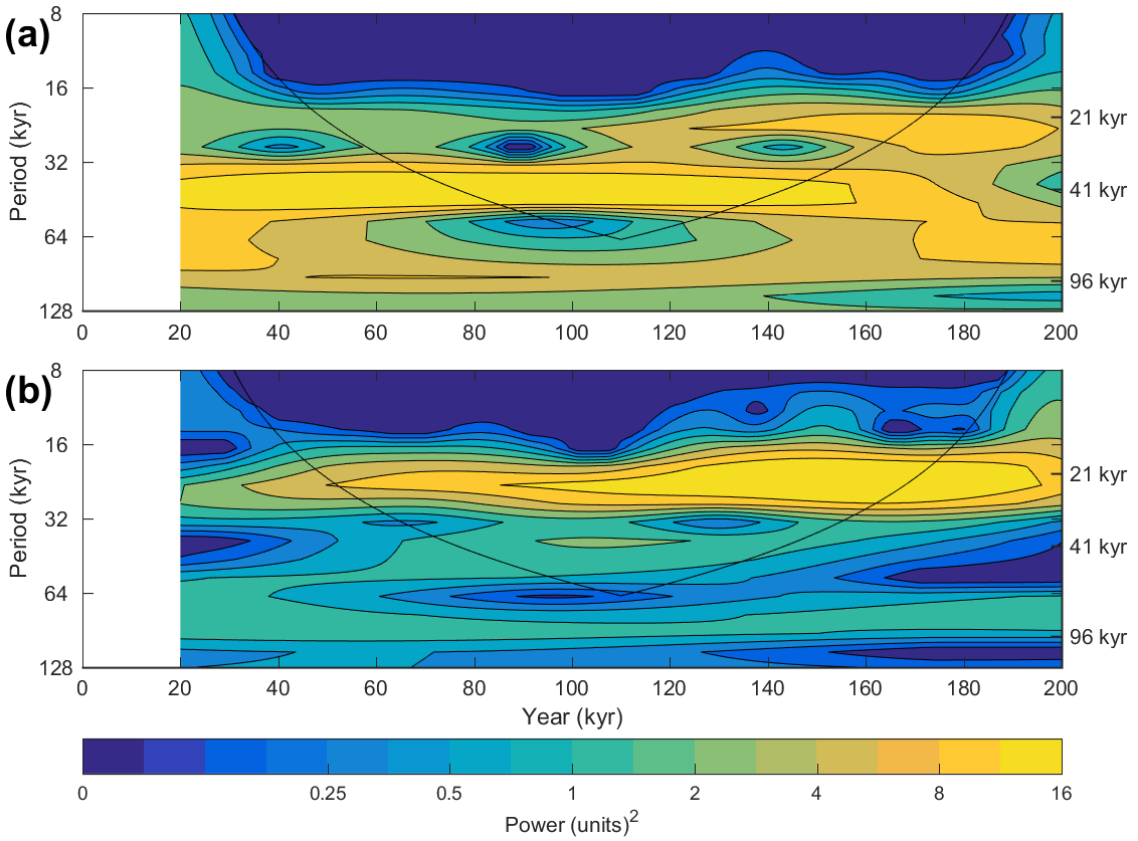

Figure 3.16. The wavelet power spectrum for the next 200 kyr for the Central England grid box. Wavelet analysis was performed on data for 20 kyr AP onwards, for: (a) emulated grid box mean annual SAT (°C; blue line in Figure 3.14c), and (b) emulated grid box mean annual precipitation (mm day^{-1}; blue line in Figure 3.15c). Both variables were modelled every 1 kyr using the modice emulator, for the 5000 Pg C emissions scenario. The data are normalised separately by: (a) the mean variance for the analysed SAT data (σ2 = 0.14°C), and (b) the variance for the analysed precipitation data (σ^2 = 0.003°C).

For future SAT, Figure 3.16a suggests that, up until ~160 kyr, the obliquity cycle acts as the dominant influence, resulting in temperature oscillations with a periodicity of approximately 41 kyr. This is confirmed by Figure 3.14c, which shows that the major peaks in SAT generally coincide with periods of high obliquity. Over this period, precession has a far more limited influence, likely due to eccentricity being relatively low until ~110 kyr (Figure 3.14a). However, from ~120 kyr AP onwards, concurrently with increasing eccentricity, precession becomes a more significant forcing on climate, resulting in SAT peaks approximately every 21 kyr. In contrast, precession appears to be the dominant forcing on precipitation for the Central England grid box for the entire 20-200 kyr AP period (Figures 3.15c and 3.16b). This signal is particularly strong after ~120 kyr AP, due to higher eccentricity.

3.8 Limitations

There are a number of limitations associated with the methodology outlined above, particularly relating to the assumptions that it is based on and its application to different periods of time. Although these have mostly been discussed briefly in the preceding sections, here they are summarised them together.

- As noted previously, the carbon cycle in the emulator is not coupled to the climate, since the atmospheric CO_2 concentration is prescribed. The methodology thus assumes that there will be no unexpected non-linearities in the carbon cycle, and that changes in climate that are different from those in *c*GENIE do not feed back to the carbon cycle. This may be of particular importance when simulating future climates, when the natural carbon cycle is expected to be significantly perturbed due to ongoing anthropogenic emissions of CO_2, in a way that may not be fully represented in *c*GENIE. There is also uncertainty surrounding the dynamics of the carbon cycle over long periods of time, such as the role of the silicate weathering mechanism, although the observation that different carbon cycle models generally produce fairly similar results increases our confidence (Archer et al., 2009).
- The ice sheets in the emulator are also fixed, at either modern-day or reduced extents, although expanding the range of ice sheets that can be modelled is currently being undertaken in ongoing research. This means that care needs to be taken when simulating very long periods of time. For example, neither Quaternary nor future glacial-interglacial cycles can be simulated for using the current version of the emulator. Furthermore, even during the Pliocene, it is likely that the extent of ice sheets in the Northern Hemisphere varied beyond the range simulated in this study (Willeit et al., 2015), and the emulator in its current form cannot represent this.
- In the context of the Pliocene, the land-sea mask and orography used in the simulation of Pliocene climate are fixed and appropriate to modern-day conditions, whereas the PRISM4 reconstruction of paleogeography suggests that there may have been considerably different in some regions, for example the region of the Hudson Bay is thought to have been land in the Pliocene (Dowsett et al., 2016).
- Due to both the carbon cycle and ice sheets being prescribed, interactions between these components of the climate system can also not be simulated. These include natural changes in CO_2 which have been found to accompany past glacial-interglacial cycles, with glacial periods over the last 800 kyr exhibiting CO_2 concentrations of

approximately 180 to 200 ppmv (Petit et al., 1999), whereas interglacial periods demonstrated concentrations of 240 to 290 ppmv (Luthi et al., 2008). Changes in the ice sheets in response to atmospheric CO_2 can also not be modelled, such as the likely future melting of the GrIS and AIS in response to anthropogenic CO_2 emissions. Various studies have modelled the response of the ice sheets to future climate warming, finding that the ice sheets may experience significantly increased melt. In fact, for scenarios with high CO_2 emissions (>~5000 Pg C), it has been suggested that the GrIS and AIS may be almost entirely melted within the next few thousand years (e.g. Huybrechts et al., 2011, Winkelmann et al., 2015, DeConto and Pollard, 2016), which would cause significant changes in deep ocean circulation and ocean stratification. These ocean changes cannot be captured by the current version of the methodology and, whilst their impacts on global and regional climate are uncertain, they are expected to be long-term. The melting of the ice sheets would also cause significant increases in global sea level, of approximately 70 m if both the GrIS and AIS melted, which would strongly affect the global land-sea mask and regional climates, and which cannot be represented using the current methodology. This sea level rise would also have serious implications for radioactive waste repositories located in relatively low-lying coastal regions that are vulnerable to sea level rise, such as in northern Europe.

- Since the emulator models climate via a series of snapshots rather than a truly transient simulation, it is not able to capture deviations from a stationary response. As a consequence, the methodology becomes inappropriate if such transient changes in the deep ocean are found to be important for controlling surface climate evolution.
- The emulator presented in this study is only suitable for modelling transient climate changes on timescales of several millennia or longer, as a number of shorter-term processes in the climate and carbon cycle are not represented. These include internal variability in the climate system, such as interannual variability, North Atlantic Oscillation (NAO), and El Niño – Southern Oscillation (ENSO), as well as radiative forcing occurring on shorter timescales (e.g. volcanic activity), and terrestrial carbon cycle processes. On these timescales, transient simulations run using complex models such as GCMs or EMICS are most appropriate.

As a consequence of these limitations, care needs to be taken when applying the emulator to ensure that its application is appropriate. For example, when considering future

climate, the way in which future carbon dioxide concentration have been modelled, and the ice sheet configurations modelled, mean that this methodology is only applicable on timescales up until the next glacial inception. After this, atmospheric CO_2 would be expected to change in response to the initiation of glacial conditions, accompanied by the expansion of the ice sheets, decreasing sea level, and the climatic changes that would results from these changes. A number of studies have modelled the possible timing of the next glacial inception, finding that for CO_2 scenarios with medium emissions the current interglacial period may end in approximately 130 kyr (Archer and Ganopolski, 2005, Ganopolski et al., 2016). However, for high emissions of 5000 Pg C, glacial inception may be delayed for more than 500 kyr (Archer and Ganopolski, 2005). A study by Brandefelt et al. (2013) estimated that for permafrost development to occur at Forsmark, Sweden during the insolation minima at 17 and 54 kyr AP, atmospheric CO_2 concentrations of ~210 ppmv or less and ~250 ppmv or less would be required, respectively. In light of the long atmospheric lifetime of CO_2 emissions that has been discussed, low concentrations such as these are unlikely in the next few tens of thousands of years; however, they cannot be entirely excluded. In order to account for this limitation, the emulator could be extended to include glacial states, meaning that it could be applied to future climate on a longer timescale, as well as to the Quaternary, if the evolution of CO_2 and ice volume were known (e.g. from a transient EMIC or conceptual model simulation). Thus, when emulating long-term climate, careful consideration should be given to what assumptions are being made and whether the methodology is appropriate for the conditions being modelled.

Bearing in mind these limitations, the methodology described in this paper is a useful and powerful tool for simulating long-term past and future climatic changes, as well as for exploring the dynamics and sensitivities of the climate system.

3.9 Summary and Conclusions

In this study, long-term continuous projections of future climate evolution are presented at the spatial resolution of a GCM, via the use of a statistical emulator. The emulator was calibrated on two ensembles of simulations with varied orbital and atmospheric CO_2 conditions and modern day continental ice sheet extents, produced using the HadCM3 climate model. The method presented by Gregory et al. (2004) to calculate the steady-state global temperature change for a simulation, by regressing the net radiative flux at the top of the atmosphere against the change in global SAT, was utilised to calculate the equilibrated SAT data for these ensembles,

as it was not feasible to run the experiments to equilibrium due to the associated time and computer resources needed. A number of simulations testing the sensitivity of SAT to the extent of the GrIS and WAIS suggest that the response of SAT is fairly linear regardless of orbit, and that the largest changes are generally local to regions that are ice free. The mean SAT anomaly identified across these experiments was then applied to the equilibrated SAT results of the modern-day ice sheet extent ensembles, to generate two equivalent ensembles with reduced ice sheets.

Output data from the modern-day and reduced ice sheet ensembles were then used to calibrate separate emulators, which were optimised and then validated using a leave-one-out approach, resulting in satisfactory performance results. A number of useful applications of the emulator are discussed, which may not be possible using other modelling approaches at the same temporal and spatial resolution. Firstly, a particular benefit of the emulator is that it can be used to produce time series of climatic variables that cover long periods of time (i.e. several thousand years or more) at a GCM resolution, accompanied by an estimation of the uncertainty in the form of the posterior variance. This would not be feasible using GCMs due to the significant time and computational requirements involved. The global grid coverage of the data also means that the evolution of a climate variable at a particular grid box can be examined, allowing for comparisons to data at a regional or local scale, such as palaeo-proxy data, or for the evolution of climate at a specific site to be studied. However, further downscaling of the data may also be necessary or beneficial, via further modelling such as proxy modelling, impact models or regional climate models, or via statistical downscaling techniques. Secondly, the influence of orbital forcing on climate can be assessed. This effect may be visualised with a continuous wavelet analysis on the time series data for a particular CO_2 emissions scenario, which will identify the orbital frequencies dominating at different times. The spatial distribution of orbital timescale variability can also be simulated, by plotting the standard deviation for a climate variable for each grid box, taking into account the emulator posterior variance. Finally, the emulator can be used to back-calculate past atmospheric CO_2 concentrations based on proxy climate data. Through an inversion, atmospheric CO_2 concentrations can be estimated using SST proxy data, based on a linear relationship between emulated grid box mean annual SAT and prescribed CO_2 concentration. Estimated CO_2 can then be compared with palaeo CO_2 concentration proxy records.

To illustrate these potential applications, the emulator was applied at 1 kyr intervals to the late Pliocene (3300-2800 kyr BP) for atmospheric CO_2 concentrations of 280, 350 and 400 ppmv, and compared the emulated SATs at specific grid boxes to SSTs determined from proxy

data from a number of ODP/IODP sites. The wavelet power spectrum for SAT at each site was also produced, and the dominant orbital frequency assessed. In addition, the SST proxy data was used to estimate atmospheric CO_2 concentrations, based on a linear relationship between emulated grid box mean annual SAT and prescribed CO_2 concentration. It is found that:

- Temperature estimates from the emulator and proxy data show greater similarity at the equatorial sites than at the high latitude sites. Discrepancies may be the result of seasonal biases in the proxy data, unknown changes in the climate and/or carbon cycle, issues with the tuning of parts of the record, biases in the GCM, or errors in the emulator.
- The response of emulated SAT appears to be dominated by a combination of precessional and eccentricity forcing from 3300 kyr to approximately 2900 kyr, after which obliquity begins to have an increased influence.
- Regions with a particularly large response to orbital forcing include the high latitudes and monsoon regions (Figure 3.9b).
- The CO_2 concentrations derived from tropical ODP/IODP sites show relatively similar concentrations to CO_2 proxy records for the same period, although the concentrations derived from higher latitude sites are generally significantly higher than the proxy data.

The emulator was also applied to the next 200 kyr, as long-term future simulations such as these have relevance to the geological disposal of solid radioactive wastes. The continuous evolution of mean annual SAT and precipitation at a number of sites in Europe are presented, for four scenarios with anthropogenic CO_2 emissions of 500, 1000, 2000 and 5000 Pg C. A spectral wavelet analysis was also performed on the SAT and precipitation data for the Central England grid box. The data suggests that:

- SAT and, to a lesser extent, precipitation exhibit a relatively rapid decline back towards pre-industrial values over the next 20 kyr, as excess atmospheric CO_2 is removed by the long-term carbon cycle.
- Following this, SAT fluctuates due to orbital forcing on an approximate 41 kyr obliquity timescale until ~160 kyr AP, before the influence of precession increases with increasing eccentricity from ~120 kyr AP.
- Conversely, precipitation variations over the entire 200 kyr period demonstrate a strong precessional signal.

Overall, it is found that the emulator provides a useful and powerful tool for rapidly simulating the long-term evolution of climate, both past and future, due to its relatively high spatial resolution and relatively low computational cost. Illustrative examples have been presented of a number of different possible applications, which it is believed make it suitable for tackling a wide range of climate questions.

The emulator presented in this chapter can be applied to model long-term future climate change following the steps described in the framework in Section 1.5 of Chapter 1. Here, it was forced with future orbital variations, and atmospheric CO_2 time series data that were produced using the impulse response function developed in Chapter 2. The emulator methodology is developed further in the next chapter by increasing the maximum atmospheric CO_2 concentration that can be simulated using the emulator, allowing a wider range of anthropogenic CO_2 emissions scenarios to be projected.

CHAPTER 4

Extended analysis of the emulator

In the previous chapter, an emulator was described that can be used to project the long-term evolution of climate. It was used to model changes in SAT and precipitation occurring over hundreds of thousands of years in the late Pliocene and the future for several CO_2 scenarios. This emulator was calibrated only on SAT data (before being used to project SAT and precipitation), and is applicable to CO_2 concentrations of up to 2000 ppmv. This chapter presents further analysis of this emulator, including comparing the performance of emulators calibrated separately on SAT and precipitation data, as opposed to just being calibrated on SAT data. In addition, the range of GCM data that the emulator is calibrated on is extended to include very high atmospheric CO_2 concentrations, thus increasing the upper CO_2 limit that can be modelled.

4.1 Introduction

In the first part of this chapter, additional analysis of the *modice_60* emulator detailed in Chapter 3 is presented. Specifically, the principal components that were retained during the calibration of the emulator are examined (Section 4.2), to see if they provide any insight into the physical processes associated with climate. In addition, the sensitivity of emulated precipitation to the method of optimising the hyperparameters is tested, by comparing the use of

hyperparameters optimised on SAT data with the use of hyperparameters optimised on precipitation data (Section 4.3). Ideally, there would be one emulator (optimised on SAT) that would then be applied to model all climatic variables, meaning that the variables would be physically consistent with each other. However, SAT changes in a relatively linear manner with $\ln(CO_2)$, which may mean that variables that exhibit greater non-linearity may be less well reproduced by the emulator. Therefore, the ability of the emulator to model precipitation, which exhibits a relatively non-linear response to $\ln(CO_2)$, was tested, to ascertain if the use of one emulator version is appropriate.

The emulator described in Chapter 3 is applicable to atmospheric CO_2 concentrations ranging from 250 ppmv to 1900 ppmv. It was stated that, whilst AOGCM experiments were performed which sampled CO_2 up to 3600 ppmv, only experiments with CO_2 concentrations of 2000 ppmv or less were used to calibrate the emulator, due to a runaway warming feedback that caused the SAT in the experiments with CO_2 higher than this to increase rapidly and non-linearly over time. Consequently, these experiments were excluded from the emulator presented in Chapter 3.

In the *c*GENIE simulations described in Chapter 2, a peak CO_2 concentration of ~2000 ppmv is equivalent to total CO_2 emissions of ~6000 Pg C. Whilst fossil fuel reserves and resources are currently estimated to be slightly less than this amount (McGlade and Ekins, 2015), this does not take into account additional resources that may be useable in the future (either due to technological advances or oil and/or gas exploration), such as methane clathrates (Rogner, 1997), or natural climate feedbacks that may result in further release of CO_2 to the atmosphere following warming, for example through the melting of permafrost (Oechel et al., 1993, Zimov et al., 2006). Total CO_2 emissions of 10,000 Pg C modelled using *c*GENIE, for example, resulted in a peak atmospheric CO_2 concentration of 3900 ppmv. Therefore, in this chapter one aim will be to extend the methodology to allow the emulator to be applied at higher CO_2 concentrations so that more extreme CO_2 emissions scenarios can be simulated.

Consequently, the second part of the chapter presents an emulator that is calibrated on the full set of 80 simulations comprising the *highCO_2* and *lowCO_2* ensembles, including the very high CO_2 experiments that were previously excluded (Section 4.4). As a result, this emulator is suitable for modelling atmospheric CO_2 concentrations of up to 3600 ppmv, which is necessary for worst-case emissions scenarios that assume very high future CO_2 emissions. The effects of the runaway warming feedback in the very high CO_2 experiments are corrected for using a statistical approach (Section 4.4.1), and an emulator is then created using the corrected climate

data. This emulator is calibrated and evaluated (Section 4.4.2), before being used to project long-term future changes in SAT and precipitation (Section 4.4.3).

4.2 Analysis of principal components

As mentioned in the previous chapter (Section 3.3), a PCA (principal component analysis) was performed on the raw climate data produced by HadCM3 before it was used to calibrate the *modice_60* emulator. This emulator is so called because it is calibrated on 60 experiments – the full *lowCO_2* ensemble of 40 experiments, and 20 experiments from the *highCO_2* ensemble, sampling CO_2 up to 2000 ppmv (rather than the maximum of 3600 ppmv). This PCA method reduced the dimension of the global gridded output data, meaning that one emulator for the whole global grid could be constructed, rather than separate emulators for individual grid boxes. It works by mathematically analysing the gridded data (e.g. for SAT) for all of the simulations (60), and decomposing the data into a linear combination of map patterns (eigenvectors). Each of these PCs has an associated eigenvalue that describes the relative amount of variance that the PC accounts for, and these are sorted by decreasing eigenvalue. Hence, the first eigenvector explains the most variance, the second explains the second-most variance, etc. The number of PCs that the data are fully represented by is equal to the number of simulations analysed, although in practice only a relatively small number of the eigenvectors are retained. Here, these were the first components (highest eigenvalues) that accounted for the majority of the variance in the data, and the exact number retained was determined during the optimisation and evaluation of the emulator, described in Section 3.5.2 of Chapter 3. For the *modice_60* emulator, 13 PCs are retained, accounting for 87% of the total variance. The percentage of the total variance that each of the first 10 retained PCs represents is shown in Figure 4.1. Combined, these 10 PCs account for 85% of the total variance. For each simulation, and its unique input conditions (CO_2 and orbital), the emulator assigned a weighting to each of the retained PCs. When the weighted PCs for a simulation were combined with a map of mean SAT (averaged across the 60 experiments), the gridded SAT data for that simulation was reproduced. A similar method is then applied by the emulator to provide a prediction of SAT for unsimulated situations, based on their input conditions.

The PCA is a mathematical procedure, which means that the PCs, particularly those other than the first, are not necessarily related to physical processes. However, several of the PCs exhibited spatial patterns that may be linked to changes in specific parts of, or processes in, the

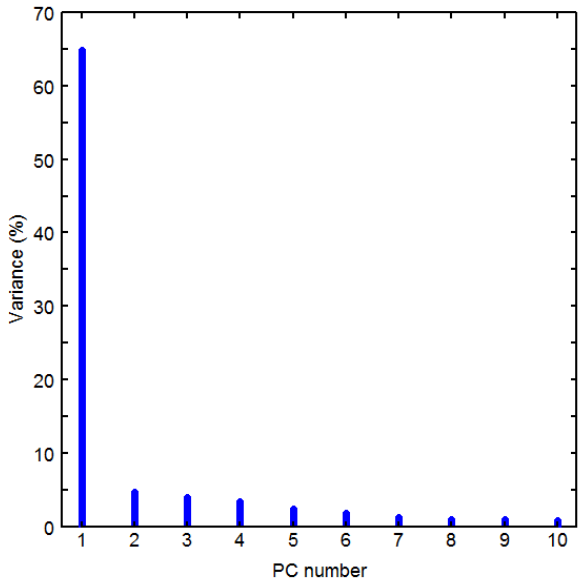

Figure 4.1.Percentage of the total variance represented by PCs 1-10 for SAT (°C) for the modice_60 emulator.

Earth system that are expected to occur in response to changes in atmospheric CO_2 concentration and/or orbital conditions. Therefore, by examining them it may be possible to learn something about the physical mechanisms occurring in the Earth system. All PCs discussed here are from the SAT *modice_60* emulator.

The first 10 retained PCs are illustrated in Figure 4.2. All of the values of the PCs are positive in the global mean, apart from PC1 which has negative values. The sign of the values assigned during the PCA is arbitrary, since if the sign convention of the PC is reversed, as in the case of PC 1, the sign of the associated eigenvalue (which the PC is multiplied by) is also reversed. This means for PC 1 the associated eigenvalue is negative, hence when the PC and eigenvalue are multiplied, the resulting signal is positive.

PC 1, shown in Figure 2a, accounts for the most variance (65%) and is therefore most likely to be suitable for physical interpretation. It shows relatively large SAT changes at high latitudes, particularly in the north, as well as over land. A very similar pattern of warming occurs as a result of an increase in atmospheric CO_2. This is illustrated by Figure 4.3, which is the mean annual SAT anomaly compared with pre-industrial for an idealised simulation with doubled pre-industrial atmospheric CO_2 (560 ppmv). All other conditions (i.e. orbital and ice sheets) were the same as in the pre-industrial simulation. It is not unexpected that the first PC resembles the SAT response to increased CO_2, given that the majority of the simulations in the two ensembles used for calibration (*highCO_2* and *lowCO_2*) had CO_2 concentrations that were significantly higher than

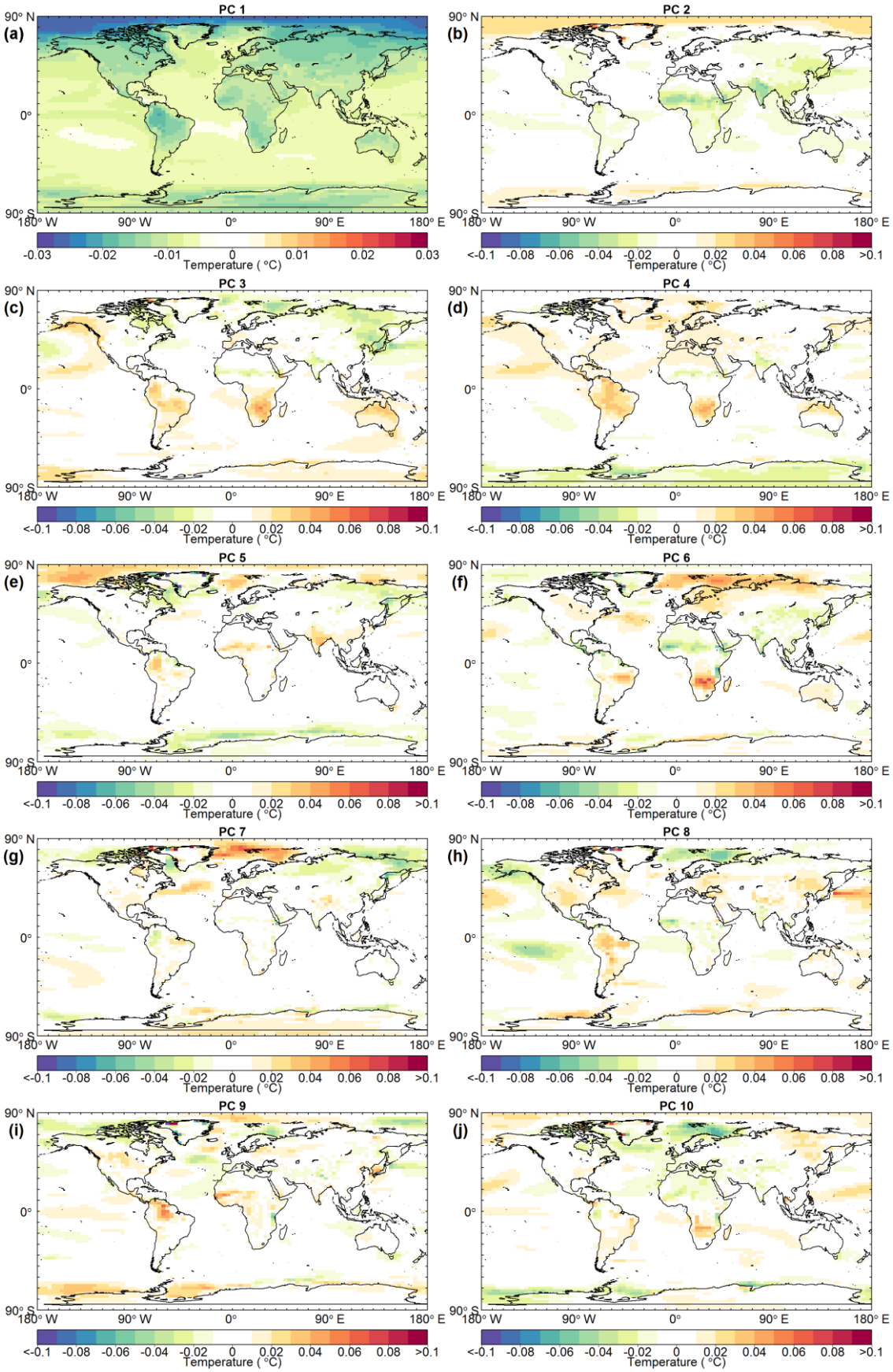

Figure 4.2. PCs 1-10 for SAT (°C) for the modice_60 emulator. Note the different scale of PC 1 and the subsequent PCs.

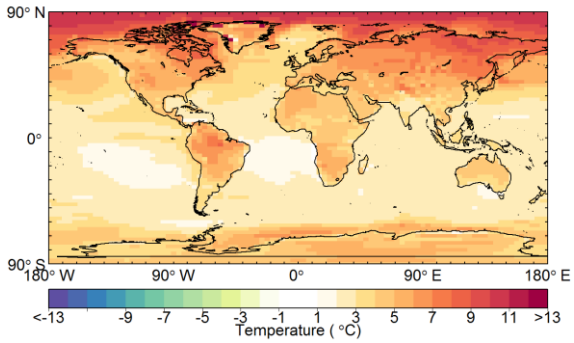

Figure 4.3. Mean annual SAT anomaly (°C) for 2x CO_2 simulation (compared with pre-industrial).

pre-industrial. It is, therefore, likely to be the dominant forcing on climate in many of the simulations, particularly when mean annual rather than seasonal SAT is being considered. Amplification of warming at high latitudes is exhibited by a large range of models (e.g. Holland and Bitz, 2003, Collins et al., 2013), and is largely the result of ice-albedo feedbacks (Hall, 2004, Kumar et al., 2010).

PCs 2 to 6 appear to be at least partly related to monsoonal changes, with the greatest SAT changes occurring in monsoonal areas, as illustrated in Figure 4.2. For example, the second PC (Figure 4.2b) exhibits relatively large changes in the Northern Hemisphere monsoonal regions, namely over North Africa, India and East Asia. On the other hand, PCs 3 and 4 (Figures 4.2c and 4.2d) show variations in the Southern Hemisphere monsoonal regions of South America, South Africa and Australia. There is still significant uncertainty about the response of monsoons to future changes in climate driven by increased atmospheric CO_2 concentrations, with models often projecting different responses for different regions (Christensen et al., 2013). Prediction is further complicated by the range of processes and conditions that can affect monsoons, including atmospheric moisture content, atmospheric circulation, and the land-sea temperature difference, as well as cyclical climate phenomena operating on a range of timescales, including the ENSO, the Pacific Decadal Oscillation and the Atlantic Multidecadal Oscillation (Christensen et al., 2013, Lu et al., 2006, Krishnan and Sugi, 2003). Additionally, the response of SST to warming may have an impact, which may vary between different models, contributing to variance in projections. On longer timescales, a number of studies using proxy data and/or model simulations of past climates have suggested that the periodicity and phasing of monsoons is also influenced by orbital variations, possibly through the impact of changes in northern summer insolation on precessional timescales (e.g. Kutzbach, 1981, Kutzbach and Liu, 1997, Yuan et al., 2004).

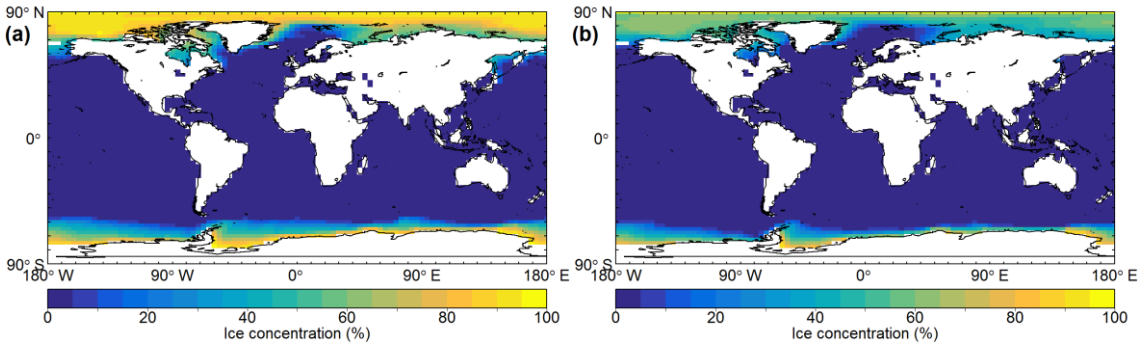

Figure 4.4. Mean annual sea-ice concentration (%) for: (a) pre-industrial simulation and (b) 2x CO_2 simulation.

Several the PCs exhibit spatial variations in SAT that are similar to those related to changes in sea-ice, including PCs 3 and PCs 5 to 9 (Figures 4.2c and 4.2e to 4.2i). The outer sea-ice boundaries in the Arctic and Southern Oceans, including parts of the Barents, Greenland, and Bering seas in the north and the Weddell, Bellingshausen, and Amundsen Seas in the south, show particular sensitivity to warming scenarios, due to sea-ice retreat (Figure 4.4). This decrease in sea-ice cover results in increased exposure of the darker ocean surface, reducing the surface albedo and leading to further warming (ice-albedo feedback), as illustrated in Figure 4.5.

Finally, several of the PCs appear to be related to changes in AMOC, such as PCs 5 and 10 (Figures 4.2e and 4.2j), as indicated by the occurrence of relatively large changes in SAT in North Atlantic regions that are associated with the formation of North Atlantic Deep Water (NADW). This deep-water mass is formed when cold, dense surface water sinks in the Labrador Sea and Greenland-Iceland-Norway Sea, releasing heat to the atmosphere. The strength of the AMOC is projected to decrease under future warming scenarios, as a result of increased SAT and precipitation at high northern latitudes (Collins et al., 2013). Together, these changes act to reduce the density of high latitude surface waters, increasing their stability and reducing the strength of the AMOC.

There are various other ways in which the data can be visualised that may provide further insight into the validity of these tentative interpretations linking individual PCs and climatic changes. One method is to examine the relationship between the input conditions and the amplitudes of the PCs. These amplitudes are the right singular vectors of **Y**, produced during the PCA, and are denoted **V** in Equation 3.1 of Chapter 3. For each of the 60 experiments used to calibrated the *modice_60* emulator, every PC is assigned a weighting (**V**) that defines the contribution of the PC to reproducing the full spatial field of mean annual SAT for that experiment.

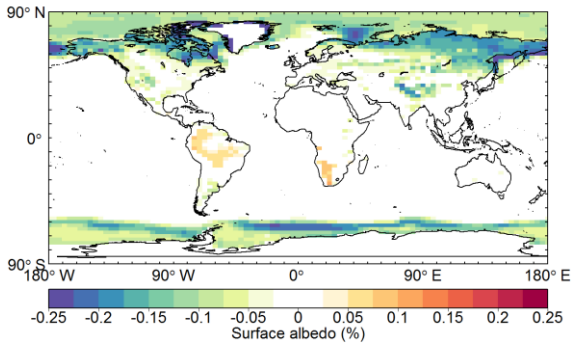

Figure 4.5. Mean annual surface albedo anomaly (%) for 2x CO_2 simulation (compared with pre-industrial).

The majority of the retained PCs, particularly the lower-order PCs, do not exhibit a significant correlation with any of the input parameters. This is likely due to the consideration that, as you move down the list of PCs, they account for a decreasing amount of the total variance, and thus are likely to increasingly represent minor fluctuations in SAT that may only occur in a small number of experiments. However, the amplitudes of the first few PCs were found to demonstrate a correlation with some of the input parameters, as shown in Figure 4.6. The implications of these results are discussed below.

Another method of visualising the PCs, whilst getting an indication of the climate forcings that they may be capturing, is to look at the change in the contribution of each PC for experiments with different input conditions. This is illustrated in Figure 4.7, for four idealised experiments produced using the *modice_60* emulator. The input parameters of these experiments are detailed in Table 4.1. In Figure 4.7, the amplitudes of the first ten PCs are compared for the different experiments, and the variation in these amplitudes can give an indication of the climate forcing(s) that the PCs may be capturing.

Based on the spatial trends shown in Figure 4.2a, the first PC was attributed to CO_2 forcing, and this theory is supported by Figures 4.6 and 4.7. Figure 4.6 demonstrates a strong negative correlation between the amplitude of PC 1 for the 60 experiments and the atmospheric CO_2 concentration, with the experiments with very high CO_2 having an increasingly large negative amplitude. PC 1 consists of negative values (Figure 4.2a) and so, for CO_2 concentrations of approximately 500 ppmv or higher, this combines with the negative amplitude (**V**) and the positive eigenvalue for PC 1 (**S** in Equation 3.1 of Chapter 3) to produce a positive signal. Figure 4.7 shows that the amplitudes of PC 1 are very similar for the three experiments with the same atmospheric CO_2 concentration (PI, 6 kyr BP and 54 kyr AP), but significantly smaller for the experiment with 2xCO_2. This decrease in amplitude is consistent with Figure 4.6 which shows that the amplitude of PC 1 generally decreases as atmospheric CO_2 increases. The amplitude for

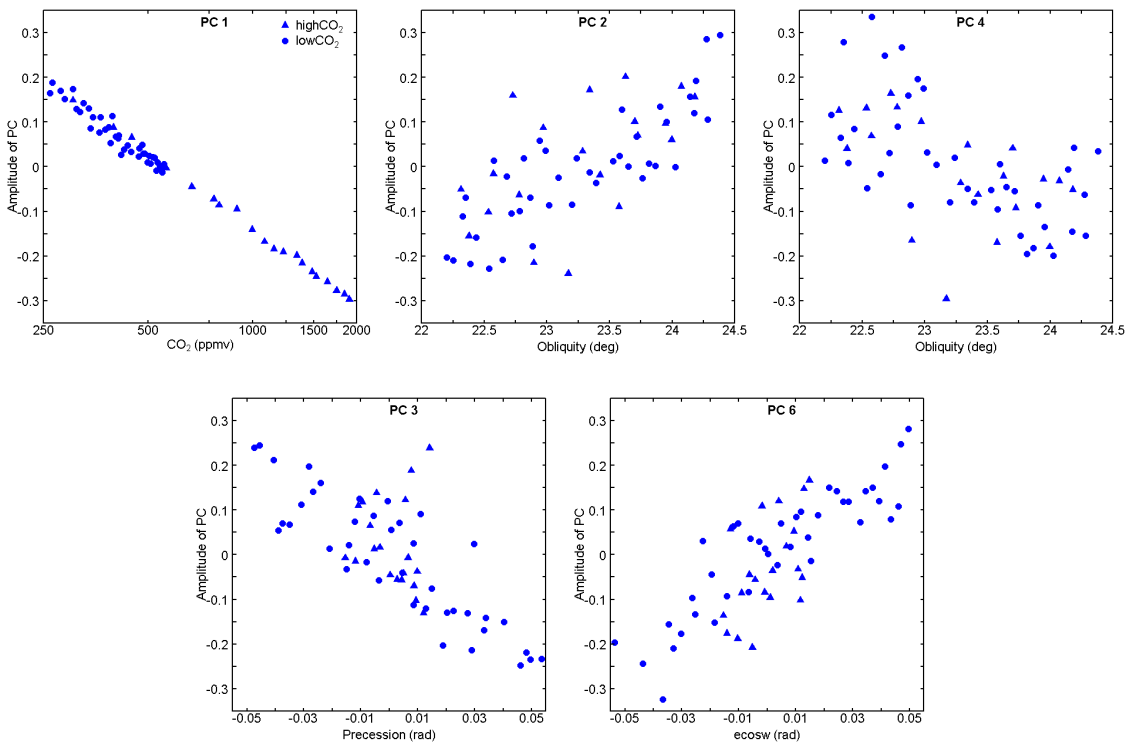

Figure 4.6. Amplitudes of PCs 1-4 and PC 6 for the 60 experiments used to calibrate the modice_60 emulator, compared to different input parameters for the experiments (CO_2, obliquity, esinϖ (precession), and ecosϖ).

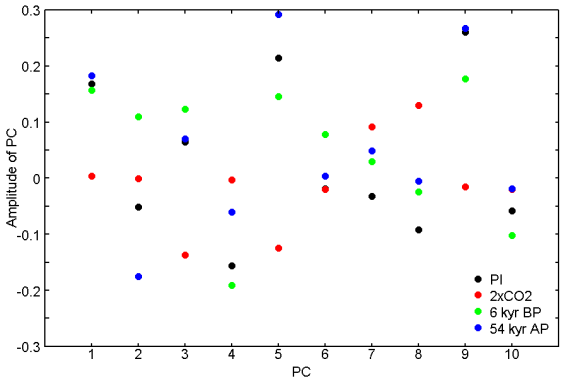

Figure 4.7. Amplitudes of the first 10 PCs for four idealised experiments: pre-industrial orbital and CO_2 conditions (PI; black), doubled pre-industrial CO_2 (2xCO_2; red), orbital conditions at -6 kyr BP (green), and orbital conditions at 54 kyr AP (blue).

the 2xCO_2 experiment in Figure 4.7 is close to zero, compared to the other experiments that have positive amplitudes, which may initially suggest a lower CO_2 signal for this experiment compared to the other experiments. However, during the PCA on the experiments used to calibrate the emulator, the average SAT is calculated across the experiments, giving a grid of mean SAT data covering the Earth's surface. This mean data is then subtracted from the original SAT data, and the SVD then performed. To reproduce the original data for an experiment, the eigenvector and eigenvalue for the experiment are multiplied, and the resulting spatial data is added to the

Table 4.1. Input parameters for four idealised experiments: pre-industrial orbital and CO_2 conditions (PI), doubled pre-industrial CO_2 ($2xCO_2$), orbital conditions at -6 kyr BP, and orbital conditions at 54 kyr AP. Details of the orbital parameters – obliquity (ε), eccentricity (e), and longitude of perihelion (ϖ) - and atmospheric CO_2 concentration are provided.

Experiment	ε (°)	e -	ϖ (°)	CO_2 (ppmv)
Pre-industrial	23.44	0.0163	102.9	280
$2xCO_2$	23.44	0.0163	102.9	560
6 kyr BP	24.10	0.0187	1.4	280
54 kyr AP	22.59	0.0115	87.1	280

overall mean. The same process is also applied when calculating the emulators prediction of SAT for a new experiment, such as the $2xCO_2$ experiment. The mean data demonstrates a signal similar to that shown by PC 1 in Figure 4.2a (although with positive values), which has been shown to represent warming due to increased atmospheric CO_2 concentration. Therefore, the positive amplitudes for PC 1 shown in Figure 4.7 for the pre-industrial, 6 kyr BP, and 54 kyr AP experiments (which have CO_2 concentrations of 280 ppmv) combine with the negative spatial data for PC 1 (Figure 4.2a) to give a negative signal, with is then added to the positive mean data (along with the other PCs), acting to reduce some of the warming signal in the mean data. Conversely, the $2xCO_2$ experiment has an amplitude of close to zero for PC 1, which means the warming signal captured in the mean data is not significantly diminished when the PCs and mean SAT are summed.

A number of other PCs also show a difference in amplitude between the PI and $2xCO_2$ experiments, particularly PCs 3, 4, 5, 8, and 9, suggesting that these also represent some of the response of SAT to a doubling of CO_2, (given that the two experiments have the same orbital configurations). This demonstrates that the effects on SAT of a particular forcing are not necessarily just captured by one PC.

PCs 2 and 4 show a correlation with obliquity, although the first shows a positive correlation and the second, a negative one (Figure 4.6). This trend can also be seen in Figure 4.7 in the contrary responses of the amplitudes of the two PCs for the 6 kyr BP and 54 kyr AP experiments compared with the pre-industrial one. Conversely, PCs 3 and 6 are related to precession ($e\sin\varpi$) and $e\cos\varpi$, respectively (Figure 4.6).

Figure 4.7 suggests that the majority of the PCs represent SAT variations driven by several different forcings, since there are differences in the amplitudes for all four experiments. The exceptions to this are PC 1, which primarily captures the SAT response to atmospheric CO_2

concentration, and PC 6, which appears to only represent orbital variations. This conclusion is drawn for PC 6 given that the amplitudes for the pre-industrial and 2xCO_2 experiments, which have identical orbital parameters, are essentially the same, with the point on Figure 4.7 representing the 2xCO_2 experiment overlying the point for the pre-industrial experiment.

4.3 Sensitivity to hyperparameters

When emulating variables other than the standard SAT, there are several things that must be considered, including the selection of the hyperparameters (length scales and nugget) used in the emulator and the number of PCs retained. One option is to use the optimised hyperparameters that were selected for the SAT emulator, which has the benefits of being relatively simple, and providing projections for different variables that are physically consistent. On the other hand, the hyperparameters can be optimised separately for each variable, potentially improving the performance of the emulator; as detailed in Section 3.5.2 in Chapter 3, the optimised hyperparameters values were selected using a leave-one-out method, where each of the experiments in turn was left out during emulator calibration and then reproduced using the emulator, with the emulator configuration (hyperparameter values and number of PCs) that performed best being selected as the final configuration.

Here, the two methods are compared for precipitation data, to assess whether there is a significant difference in the results of the leave-one-out validation. For the pre-industrial ice sheet configuration (*modice*), one emulator was optimised based on SAT data (i.e. the *modice_60* emulator presented in Chapter 3 and used to emulated precipitation in Section 3.7.1), and the other emulator was optimised based on precipitation data. Both were then calibrated using precipitation data and evaluated using the leave-one-out methodology. The emulator optimised on SAT retains 13 PCs, and has length scales (δ) of 7.509 (ε), 3.361 ($e\sin\varpi$), 3.799 ($e\cos\varpi$), 0.881 (CO_2) and a nugget of 0.0631. On the other hand, the emulator optimised on precipitation retains 15 PCs, and has length scales of 11.165 (ε), 3.320 ($e\sin\varpi$), 3.664 ($e\cos\varpi$), 1.380 (CO_2) and a nugget of 0.028.

The results of the leave-one-out analysis are presented in Figure 4.8. It was found that there was very little difference between the performances of the two emulators. Figures 4.8a and 4.8b show the percentage of grid boxes for each left-out experiment estimated by the corresponding emulator within different standard deviation bands, and exhibit very similar results. This is both in terms of the performance of the two emulators overall – most experiments

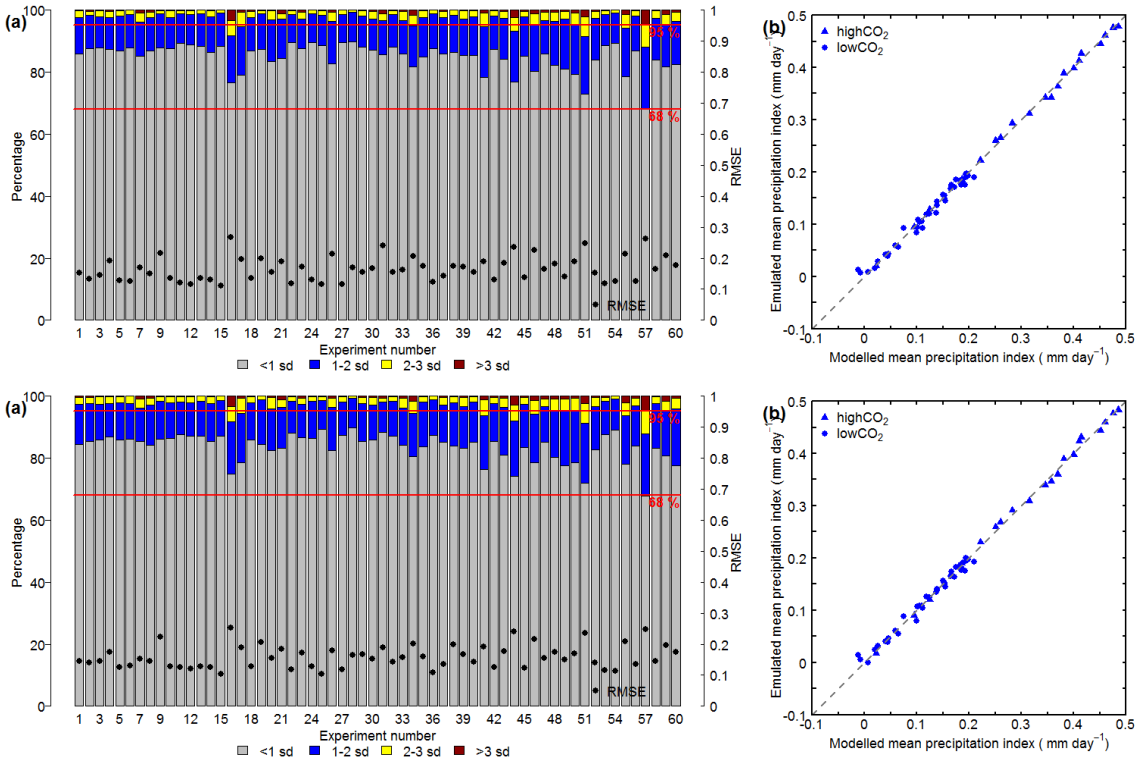

Figure 4.8. Evaluation of emulator performance for the precipitation modice_60 emulator, optimised on: (a) + (b) SAT data, and (c) + (d) precipitation data. (a) + (c) Bars give the percentage of grid boxes for which the emulator predicts the precipitation of the left-out experiment to within 1, 2, 3 and more than 3 standard deviations (sd). Also shown is the RMSE for the experiments (black circles). Red lines indicate 68% and 95%. (b) + (d) Average global mean annual precipitation index (°C) calculated by the emulator and the GCM for the lowCO_2 (circles) and highCO_2 (triangles) modice_60 ensembles. The 1:1 line (dashed) is included for reference. Note: this is the mean value for the GCM output data grid assuming all grid boxes are of equal size, hence not taking into account variations in grid box area. Precipitation is shown as an anomaly compared with the pre-industrial control simulation.

are reproduced with fewer than 5% of grid boxes showing deviations of more than 2 standard deviations – and in terms of how well individual experiments are reproduced relative to each other – for example, the experiments with the highest RMSE are numbers 16, 44, 51, and 57 in both emulators. Neither of the emulators produce any significant outliers when the emulated average global mean annual precipitation index for the experiments is compared with that of the original GCM data, shown in Figures 4.8b and 4.8d.

The similarity of the performance results of the two emulators suggests that it may be appropriate to use the emulator configuration that was optimised based on SAT data for emulating other climate variables, rather than optimising separate emulators calibrated on individual variables. Along with the simplicity this provides, it has the added advantage that estimates of the different variables will be consistent with each other.

For precipitation, the above assumption that a single emulator configuration is appropriate for multiple variables is certainly true. Figure 4.9 shows emulated mean annual

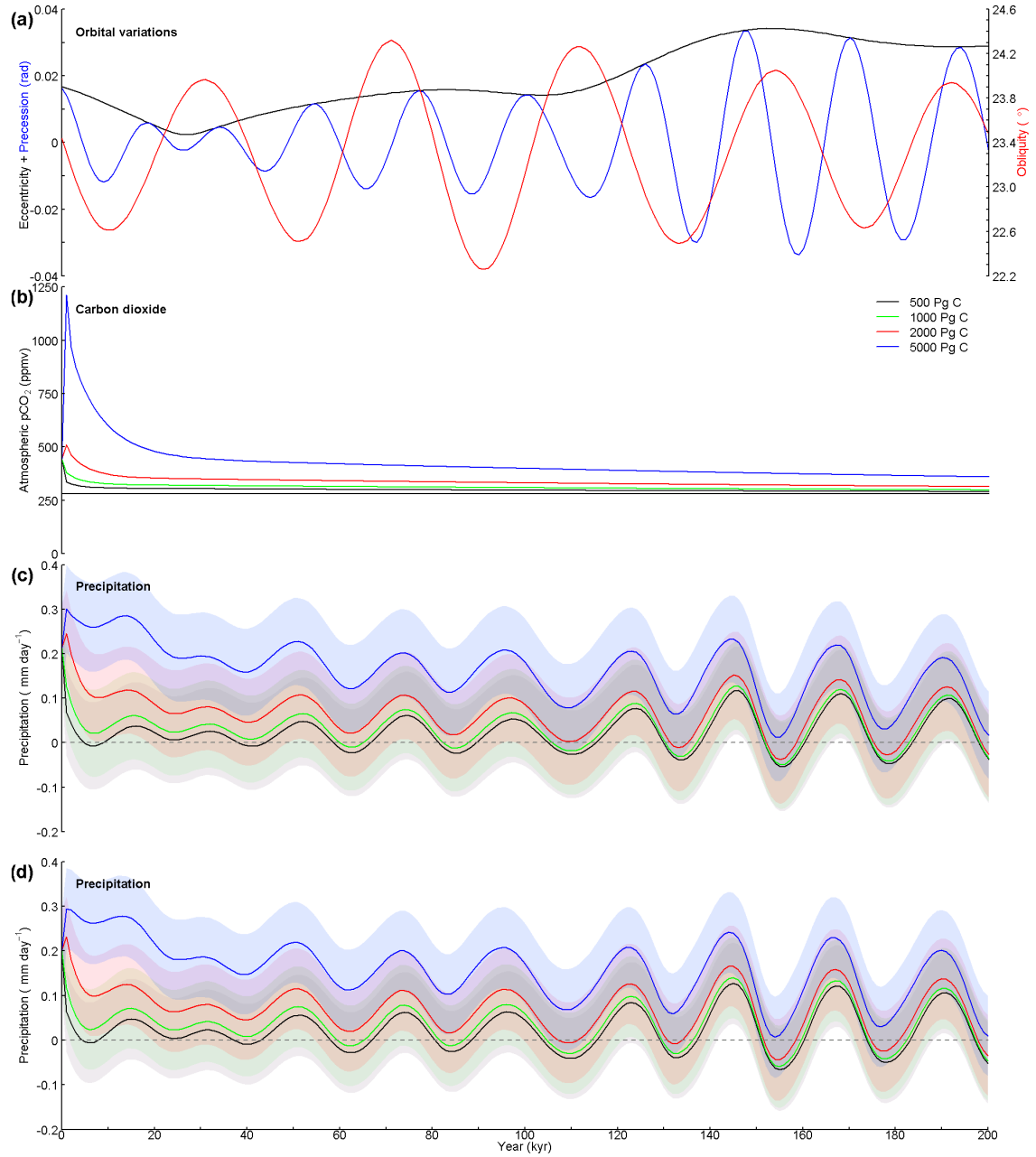

Figure 4.9. Emulation of precipitation for the next 200 kyr at the Central England grid box. (a) Time series of orbital variations (Laskar et al., 2004), showing eccentricity (black) and precession (radians; blue) on the left axis, and obliquity (degrees; red) on the right axis. (b) Time series of atmospheric pCO_2 (ppmv), predicted using the impulse response function discussed in Chapter 2. The pre-industrial CO_2 concentration is also shown (black line). (c) + (d) Time series of emulated mean annual precipitation (mm day^{-1}), modelled every 1 kyr, for four CO_2 emissions scenarios; 500 Pg C (black), 1000 Pg C (green), 2000 Pg C (red) and 5000 Pg C (blue). Modelled using the modice_60 emulator optimised on: (c) SAT data, and (d) precipitation data. Error bands represent the emulated grid box posterior variance (1 standard deviation). Precipitation is shown as an anomaly compared with the pre-industrial control simulation.

precipitation for the next 200 kyr for the Central England grid box as projected by each emulator (i.e. one optimised on SAT data and one on precipitation data). For all CO_2 scenarios, precipitation is very similar for both emulators, with only minor differences in projected values and uncertainties. The uncertainty for the grid box is slightly lower in the emulator optimised on precipitation data, with an average standard deviation for the period of 0.090 mm day^{-1}, as

opposed to 0.098 mm day^{-1} for the emulator optimised on SAT. However, the error is relatively small compared with the uncertainty due to the emissions scenario.

In the above emulators, the hyperparameter values for the emulator optimised on precipitation were fairly similar to those for the emulator optimised on SAT. The largest differences were the length scales for obliquity (ε) and CO_2, although both of these parameters vary by a similar proportion. This suggests that the responses of SAT and precipitation to the input parameters are fairly similar, particularly the reasonably linear response to the three orbital parameters compared with CO_2, indicated by their relatively large values. In terms of the different numbers of PCs retained by the two emulators, the weighted PCs account for progressively less variance, meaning that, after the first few, the impact that each has on the results of the emulator will get progressively smaller. Hence, increasing the number of retained PCs from 13 to 15 does not have a large impact on the overall emulator performance. For the latter PCs, it may also be that some of the PCs capture the variance only relevant to a relatively small number of simulations. Thus, their inclusion or exclusion may affect the reproduction of particular experiments, rather than the entire ensemble, although there is little evidence for this from Figure 4.8.

A potential weakness of the approach of using an emulator optimised on SAT data for other climate variables is that the hyperparameters may not be fully optimised for the variable being emulated. This is less likely to be a significant issue for variables that respond to CO_2 and orbital forcings in a similar way to SAT, or that are themselves predominantly driven by changes in SAT. However, the performance of the emulator optimised on SAT data has been tested here using a variable that changes non-linearly with the four forcings used (precipitation), and there was found to be very little loss in performance compared with an emulator optimised on precipitation. It is therefore concluded that use of a single optimised emulator for different variables is appropriate. This has the advantage that projected changes in the different climate variables will be physically consistent with each other, reducing the likelihood of unrealistic combinations of changes. It should also improve the coherence of estimating derived variables, such as potential evapotranspiration or soil moisture deficit, that depend on more than one output from the climate model.

4.4 An emulator using the full *highCO$_2$* ensemble

4.4.1 AOGCM simulations with very high CO_2

In this section, an emulator is presented that was calibrated using the full set of 80 simulations that were run using HadCM3; 40 experiments from each of the *highCO$_2$* and *lowCO$_2$* ensembles. This is in contrast to the emulator described in Chapter 3, which was calibrated on 60 experiments with CO_2 concentrations of up to 1900 ppmv. All simulations used here had modern-day ice sheet configurations, hence the experiments and accompanying emulators are referred to as *modice* (as opposed to *lowice*). Full details of the *highCO$_2$* and *lowCO$_2$* ensembles are given in Chapter 3, including justification for the chosen orbital and CO_2 parameter ranges, and an account of the use of Latin hypercube sampling to generate the 80 experiments. In the previous chapter, it was noted that all experiments were run for a total of 500 model years, apart from six experiments in the *highCO$_2$* ensemble which had atmospheric CO_2 concentrations of greater than 3100 ppmv. In these cases, the climate became unstable and warming rapidly increased several hundred years into the simulation. This eventually caused the model to crash before completion of the simulation. Runaway warming trends were also evident in experiments with a CO_2 concentration of ~2600 ppmv or higher, although these experiments ran for the full 500 years without crashing. The extreme warming was the result of a runaway positive feedback caused by the height of the ozone layer in the model being prescribed, rather than being able to respond to changes in climate.

Firstly, in this section, the simulations which exhibit runaway warming are identified (Section 4.4.1.1, Figure 4.11). Following this, these simulations are corrected using a relationship developed from experiments that did not experience runaway warming, thus removing the runaway warming signal from the very high CO_2 experiments (Section 4.4.1.2, Figures 4.12 and 4.16). Finally, the fully-equilibrated spatial SAT data for the corrected experiments is calculated based on the ratio between equilibrated mean global SAT calculated using Gregory plots and the mean global SAT at the end of the model simulations (Section 4.4.1.2.3, Figures 4.17, 4.18, and 4.19).

4.4.1.1 Identification of experiments with runaway warming

A threshold-based approach was applied to identify the experiments which experienced a runaway warming feedback, based on the rate of change over time of the global mean decadal net downward radiative flux at the top of the atmosphere. Standard experiments exhibited a relatively rapid increase in the rate of change of the net downward radiative flux over the first 50 or so years, due to SAT rapidly increasing over this period as the model adjusted to the CO_2 concentration, affecting the outgoing radiation flux which then impacted the net downward flux. This rapid warming was followed by more gradual warming for the remainder of the modelled period, or equilibration of the SAT for simulations with lower CO_2. In both cases, this resulted in the rate of change levelling out at a value of slightly higher than 0 W m^{-2} per decade, with some minor fluctuations due to interdecadal variations, as demonstrated by Figure 4.10a for the first ~450 years of the simulation. This steady rate of change continued to the end of the experiments, as the net downward radiative flux approached equilibrium. However, in the experiments that demonstrated runaway warming, a rapid increase in the rate of change occurred several hundred years into the experiment, as increasing global temperatures caused a decrease in outgoing shortwave radiation due to more radiation being trapped by the atmosphere, and an increase in outgoing longwave radiation as a result of higher global temperatures. Therefore, a relatively large increase in the rate of change was taken to indicate the onset of runaway warming, illustrated by Figure 4.10b.

For this methodology, a 50-year moving average of the global mean decadal TOA net downward radiative flux was calculated for all experiments in the *highCO_2* ensemble, in order to remove short-term variations, and rate of change of the moving average was then calculated. The standard deviation of these data from 100 years onwards was calculated for all experiments with CO_2 concentrations of less than 2500 ppmv, a value which was identified, based on visual inspection of the results, as an approximate threshold for runaway warming. As a result, only the period of steady rate of change was included, and not the initial rapid increase in the rate of change. The tolerance in the rate of change was set at 3 standard deviations above the mean, and the exceedance of this tolerance was tested for over the final 300 years of each experiment. This approach assumes that the first 200 years of data for all *highCO_2* experiments is “correct”, i.e. unaffected by the runaway positive feedback. This assumption was initially based on visual inspection of the data, and subsequently supported by the results of this analysis. Therefore, the first condition for an experiment with runaway warming to meet was:

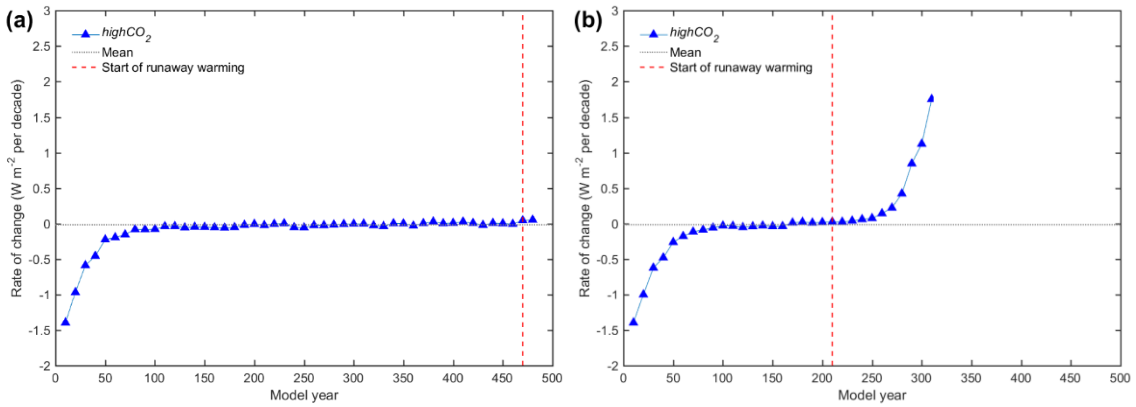

Figure 4.10. The rate of change for the 50-year moving average of the net downward radiation flux (triangles and solid line; W m^{-2} per decade) over the course of the simulation for experiments: (a) modice_highCO2_38, and (b) modice_highCO2_36. Also shown is the average rate of change for model years 100-500 for the simulations with CO_2 concentrations of less than 2500 ppmv (grey dotted line). The decade when runaway warming was identified to have begun is also indicated (red dashed line)).

Condition I. The rate of change of the 50-year moving average exceeded 3 standard deviations above the mean within the final 300 years of the experiment

A number of additional conditions were applied to help determine if the exceedance of the rate of change threshold was due to runaway warming or simply extreme isolated fluctuations. These constraints were related to the decade at which the exceedance occurred (note: the rate of change was calculated from a 50-year moving average of the radiative forcing data), whether the exceedance was a single isolated event or a number of adjacent events occurred, and the atmospheric CO_2 concentration of the simulation. The experiment was assumed to be demonstrating runaway warming at the first decade of the tolerance for the rate of change being passed if the following conditions were met:

Condition II. The CO_2 concentration was greater than 2500 ppmv

AND EITHER

Condition III. For a single isolated exceedance event as per Condition I, the exceedance occurred at decade 48 (the final value of the rate of change of the moving-average)

OR

Condition IV. Two or more adjacent exceedance events occurred in series

In addition to the six experiments that crashed, six others that ran to completion were identified as exhibiting runaway warming. These experiments, which had CO_2 concentrations of

2600 ppmv and higher, are detailed in Table 4.2. This list is a subset of the full set of 80 experiments presented in Table 3.2 in Chapter 3. Also provided is the decade when the runaway warming began, and the average global annual mean SAT anomaly compared with pre-industrial for this decade. Generally, the higher the CO_2 concentration, the earlier in the simulation the runaway warming began. Figure 4.10 shows the rate of change of the 50-year moving average of net downward radiation flux over the course of the simulation for the lowest and highest CO_2 experiments that were identified to exhibit runaway warming. These were experiments *modice_highCO2_38* (CO_2 2623.9 ppmv) and *modice_highCO2_36* (CO_2 3588.9 ppmv), respectively.

The full methodology used to identify the experiments that experienced runaway warming is summarised in a flow chart in Figure 4.11.

4.4.1.2 Calculation of equilibrated climate

The equilibrated SAT for the 12 experiments in Table 4.2 was estimated, thus correcting for the impact of the runaway warming, based on the trends exhibited by the other 68

Table 4.2. Modice experiments that experienced the runaway warming feedback, including their atmospheric CO_2 concentration, the first decade at which the warming was identified to occur, and the average global mean annual SAT (°C) for this decade. SAT is shown as an anomaly compared with the pre-industrial control simulation.

Ensemble	Experiment #	CO_2 (ppmv)	First decade of runaway warming	Mean annual SAT °C
highCO₂	38	2623.9	47	12.8
	37	2760.4	48	13.1
	24	2845.7	29	11.7
	20	2890.4	44	13.2
	27	2951.8	39	13.2
	6	3049.0	37	12.9
	10	3139.3	27	12.2
	40	3188.8	29	12.1
	1	3348.2	24	11.9
	13	3372.4	26	12.5
	26	3516.0	22	11.9
	36	3588.9	21	12.3

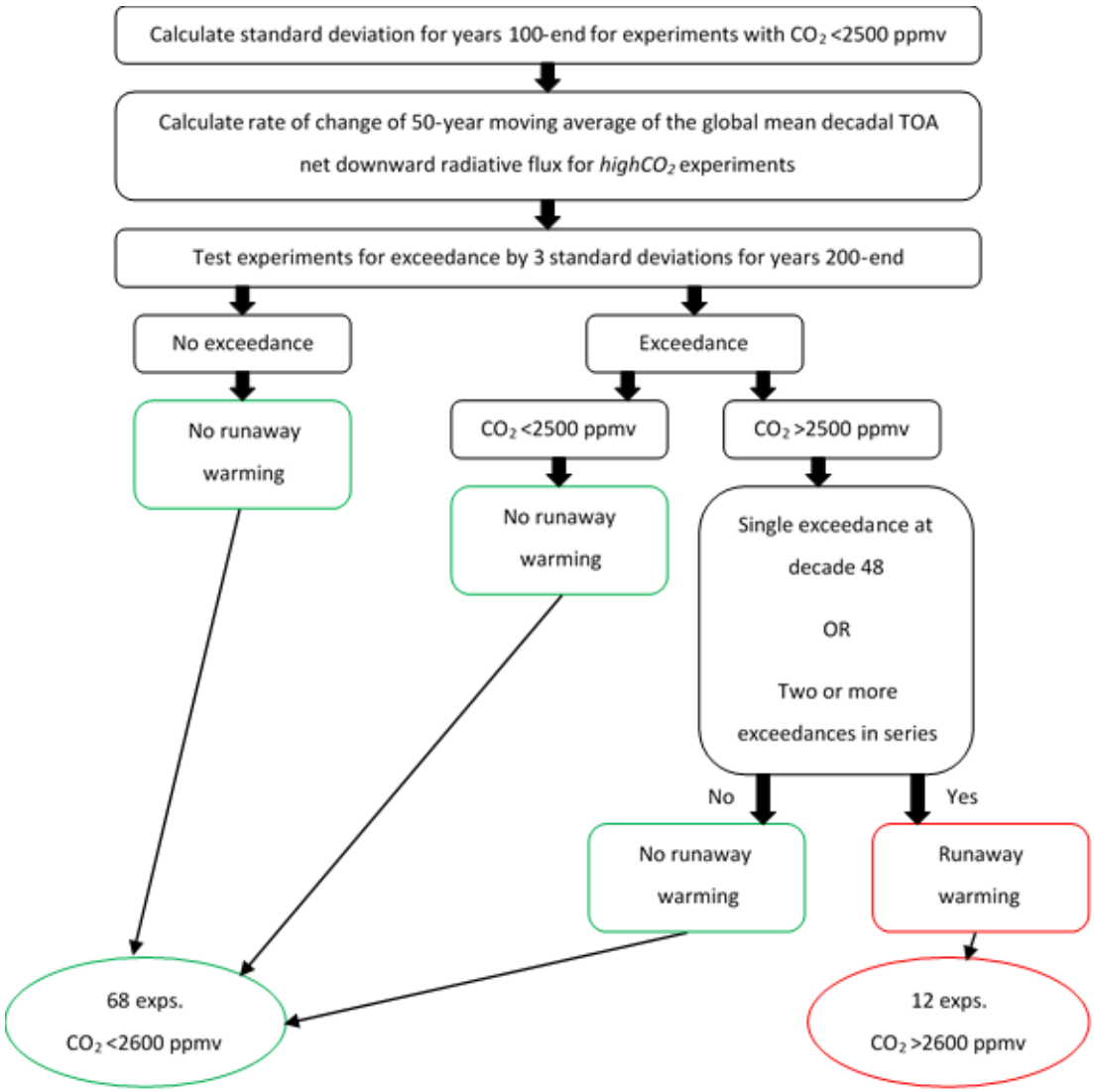

Figure 4.11. Flow chart summarizing the methodology used to identify which experiments experienced runaway warming (red) and which did not (green). The thin black arrows indicate the results of the method; in this case, a list of experiments that show runaway warming and a list that do not.

experiments in the *highCO_2* and *lowCO_2* ensembles. Table 4.2 suggests that the first occurrence of runaway warming was detected in the 21st decade, or approximately 210 years into the experiment. Therefore, as before, it was assumed that the data for at least the first 200 years of all simulations was unaffected by the runaway warming. Briefly, Gregory plots (see Section 4.4.1.2.1) were produced, and then the ratio between equilibrated SAT after 200 years and after the full 500 years derived from these were used in a pattern-scaling technique that was applied to the experiments with runaway warming. The full methodology is described below.

4.4.1.2.1 Gregory plots

Gregory plots were produced for all 80 experiments in the *highCO₂* and *lowCO₂* ensembles, as summarised in Figure 4.12. A detailed description of the Gregory plot methodology (Gregory et al., 2004) is available in Chapter 3. However, briefly, the net radiative flux at the top of the atmosphere (N; W m^{-2}) was regressed against the global average SAT change (ΔT; °C). The intercept of the line at ΔT=0 is the effective radiative forcing (F; W m^{-2}; positive downwards), the slope of the line is the climate feedback parameter (α; W m^{-2} °C^{-1}), and the intercept of the line at N=0 provides an estimate of the equilibrium SAT change for the experiment compared with the control simulation (°C), denoted ΔT_{eq}^{g} to indicate that it was calculated from the Gregory plots using the full 500 years of model data (unless otherwise specified).

For experiments with CO_2 <2600 ppmv

For the 28 experiments in the *highCO₂* ensemble that had a CO_2 concentration of less than 2600 ppmv (i.e. that were not identified to experience runaway warming), and for the entire *lowCO₂* ensemble, Gregory plots based on the first 200 years and full 500 years of model data were produced, providing estimates for ΔT_{200eq}^{g} and ΔT_{eq}^{g}, respectively. A more consistent naming convention would be ΔT_{500eq}^{g}, but ΔT_{eq}^{g} is used for consistency with the published paper which is included as Chapter 3. The estimates of ΔT_{200eq}^{g} for the *lowCO₂* and *highCO₂ modice* ensembles ranged from a minimum of -0.4°C (CO_2 264.5 ppmv) to a maximum of 13.7°C (CO_2 2582.1 ppmv), whilst ΔT_{eq}^{g} ranged from -0.4°C (CO_2 264.5 ppmv) to 18.4°C (CO_2 2582.1 ppmv). Experiments with CO_2 below or near to pre-industrial levels tended to reach equilibrium by the end of the 500 years, which meant that a Gregory plot was not necessary, hence ΔT_{200eq}^{g} and ΔT_{eq}^{g} were taken to be the same as the SAT change at 500 years calculated directly from the GCM model data (calculated by averaging the final 50 years of the experiment; ΔT_{500}) in these cases.

Figure 4.13 illustrates the Gregory plots for two *modice* experiments, *modice_lowCO2_13* (CO_2 555.6 ppmv) and *modice_highCO2_17* (CO_2 1151.6 ppmv). One plot uses data from model years 1-200 (Figure 4.13a) and the other from years 1-500 (Figure 4.13b). These experiments were selected as they have CO_2 values nearest to the 2x and 4x pre-industrial CO_2 scenarios that are commonly used in idealised future climate experiments. For each experiment, mean annual data was plotted for years 1-20 of the simulation, and mean decadal data for subsequent years (up to either year 200 or year 500). The regression fits were to mean annual data in each case, and years 1-20 and years 21 onwards were fitted separately. For the

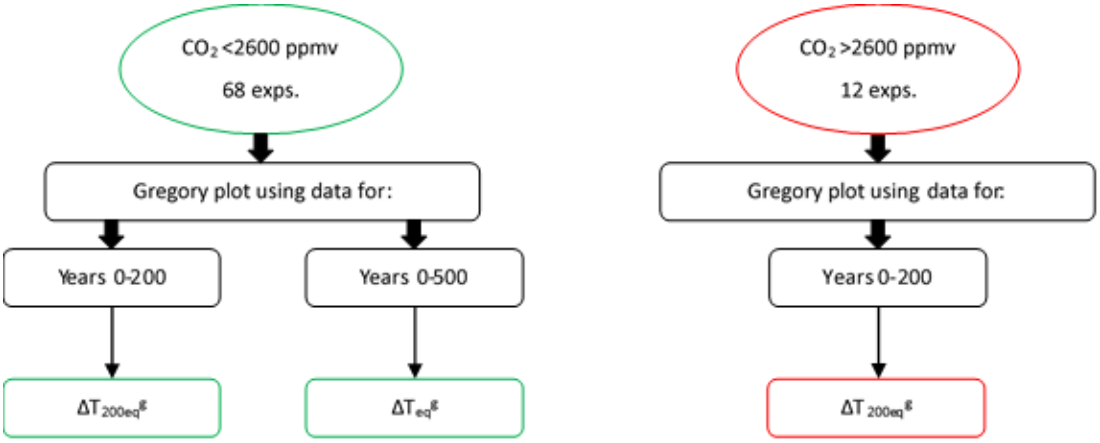

Figure 4.12. Flow charts summarizing the application of the Gregory plot methodology to calculate the global mean equilibrated SAT change for the experiments with CO_2 <2600 ppmv (no runaway warming; green), and CO_2 >2600 ppmv (with runaway warming; red). The thin black arrows indicate the results of the method; in this case, the equilibrium SAT change based on the first 200 years of model data (ΔT_{200eq}^{g}), and based on the full 500 years of model data (ΔT_{eq}^{g}).

approximate 2xCO_2 and 4xCO_2 experiments, respectively, ΔT_{200eq}^{g} was estimated to be 4.3°C and 8.4°C, and ΔT_{eq}^{g} to be 4.4°C and 8.9°C.

For experiments with CO_2 >2600 ppmv (i.e. with runaway warming)

For the 12 runaway warming experiments from the *highCO_2* ensemble (Table 4.2), Gregory plots using only the first 200 years of data were plotted, and ΔT_{200eq}^{g} was calculated. As mentioned previously, it was assumed that the data for at least the first 200 years of these simulations was unaffected by the runaway warming.

4.4.1.2.2 Correction of increased warming

For experiments with CO_2 <2600 ppmv

Figure 4.14a compares the ΔT_{200eq}^{g} and ΔT_{eq}^{g} values estimated from the Gregory plots for the experiments with a CO_2 concentration of less than 2600 ppmv. At lower CO_2 concentrations, the data points in Figure 4.14a generally remain close to the 1:1 line, as the climate was relatively close to equilibrium 200 years into the experiment. As CO_2 increased, a comparatively greater proportion of the total climate change was yet to occur between model years 200 and 500, causing the difference between ΔT_{200eq}^{g} and ΔT_{eq}^{g} to gradually increase. However, a significant increase in the difference occurred when very high CO_2 concentrations (≥2000 ppmv; ~11.4°C on the x-axis of Figure 4.14a) were reached. This was a consequence of the slope of the 21-500 yr regression line on the Gregory plots becoming shallower with time, particularly as the CO_2 concentration increased, resulting in the *N*=0 intercept occurring at increasingly higher temperatures. As discussed in the previous chapter, the cause of this may be related to an

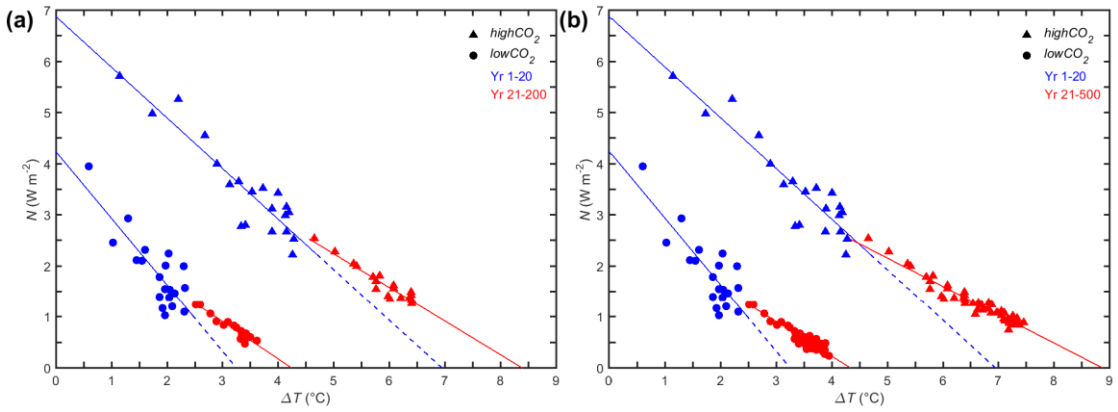

Figure 4.13. Gregory plots showing change in TOA net downward radiation flux (N; W m^{-2}) as a function of change in global mean annual SAT (ΔT; °C) for approximate 2xCO_2 (modice_lowCO2_13; circles) and 4xCO_2 (modice_highCO2_17; triangles) experiments. (a) Plot using data for model years 1-200. Lines show regression fits to the global mean annual data points for years 1-20 (blue) and years 21-200 (red). Data points are mean annual data for years 1-20 (blue) and mean decadal data for years 21-200 (red). The ΔT intercepts (N=0) of the red lines give the estimated equilibrated SAT ($\Delta T_{200eq}{}^{g}$) for the two experiments. (b) Plot using data for model years 1-500. Lines show regression fits to the global mean annual data points for years 1-20 (blue) and years 21-500 (red). Data points are mean annual data for years 1-20 (blue) and mean decadal data for years 21-500 (red). The ΔT intercepts (N=0) of the red lines give the estimated equilibrated SAT ($\Delta T_{eq}{}^{g}$) for the two experiments. The ΔT intercepts of the dashed blue lines represent the equilibrium that the experiment would have reached if the feedback strengths in the first 20 years had been maintained. SAT is shown as an anomaly compared with the pre-industrial control simulation.

increase in the sensitivity of the climate system to the radiative forcing over time (Gregory et al., 2004, Andrews et al., 2015). Suggested mechanisms for this include non-linearity in short-wave cloud feedback processes (Andrews et al., 2012, Andrews et al., 2015), changes in the pattern of warming at the surface of the ocean (Williams et al., 2008), and variations in ocean heat uptake(Held et al., 2010, Winton et al., 2010, Geoffroy et al., 2013). For the experiments with relatively high CO_2, it is also possible that runaway warming has been instigated and that the method used to identify this process that is described in Section 4.3.1.1 was not sensitive enough for some experiments.

The approach was therefore taken whereby both the original $\Delta T_{eq}{}^{g}$ data and a modified version of the data, where the runaway warming has been corrected for (Figure 4.14b), were used to train the emulator, allowing the results of both versions to be compared. To correct for the non-linearity in the estimation of $\Delta T_{eq}{}^{g}$, a linear function was fitted to the $\Delta T_{eq}{}^{g}$ vs ln(CO_2) curve for the experiments with CO_2 concentrations less than 2000 ppmv (60 experiments), represented by the black line in Figure 4.15a. This linear function was then used to predict a corrected version of $\Delta T_{eq}{}^{g}$ for the eight experiments with CO_2 concentrations between 2000 ppmv and 2600 ppmv, in which the effect of the postulated runaway warming is thus removed.

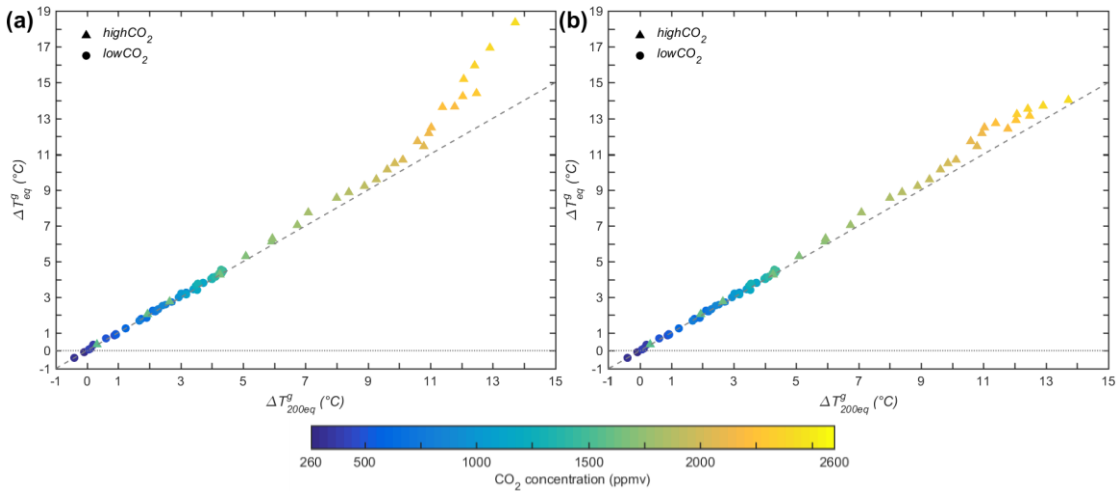

Figure 4.14. Equilibrated global mean annual change in SAT (°C) estimated using the methodology of Gregory et al. (2004) for the lowCO_2 (circles) and highCO_2 (experiments with CO_2 less than 2600 ppmv; triangles) modice ensembles calculated using data for years 1-200 ($\Delta T_{200eq}{}^g$) and years 1-500 ($\Delta T_{eq}{}^g$). The colours of the points indicate the CO_2 concentration of the experiment, from low (blue) to high (yellow). The 1:1 line (dashed) is included for reference. Two versions of the $\Delta T_{eq}{}^g$ data are presented (affecting only the eight simulations with highest CO_2): (a) the original $\Delta T_{eq}{}^g$ calculated directly from the Gregory plot, and (b) the modified $\Delta T_{eq}{}^g$ data where the additional warming has been corrected for using a linear function. SAT is shown as an anomaly compared with the pre-industrial control simulation.

For experiments with CO_2 >2600 ppmv (i.e. with runaway warming)

This method was also used to correct the 12 *highCO_2* experiments listed in Table 4.2, which had CO_2 concentrations of greater than 2600 ppmv, and were identified to exhibit runaway warming in Section 4.3.1.1. For these, Gregory plots were used to calculate values of $\Delta T_{200eq}{}^g$ (see Section 4.4.1.2.1 for full description of methodology), and a similar relatively large increase in $\Delta T_{200eq}{}^g$ value was exhibited for these experiments compared with the experiments with lower CO_2 concentrations. Therefore, in this case, the linear function was fit to the values of $\Delta T_{200eq}{}^g$ for the *highCO_2* experiments with CO_2 concentrations of up to 2600 ppmv (black line in Figure 4.15b), and then applied to predict the corrected $\Delta T_{200eq}{}^g$ for experiments with CO_2 higher than this, as shown in Figure 4.15b.

A summary of the approach used to correct the data for runaway warming is shown in Figure 4.16. Both the original and corrected versions of the data are used in further analysis. Use of the original data assumes that there are non-linearities in the response of climate to CO_2 forcing which are not yet well understood. Several studies have suggested that this may, in fact, be the case. The second method, which used the corrected data, assumes that climate responds linearly to increasing CO_2, and hence that the non-linearity can be explained by spin-up and/or runaway warming issues.

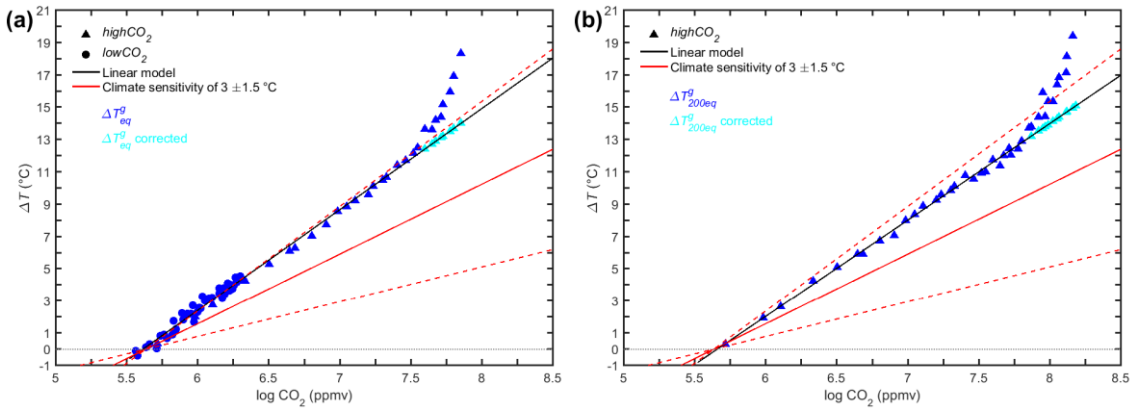

Figure 4.15. Global mean annual change in SAT (°C) estimated using the methodology of Gregory et al. (2004) against log(CO_2) (ppmv), showing both the original (blue) and corrected (cyan) versions of: (a) ΔT_{eq}^{g} for the lowCO_2 (circles) and highCO_2 (triangles) modice ensembles, and (b) ΔT_{200eq}^{g} for the highCO_2 (triangles) modice ensemble. Also shown is the linear function used to calculate the corrected data, and the idealised relationship between log(CO_2) and ΔT (red lines) for a climate sensitivity of 3°C (solid), 1.5°C (lower dashed) and 4.5°C (upper dashed) (IPCC, 2013). SAT is shown as an anomaly compared with the pre-industrial control simulation.

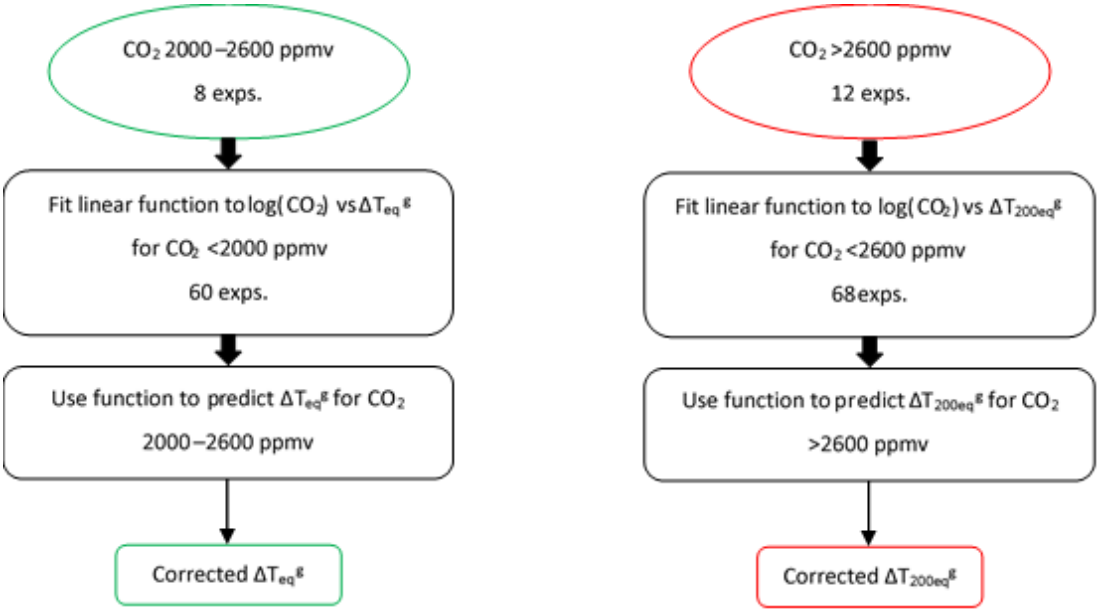

Figure 4.16. Flow charts summarizing the methodology used to calculate global mean SAT change data which has been corrected for runaway warming, applied to experiments with CO_2 2000–2600 ppmv (green) and experiments with CO_2 >2600 ppmv (red). The thin black arrows indicate the results of the method; in this case, the corrected global mean equilibrium SAT change based on the full 500 years of model data (corrected ΔT_{eq}^{g}) for the experiments with CO_2 2000–2600 ppmv, and based on the first 200 years of model data (corrected ΔT_{200eq}^{g}) for the experiments with CO_2 >2600 ppmv.

4.4.1.2.3 Equilibrated climate

For experiments with CO_2 <2600 ppmv

For the eight experiments with atmospheric CO_2 concentrations between 2000 and 2600 ppmv, the fully equilibrated climate anomaly (denoted ΔT_{eq}) was calculated using the same pattern scaling approach as for the experiments with CO_2 of less than 2000 ppmv, which is

described in Section 3.4.6 in Chapter 3 and summarised in Figure 4.17. That is, the ratio between ΔT_{eq}^{g} and ΔT_{500} was calculated for each experiment, where ΔT_{500} is the global mean SAT anomaly calculated directly from the GCM model data by averaging the final 50 years of the experiment. This ratio was calculated for both the original ΔT_{eq}^{g} data and the corrected ΔT_{eq}^{g} data. The spatial field of mean annual SAT anomaly for each experiment (average of final 50 years) was then multiplied by this ratio (both original and corrected), under the assumption that the ratio was equally applicable to all grid boxes.

For experiments with CO_2 >2600 ppmv (i.e. with runaway warming)

The Gregory plots provided values for ΔT_{200eq}^{g} and ΔT_{eq}^{g} for the 68 experiments with atmospheric CO_2 of less than 2600 ppmv, and ΔT_{200eq}^{g} values for the 12 experiments with CO_2 of above this that were affected by runaway warming. Thus, to calculate ΔT_{eq}^{g} for these experiments, a linear regression was performed on the ΔT_{200eq}^{g} vs ΔT_{eq}^{g} data (both original and corrected) for the lower CO_2 experiments.

For the original data, a cubic function ($R^2 = 0.997$) was found to provide the best fit, which was confirmed by an F Test. On the other hand, the corrected data was better approximated using a linear function ($R^2 = 0.998$), with an F Test suggesting that increasing the number of free parameters did not significantly improve the quality of the fit. The selection of these functions was supported by the trends in the data in Figure 4.14, as there was a slight curve in the data points at higher CO_2 concentrations in the original data (Figure 4.14a), whereas the corrected data were more linear (Figure 4.14b). The performance of the two functions was evaluated by excluding 7 simulations covering a range of CO_2 values from the regression, and then calculating ΔT_{eq}^{g} from ΔT_{200eq}^{g}, with percentage errors of less than 8%, and generally much lower than this.

Next, the appropriate regression function was applied to the experiments with runway warming, producing an estimate of the equilibrated ΔT_{eq}^{g} (both an original and corrected version) from the ΔT_{200eq}^{g} data. The final estimates of ΔT_{eq}^{g} for this selection of simulations from the *highCO_2 modice* ensemble range from a minimum of 18.4°C (CO_2 2623.9 ppmv) to a maximum of 56.7°C (CO_2 3588.9 ppmv) for the original data, and 14.2°C (CO_2 2623.9 ppmv) to 16.2°C (CO_2 3588.9 ppmv) for the corrected data. A summary of this method is presented in Figure 4.18.

The global mean SAT at year 200 was calculated for the simulations, by taking the global average of the mean annual data for model years 181-200, giving ΔT_{200}. The ratio between ΔT_{eq}^{g} and ΔT_{200} for each experiment was then calculated ($\Delta T_{eq}^{g}/\Delta T_{200}$), which represents the ratio of the total change over all time (500 simulation years plus any additional time to reach equilibrium)

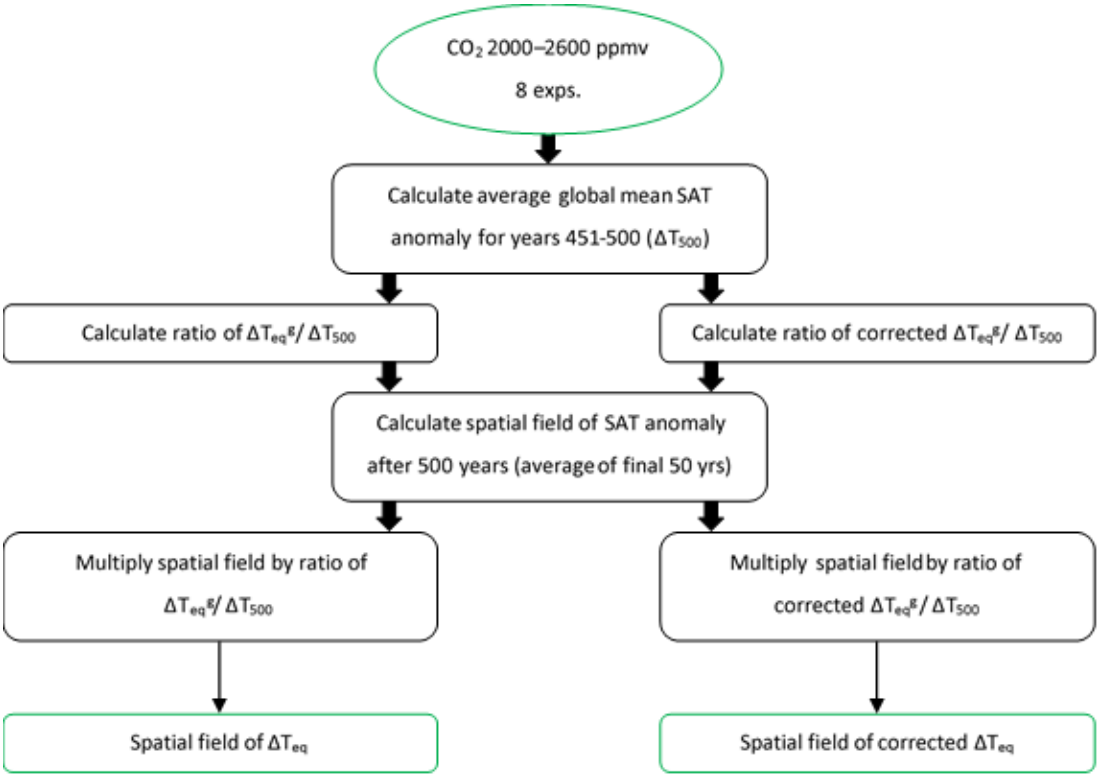

Figure 4.17. Flow chart summarizing the methodology used to calculate the spatial field of fully equilibrated mean annual SAT change for the experiments with CO_2 2000–2600 ppmv (green). The thin black arrows indicate the results of the method; in this case, the spatial field of equilibrated SAT change (ΔT_{eq}) based on the original data, and the version which has been corrected for runaway warming (corrected ΔT_{eq}).

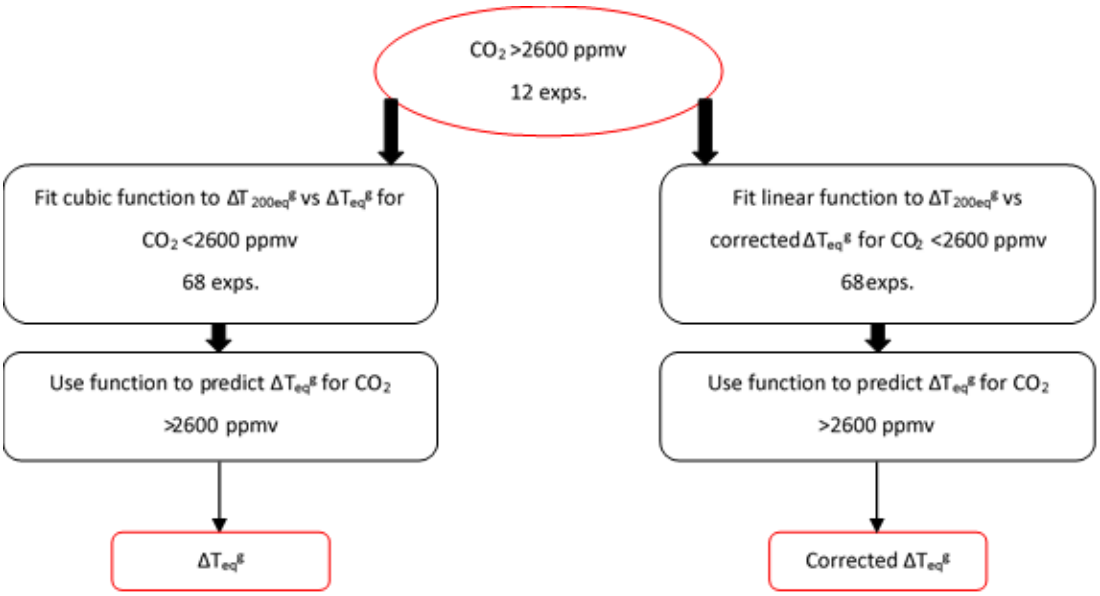

Figure 4.18. Flow chart summarizing the methodology used to calculate global mean equilibrated SAT change data based on the full 500 years of model data for the experiments with CO_2 >2600 ppmv (red). The thin black arrows indicate the results of the method; in this case, the global mean equilibrium SAT change (ΔT_{eq}^{g}) based on the original data, and the version which has been corrected for runaway warming (corrected ΔT_{eq}^{g}).

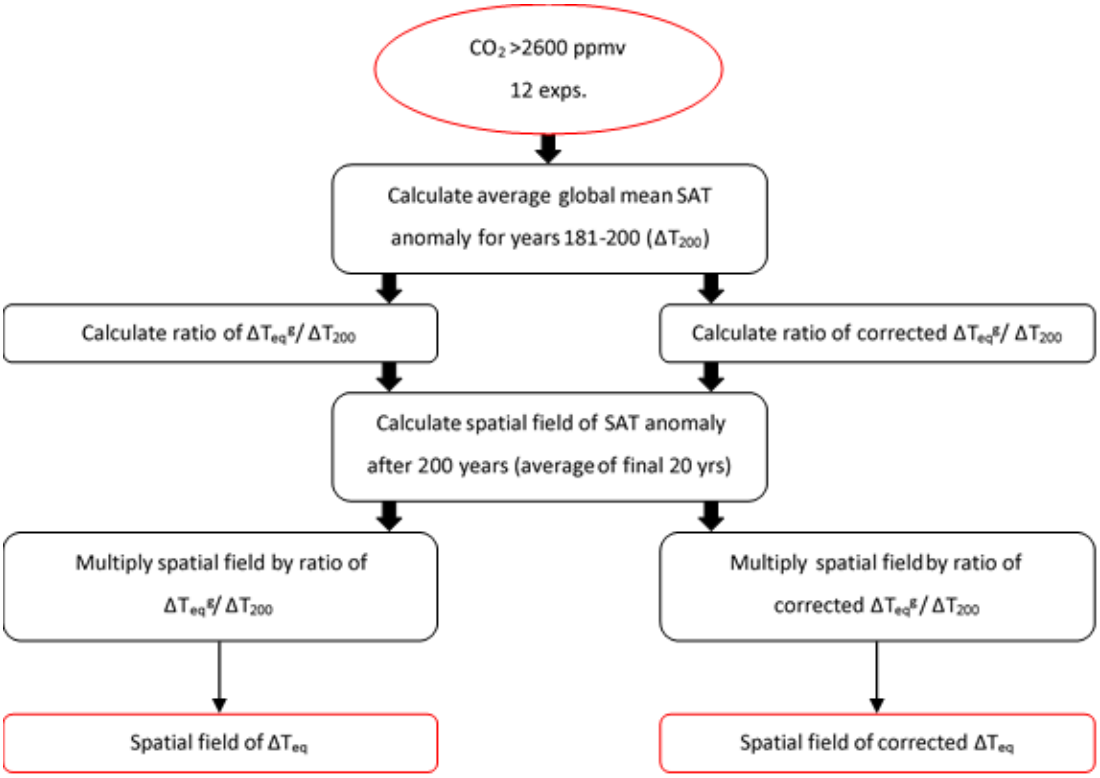

Figure 4.19. Flow chart summarizing the methodology used to calculate the spatial field of fully equilibrated mean annual SAT change for the experiments with CO_2 >2600 ppmv (red). The thin black arrows indicate the results of the method; in this case, the spatial field of equilibrated SAT change (ΔT_{eq}) based on the original data, and the version which has been corrected for runaway warming (corrected ΔT_{eq}).

to the fraction of that change that has occurred within the first 200 years of the simulation. To estimate the fully equilibrated climate anomaly (ΔT_{eq}), the global-scale spatial field of the mean annual SAT anomaly at year 200 (averaged over model years 181-200) was multiplied by the $\Delta T_{eq}{}^g / \Delta T_{200}$ ratio. This was done for both the original and corrected data, as summarised in Figure 4.19. The ratio identified for each experiment was assumed to be equally applicable to all grid boxes.

The equilibrated global mean annual SAT anomaly compared to pre-industrial (ΔT_{eq}) for all 80 simulations in the two *modice* ensembles is plotted against ln(CO_2) in Figure 4.20. Also plotted on Figure 4.20 are a number of lines illustrating idealised relationships between ΔT_{eq} and CO_2 based on a range of climate sensitivities. The most recent IPCC report suggested that the likely range for equilibrium climate sensitivity is 1.5°C to 4.5°C (IPCC, 2013), hence sensitivities of 1.5°C, 3°C and 4.5°C have been plotted. The final temperature estimates for the corrected data are generally in line with the expected response (red lines), whereas the uncorrected temperatures for the high CO_2 simulations move increasingly away from this idealised line. As mentioned previously, this may be due to non-linearities in the response of climate to high CO_2 concentrations, or due to the runaway warming feedback. The corrected ΔT_{eq} data generally

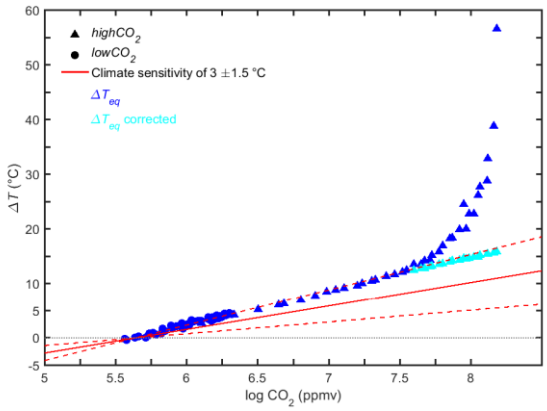

Figure 4.20. Equilibrated global mean annual change in SAT (ΔT_{eq}; °C), estimated using the methodology of Gregory et al. (2004) against ln(CO_2) (ppmv), showing both the original (blue) and corrected (cyan) versions of the data, for the lowCO_2 (circles) and highCO_2 (triangles) modice ensembles. Also shown is the linear function used to calculate the corrected data, and the idealised relationship between log(CO_2) and ΔT (red lines) for a climate sensitivity of 3°C (solid), 1.5°C (lower dashed) and 4.5°C (upper dashed) (IPCC, 2013). SAT is shown as an anomaly compared with the pre-industrial control simulation.

follows the upper line, equivalent to an equilibrium climate sensitivity of 4.5°C. A previous estimate for the sensitivity of HadCM3 was lower than this, being approximately 3.3°C (Williams et al., 2001). The possible reasons for this difference are discussed in Chapter 3 Section 3.4.6.2.

4.4.2 Calibration and evaluation of the emulator

In this section, the emulator is evaluated following the same process as described in Chapter 3 Section 3.5. The full *highCO_2* and *lowCO_2* ensembles (80 simulations) were used to calibrate the emulator, making it applicable to concentrations of 250 ppmv to 3600 ppmv. This is in contrast to the emulators presented in Chapter 3, which were calibrated on a subset of simulations and hence were suitable for modelling CO_2 concentrations of 1900 ppmv or less. Briefly, the emulator was calibrated on the combined *highCO_2* and *lowCO_2* ensembles, with four input parameters being used (ln(CO_2), obliquity, $e\sin\varpi$ and $e\cos\varpi$). A leave-one-out cross-validation approach was utilised to assess the performance of emulator, for which a series of emulators were constructed using different numbers of PCs and different values for the correlation length hyperparameters. For each configuration, each simulation was excluded in turn, and the emulator calibrated (i.e. resulting in 80 emulators). Each emulator was then used to reproduce the corresponding left-out experiment. The performances of the different emulator configurations were compared via the RMSE averaged across all the 80 emulators, and the proportion of grid box SATs reproduced within different standard deviation bands. The results presented in this section are applicable to modern-day ice sheets (*modice*). Under the high CO_2

emissions scenarios, the continental ice sheets may be expected to be smaller, at least for some of the 200 kyr period. However, as was noted in Section 3.8 of Chapter 3, the emulator is not able to simulate interactive ice sheets that vary in response to changes in climate. In addition, Figure 3.4a of the previous chapter illustrates the mean annual SAT anomaly averaged across five *lowice* experiments compared with their *modice* equivalents, demonstrating that the largest anomalies occur locally to the GrIS and AIS, with only very small anomalies exhibited for other areas. The ice sheet extent is, therefore, expected to have a limited impact on the Central England site for the emulator configuration presented in this thesis. Hence, modern-day ice sheet extents were selected.

4.4.2.1 Optimisation of hyperparameters

For brevity, only one version of the emulator is selected for further analysis and application to the future. Therefore, the assumption is made that the runaway warming was caused by a runaway positive feedback in the model that occurred at very high CO_2 concentrations. Hence, for the rest of the analysis in this chapter, the corrected version of the equilibrated SAT data (ΔT_{eq}) was used. This emulator will henceforth be referred to as *modice_80_c*, since it is calibrated on the full set of 80 GCM simulations and uses the corrected data (*_c*). The emulator was calibrated and evaluated using the leave-one-out validation technique, with the best performing emulator configuration being selected as the final optimised version. As in Chapter 3 Section 3.5, different emulator configurations retaining 5 to 20 PCs were tested, and for each emulator configuration, the correlation length scales δ and nugget v were optimised by maximization of the penalised likelihood.

It was found that an emulator retaining 15 PCs has the lowest RMSE and a relatively low percentage of grid boxes with errors of more than 2 standard deviations. The 15 PCs account for 89% of total variance. The scales δ for the *modice_80_c* emulator are 5.904 (ε), 3.324 ($e\sin\varpi$), 3.928 ($e\cos\varpi$), 0.381 (CO_2), and the nugget is 0.121. Figure 4.21 evaluates the performance of the emulator, finding that the RMSE values are generally fairly low (Figure 4.21a), and the emulated global mean SAT index values are similar to the equivalent GCM values, with no obvious outliers (Figure 4.21b). As with all of the emulators described, both in this chapter and the last, several of the experiments perform relatively poorly, exhibiting large errors compared with the other simulations. On visual inspection of the global standard errors, no systematic errors appear to occur in particular regions in these experiments. The CO_2 concentrations are

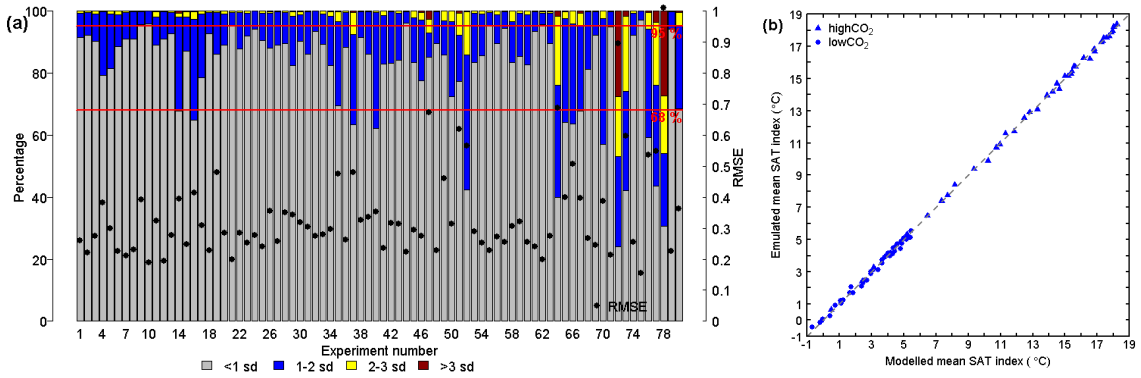

Figure 4.21. Evaluation of emulator performance for the modice_80_c emulator calibrated on the corrected SAT data. (a) Bars give the percentage of grid boxes for which the emulator predicts the SAT of the left-out experiment to within 1, 2, 3 and more than 3 standard deviations (sd). Also shown is the RMSE for the experiments (black circles). Red lines indicate 68% and 95%. (b) Mean annual SAT index (°C) calculated by the emulator and the GCM for the lowCO_2 (circles) and highCO_2 (triangles) modice ensembles. The 1:1 line (dashed) is included for reference. Note: this is the mean value for the GCM output data grid assuming all grid boxes are of equal size, hence not taking into account variations in grid box area. SAT is shown as an anomaly compared with the pre-industrial control simulation.

relatively high, although they are not always the highest values, and the other input parameters are not particularly similar.

In summary, the calibration and evaluation shows that the emulator is able to reproduce the left-out ensemble simulations reasonably well, with no obvious systematic errors in its predictions. It allows global climate development over long periods of time (several million years) to be simulated. However, a number of conditions apply, including that the atmospheric CO_2 concentrations are within the limits of those used to calibrate the selected emulator, ice sheets are similar to their modern-day configurations, and the topography and land-sea mask are unchanged.

In the next section, the emulator is applied to the next 200 kyr, to simulate a number of future climate-change scenarios.

4.4.3 Application of the emulator to the future

The *modice_80_c* emulator was used to simulate the evolution of SAT and precipitation over the next 200 kyr. The CO_2 emissions scenarios were the four logistic scenarios used in Chapters 2 and 3, with total emissions of 500-5000 Pg C. An additional scenario was also included, with emissions totalling 8000 Pg C, since the *modice_80_c* emulator has a higher CO_2 concentration limit compared with the emulator described in the previous chapter.

In Chapter 3, climate evolution at several different European grid-box locations was presented, whereas here only one location is presented for brevity. The Central England grid box was selected, due to its relevance to radioactive waste disposal in the UK, an issue which contributed to the design and funding of this research project. The projected future change in SAT and precipitation (compared to pre-industrial), along with the emulated uncertainty (1 standard deviation), estimated by the emulator for this grid box for the CO_2 scenarios is shown in Figure 4.22.

The projected evolutions of SAT and precipitation presented here for the 500-5000 Pg C scenarios are very similar to those predicted for the equivalent CO_2 scenarios in Section 7 of Chapter 3 using the *modice_60* emulator. This is both in terms of the degree of change in response to atmospheric CO_2, but also the orbital frequencies that are evident in the data.

For SAT (Figure 4.22c), the emulator projects an initial rapid warming followed by a more gradual cooling accompanied by periodic oscillations. The peak SAT increase for the 8000 Pg C and 500 Pg C scenarios are 13.8 ± 0.3°C and 3.4 ± 0.3°C, respectively (Figure 4.22c).

Emulated precipitation for the Central England grid box (Figure 4.22d) generally demonstrates a relatively similar trend to SAT, with an increase in precipitation over the first 1 kyr of up to 0.3 ± 0.1 mm day^{-1} for CO_2 emissions of 2000 Pg C or less, as a result of the accompanying increase in SAT. Orbital timescale variations then become dominant after several tens of thousands of years.

However, simulated precipitation for the first 1 kyr is slightly different following total emissions of 5000 and 8000 Pg C, compared with the scenarios with lower CO_2 emissions. For the 5000 Pg C scenario, the initial increase is relatively small, and is actually surpassed by the next increase in precipitation driven by orbital variations. A similar trend for the Central England grid box under the same CO_2 scenario was also projected in Figure 3.15 of Chapter 3. The new CO_2 scenario with emissions of 8000 Pg C exhibits a decrease in precipitation for the first 1 kyr, after which it increases and adopts a similar trend to the other scenarios. This is caused by high temperatures resulting in decreased precipitation over Southern Europe. This drying occurs at 1 kyr for the 5000 Pg C scenario, but is mainly concentrated over Spain and parts of the Mediterranean Basin, as highlighted by the emulated reduction in rainfall for the Spain grid box in Figure 3.15 in the previous chapter. As a result, the Central England grid box does not experience a decrease in precipitation, but also does not increase as much as in the lower CO_2 scenarios. For emissions of 8000 Pg C, the reduction in precipitation is greater and the area affected is larger and extends further north into central Europe. Consequently, precipitation over

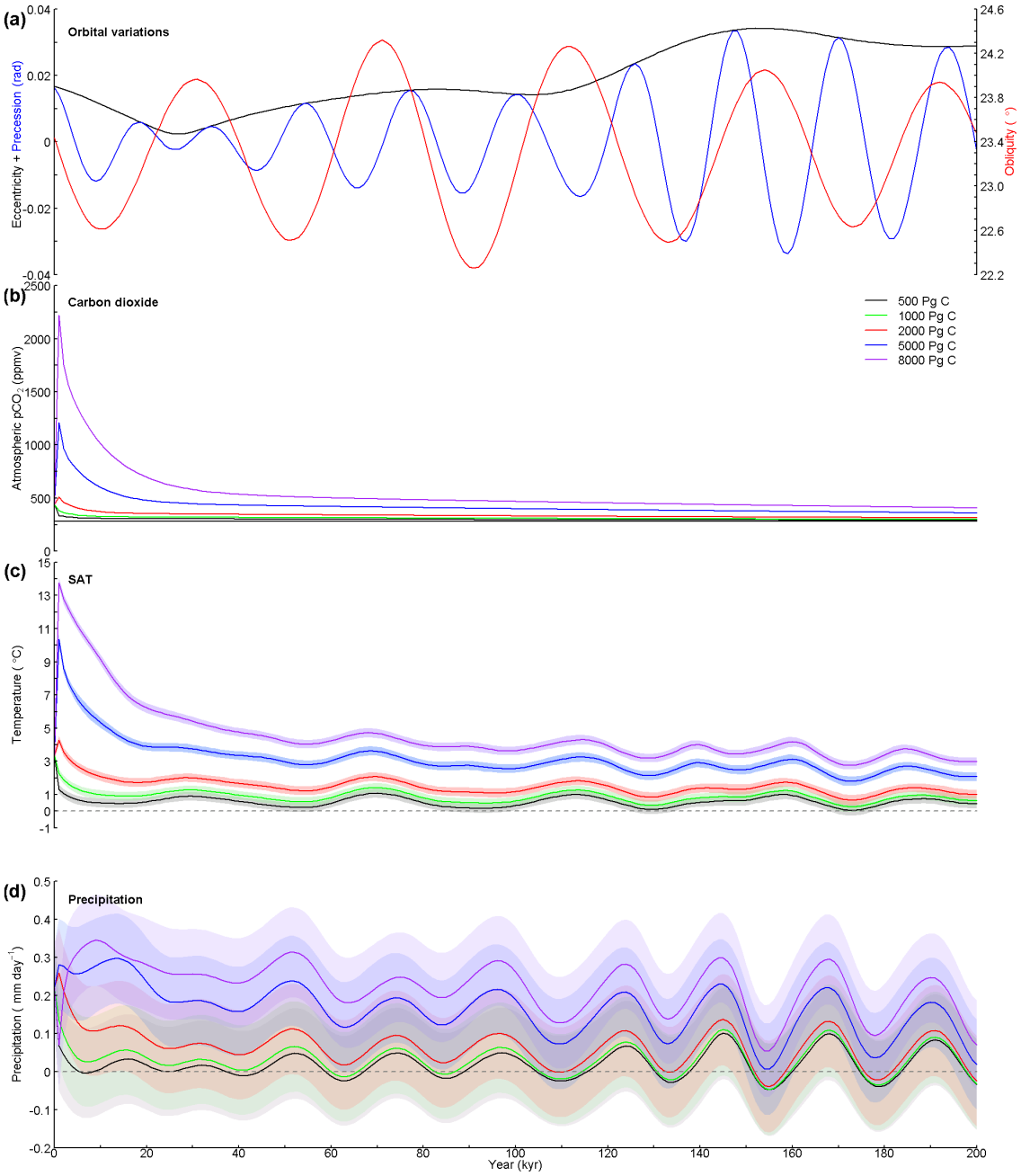

Figure 4.22. Emulation of climate evolution for the next 200 kyr at the Central England grid box. (a) Time series of orbital variations (Laskar et al., 2004), showing eccentricity (black) and precession (radians; blue) on the left axis, and obliquity (degrees; red) on the right axis. (b) Time series of atmospheric pCO_2 (ppmv), predicted using the impulse response function discussed in Chapter 2. The pre-industrial CO_2 concentration is also shown (black line). Time series of: (c) emulated mean annual SAT (°C), and (d) emulated mean annual precipitation (mm day^{-1}). Climate variables are modelled every 1 kyr, using the modice_80_c emulator, for five CO_2 emissions scenarios; 500 Pg C (black), 1000 Pg C (green), 2000 Pg C (red), 5000 Pg C (blue) and 8000 Pg C (purple). Error bands represent the emulated grid box posterior variance (1 standard deviation). SAT is shown as an anomaly compared with the pre-industrial control simulation.

Central England is lower than for the previous kyr when SAT was lower. As noted in Chapter 3, decreased precipitation over the Mediterranean has been projected by a range of models for the RCP8.5 scenario (Collins et al., 2013).

As mentioned previously, the climate projections presented here are similar to those predicted for the equivalent CO_2 scenarios by the emulator in Section 7 of the previous chapter. The dominant influence of precession on precipitation fluctuations over the next 200 kyr, and precession with some modulation by obliquity on SAT, is robust across all the versions of the emulator presented in this thesis, and for all CO_2 scenarios used.

4.5 Summary and Conclusions

In this chapter, further analysis of the emulator has been presented. Firstly, the results of the PCA have been examined, with a number of PCs being tentatively linked to physical mechanisms in the Earth system. The emulator's application to precipitation has also been investigated, and specifically the performance of the emulator that uses hyperparameters (length scales and nugget) and number of retained PCs optimised on SAT data is compared to one that is optimised on precipitation data. It is found that:

- A number of retained PCs exhibit spatial variations that may be associated with warming due to CO_2 (particularly increased warming over land and at high latitudes), and variations in monsoons, sea-ice, and AMOC.
- There is no great loss in emulator performance when hyperparameters optimised on SAT data are applied to emulate precipitation, compared with hyperparameters optimised on precipitation data. This suggests that it is appropriate to use one set of hyperparameters and number of PCs (optimised on SAT) for a range of climate variables, rather than optimising separately for different variables.

Secondly, a number of versions of the emulator are discussed that are calibrated on SAT data for the full *highCO_2* and *lowCO_2* ensembles, making the emulators suitable for modelling CO_2 concentrations up to 3600 ppmv, compared with the 2000 ppmv limit of the emulators described in Chapter 3 (*modice_60*, *lowice_60*). Experiments with CO_2 concentrations of 2600 ppmv or higher exhibited runaway warming during the course of the simulation. Gregory plots were produced for the experiments with CO_2 lower than this, and a linear regression was performed on the results. This provided a function which was then used to calculate the equilibrated SAT that the experiments with runaway warming would have reached in the absence of the runaway warming feedback. It was also observed that the equilibrated warming displayed by experiments with CO_2 concentrations of 2000 ppmv or higher moved increasingly away from a linear temperature-ln(CO_2) relationship, possibly caused by non-linearities in climate feedbacks

or runaway warming. Consequently, the increased warming in these data was corrected for using a linear function that was fit to the results for experiments with lower CO_2 concentrations. The validity of the assumption that the runaway warming was the result of a property in the GCM (and therefore not representative of the real world) could be tested in future work by running high CO_2 simulations using a range of models with enhanced process representation, including a vertical ozone profile that can be updated in response to changes in climate.

Based on the assumption that the runaway warming was the result of errors in the model, the corrected SAT data was used to optimise and calibrate the emulator, denoted *modice_80_c* (as all 80 experiments were used, some of which had been corrected). It was used then to project the evolution of SAT and precipitation over the next 200 kyr, finding that:

- The emulator produced projections of SAT and precipitation that were similar to those produced by the *modice_60* emulator described in Chapter 3.
- The emulator uncertainty for the variables was also similar to that displayed in the previous chapter.
- The orbital signals evident in the time series data are similar to those discussed in Chapter 3, with SAT appearing to be initially influenced by obliquity and then later by precession, and with precipitation variations occurring on a precessional timescale.

The emulator presented here complements the ones described in Chapter 3, increasing the upper CO_2 limit that can be modelled to 3600 ppmv, meaning a larger range of CO_2 scenarios can be emulated. This is particularly relevant to projections of future changes in climate following high emissions for business-as-usual scenarios.

CHAPTER 5

Application of the framework: A case study

The previous chapters of this thesis (Chapters 2, 3, and 4) have focussed on different aspects of the issue of long-term climate change assessment. Here, the ideas and methods presented in the earlier chapters are combined in the form of a case study. The framework described in Chapter 1 presents a method for addressing long-term climate change in the context of radioactive waste disposal, and this chapter provides an illustration of the application of this framework to a new illustrative site, being Yucca Mountain in the USA. It demonstrates how the framework can be used to produce time series data for various climatic variables under a new relatively extreme anthropogenic CO_2 emissions scenario, and discusses the potential implications of the results to radioactive waste disposal.

5.1 Introduction

The flow chart developed by MODARIA WG6 (MODARIA Working Group 6, 2016), showing how different climate models can be applied to investigate climate changes occurring over different timescales in the context of post-closure radiological impact assessments for nuclear waste repositories, is shown in Figure 5.1. The steps that have been addressed in this thesis are highlighted in red, and are presented in greater detail in the proposed framework

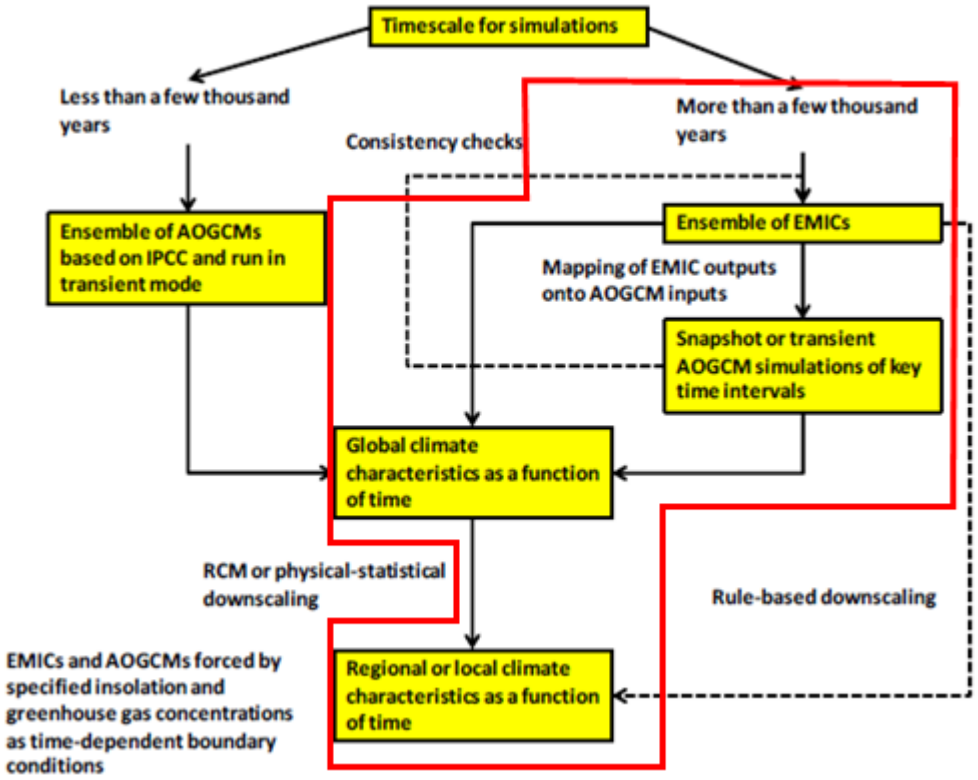

Figure 5.1. Selection of climate models for use in post-closure radiological impact assessments for nuclear waste repositories. The red box indicates the steps addressed in this thesis. Source: Modified from Figure 4.1 (p. 47) of MODARIA Working Group 6 (2016).

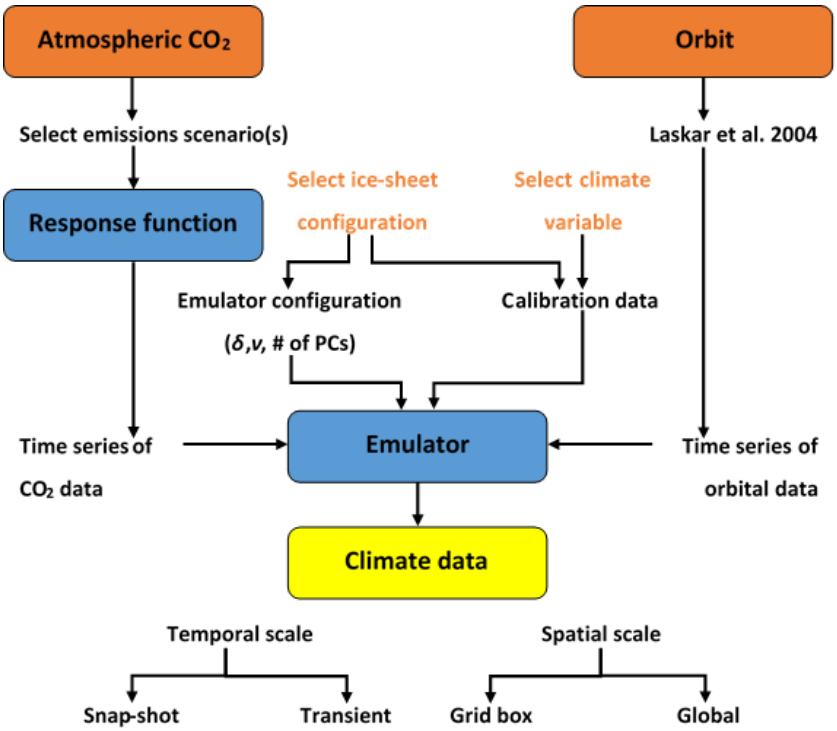

Figure 5.2. Proposed framework for addressing long-term climate change in the context of post-closure performance assessments for radioactive waste repositories (fully described in Chapter 1 Section 1.5).

for addressing long-term climate change illustrated in Figure 5.2, around which this thesis is based and which was described in Section 1.5 of Chapter 1. The orange boxes represent the main forcings on climate that are relevant on the timescales of interest for the disposal of radioactive wastes (from several kyr up to 1 Myr), and the blue boxes represent the tools developed and described in this thesis, being the CO_2 response function (Chapter 2) and the climate emulator (Chapters 3 and 4). These tools can be applied to ultimately produce the climate data required for post-closure radiological impact assessments (yellow box).

This chapter presents a case study illustrating the application of the full methodology for modelling long-term future climate evolution (Figure 5.2). The case study region is Yucca Mountain in Nevada, shown in Figure 5.3, which is the location of the proposed first U.S. repository for spent nuclear fuel and high-level waste defined under the U.S. Nuclear Waste Policy Act as amended in 1987. This location was selected because it is a new site that has not been used in previous chapters. It is also at a lower latitude than previous sites, which means that it is less likely to be affected by future glaciations, thus making the methodology that has been developed here well suited to it. It should be noted that in this chapter (and thesis), the Yucca Mountain site is used purely for illustrative purposes. No conclusions are drawn and no recommendations or interpretations of the results are made in terms of the safety of the site for the disposal of radioactive wastes. The sole aim of this chapter is to illustrate the application of the proposed framework to an example site and to present climate data that could aid understanding of the long-term evolution of climate in the region.

If approved, the Yucca Mountain facility would be constructed approximately 300 m BGL in a flat-topped volcanic ridge, pictured in Figure 5.3. Whilst it is located in a thick unsaturated zone, intense rainfall events can lead to groundwater flows occurring down to repository depth. After an initial cooling period, when wall temperatures drop below the local boiling point, those waters can enter the drifts and result in corrosion of the engineered barriers, which are proposed to include titanium drip shields as well as corrosion-resistant packages. Following package failure, contaminated water could percolate further downward to reach the regional groundwater table and flow sub-horizontally to Amargosa Valley (Figure 5.3), where it would be subject to well abstraction and could be used for a variety of purposes (for example domestic use, animal watering, and intense crop irrigation, including alfalfa for animal feed).

As a result of these considerations, there is considerable interest in climates that are wetter than that at the present day, or in which more extreme events occur. These concerns are particularly relevant due to the fact that increasing anthropogenic CO_2 emissions are expected

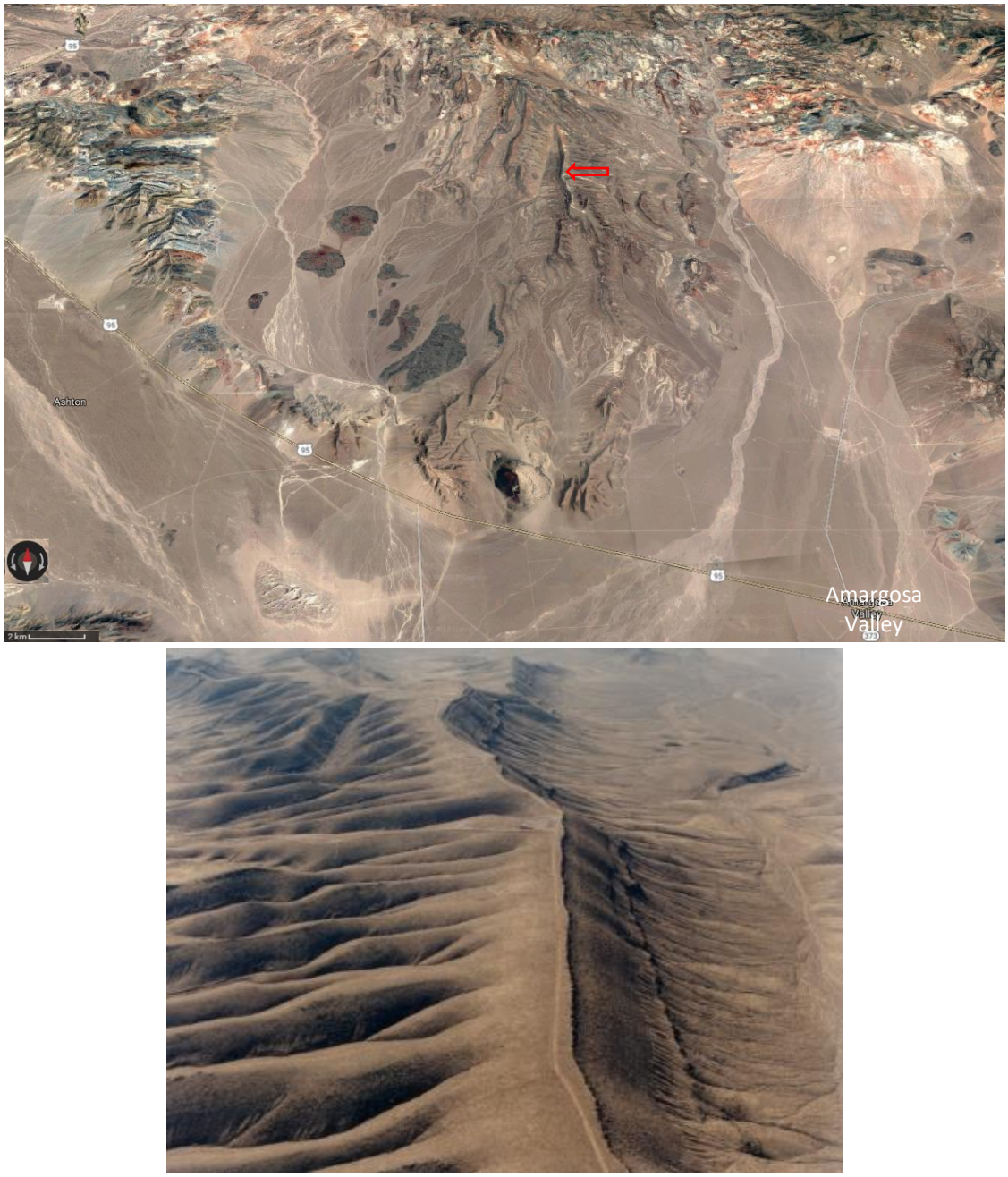

Figure 5.3. Top panel: Satellite image showing location of Yucca Mountain (red arrow) in Nevada, USA. Also show is Amargosa Valley. Source: Google Maps 2017. Bottom panel: The Yucca Mountain volcanic ridge. Source: Taken from U.S. DOE website (https://energy.gov/photos/yucca-mountain).

to lead to a warmer, wetter climate on average, with a shift to stronger more intense individual storms as temperatures increase (Cayan et al., 2013, Collins et al., 2013). Both these conditions could lead to greater penetration of precipitation to repository depth. In this context, the U.S. Department of Energy (DOE) has identified three climate states for consideration in its environmental impact statement (EIS) for the Yucca Mountain repository, based on palaeo-proxy data for the region: relatively warm and wet (compared to present-day) monsoonal, glacial

transition, and full glacial (DOE, 2002, Sharpe, 2007, NRC, 2016). Additionally, the State of Nevada has filed a large number of contentions with the U.S. Nuclear Regulatory Commission (NRC) in opposition to the DOE license application for the repository, several of which argue that the long-term impacts of increased atmospheric CO_2 on climate have not been fully considered, particularly the likely increase in precipitation in the south-west U.S. that is expected to accompany future warming (State of Nevada, 2008). Several contentions also suggest that more detailed precipitation and infiltration modelling for the site should be performed in order to properly characterise and assess future changes in precipitation and groundwater flow, particularly in relation to high-intensity rainfall events.

The amount of infiltration, and the rate at which it occurs, is mediated by changes in soil moisture characteristics, which are, in turn, determined by the combined effects of local changes in temperature and precipitation. Thus, the evolution of climate over the next 1 Myr for the grid box that contains the Yucca Mountain site is investigated in this chapter. One CO_2 scenario is modelled, which has not been utilised previously, and which represents a worst-case scenario with very high CO_2 emissions. A wider range of climate variables are also assessed compared with previous chapters. Future changes in SAT and precipitation are emulated, as they were in Chapters 3 and 4. However, in these previous chapters, it was found that these climate variables fluctuated with different periodicities in time, such that it is not obvious at which periods the soil moisture conditions will result in the greatest levels of infiltration and hence be most prejudicial to repository safety. As a result, soil temperature and soil moisture are also emulated, as they are among the range of climate variables that can be modelled using HadCM3. From the emulated soil moisture data, the critical periods for infiltration may be identified.

A caveat of this method is that the HadCM3 model (and hence the emulator) assume a generic soil column that is homogenous across the grid-box, with soil layers of fixed depth. However, in reality, the soils at Yucca Mountain are strongly heterogeneous and horizontally structured, which has been found to have a significant impact on spatial variations in infiltration, along with bedrock and vegetation characteristics (DOE, 2008). To produce projections that are site-specific, temperature and precipitation data from the emulator or HadCM3 could be used to force the more sophisticated, heterogeneous soil models developed for Yucca Mountain or applied elsewhere. Furthermore, a number of the contentions relating to the Yucca Mountain site stress the need for the application of a suitable infiltration model that is able to assess the full range of flow pathways that occur at the site, including, for example, subsurface lateral flow and overland flow due to the arid conditions of the environment (State of Nevada, 2008). The requirement for site-specific data used to calibrate and validate the models is also emphasised,

including precipitation data and soil and rock properties. It is noted, for instance, that soil properties are vital to the modelling of net infiltration, and that the infiltration model used for Yucca Mountain demonstrates high sensitivity to the soil depth parameter, thus highlighting the need for local characterization data and site-specific process modelling.

It should also be noted that, in its current form, the emulator cannot be used to examine changes in the characteristics of extreme precipitation events. A possible direction for future research, therefore, would be to investigate potential changes in the frequency and intensity of extreme precipitation events at Yucca Mountain.

In this chapter, details of the methodology are described in Section 5.2, including the forcing data applied for the next 1 Myr and the configuration of the emulator. The results produced by the emulator are described in Section 5.3, and their implications discussed in Section 5.4, before the conclusions of this chapter are presented in Section 5.5.

5.2 Methods

In order to run the emulator, which was used to produce the projections of future climate, a number of steps needed to be completed first, shown in orange (box or text colour) in Figure 5.2. Broadly, these steps provided the future climate forcing data to be applied, including atmospheric CO_2 concentration and orbital data (orange boxes), and the emulator configuration to be used (orange text).

5.2.1 Data for the next 1 Myr

The emulator was forced with changes in atmospheric CO_2 concentration and orbital conditions for the next 1 Myr. As in Chapters 3 and 4, the climate was modelled at 1 kyr intervals, producing a continuous projection for the next 1 Myr.

For atmospheric CO_2, the 10,000 Pg C emissions scenario of Winkelmann et al. (2015) was used. Similarly to the emissions scenarios used in Chapters 3 and 4, this scenario was based on a logistic equation (Caldeira and Wickett, 2005), and resulted in total emissions of 10,000 Pg C being released to the atmosphere over the first few hundred years of the simulation after 2010. Whist remaining fossil fuel reserves that are currently potentially technically and economically viable have been estimated to be approximately 1000 Pg C, fossil fuel resources (where economic

extraction may be feasible in the future) are estimated at ~4000 Pg C (McGlade and Ekins, 2015), and nonconventional resources such as methane clathrates could be as high as 20-25,000 Pg C (Rogner, 1997). Consequently, the worst-case emissions scenario presented here was selected so that the emissions pathway that ultimately is followed will likely be bounded by this scenario. The impulse response function described in Chapter 2 was used to calculate the evolution of atmospheric CO_2 concentration based on this emissions scenario, which is illustrated in Figure 5.5b. Atmospheric CO_2 peaks at 2973 ppmv 1 kyr AP, immediately following the emissions period. It then declines, relatively rapidly initially, and then more slowly over longer timescales of hundreds of thousands of years. At 1 Myr AP, the atmospheric CO_2 perturbation has almost entirely decayed, restoring the CO_2 concentration to 286 ppmv, close to pre-industrial values.

The astronomical parameters of longitude of perihelion (ϖ), obliquity (ε), and eccentricity (e) were calculated using the Laskar et al. (2004) solution. Longitude of perihelion and eccentricity were combined under the forms $e\sin\varpi$ and $e\cos\varpi$ for input into the emulator.

In summary, the emulator configuration applied here was identical to that described and applied in Section 4.4 of Chapter 4. The only difference is that, in this chapter, a different site was studied (Yucca Mountain), a different CO_2 scenario was assumed (10,000 Pg C), and a wider range of climate variables was emulated (SAT, precipitation, soil temperature and soil moisture).

5.2.2 Emulator configuration

The emulator configuration and the data used for calibration were chosen based on which continental ice sheet configuration was required (either *modice* or *lowice*), and which climate variable was being modelled.

Here, the modern-day (*modice)* ice sheet configuration was selected. As is described in more detail in the next section, a high CO_2 emissions scenario was assumed, which may suggest that increased ice melt in response to higher global mean temperatures would make the assumption of reduced ice sheet extents more appropriate. This assumption may be further supported by the prospect that once the GrIS has fully melted in response to warming, the resultant decrease in albedo may be sufficient to prevent the re-nucleation of the ice sheet until regional temperatures are significantly lower than present-day (an example of hysteresis in the Earth system). Therefore, particularly if accompanied by long-term atmospheric CO_2 concentrations that are similar or slightly higher than present-day, it could take tens of thousands of years or longer for the GrIS to regrow to a large and permanent ice sheet. Conversely, Figure

2.4 in Chapter 2 suggests that for total emissions of 10,000 Pg C, approximately 75% of the excess atmospheric CO_2 is removed from the atmosphere within 10 kyr of the CO_2 release. This means that very high atmospheric CO_2 concentrations, and the resultant increase in radiative forcing, will only occur for a relatively small proportion of the time, with the majority of the 1 Myr period having CO_2 concentrations that are much lower. In addition, Figure 3.4a in Chapter 3 shows the mean annual SAT anomaly averaged across five *lowice* experiments compared with their *modice* equivalents, demonstrating that the largest anomalies occur locally to the GrIS and AIS, with only very small anomalies exhibited for other areas. Therefore, the ice sheet configuration will have very little impact at the case study site, given that it is far removed from the high-latitudes. Hence, modern-day ice sheet extents were selected.

The *modice_80_c* emulator was utilised, which was described, optimised and evaluated in Section 4.4.2 of the previous chapter. This emulator was selected because it allows atmospheric CO_2 concentrations of up to 3600 ppmv to be modelled, which was necessary for the emissions scenario used here. The *modice_60* emulator, applicable up to 1900 ppmv (Chapter 3), had upper CO_2 limits that were too low.

The emulator was calibrated using the full *highCO_2* and *lowCO_2* ensembles, which comprised 80 simulations in total. Due to a runaway warming feedback that caused accelerated warming to occur part way into the simulations that had CO_2 concentrations of 2000 ppmv or higher, the equilibrated data for each variable (denoted ΔT_{eq}^{g} for SAT) were corrected based on a linear function, thus removing the impact of the runaway warming. Details of this correction can be found in Chapter 4. The emulator was optimised on SAT data, and this configuration (i.e. same number of retained PCs and hyperparameter values) was then also applied to emulate the other variables. This approach ensures that the results for the variables are consistent with each other. As detailed in Section 4.4.2 of Chapter 4, the optimised emulator retained 15 PCs, and had scales δ of 5.904 (ε), 3.324 ($e\sin\varpi$), 3.928 ($e\cos\varpi$), 0.381 (CO_2), and a nugget of 0.121.

For the Yucca Mountain site, the location of which on the HadCM3 grid is illustrated in Figure 5.4, several other climate variables were modelled in addition to SAT and precipitation. These were soil temperature and soil moisture for two soil layers – the top layer which represents soil from the surface down to 0.1 m, and the bottom layer of soil from 0.65 m down to 2 m. It should be noted that this was a generic soil, and not specific to the Yucca Mountain site. For each variable in turn, the emulator was calibrated on the estimated equilibrated HadCM3 data for the 80 experiments, and then forced with the future climate forcing data (described in the next section) to provide a projection of the evolution of the variable over the next 1 Myr.

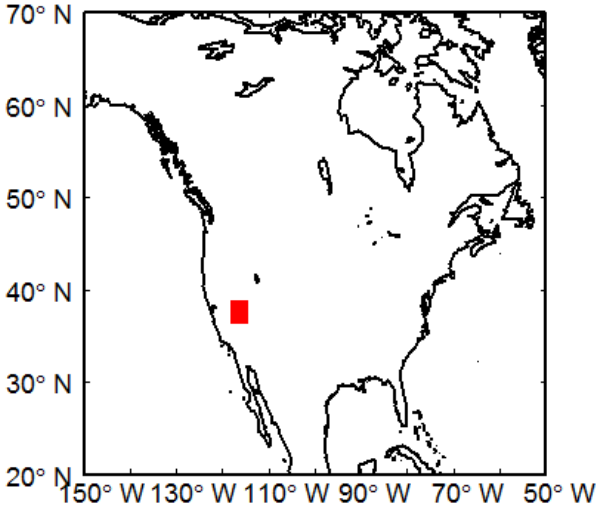

Figure 5.4. Map of North America highlighting the grid box that represents the Yucca Mountain case study site.

5.3 Results

The emulator was used to produce time series data representing the continuous evolution of various climatic variables for the next 1 Myr, based on the orbital and CO_2 forcings described above. Figure 5.5 illustrates the CO_2 and orbital forcing, and the future evolution of SAT and precipitation at the grid box representing Yucca Mountain, and Figure 5.6 shows changes in soil temperature and soil moisture for the top and bottom layers of soil that are included in HadCM3. The estimated uncertainty in the projections is also shown, defined as 1 standard deviation of the emulated grid box posterior variance, and all climate variables are presented as an anomaly compared to pre-industrial. Figure 5.5 is comparable to Figure 4.22 in the previous chapter, for which the same emulator was used (*modice_80_c*) but with a range of scenarios with lower total emissions (500-8000 Pg C).

For the early part of the simulation, all the variables exhibit trends similar to that shown by the atmospheric CO_2 concentration (Figure 5.5b), with a considerable increase over the first few thousand years immediately following emissions. Mean annual SAT for the grid box peaks at 22.2 ± 0.3°C (above pre-industrial), precipitation reaches a maximum of 0.6 ± 0.1 mm day^{-1}, and soil temperature increases to 20.9 ± 0.4°C and 21.1 ± 0.4°C in the top and bottom soil layers, respectively. A relatively rapid decline then occurs until approximately 50 kyr AP, which is the result of a large proportion of the atmospheric CO_2 perturbation being taken up from the atmosphere by carbon cycle processes, described in Chapter 2. Following this, the variables generally gradually decrease back towards pre-industrial values, with oscillations resulting from

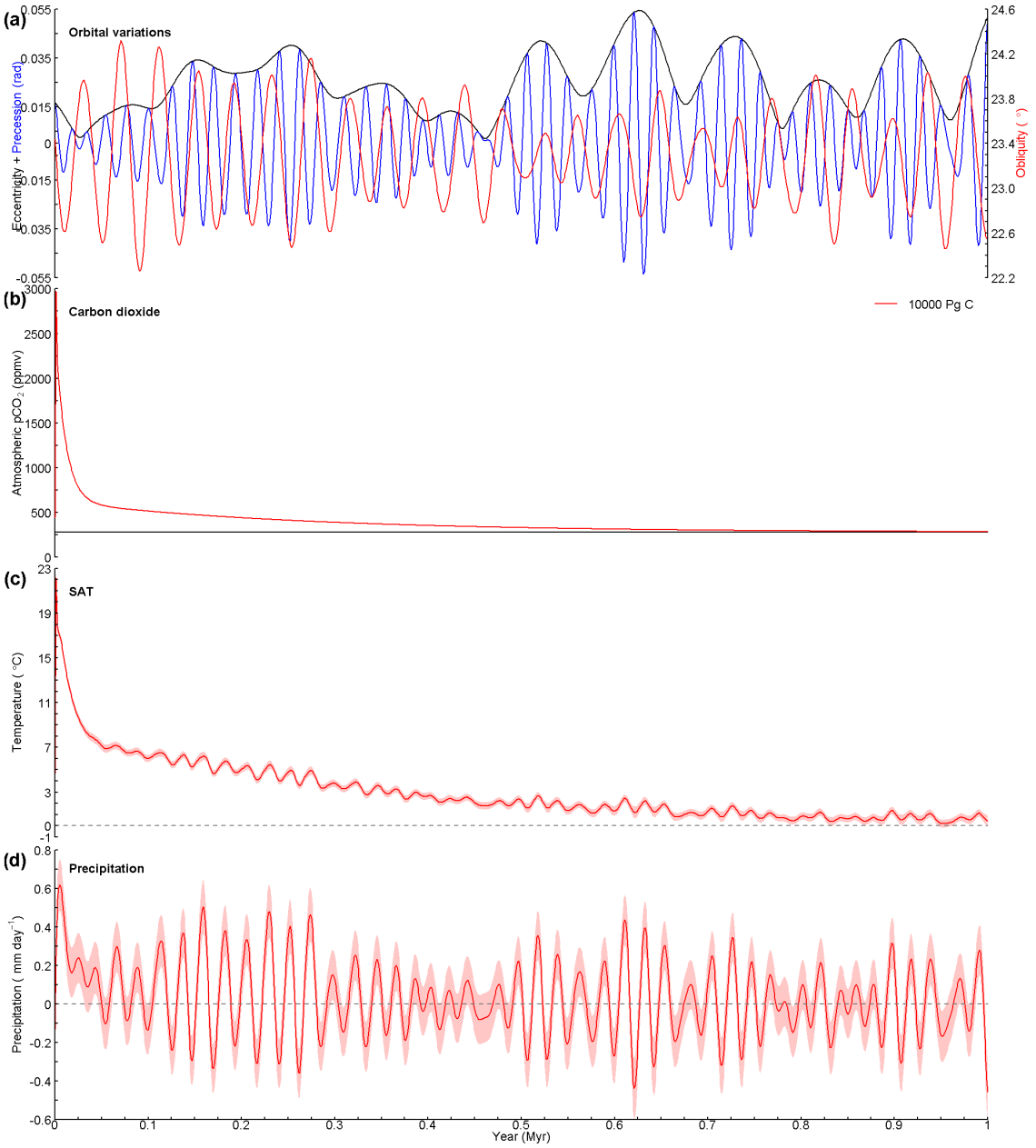

Figure 5.5. Emulation of climate evolution for the next 1 Myr at the Yucca Mountain grid box for the 10,000 Pg C emissions scenario. (a) Time series of orbital variations (Laskar et al., 2004), showing eccentricity (black) and precession (radians; blue) on the left axis, and obliquity (degrees; red) on the right axis. (b) Time series of atmospheric pCO_2 (ppmv), predicted using the impulse response function discussed in Chapter 2. The pre-industrial CO_2 concentration is also shown (black line). Time series of: (c) emulated mean annual SAT (°C), and (d) emulated mean annual precipitation (mm day^{-1}). Climate variables are modelled every 1 kyr, using the modice_80_c emulator. Error bands represent the emulated grid box posterior variance (1 standard deviation). Variables are shown as an anomaly compared with the pre-industrial control simulation.

variations in the orbital parameters superimposed on top of this trend. Even after 1 Myr, the temperature variables have not yet returned to pre-industrial levels, demonstrating the possible long-lived impacts of substantial anthropogenic emissions. Soil moisture is the exception, which does not appear to demonstrate an initial significant deviation associated with high warming (Figures 5.6c and 5.6d). The upper layer shows a modest early increase, which subsides within

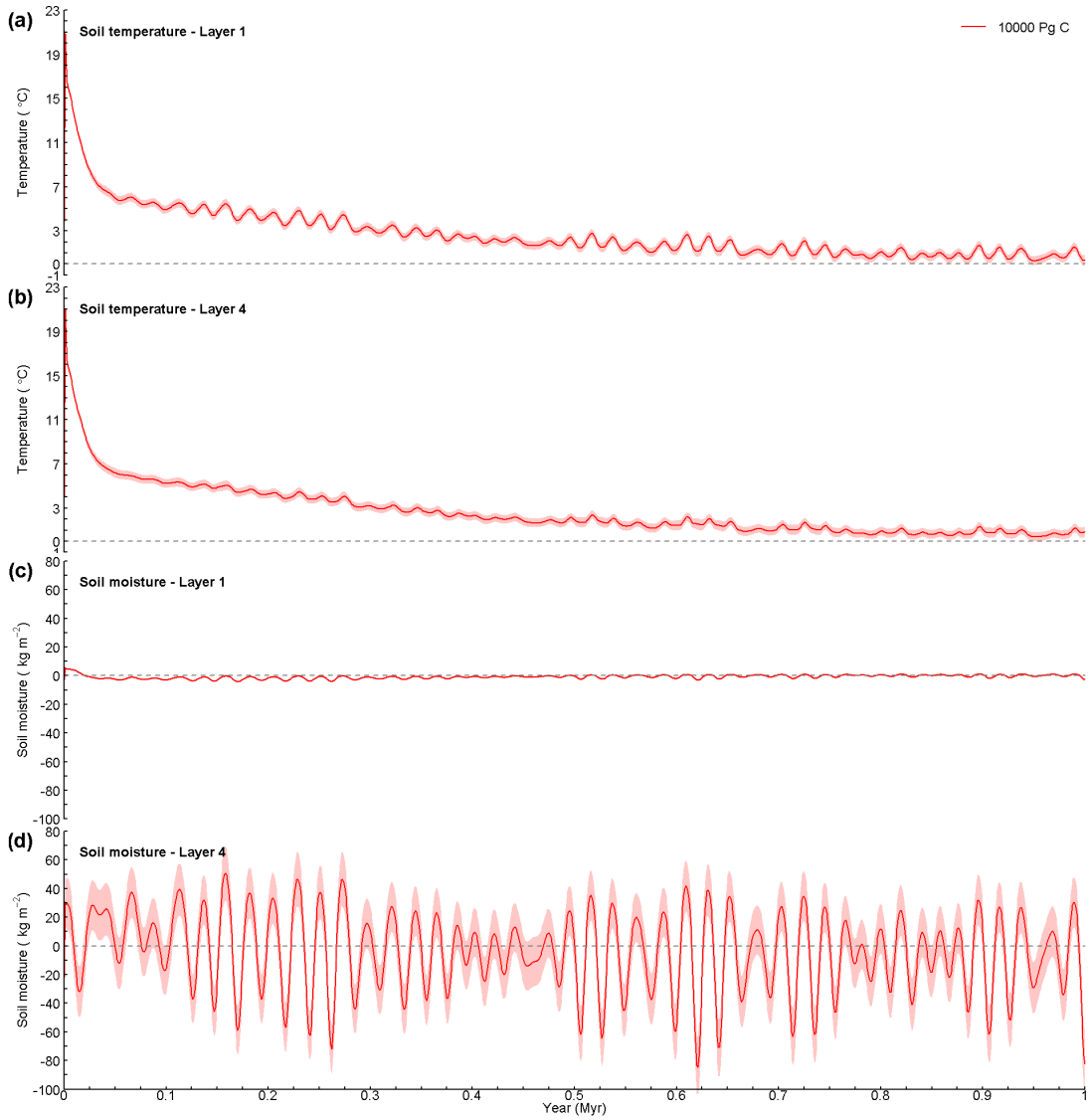

Figure 5.6. Emulation of climate evolution for the next 1 Myr at the Yucca Mountain grid box for the 10,000 Pg C emissions scenario. Time series of: (a) and (b) emulated mean annual soil temperature (°C; top and bottom soil layers), and (c) and (d) emulated mean annual soil moisture (kg m^{-2}; top and bottom soil layers). Climate variables are modelled every 1 kyr, using the modice_80_c emulator. Error bands represent the emulated grid box posterior variance (1 standard deviation). Variables are shown as an anomaly compared with the pre-industrial control simulation.

approximately 25 kyr. However, the response of soil moisture in the lower layer appears to be dominated by changes in orbital forcing, even during the period of very high warming.

The uncertainty associated with SAT and precipitation is of a similar magnitude to that demonstrated in Figure 4.22 in Chapter 4, and Figures 3.14 and 3.15 in Chapter 3 for the same variables. For these variables, as well as the soil variables, the emulated uncertainty is relatively small when compared with the fluctuations that occur as a result of the orbital and CO_2 forcings.

The change in SAT for approximately the first 100 kyr is driven largely by the increased atmospheric CO_2 concentration, with some evidence of obliquity forcing (Figure 5.5c). This

coincides with eccentricity being relatively low (Figure 5.5a). From approximately 100 kyr onwards, in keeping with the results of Chapter 3 and Figure 4.22 in Chapter 4, precession has an increased impact on the pacing of SAT fluctuations, particularly during the periods when eccentricity is relatively high. During these periods, eccentricity also has an increased influence, demonstrated by the larger amplitudes of the temperature fluctuations. A similar trend is exhibited by the soil temperature data, although the magnitude of the orbital-driven fluctuations gets progressively smaller as soil depth increases (Figures 5.6a and 5.6b). This is due to the deeper layers of soil being increasingly more insulated from temperature variations at the surface.

Conversely, the oscillations in precipitation over the next 1 Myr appear to show stronger precessional forcing, which is at its strongest when eccentricity is high (Figure 5.5d). Soil moisture exhibits similar trends and timescales of change to precipitation, being primarily driven by precession (Figures 5.6c and 5.6d). The sensitivity of soil moisture to climatic changes appears to be lower in the surface layer than in the deepest soil layer, with significantly larger variations in moisture content observed in the lower layer. This may be related to changes in evapotranspiration at the land surface. During warmer periods, both SAT and precipitation increase, but this is also accompanied by an increase in evapotranspiration, particularly from the surface soil layer, resulting in a more muted response of surface soil moisture to increased precipitation. Water continues to be transferred down to the deeper soil layers via infiltration and percolation, which consequently exhibit higher typical moisture contents with larger fluctuations.

5.4 Discussion

5.4.1 Future climate

The results of the emulator suggest that future climate at the Yucca Mountain site will change in response to both orbital and anthropogenic CO_2 forcing. Under the emissions scenario explored here, the most extreme changes in the climate variables considered here generally occur within the first 50 kyr, immediately following the emissions period when atmospheric CO_2 concentrations are very high. Following this, climate conditions tend to gradually return towards pre-industrial conditions, with orbitally-forced fluctuations becoming more evident. Mean

annual SAT at the site is projected to increase by a maximum of 22.2 ± 0.3°C, whilst precipitation increases by 0.6 ± 0.1 mm day^{-1}. Winkelmann et al. (2015) projected a maximum warming of around 11°C for the same 10,000 Pg C emissions scenario, although this was for global mean temperature rather than a single grid box temperature, and was modelled using the EMIC *c*GENIE. In reality, the degree of human-induced climate change will be dependent on the total emissions that are released to the atmosphere, with lower emissions expected to result in lower levels of warming, as illustrated in Chapters 3 and 4. However, the amount of CO_2 that will be emitted in the future is not known; thus, a very high emissions scenario was selected to represent a bounding scenario. Even relatively modest estimates of total emissions have been found to result in relatively large changes in climate compared to those driven by orbital changes (see, for example, 500 Pg C scenario in Chapters 3 and 4).

5.4.2 Implications of climate changes and uncertainties

Whether as a result of orbital or CO_2 forcing, fluctuations in climate could have implications for the safety assessment of the deep geological disposal facility that has been proposed to be sited at Yucca Mountain. In particular, variations in precipitation, both in terms of its intensity and its spatial and temporal distribution, could result in changes to the amount and distribution of water that percolates deep below ground level.

This is particularly relevant for the Yucca Mountain facility, which is located in the unsaturated zone in fractured rock. For repositories such as this, the main considerations are changes to the amount of flow through the waste emplacement tunnels or vaults, the chemical composition of the ground water, and the properties of the flow path, such as flow velocity (Stuckless, 2012). The transit time for water that has come into contact with the waste packages to percolate down to the saturated zone and then move sub-horizontally to areas where it may be abstracted from wells or discharge at the ground surface is also of importance, potentially affecting the concentration of radionuclides in the abstracted or discharging groundwater. As such the results presented here, in particular hydrological variables such as soil moisture and precipitation, may be of interest for safety assessments, due to their implications for infiltration.

A significant amount of infiltration modelling has been carried out for the Yucca Mountain region, due to it being one of the main controls on the transit times of radionuclides in ground water to the surface (e.g. Stuckless and Levich, 2007, Stuckless, 2012, DOE, 2008). The DOE applied the net infiltration model MASSIF (Mass Accounting System for Soil Infiltration and

Flow) (SNL, 2008a) to a ~125 km^2 area of the region (DOE, 2008). The model includes representation of flow of water through the soil layer, evapotranspiration processes, surface runoff and infiltration from the soil into the bedrock. It was forced by daily climate data (precipitation, temperature and wind speed) derived from historical weather records from Yucca Mountain and a number of analogue sites for the future climate scenarios (monsoon and glacial transition). The model domain also included vegetation and geologic data specific to the site, including plant height, types of soil and bedrock and their spatial distributions, the depth of soil types over the area, and other site characteristics (e.g. elevation).

For each of the future climate states, two replicates of 20 realizations of input parameters values were produced using Latin Hypercube sampling, to test the sensitivity of the model. For the future monsoon climate state, the model projected an increase in infiltration at the site, with the median (min – max) of the spatially-averaged infiltration increasing from 13 mm yr^{-1} (2.0 – 35.4 mm yr^{-1}) for the modern-day to 22.8 mm yr^{-1} (2.4 – 83.4 mm yr^{-1}). For the glacial transition, infiltration increased by a similar amount to 28.5 mm yr^{-1} (6.6 – 64.7 mm yr^{-1}).

It was found that the spatial variability of net infiltration in the model was dependent on spatial variations in precipitation and the properties of soil, bedrock and vegetation. The lateral distribution of water via runoff pathways was also found to have an impact. For the Yucca Mountain region as a whole, LeCain and Stuckless (2012) concluded that infiltration was controlled by a range of climatic variables including solar radiation, temperature, relative humidity and precipitation, based on estimates made using a range of methods, including physical, empirical, and geochemical approaches and water-mass balances.

The sensitivity of infiltration to the identified factors highlights the need in modelling studies to use climatic data (e.g. precipitation and temperature) with a high spatial resolution, and to use detailed rock, soil and vegetation characteristics data that are specific to the site. Due to the potential importance of lateral flow pathways, one of the contentions opposing the Yucca Mountain facility relates to the lack of representation of these pathways in the MASSIF infiltration model and the lack of observational data for this type of flow, suggesting that better representation of these hydrological processes would improve infiltration estimates (State of Nevada, 2008). It was also recommended in several contentions that better observational data from the site is required to properly calibrate and validate the infiltration model, including precipitation, soil and rock properties, and streamflow data, thus further reinforcing the argument for site-specific data and modelling using models that are appropriate to the site conditions.

As mentioned previously, the DOE adopted the approach of considering three future climate states based on past climates: monsoon, glacial transition and full glacial (DOE, 2002), thus not taking into account future changes in climate driven by anthropogenic CO_2 emissions. Several of the contentions submitted to the NRC propose that this is not appropriate (State of Nevada, 2008), given that a range of studies (including Chapter 2 of this thesis) suggest that the atmospheric CO_2 perturbation caused by anthropogenic emissions, and the resultant climate changes, will be long-lasting, potentially affecting the timing of the next glacial inception (Berger and Loutre, 2002, Archer, 2005, Archer and Ganopolski, 2005). Indeed, the results presented in this chapter suggest that significant warming of up to ~21°C may occur in the region under the applied anthropogenic CO_2 emissions scenario. Under present day conditions, in-situ temperature sensors suggest that SATs at Yucca Mountain vary from ~6°C in the winter up to ~29°C in the summer (Sharpe, 2007). A large increase in SAT in response to anthropogenic CO_2 forcing, as suggested here, could have significant implications for local conditions such as infiltration and subsurface hydrology, as well as for the sustainability of agriculture in the Amargosa Valley, which already requires high rates of groundwater abstraction. In response to the contentions, it was therefore recommended that anthropogenically-driven climatic changes should be taken into account, and it is for an application such as this that the framework and modelling tools presented here would be suitable; to supply transient climate data that could be downscaled and used to force models (e.g. infiltration) that are applicable at the site scale.

Although not taken into account in this methodology, the impacts of changes in the frequency and intensity of episodic flow events may also be of importance to facilities located in the unsaturated zone, in terms of changes to groundwater and the degree of ground saturation. It was noted by Lord et al. (2015) that the Yucca Mountain facility "is thought to be vulnerable to high-intensity fluvial episodes in a warmer wetter climate through their impact on infiltration (Stuckless, 2012, Thorne, 2013). This highlights that, while regional changes in temperature and precipitation are important, modifications to atmospheric and oceanic circulation regimes are also of interest due to their influences on local and regional climates". An example of this relates to atmospheric rivers, which transport large amounts of water vapour from the over Pacific Ocean to the Southwest U.S., and are projected to carry more water vapour as global temperatures increase, increasing the risk of storm and flooding events (Gershunov et al., 2013). As such, future work could also focus on emulating extreme precipitation events.

A caveat of the results is that the projected changes in climate do not take into account future glacial-interglacial cycles which are expected to occur based on paleo records of past climate (e.g. Petit et al., 1999). As a result, the DOE identified a glacial transition and full glacial

as climate states of interest in the EIS for Yucca Mountain (DOE, 2002). The site is not located in a region that has been previously glaciated, and thus is unlikely to be directly impacted by the formation of an ice sheet in its vicinity (e.g. through hydrogeological changes, surface erosion, etc.). Nonetheless, the build-up of ice at higher latitudes in North America, and the resultant increase in land surface height and isostatic changes, could result in regional changes to atmospheric circulation. This has the potential to impact SAT, precipitation and/or winds at the Yucca Mountain site. Transitions between glacial and interglacial regimes can also result in large changes in global climate, such as the significant global cooling that occurs during glacial periods, linked to reductions in atmospheric CO_2 concentration (e.g. Petit et al., 1999).

However, it was suggested in Chapter 3, as well as by a number of other studies (e.g. Berger and Loutre, 2002, Archer and Ganopolski, 2005, Lord et al., 2015, Ganopolski et al., 2016) that the next glaciation may be significantly delayed as a result of warming caused by anthropogenic emissions. For example, these studies found that emissions of 1000 Pg C resulted in the current interglacial lasting for at least the next 100 kyr, whereas emissions of 5000 Pg C delayed the next glacial inception for at least 500 kyr. Under the emissions scenario assumed here, it may be expected that the current interglacial would be delayed even longer, making the changes induced by anthropogenic warming of greater importance, at least for the next few hundreds of thousands of years.

As discussed previously, the emulation approach applied here assumes modern-day ice sheet extents, which may not be appropriate for parts of the 1 Myr period. This is partly due to future glacial-interglacial cycles, but also to the potential for significant or complete melting of the GrIS and AIS sheets as a result of increased atmospheric CO_2 concentrations following anthropogenic emissions (Huybrechts et al., 2011, Winkelmann et al., 2015). However, in Figure 3.4a in Chapter 3 it was found that the changes in mean annual SAT that occurred as a result of a reduction in the size of the continental ice sheets occurred locally to the ice sheets, with only very small anomalies exhibited for other regions of the Earth surface. Due to the low latitude location of the site, therefore, the reduction in the ice sheet extents is expected to have very little impact on the local climate. It is possible that the process of the ice sheets melting may result in changes to global climate, through reductions in the strength of the AMOC due to freshening of surface ocean waters and the resulting redistribution of heat across the latitudes. However, in order to simulate this, an interactive ice sheet model would need to be utilised, along with the ability to run long (>10^3 yr) transient experiments. Hence, this is beyond the scope of this study. Natural variations in atmospheric carbon are also not considered in this method, but the very high anthropogenic emissions scenario applied here means that the variations in

CO_2 concentration driven by anthropogenic emissions will be considerably larger than those that may occur due to natural variations, at least for several hundred thousand years.

The data presented here can be utilised in safety assessments for nuclear waste repositories. Depending on the application, downscaling to regional or local scale may be required, and the temporal resolution of the data may need to be increased. Suitably spatially and temporally downscaled data could then be used to drive landscape-development models which, due to the nature of the process of landscape development and the range of properties that affect it, may need to be site specific, or at least appropriate to the geological setting of the repository. Information about the future evolution of the site could then be used in dose assessment modelling, to assess the long-term safety of the repository and help ensure that the likely level of exposure of humans and the environment to radioactive materials released from the repository are compliant with regulatory requirements.

5.5 Summary and Conclusions

This chapter presents a case study illustrating the application of the proposed framework for modelling long-term future climate evolution that has been presented in this thesis. The *modice_80_c* emulator was used to project the evolution of climate over the next 1 Myr, for the grid box representing Yucca Mountain, which is the proposed location for a deep geological repository in the USA.

The emulator was forced with orbital and CO_2 data for the next 1 Myr. The impulse response function was used to calculate the long-term evolution of atmospheric CO_2 concentration following anthropogenic emissions. To account for the uncertainty associated with the scale of future anthropogenic CO_2 emissions, a bounding emissions scenario was assumed, with CO_2 emissions totalling 10,000 Pg C. Several climate variables were then modelled using the emulator, including SAT, precipitation, and soil properties. It was found that:

- All variables are strongly affected by the high anthropogenic CO_2 concentrations experienced in the first ~50 kyr of the simulation. The exception to this is bottom layer soil moisture, which appears to be primarily forced by orbital variations.
- SAT and soil temperature appear to be initially influenced by obliquity and then later by precession, whereas precipitation and soil moisture variations occur on a precessional timescale.

- The projected degree of change in SAT and precipitation, the orbital signals evident in the time series data, and the emulator uncertainty are all similar to those described in Chapters 3 and 4 for different sites and/or emissions scenarios and/or modelled using different emulator configurations.
- The time series data presented are suitable for use in landscape-development and dose assessment modelling, as part of a post-closure safety assessment for a radioactive waste disposal facility.

It has been shown that the proposed framework provides a clear and relatively simple approach to modelling long-term climate change. One of the significant advantages of the methodology is that it can easily be adapted to account for a range of different assumptions, including a wide range of future anthropogenic CO_2 emissions, and two different configurations for the continental ice sheets. The emulator can provide data for a variety of climate variables, at the resolution of a GCM, meaning that climate data for any global location can be extracted. Both the emulator and the impulse response function are also significantly faster to run than traditional models, such as EMICs and GCMs, and require no additional computing power than that provided by a normal desktop computer. It is therefore suggested that this framework, and the tools developed within it, provide a useful approach to considering long-term future climate change within the context of post-closure performance assessments for repositories for the disposal of radioactive wastes.

CHAPTER 6

Conclusions

The main aims of the work described in this thesis were to develop a framework for addressing long-term future climate change within the context of post-closure performance assessments for disposal of radioactive wastes, and to investigate possible changes in climate over the next 100 kyr or more in response to forcing from changes in the orbital parameters of the Earth and anthropogenic CO_2 emissions. It also aimed to develop a number of statistical tools, including an impulse response function which allows the rapid projection of the response of future atmospheric CO_2 concentration to anthropogenic CO_2 emissions, and an emulator which can project the evolution of different climate variables over timescales of up to 1 Myr. Finally, it aimed to provide an illustration of the application of the framework to an example site.

This chapter summarises the principal findings of the thesis with respect to the aims and objectives outlined in Section 1.4. It also discusses several ways in which this work can be improved and developed further.

6.1 New methods developed

The main results of the work described in this thesis are the proposed framework for addressing long-term climate change within the context of post-close performance assessments

for disposal of radioactive wastes, and the two tools that have been developed, based on different complexity Earth system models. These tools allow long-term (>1 kyr) changes in different aspects of climate to be simulated rapidly using relatively small computational resources.

Firstly, the impulse response function was developed, which provides a simple and practical tool for rapidly projecting the implications of any temporal pattern of CO_2 emissions on atmospheric CO_2 concentrations. Its primary advantage is that it can be used across a large range of emissions sizes and rates of release and removes the need for long simulations using computationally expensive models. It was developed based on the results of a series of simulations with pulse CO_2 emissions ranging from 1000 to 20,000 Pg C, modelled using the *c*GENIE Earth system model.

The second tool is a statistical emulator that can be used to produce long-term continuous (every 1 kyr) projections of climate evolution at the spatial resolution of a GCM, again with relatively low temporal and computational cost. The emulator was calibrated on two 40-member ensembles of simulations with varied orbital conditions and atmospheric CO_2 concentrations (deemed to be the primary forcings on climate on the timescales being considered here), produced using the HadCM3 GCM. It can be used to project changes in past and future climate, as long as the input parameter values (orbital and CO_2) are within the wide range that were sampled in the experiment ensembles, including CO_2 concentrations of up to 3600 ppmv.

The emulator was used to model the long-term response of future climate to different CO_2 emissions by using as input a number of atmospheric CO_2 trajectories produced using the impulse response function. A key benefit of the emulator is the global coverage and relatively high spatial resolution of the data produced, particularly considering the relatively high complexity of the underlying climate model (GCM). This means that results can be viewed at a grid box scale, allowing climatic changes in the region (grid box) of individual radioactive waste repositories to be examined. Time series data produced using the emulator, for both primary climatic and derived, climate-related variables, are suitable for use in landscape-development and dose assessment modelling, as part of a post-closure safety assessment for a radioactive waste disposal facility.

6.2 Summary of scientific results

6.2.1 The "long tail" of excess atmospheric CO_2

The response of the long-term global carbon cycle to a range of instantaneous pulse CO_2 emissions was investigated in Chapter 2 using the *c*GENIE model. To examine how the dynamics of this response change depending on the total emissions, a multi-exponential analysis was carried out on the atmospheric CO_2 decay curves for the emissions scenarios. Five exponential components were found to result in the optimal fit. The following observations were made:

- It was suggested that the shorter (<1 kyr) timescales of decay likely represent a range of ocean circulation, carbonate chemistry, and air-sea gas exchange processes, based on their *e*-folding timescales of approximately 1.2 yr, 36 yr, and 730 yr.
- The fractional removal of excess atmospheric CO_2 from the atmosphere by these three components was found to depend strongly and non-linearly on the total emissions released, with the fraction removed decreasing as total emissions increase. This highlights how the buffering and CO_2 uptake by the ocean on anthropogenic timescales progressively saturates with increasing total emissions.
- The fraction of excess CO_2 taken up from the atmosphere on a timescale of approximately 11 kyr via carbonate weathering and burial (fourth exponential component) progressively increases with increasing emissions, although at a progressively slower rate for higher total emissions. This change in the dynamics acts to compensate for the reduced uptake by the processes occurring on shorter timescales.
- In contrast to the shorter-term ocean dynamics and carbonate weathering processes, the *e*-folding timescale (~268 kyr) for the silicate feedback (fifth exponential component), as well as its relative importance in removal of the CO_2 perturbation from the atmosphere, was almost independent of the total emissions.

Based on this multi-exponential analysis, an impulse response function was developed that is able to reproduce model-predicted atmospheric CO_2 data following emissions of up to 20,000 Pg C. Two versions of the function were developed: one for instantaneous pulse emissions and one based on a convolution analysis allowing time-dependent CO_2 emissions to be modelled. On multi-millennial timescales or longer, both functions were able to reproduce the atmospheric

CO_2 time series data for different emissions scenarios produced using the *c*GENIE model with relatively small percentage errors.

6.2.2 Long-term changes in global climate

A statistical emulator has been developed that has been calibrated based on two ensembles (*highCO_2* and *lowCO_2*) of 500-year simulations with varied orbital conditions and atmospheric CO_2 concentrations performed using HadCM3. Two versions of the emulator are discussed herein; one with modern-day continental ice sheet extents and one with reduced ice sheet extents. The largest impact on climate of this reduction in continental ice was generally found to be limited to the vicinity of the ice sheets, with only very small climate changes observed globally.

The results of the PCA underpinning this emulator are examined in Sections 4.2 and 4.3 of Chapter 4, with a number of PCs being tentatively linked to physical mechanisms in the Earth system. The emulator's application to precipitation was also investigated, and specifically the performance of the emulator that uses hyperparameters (length scales and nugget) and number of retained PCs optimised on SAT data is compared to one that is optimised on precipitation data. It was found that:

- A number of retained PCs exhibit spatial variations that may be associated with warming due to CO_2 (particularly increased warming over land and at high latitudes), and variations in monsoons, sea-ice, and AMOC.
- There is no great loss in emulator performance when hyperparameters optimised on SAT data are applied to emulate precipitation, compared with hyperparameters optimised on precipitation data. This suggests that it is appropriate to use one set of hyperparameters and number of PCs (optimised on SAT) for a range of climate variables, rather than optimising separately for different variables.

The *highCO_2* and *lowCO_2* ensembles each contained 40 simulations, but the emulator presented in Chapter 3, and Sections 4.2 and 4.3 of Chapter 4, was only calibrated on simulations with a CO_2 concentration of less than 2000 ppmv, totalling 60 simulations (*modice_60* emulator). On the other hand, the emulator applied in Section 4.4 of Chapter 4, and Chapter 5 was calibrated on the full set of 80 simulations, meaning it can be used to simulate CO_2 concentrations of up to 3600 ppmv. GCM simulations with CO_2 concentrations higher than 2000 ppmv were found to exhibit runaway warming, and the assumption was made that this was the result of a runaway

positive feedback in the GCM relating to the vertical ozone distribution in the atmosphere being prescribed rather than interactive. As a consequence, the impact of the runaway warming was corrected for in the GCM simulations before they were used to calibrate the *modice_80_c* emulator.

The emulator can be used for a number of different applications, making it suitable for tackling a wide range of climate questions. One such application is to produce time series of climatic variables that cover long periods of time (i.e. several thousand years or more) at a GCM resolution, whilst producing an estimation of the uncertainty associated with the projection. This would not be feasible using GCMs due to the significant time and computational requirements involved, and allows for comparison with palaeo-proxy climate data. A continuous wavelet analysis can be performed on the time series data, to identify the orbital frequencies dominating at different times. Finally, through an inversion technique, the emulator can be used to estimate past atmospheric CO_2 concentrations based on proxy climate data, which can then be compared with palaeo-CO_2 proxy records. These applications have been illustrated by using the emulator to simulate the long-term evolution of past and future climate.

6.2.2.1 Pliocene climate

In Chapter 3, it is described how the emulator was applied at 1 kyr intervals to the late Pliocene (3300-2800 kyr BP) for atmospheric CO_2 concentrations of 280, 350 and 400 ppmv, and the emulated SATs at specific grid boxes were compared with SSTs determined from proxy data from a number of ODP/IODP sites. The wavelet power spectrum for SAT at each site was also produced, and the dominant orbital frequency assessed. In addition, the SST proxy data were used to estimate atmospheric CO_2 concentrations, based on a linear relationship between emulated grid box mean annual SAT and prescribed CO_2 concentration. It was found that:

- Temperature estimates from the emulator and proxy data show greater similarity at the equatorial sites than at the high latitude sites. Discrepancies may be the result of biases in the GCM, errors in the emulator, seasonal biases in the proxy data, unknown changes in the climate and/or carbon cycle, or issues with the tuning of parts of the record.
- The response of emulated SAT appears to be dominated by a combination of precessional and eccentricity forcing from 3300 kyr BP to approximately 2900 kyr BP, after which obliquity begins to have an increased influence.

- Regions with a particularly large response to orbital forcing include the high latitudes and monsoon regions.
- The CO_2 reconstructions from tropical ODP/IODP sites show relatively similar concentrations to CO_2 proxy records for the same period, although, for the higher latitude sites, concentrations are generally significantly higher than those inferred from the proxy data.

6.2.2.2 Future climate

The emulator was also used to simulate climate for over the next 200 kyr in Chapter 3 and Section 4.4 of Chapter 4 (*modice_60* emulator configuration) and next 1 Myr Chapter 5 (*modice_80_c* emulator configuration). Climate was emulated at 1 kyr intervals for selected CO_2 scenarios with anthropogenic emissions of 500, 1000, 2000, 5000, 8000 or 10,000 Pg C. The evolution of climate at various sites relevant to radioactive waste disposal was examined, including Forsmark, Sweden, Central England, and Yucca Mountain, USA. The climate variables that were emulated were SAT, precipitation, soil temperature and soil moisture. A spectral wavelet analysis was also performed on the SAT and precipitation data for the Central England grid box. The data suggests that:

- All climate variables are strongly affected by the anthropogenic CO_2 concentrations experienced in the first several tens of thousands of years of the simulation, with the length of time increasing as emissions increase. The exception to this is bottom layer soil moisture at Yucca Mountain, which appears to be primarily forced by orbital variations.
- The climate variables, therefore, generally exhibit a relatively rapid decline back towards pre-industrial values over the next 20-50 kyr (depending on total emissions), as excess atmospheric CO_2 is removed by the long-term carbon cycle.
- Following this, SAT and soil temperature fluctuate due to orbital forcing on an approximate 41 kyr obliquity timescale until ~160 kyr AP, before the influence of precession increases with increasing eccentricity from ~120 kyr AP.
- Conversely, precipitation and soil moisture variations demonstrate a strong precessional signal.
- The projected degree of change in SAT and precipitation, the orbital signals evident in the time series data, and the emulator uncertainty are generally consistent across the different sites and/or emissions scenarios and/or emulator configurations.

- The time series data presented are suitable for use in landscape-development and dose assessment modelling, as part of a post-closure safety assessment for a radioactive waste disposal facility.

6.2.3 A framework for projecting long-term future climate changes

This thesis presents an updated framework for projecting long-term future climate changes within the context of post-closure performance assessments for disposal of radioactive wastes (Chapter 1 Section 1.5). The application of the framework is illustrated in a case study presented in Chapter 5, where climate evolution over the next 1 Myr is emulated for the grid box representing Yucca Mountain, which is the proposed location for a deep geological repository in the USA.

It has been shown that the proposed framework provides a clear and relatively simple approach to modelling long-term climate change. One of the significant advantages of the methodology is that it can easily be adapted to account for a range of different assumptions, including a wide range of future anthropogenic CO_2 emissions, and two different configurations for the continental ice sheets. A variety of different climate variables can be simulated using the emulator, at the resolution of a GCM, meaning that climate data for any global location can be extracted and examined. Both the emulator and the impulse response function are also significantly faster to run than traditional models, such as EMICs and GCMs, and require computational resources no more sophisticated than a standard desktop computer or laptop. It is therefore suggested that this framework, and the tools developed within it, provide a useful approach to considering long-term future climate change within the context of post-closure performance assessments for repositories for the disposal of radioactive wastes.

6.3 Future work

Various suggestions for improvement and further research are discussed in earlier sections of this thesis. This section describes in more detail how this work can be enhanced and developed further, and includes suggested improvements for the modelling of the long-term carbon cycle, the GCM modelling, and the application of the proposed framework in post-closure performance assessments for radioactive waste repositories.

6.3.1 Extending the long-term carbon cycle modelling

In terms of long-term carbon cycle modelling, there are still relatively large uncertainties associated with the silicate weathering feedback, which is assumed to restore atmospheric CO_2 to its original state over hundreds of thousands to millions of years (Berner and Caldeira, 1997, Berner, 1999). In particular, uncertainties in the strength and dynamical characteristics of this feedback should be explored, both in the GENIE model as well as other models that include this process. The sensitivity of the modelled Earth system to the representation and parametrisation of the weathering mechanism in the model should also be explored, in particular the impact on atmospheric CO_2 concentration. A greater understanding of the silicate weathering feedback may suggest whether the assumed importance of this mechanism in helping to maintain a steady concentration of atmospheric CO_2 is valid, whilst improving model projections of the atmospheric lifetime of a CO_2 emission.

The impact of excess atmospheric CO_2 on other carbon cycle processes and feedbacks could also be explored, including the terrestrial biosphere, permafrost and the organic carbon cycle. For example, the burial of organic carbon in marine sediments is thought to be enhanced under conditions of increased nutrient supply from weathering and hence marine productivity, as well as under reduced ocean oxygenation that is generally associated with a warmer climate (Bains et al., 2000, Zachos and Dickens, 2000). These additional feedbacks, which operate on both short and long timescales, may affect the uptake of an atmospheric CO_2 perturbation by the land and ocean, and should therefore be taken into account.

Finally, natural variations in atmosphere CO_2 concentration are not represented; only the response of atmospheric CO_2 to anthropogenic emissions. Processes such as volcanic outgassing can release CO_2 into the atmosphere, causing the CO_2 concentration to vary and resulting in an imbalance with weathering. Furthermore, glacial-interglacial cycles are thought to be accompanied by fluctuations in atmospheric CO_2, with the CO_2 concentration over the last 400 kyr ranging from ~180 – 200 ppmv during glacial periods to ~270 – 290 ppmv during interglacial periods (Petit et al., 1999). On the timescales being considered here, these processes are likely to be relevant. These natural variations presumably reflect additional processes and feedbacks within the Earth system that need to be identified and represented in the climate models used.

6.3.2 Extending the GCM modelling and emulation

The predictive capability of the emulator could be improved and the range of questions that it could be used to address could be extended if a wider range of ice sheet extents was used. In the current version, the experiment ensembles were run with modern-day and reduced (Pliocene) ice sheet configurations only, meaning that projections of past and future climate include the assumption that the ice sheets do not significantly increase in size relative to the present day. It was shown in Chapter 3 that reducing the size of the ice sheets from their modern-day extents only had a relatively small impact on SAT, and that the majority of this change was limited to regions in close proximity to the ice sheets. However, on timescales of a million years the ice sheets would be expected to vary in size significantly, particularly in response to high levels of anthropogenic CO_2 emissions (that might result in a substantial reduction in the size of the EAIS) and as a result of glacial-interglacial cycles.

One way to extend the range of ice sheet configurations considered, which is currently being undertaken in the framework of a project funded by Posiva and SKB, is to run an ensemble of simulations using HadCM3 with prescribed ice sheet extents varying between their maximum and minimum extents as seen since the LGM. Peltier (2004), for example, developed the ICE-5G ice sheet reconstructions for the last ~120 kyr that have been used in a number of studies to produce sets of simulations with varying ice sheet extents (e.g. Singarayer and Valdes, 2010, Araya-Melo et al., 2015). In fact, Araya-Melo et al. (2015) developed a statistical emulator similar to the one presented in this thesis, but with five input dimensions – the four included here plus an index value for ice sheet volume. Including a wide range of ice sheet configurations as an active input parameter to the emulator would allow improved emulation of climate during periods when the ice sheets would be expected to have changed in size, such as extreme global warming scenarios. It would also mean that it may be possible to emulate variations between glacial and interglacial conditions.

In Chapters 4 and 5, the GCM experiments with atmospheric CO_2 concentrations higher than ~2000 ppmv showed evidence of runaway warming which, in the very high CO_2 experiments, resulted in the model crashing before completion. This runaway warming was assumed to be the result of a property in the GCM, related to the prescribed distribution of atmospheric ozone, and therefore not representative of the real world. Future work could test the validity of this assumption, by running the high CO_2 simulations using HadCM3 or an alternative climate model but with a vertical ozone profile that is updated in response to changes in climate. If it is found that the runaway warming does not occur with a variable ozone profile,

then the assumption that the runaway warming was an error in the model is correct. If the warming is still evident, then further research into non-linear warming at high CO_2 concentrations may be required.

In this thesis, only changes in annual mean climate have been explored. The emulator could be used further to investigate long-term seasonal or monthly variations, by calibrating it on these GCM data. This may be of interest in the case of radioactive waste repositories for which climate conditions occurring at specific times in the year are particularly relevant to long-term safety. Examples may include seasonal climate conditions at high northern latitudes and their impact on the formation and melting of permafrost, or summer temperature and precipitation changes in lower latitude regions that are vulnerable to desertification. This extension to the emulator may also applicable to modelling seasonal climate phenomena such as monsoons.

6.3.3 Further tailoring of the climate change data for use in PCPAs

Work could be carried out to further tailor the climate change data produced by the emulator for use in post-closure performance assessments. An example of this would be to increase the spatial and/or temporal resolution of the data. Downscaling techniques could be used to produce regional or local scale data, rather than grid-box scale. This could be done using statistical downscaling, or by dynamical downscaling by running a RCM for a particular region forced by the climate data generated by the emulator. These downscaling methods can also be used to increase the temporal resolution of the data. Such data may be of use in performance assessments, as input to site-specific models that require data of a high spatial and/or temporal resolution, including landscape, infiltration and permafrost models.

Climatic phenomena that are of particular interest at specific disposal sites could also be investigated by developing the emulator further. For example, for sites at high northern latitudes in regions that have previously been glaciated, such as Forsmark, Sweden, the initiation of the next glaciation is of particular relevance. The timing of glacial inception is important, as well as the severity of the glaciation, including the development and characteristics of a European ice sheet and depth and extent of permafrost. Extending the emulator further to include variable ice sheet extents as an input parameter, as discussed in the previous section, could allow investigation of issues such as these. In contrast, at the Yucca Mountain site, changes in the frequency and intensity of extreme precipitation events are of particular relevance. The emulator

could therefore be developed to allow exploration of climate changes that are of specific interest at individual sites.

6.3.4 Repeating the methodology with other models

Finally, the methodology presented here could be repeated with a variety of other models. This includes the CO_2 simulations from Chapter 2, which could be run using other EMICs that include a representation of the long-term carbon cycle, such as the LOVECLIM model (Goosse et al., 2010) or the University of Victoria (UVic) model (Weaver et al., 2001). The ensembles of HadCM3 simulations could also be repeated using different GCMs, and the emulator recalibrated on this data.

Using a range of models allows an increased understanding of the uncertainties associated with the model projections. These include conceptual uncertainties, which can be observed in the different ways in which the models are structured, and parameter uncertainties, expressed through the parameterization of certain processes in each model and the choice of parameter values that are used. Boundary conditions are also uncertain, and, in particular, for future climate projections, the total amount of anthropogenic CO_2 that will be emitted. This has been addressed in this thesis by simulating a large range of CO_2 scenarios varying from relatively low emissions up to very high bounding-scenario emissions. To account for model uncertainty, ensembles of models are often used for projecting past and future climates (where time and computational resources permit), for both snapshot and transient simulations (Braconnot et al., 2007, Archer et al., 2009, IPCC, 2013, Taylor et al., 2012, Friedlingstein et al., 2006). Repeating the methodology presented in this thesis with a larger range of models would allow the model uncertainties to be better understood, and therefore increase our confidence in the climate changes projections.

APPENDICES

The contents of these appendices have been published as Supplementary Information to the study by Lord et al. (2016). The material here is identical to that in the Supplementary Information of the published paper, except that the figures and tables have been renumbered so as to be consistent with the main thesis.

Appendix A

Acceleration module

Despite the choice of an Earth system model configuration with a relatively low horizontal and vertical resolution in the ocean, simulation of 1 Myr of CO_2 decay would still take approximately ~60 days on a typical single CPU core. While this computational requirement situation is not technically prohibitive, it does tend to steer modelling towards a methodology of one-off experiments to make a single projection, rather than a more iterative methodology involving running a model experiment, analysing and learning from the results, and then revising the experimental design and output, and repeating. For global biogeochemical systems that stabilise on much longer timescales, for example lithium (~1 Myr (Huh et al., 1998)) or calcium (0.5-1.0 Myr (Fantle and Tipper, 2014)) isotopes, or perhaps a carbon cycle state with a much higher initial concentration of atmospheric CO_2 and ocean DIC, the required run-time (to simulate >>1 Myr) would be prohibitive.

Berner et al. (1983) and Lasaga et al. (1985) recognised that on longer timescales the oceans may be considered to be approximately in steady state with respect to the longer-term rock cycles. This insight is made use of here by recognizing that during the last 90% or more of this time interval, the only significant dynamical process relates to the imbalance between enhanced rates of silicate weathering and CO_2 out-gassing and burial of $CaCO_3$ in marine sediments. Furthermore, for much of the first 100 kyr after emissions cease, imbalances between total (including carbonate) weathering and sedimentation dominate the dynamics of

atmospheric CO_2 drawdown (Ridgwell and Hargreaves, 2007) rather than CO_2 drawdown being rate-limited by ocean transport and air-sea gas exchange. A corollary to the long timescales of these processes is that the rate of atmospheric CO_2 removal and hence changes in climate and ocean circulation will be extremely gradual over much of the total (ca. 1 Myr) interval of CO_2 removal. In the situation of a virtually invariant state of ocean transport and climate, there will be no change in nutrient supply to the ocean surface. Hence, biological export production and consequential remineralisation and release of nutrients and other dissolved tracers in the ocean interior should be invariant, as should rates and patterns of air-sea gas exchange. As the distribution of dissolved tracers in the ocean is primarily a function of the above processes (and ocean circulation), it follows that gradients of dissolved carbon, alkalinity, nutrients etc. will also be invariant. The impact of any imbalance between the products of weathering and sedimentation will hence, to first-order, be a change in the mean concentrations of DIC and ALK (and Ca^{2+}), rather than any change in their gradients in the ocean.

The tendency for there to be a timescale separation between processes controlling tracer gradients in the ocean vs. mean concentration forms the basis for a new module in *c*GENIE. In this, for any given time-step, *c*GENIE treats the ocean as a single box, solving explicitly for weathering and sedimentation on the model grid and then applying the mass difference uniformly throughout the ocean (preserving the tracer gradients). Because changes in DIC and ALK (and $[Ca^{2+}]$) will generally affect the value of atmospheric pCO_2, the equilibrium partitioning of CO_2 between ocean and atmosphere is re-calculated and carbon is re-distributed between the ocean and atmosphere accordingly.

Even very slow changes in atmospheric CO_2 will eventually lead to appreciable changes in surface temperatures and ocean circulation. Hence *c*GENIE is switched between intervals of accelerated and non-accelerated operation, with the time interval over which the model is either in accelerated or non-accelerated mode set to an integer multiple of one year in order to allow for seasonally-varying model configurations to be used. By doing this, the overall model is sped up whilst ensuring that climate and carbon cycle conditions do not stray too far from those that would be projected by a full implementation of the *c*GENIE model when CO_2 changes are slow. For long timescale problems of isotopic (e.g. δ^7Li, $\delta^{44}Ca$) equilibrium of the ocean, alternating between e.g. intervals of >900 years accelerated to <100 years non-accelerated computation for a system with an already equilibrated climate and ocean circulation produces a result virtually indistinguishable from the full model on timescales of 1 Myr. The situation in this thesis is more challenging as changes in climate and CO_2 uptake by the ocean are initially rapid, and only subsequently gradually decline to a very gradual adjustment of weathering vs. sedimentation.

Therefore, the ratio between accelerated and non-accelerated is allowed to start small (i.e. an iteration in which non-accelerated running dominates) and then progressively increase until each iteration is instead dominated by an accelerated phase. This is discussed in greater detail below.

The above reasoning and hence ability to accelerate the simulation of the long tail of atmospheric CO_2 would be somewhat less applicable if a full geological organic carbon sub-cycle was included that allowed for the weathering supply of phosphorous to the ocean (a key phytoplankton nutrient and hence a master control on biological productivity and export), nor potentially if a full marine nitrogen cycle had been included (depending on the timescale to re-establish balance between nitrogen fixation and denitrification relative to CO_2 changes). A highly simplified model configuration has also been adopted, with no seasonal forcing and hence no seasonality in ocean circulation. If instead a seasonally-varying forcing had been adopted, the above arguments still hold, because with an energy-balance based atmosphere in *c*GENIE there is no inter-annual variability and the mean annual transport will still be invariant for the case of an unchanging value of atmospheric CO_2. Fully coupled GCMs would simply require a rather longer averaging period than annual in order to determine the mean ocean transport.

Appendix B

CO_2 scenarios to test the acceleration methodology

In addition to the two sets of experiments described in the main paper, a third set of experiments was also performed to assess the performance of the acceleration methodology against the full non-accelerated *c*GENIE model. For these, an historical transient experiment was conducted in which the model was forced following observed historical atmospheric CO_2 concentrations from 1750 to year 2010 CE (Meinshausen et al., 2011). The scenarios (Table A1) then followed the six illustrative scenarios of the IPCC Special Report on Emissions Scenarios (SRES) (Nakićenović and Swart, 2000) between year 2010 and 2100 CE. Emissions were then held constant at their year 2100 CE rate until 2200 CE, before being set as linearly declining to zero by year 2300 CE, resulting in total emissions ranging from ~1,500 PgC for B1 to ~6,300 PgC for A1F1 (Figure A1b). Each emissions scenario was then run under a series of different gearing ratios between non-accelerated and accelerated phases, summarised in Table A1 and including fully non-accelerated as a reference for the acceleration methodology.

Table A1. Summary of initial standard and accelerated ("_gl") cGENIE SRES model experiments. See Section A1 for full explanation of accelerated time-stepping configuration.

Experiment	Total emissions (PgC)	Release period (yr)	Model setup	Accelerated time-stepping configuration		
				Phase duration: standard/accelerated (yr)	Change in phase duration each cycle (yr)	Running speed (model years per CPU hour)
B1	1454	2010-2300	Standard	-	-	~700
A1F1	6259	2010-2300	Standard	-	-	”
B1_gl_a	1454	2010-2300	Accelerated	990/10 → 10/990	1	~800
A1F1_gl_a	6259	2010-2300	Accelerated	”	”	”
B1_gl_b	1454	2010-2300	Accelerated	990/10 → 10/990	10	~5300
A1F1_gl_b	6259	2010-2300	Accelerated	”	”	”
B1_gl_c	1454	2010-2300	Accelerated	990/10 → 100/900	10	~3000
A1F1_gl_c	6259	2010-2300	Accelerated	”	”	”
B1_gl_d	1454	2010-2300	Accelerated	990/10 → 10/90	10	~3000
A1F1_gl_d	6259	2010-2300	Accelerated	”	”	”

Appendix C

Performance of acceleration methodology

The time-histories of CO_2 emissions for the two time-dependent SRES emissions scenarios (A1F1 and B1) are shown in Figure A1b, for which emissions were released over ~300 years (year 2010-2300). These scenarios were used to evaluate the acceleration methodology. The CO_2 anomalies in the accelerated simulations compared with the equivalent standard simulation (Figure A2a) are illustrated in Figures A2b to A2e. The anomalies are small when compared with the CO_2 data from the standard model, with maximum residuals of around 6 ppmv (A1F1_gl_c), although they are generally less than 4 ppmv. All four different configurations of non-accelerated vs. accelerated running exhibited similar trends in anomalies, although the magnitude and duration varied. The relatively small magnitude of the anomalies relative to the CO_2 residual itself (< 2%) gives us confidence that the primary timescale of CO_2 decay can be successfully extracted from accelerated model pulse-decay experiments.

During accelerated periods, the uptake of excess CO_2 from the atmosphere tends to slow down, causing increased positive anomalies. This is due to changes in ocean conditions that affect the amount of CO_2 absorbed by the ocean, including the strength of the ocean overturning circulation and the flux of nutrients to and from the ocean due to variations in weathering and sedimentation. Since accelerated model time-steps assume that circulation and nutrient gradients are invariant, these gradual changes are only applied and updated during “normal”

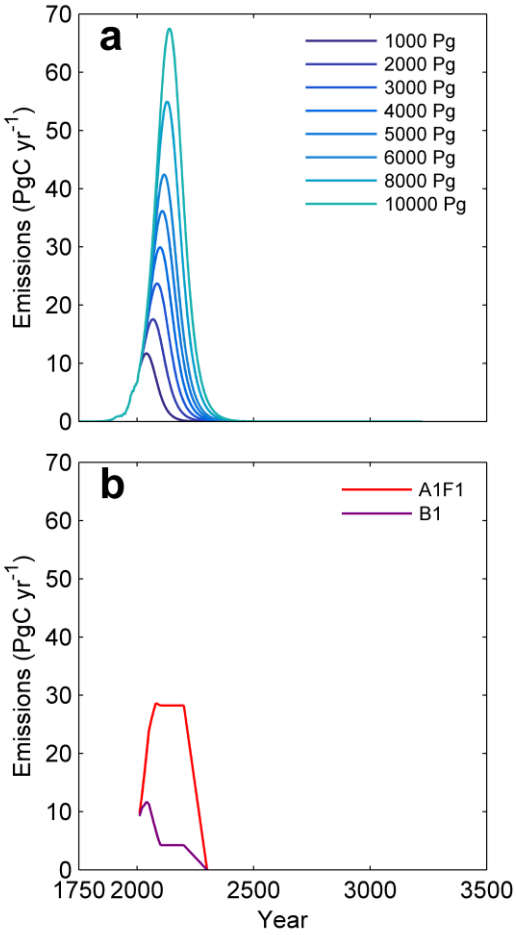

Figure A1. Time-history of anthropogenic CO_2 emissions to the atmosphere. (a) Logistics series (Table 2.1), and (b) SRES scenarios (Table A1).

phases, meaning that CO_2 draw-down is generally slower during accelerated periods. The anomalies in the last few hundred thousand years are likely due to instabilities in sea-ice cover, with generally somewhat lower coverage in the accelerated experiments over this period allowing slightly increased drawdown of CO_2.

Configuration "_a" results in the smallest anomalies overall, due to the comparatively small size of the change in phase length with each cycle of 1 year, resulting in a larger portion of the simulation being run with normal time-stepping comprising the majority of each cycle. However, this also means that this model configuration is not significantly faster than the standard *c*GENIE model when compared with the other configurations, so limiting its usefulness. Configurations "_b" and "_c" have exactly the same time-stepping and hence anomalies until around 93 kyr. After this time, "_b" has the greater anomalies due to normal time-stepping making up a smaller fraction of each cycle. Configuration "_d" reaches its final phase lengths at

around 60 kyr, resulting in slightly larger and extended anomalies than "_c" between 60 and 200 kyr.

Configuration "_b" provides the greatest reduction in running time; however it also has the largest residuals, particularly during the period of instability towards the end. Configurations "_c" and "_d" have fairly similar anomalies and running times, but "_c" has a slightly lower root mean squared error (RMSE). The ensembles of pulse emissions and SRES experiments are therefore run with a non-accelerated vs. accelerated sequence that started with a ratio of 990:10 years, and progressed towards a non-accelerated vs. accelerated sequence ratio of 100:990 years at a rate of 10 years (decremented to the non-accelerated duration, and incremented to the accelerated duration) per 1000 yr long cycle (configuration "_c").

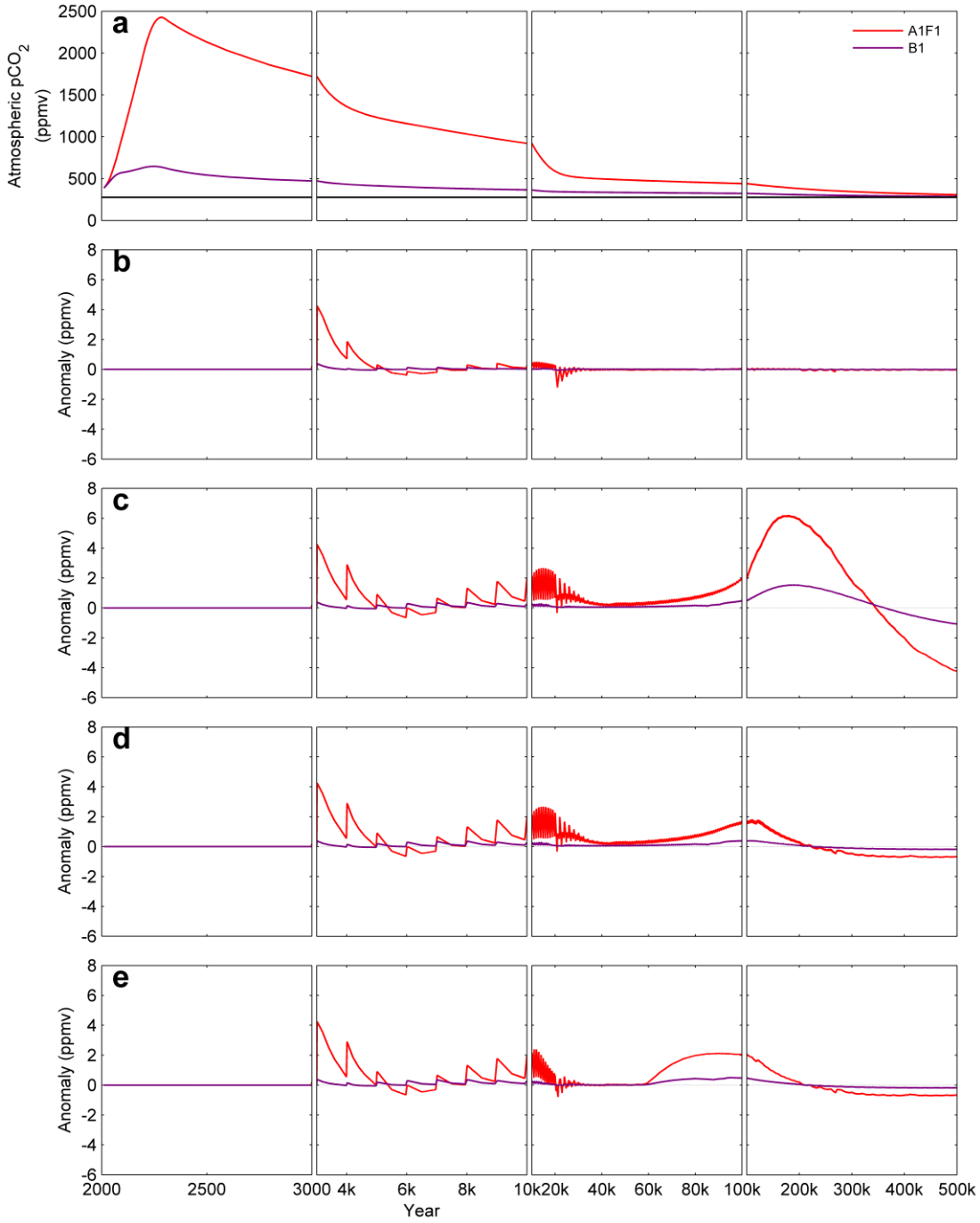

Figure A2. Atmospheric pCO_2 in response to time-dependent CO_2 emissions. (a) Long-term projection of atmospheric pCO_2 run in standard cGENIE model. Pre-industrial concentrations are shown in black. (b):(e) Anomaly in atmospheric pCO_2 in accelerated simulations (experiments "_a", "_b", "_c" and "_d" in Table A1 compared to cGENIE control simulations.

Appendix D

Fraction of emissions remaining over time

A regression analysis was performed to give the fraction of CO_2 emissions remaining in the atmosphere at 10^3, 10^4, 10^5 and 10^6 years as a function of the total emissions (Pg C) released to the atmosphere. Linear, quadratic and cubic functions were tested, and an F Test was used to assess the performance of each fit. The cubic model was identified as the best fit, significant at the 0.05 level. Consequently, the cubic regression model was used for the results described in Chapter 2 Section 2.4.1, which uses the formula:

$$fCO_2(u,t) = \varepsilon(t) + \lambda_1(t)\mu + \lambda_2(t)\mu^2 + \lambda_3(t)\mu^3 \qquad (A1)$$

where fCO_2 is the remaining atmospheric fraction and μ is the total carbon released at time 0 at the start of year 1 (Pg C). The cubic coefficient values are given in Table A2.

Table A2. Cubic regression scaling coefficients for fraction of CO_2 emissions remaining in the atmosphere at a given year as a function of total emissions (Pg C) (Equation A1; Appendix).

Parameter	*t* (Year)			
	10^3	10^4	10^5	10^6
ε	0.0991	0.0641	0.0496	0.0016
λ_1	6.64E-05	8.07E-06	-5.98E-07	1.24E-07
λ_2	-2.49E-09	1.52E-09	1.35E-10	-1.83E-11
λ_3	3.26E-14	-5.66E-14	-3.77E-15	5.70E-16

Appendix E

Additional figures and tables

Table A3. Cubic regression scaling coefficients for fitting coefficients from multi-exponential analysis as a function of total emissions (PgC) (Equations 2.4 and 2.5 of Chapter 2).

Fitting Coefficient	Parameter	*i*				
		1	2	3	4	5
A_i	α_i	0.253	0.245	0.312	0.079	0.075
	$\beta 1_i$	-4.63E-05	-3.54E-05	5.00E-05	3.96E-05	-8.57E-07
	$\beta 2_i$	3.44E-09	2.40E-09	-5.87E-09	-4.83E-10	5.89E-11
	$\beta 3_i$	-8.42E-14	-5.57E-14	1.65E-13	-1.46E-14	-1.15E-15
τ_i	γ_i	6.28	58.7	112.6	2780	246294
	$\delta 1_i$	-1.05E-03	-2.99E-03	0.121	0.816	0.450
	$\delta 2_i$	6.90E-08	6.15E-08	-7.87E-06	6.29E-06	2.55E-04
	$\delta 3_i$	-1.49E-12	1.69E-12	1.86E-10	-7.27E-10	-9.69E-09

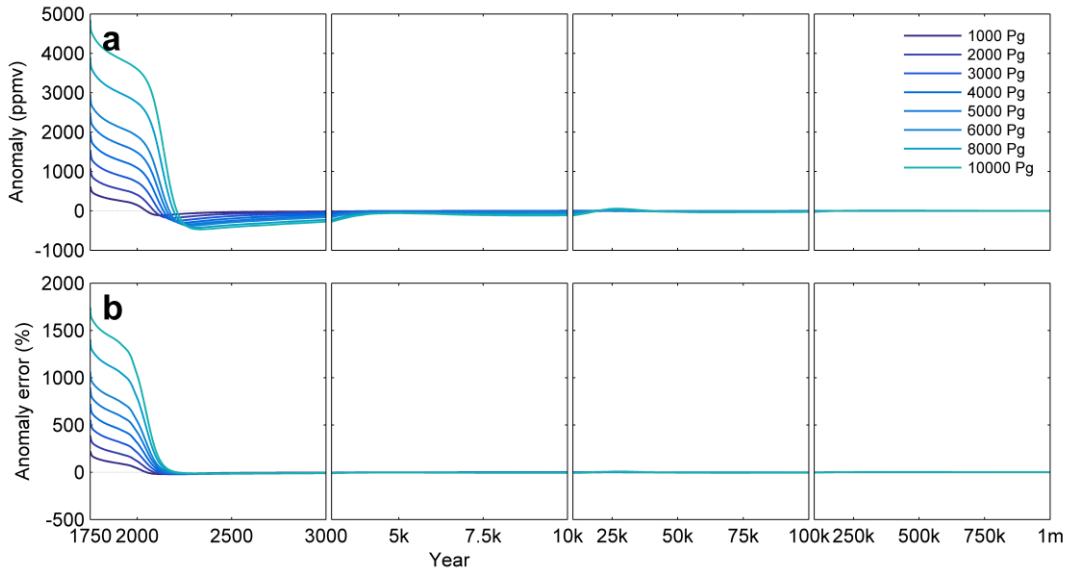

Figure A3. Logistics series scenarios for 1000-10,000 Pg C total emissions reproduced using the pulse response function (Equation 2.4 of Chapter 2). (a) Initial pCO_2 anomaly. (b) Initial pCO_2 anomaly error.

BIBLIOGRAPHY

ANDREWS, T., GREGORY, J. M. & WEBB, M. J. 2015. The dependence of radiative forcing and feedback on evolving patterns of surface temperature change in climate models. *Journal of Climate,* 28 (4), 1630-1648, DOI: 10.1175/Jcli-D-14-00545.1.

ANDREWS, T., GREGORY, J. M., WEBB, M. J. & TAYLOR, K. E. 2012. Forcing, feedbacks and climate sensitivity in CMIP5 coupled atmosphere-ocean climate models. *Geophysical Research Letters,* 39 L09712, DOI: 10.1029/2012gl051607.

ANDRIANAKIS, I. & CHALLENOR, P. G. 2012. The effect of the nugget on Gaussian process emulators of computer models. *Computational Statistics & Data Analysis,* 56 (12), 4215-4228, DOI: 10.1016/j.csda.2012.04.020.

ARAYA-MELO, P. A., CRUCIFIX, M. & BOUNCEUR, N. 2015. Global sensitivity analysis of the Indian monsoon during the Pleistocene. *Climate of the Past,* 11 (1), 45-61, DOI: 10.5194/cp-11-45-2015.

ARCHER, D. 2005. Fate of fossil fuel CO_2 in geologic time. *Journal of Geophysical Research-Oceans,* 110 C09S05, DOI: 10.1029/2004jc002625.

ARCHER, D. & BROVKIN, V. 2008. The millennial atmospheric lifetime of anthropogenic CO_2. *Climatic Change,* 90 (3), 283-297, DOI: 10.1007/s10584-008-9413-1.

ARCHER, D., EBY, M., BROVKIN, V., RIDGWELL, A., CAO, L., MIKOLAJEWICZ, U., CALDEIRA, K., MATSUMOTO, K., MUNHOVEN, G., MONTENEGRO, A. & TOKOS, K. 2009. Atmospheric lifetime of fossil fuel carbon dioxide. *Annual Review of Earth and Planetary Sciences,* 37, 117-134, DOI: 10.1146/annurev.earth.031208.100206.

ARCHER, D. & GANOPOLSKI, A. 2005. A movable trigger: Fossil fuel CO_2 and the onset of the next glaciation. *Geochemistry Geophysics Geosystems,* 6 (5), Q05003, DOI: 10.1029/2004gc000891.

ARCHER, D., KHESHGI, H. & MAIER-REIMER, E. 1997. Multiple timescales for neutralization of fossil fuel CO_2. *Geophysical Research Letters,* 24 (4), 405-408, DOI: 10.1029/97gl00168.

ARCHER, D., KHESHGI, H. & MAIER-REIMER, E. 1998. Dynamics of fossil fuel CO_2 neutralization by marine $CaCO_3$. *Global Biogeochemical Cycles,* 12 (2), 259-276, DOI: 10.1029/98gb00744.

ARMOUR, K. C., BITZ, C. M. & ROE, G. H. 2013. Time-Varying Climate Sensitivity from Regional Feedbacks. *Journal of Climate,* 26 (13), 4518-4534, DOI: 10.1175/Jcli-D-12-00544.1.

ARMSTRONG, E., VALDES, P., HOUSE, J. & SINGARAYER, J. 2016. The role of CO_2 and dynamic vegetation on the impact of temperate land-use change in the HadCM3 coupled climate model. *Earth Interactions,* 20 10, 1-20, DOI: 10.1175/Ei-D-15-0036.1.

BADGER, M. P. S., SCHMIDT, D. N., MACKENSEN, A. & PANCOST, R. D. 2013. High-resolution alkenone palaeobarometry indicates relatively stable pCO_2 during the Pliocene (3.3-2.8 Ma). *Philosophical Transactions of the Royal Society a-Mathematical Physical and Engineering Sciences,* 371 (2001), 20130094, DOI: 10.1098/rsta.2013.0094.

BAINS, S., NORRIS, R. D., CORFIELD, R. M. & FAUL, K. L. 2000. Termination of global warmth at the Palaeocene/Eocene boundary through productivity feedback. *Nature,* 407 (6801), 171-174, DOI: 10.1038/35025035.

BAMBER, J. L., RIVA, R. E. M., VERMEERSEN, B. L. A. & LEBROCQ, A. M. 2009. Reassessment of the potential sea-level rise from a collapse of the West Antarctic ice sheet. *Science,* 324 (5929), 901-903, DOI: 10.1126/science.1169335.

BARTOLI, G., HONISCH, B. & ZEEBE, R. E. 2011. Atmospheric CO_2 decline during the Pliocene intensification of Northern Hemisphere glaciations. *Paleoceanography,* 26 Pa4213, DOI: 10.1029/2010pa002055.

BASTOS, L. S. & O'HAGAN, A. 2009. Diagnostics for Gaussian Process Emulators. *Technometrics,* 51 (4), 425-438, DOI: 10.1198/Tech.2009.08019.

BECKER, J. K., LINDBORG, T. & THORNE, M. 2014. Influence of climate on landscape characteristics in safety assessments of repositories for radioactive wastes. *Journal of Environmental Radioactivity,* 138**,** 192-204.

BERGER, A. 1978. Long-term variations of daily insolation and Quaternary climatic changes. *Journal of the Atmospheric Sciences,* 35 (12)**,** 2362-2367**,** DOI: 10.1175/1520-0469(1978)035<2362:Ltvodi>2.0.Co;2.

BERGER, A. & LOUTRE, M. F. 1991. Insolation Values for the Climate of the Last 10000000 Years. *Quaternary Science Reviews,* 10 (4)**,** 297-317**,** DOI: 10.1016/0277-3791(91)90033-Q.

BERGER, A. & LOUTRE, M. F. 1996. Modelling the climate response to astronomical and CO_2 forcings. *Comptes Rendus De L Academie Des Sciences Serie Ii Fascicule a-Sciences De La Terre Et Des Planetes,* 323 (1)**,** 1-16.

BERGER, A. & LOUTRE, M. F. 2002. An exceptionally long interglacial ahead? *Science,* 297 (5585)**,** 1287-1288**,** DOI: 10.1126/science.1076120.

BERGER, A., LOUTRE, M. F. & CRUCIFIX, M. 2003. The Earth's climate in the next hundred thousand years (100 kyr). *Surveys in Geophysics,* 24 (2)**,** 117-138**,** DOI: 10.1023/A:1023233702670.

BERGER, J. O., DE OLIVEIRA, V. & SANSO, B. 2001. Objective Bayesian analysis of spatially correlated data. *Journal of the American Statistical Association,* 96 (456)**,** 1361-1374**,** DOI: 10.1198/016214501753382282.

BERNER, R. A. 1990. Atmospheric Carbon-Dioxide Levels over Phanerozoic Time. *Science,* 249 (4975)**,** 1382-1386**,** DOI: 10.1126/science.249.4975.1382.

BERNER, R. A. 1991. A Model for Atmospheric CO_2 over Phanerozoic Time. *American Journal of Science,* 291 (4)**,** 339-376**,** DOI: 10.2475/ajs.291.4.339.

BERNER, R. A. 1994. 3GEOCARB II - a Revised Model of Atmospheric CO_2 over Phanerozoic Time. *American Journal of Science,* 294 (1)**,** 56-91**,** DOI: 10.2475/ajs.294.1.56.

BERNER, R. A. 1999. A new look at the long-term carbon cycle. *GSA Today,* 9 (11)**,** 1-6.

BERNER, R. A. & CALDEIRA, K. 1997. The need for mass balance and feedback in the geochemical carbon cycle. *Geology,* 25 (10)**,** 955-956**,** DOI: 10.1130/0091-7613(1997)025.

BERNER, R. A., LASAGA, A. C. & GARRELS, R. M. 1983. The Carbonate-Silicate Geochemical Cycle and Its Effect on Atmospheric Carbon-Dioxide over the Past 100 Million Years. *American Journal of Science,* 283 (7)**,** 641-683**,** DOI: 10.2475/ajs.283.7.641.

BIOCLIM 2001. Deliverable D3: Global climatic features over the next million years and recommendation for specific situations to be considered, Agence Nationale pour la Gestion des Dechets Radioactifs (ANDRA), Parc de la Croix Blanche, 1/7 rue Jean Monnet, 92298, Châtenay-Malabry, France. Available from: www.andra.fr/bioclim/pdf/d3.pdf.

BIOCLIM 2003a. Deliverable D4/5: Global climatic characteristics, including vegetation and seasonal cycles over Europe, for snapshots over the next 200,000 years, Agence Nationale pour la Gestion des Dechets Radioactifs (ANDRA), Parc de la Croix Blanche, 1/7 rue Jean Monnet, 92298, Châtenay-Malabry, France. Available from: www.andra.fr/bioclim/pdf/d45.pdf.

BIOCLIM 2003b. Deliverable D6a: Regional climatic characteristics for the European sites at specific times: The dynamical downscaling, Agence Nationale pour la Gestion des Dechets Radioactifs (ANDRA), Parc de la Croix Blanche, 1/7 rue Jean Monnet, 92298, Châtenay-Malabry, France. Available from: www.andra.fr/bioclim/pdf/d6a.pdf.

BOSMANS, J. H. C., DRIJFHOUT, S. S., TUENTER, E., HILGEN, F. J. & LOURENS, L. J. 2015. Response of the North African summer monsoon to precession and obliquity forcings in the EC-Earth GCM. *Climate Dynamics,* 44 (1-2)**,** 279-297**,** DOI: 10.1007/s00382-014-2260-z.

BOUNCEUR, N., CRUCIFIX, M. & WILKINSON, R. D. 2015. Global sensitivity analysis of the climate-vegetation system to astronomical forcing: an emulator-based approach. *Earth System Dynamics,* 6**,** 205-224**,** DOI: 10.5194/esd-6-205-2015.

BRACONNOT, P., OTTO-BLIESNER, B., HARRISON, S., JOUSSAUME, S., PETERCHMITT, J. Y., ABE-OUCHI, A., CRUCIFIX, M., DRIESSCHAERT, E., FICHEFET, T., HEWITT, C. D., KAGEYAMA, M., KITOH, A., LAINE, A., LOUTRE, M. F., MARTI, O., MERKEL, U., RAMSTEIN, G., VALDES, P., WEBER, S. L., YU, Y. & ZHAO, Y. 2007. Results of PMIP2 coupled simulations of the Mid-Holocene and Last Glacial Maximum - Part 1: experiments and large-scale features. *Climate of the Past,* 3 (2)**,** 261-277.

BRADY, P. V. 1991. The Effect of Silicate Weathering on Global Temperature and Atmospheric CO_2. *Journal of Geophysical Research-Solid Earth,* 96 (B11)**,** 18101-18106**,** DOI: 10.1029/91jb01898.

BRANDEFELT, J., NÄSLUND, J.-O., ZHANG, Q. & HARTIKAINEN, J. 2013. The potential for cold climate and permafrost in Forsmakr in the next 60,000 years, *SKB Report,* Svensk Kärnbränslehantering AB, Stockholm, Sweden. TR-13-04. Available from: www.skb.com/publication/2652151/TR-13-04.pdf.

BROECKER, W. S. 1998. Paleocean circulation during the last deglaciation: A bipolar seesaw? *Paleoceanography,* 13 (2)**,** 119-121**,** DOI: 10.1029/97pa03707.

CALDEIRA, K. & WICKETT, M. E. 2005. Ocean model predictions of chemistry changes from carbon dioxide emissions to the atmosphere and ocean. *Journal of Geophysical Research-Oceans,* 110 (C9), C09s04**,** DOI: 10.1029/2004jc002671.

CALEY, T., MALAIZE, B., REVEL, M., DUCASSOU, E., WAINER, K., IBRAHIM, M., SHOEAIB, D., MIGEON, S. & MARIEU, V. 2011. Orbital timing of the Indian, East Asian and African boreal monsoons and the concept of a 'global monsoon'. *Quaternary Science Reviews,* 30 (25-26)**,** 3705-3715**,** DOI: 10.1016/j.quascirev.2011.09.015.

CAO, L., EBY, M., RIDGWELL, A., CALDEIRA, K., ARCHER, D., ISHIDA, A., JOOS, F., MATSUMOTO, K., MIKOLAJEWICZ, U., MOUCHET, A., ORR, J. C., PLATTNER, G. K., SCHLITZER, R., TOKOS, K., TOTTERDELL, I., TSCHUMI, T., YAMANAKA, Y. & YOOL, A. 2009. The role of ocean transport in the uptake of anthropogenic CO_2. *Biogeosciences,* 6 (3)**,** 375-390**,** DOI: 10.5194/bg-6-375-2009.

CAYAN, D., TYREE, M., KUNKEL, K. E., CASTRO, C., GERSHUNOV, A., BARSUGLI, J., RAY, A. J., OVERPECK, J., ANDERSON, M., RUSSELL, J., RAJAGOPALAN, B., RANGWALA, I. & DUFFY, P. 2013. Future Climate: Projected Average. *In:* GARFIN, G., JARDINE, A., MERIDETH, R., BLACK, M. & LEROY, S. (eds.) *Assessment of Climate Change in the Southwest United States: A Report Prepared for the National Climate Assessment.* Washington, DC: Island Press.

CHARBIT, S., PAILLARD, D. & RAMSTEIN, G. 2008. Amount of CO_2 emissions irreversibly leading to the total melting of Greenland. *Geophysical Research Letters,* 35 L12503**,** DOI: 10.1029/2008gl033472.

CHIKAMOTO, M. O., MATSUMOTO, K. & RIDGWELL, A. 2008. Response of deep-sea CaCO3 sedimentation to Atlantic meridional overturning circulation shutdown. *Journal of Geophysical Research-Biogeosciences,* 113 G03017**,** DOI: 10.1029/2007jg000669.

CHRISTENSEN, J. H., KRISHNA KUMAR, K., ALDRIAN, E., AN, S. I., CAVALCANTI, I. F. A., DE CASTRO, M., DONG, W., GOSWAMI, P., HALL, A., KANYANGA, J. K., KITOH, A., KOSSIN, J., LAU, N.-C., RENWICK, J., STEPHENSON, D. B., XIE, S.-P. & ZHOU, T. 2013. Climate phenomena and their relevance for future regional climate change. *In:* STOCKER, T. F., QIN, D., PLATTNER, G. K., TIGNOR, M., ALLEN, S. K., BOSCHUNG, J., NAUELS, A., XIA, Y., BEX, V. & MIDGLEY, P. M. (eds.) *Climate Change 2013: The Physical Science Basis. Contribution of Working Group I to the Fifth Assessment Report of the Intergovernmental Panel on Climate Change.* Cambridge, UK and New York, NY, USA: Cambridge University Press.

CIAIS, P., SABINE, C., BALA, G., BOPP, L., BROVKIN, V., CANADELL, J., CHHABRAM, A., DEFRIES, R., GALLOWAY, J., HEIMANN, M., JONES, C., LE QUERE, C., MYNENI, R. B., PIAO, S. & THORNTON, P. 2013. Carbon and Other Biogeochemical Cycles. *In:* STOCKER, T. F., QIN, D., PLATTNER, G. K., TIGNOR, M., ALLEN, S. K., BOSCHUNG, J., NAUELS, A., XIA, Y., BEX, V. & MIDGLEY, P. M. (eds.) *Climate Change 2013: The Physical Science Basis. Contribution of Working Group I to the Fifth Assessment Report of the Intergovernmental Panel on Climate Change.* Cambridge, UK and New York, USA: Cambridge University Press, pp. ISBN.

CLARK, P. U., SHAKUN, J. D., MARCOTT, S. A., MIX, A. C., EBY, M., KULP, S., LEVERMANN, A., MILNE, G. A., PFISTER, P. L., SANTER, B. D., SCHRAG, D. P., SOLOMON, S., STOCKER, T. F., STRAUSS, B. H., WEAVER, A. J., WINKELMANN, R., ARCHER, D., BARD, E., GOLDNER, A., LAMBECK, K., PIERREHUMBERT, R. T. & PLATTNER, G. K. 2016. Consequences of twenty-first-century policy for multi-millennial climate and sea-level change. *Nature Climate Change,* 6 (4)**,** 360-369**,** DOI: 10.1038/Nclimate2923.

COCHELIN, A. S. B., MYSAK, L. A. & WANG, Z. M. 2006. Simulation of long-term future climate changes with the green McGill paleoclimate model: The next glacial inception. *Climatic Change,* 79 (3-4)**,** 381-401**,** DOI: 10.1007/s10584-006-9099-1.

COLBOURN, G. 2011. *Weathering effects on the carbon cycle in an Earth System Model.* PhD Thesis, University of East Anglia, UK.

COLBOURN, G., RIDGWELL, A. & LENTON, T. 2015. The time scale of the silicate weathering negative feedback on atmospheric CO_2. *Global Biogeochemical Cycles,* 29 (5)**,** 583-596**,** DOI: 10.1002/2014GB005054.

COLBOURN, G., RIDGWELL, A. & LENTON, T. M. 2013. The Rock Geochemical Model (RokGeM) v0.9. *Geoscientific Model Development,* 6 (5)**,** 1543-1573**,** DOI: 10.5194/gmd-6-1543-2013.

COLLINS, M., KNUTTI, R., ARBLASTER, J. M., DUFRESNE, J. L., FICHEFET, T., FRIEDLINGSTEIN, P., GAO, X., GUTOWSKI, W. J., JOHNS, T., KRINNER, G., SHONGWE, M., TEBALDI, C., WEAVER, A. & WEHNER, M. 2013. Long-term climate change: projections, commitments and irreversibility. *In:* STOCKER, T. F., QIN, D., PLATTNER, G. K., TIGNOR, M., ALLEN, S. K., BOSCHUNG, J., NAUELS, A., XIA, Y., BEX, V. & MIDGLEY, P. M. (eds.) *Climate Change 2013: The Physical Science Basis. Contribution of Working Group I to the Fifth Assessment Report of the Intergovernmental Panel on Climate Change.* Cambridge, UK and New York, NY, USA: Cambridge University Press.

COX, P. M., BETTS, R. A., BUNTON, C. B., ESSERY, R. L. H., ROWNTREE, P. R. & SMITH, J. 1999. The impact of new land surface physics on the GCM simulation of climate and climate sensitivity. *Climate Dynamics,* 15 (3)**,** 183-203**,** DOI: 10.1007/s003820050276.

COX, P. M., BETTS, R. A., JONES, C. D., SPALL, S. A. & TOTTERDELL, I. J. 2000. Acceleration of global warming due to carbon-cycle feedbacks in a coupled climate model. *Nature,* 408 (6809)**,** 184-187**,** DOI: 10.1038/35041539.

COX, P. M., BETTS, R. A., JONES, C. D., SPALL, S. A. & TOTTERDELL, I. J. 2002. Modelling vegetation and the carbon cycle as interactive elements of the climate system. *In:* PEARCE, R. (ed.) *Meteorology at the Millennium.* San Diego CA, USA: Academic Press, 259-279 pp. ISBN.

CRUCIFIX, M., BRACONNOT, P., HARRISON, S. P. & OTTO-BLIESNER, B. 2005. Second phase of paleoclimate modelling intercomparison project. *Eos, Transactions American Geophysical Union,* 86 (28)**,** 264-264**,** DOI: 10.1029/2005EO280003.

CUI, Y., KUMP, L. R., RIDGWELL, A. J., CHARLES, A. J., JUNIUM, C. K., DIEFENDORF, A. F., FREEMAN, K. H., URBAN, N. M. & HARDING, I. C. 2011. Slow release of fossil carbon during the Palaeocene-Eocene Thermal Maximum. *Nature Geoscience,* 4 (7)**,** 481-485**,** DOI: 10.1038/Ngeo1179.

DECC 2014. Implementing geological disposal. A framework for the long-term management of high activity radioactive waste, Department of Energy and Climate Change. White Paper URN 14D/235. Available from: www.gov.uk/government/publications/implementing-geological-disposal.

DECONTO, R. M. & POLLARD, D. 2016. Contribution of Antarctica to past and future sea-level rise. *Nature,* 531 (7596)**,** 591-597**,** DOI: 10.1038/nature17145.

DOE 2002. Final Environmental Impact Statement for a Geologic Repository for the Disposal of Spent Nuclear Fuel and High-Level Radioactive Waste at Yucca Mountain, Nye County, Nevada, *ML032690321,* U.S. Department of Energy, Office of Civilian Radioactive Waste Management, Washington DC. DOE/EIS-0250. Available from: https://energy.gov/sites/prod/files/EIS-0250-FEIS-01-2002_0.pdf.

DOE 2008. Yucca Mountain Repository License Application: Safety Analysis Report, *ML081560400. ML090700817,* U.S. Department of Energy, Office of Civilian Radioactive Waste Management, Las Vegas, Nevada. DOE/RW–0573.

DOWSETT, H. J. 2007. The PRISM palaeoclimate reconstruction and Pliocene sea-surface temperature. *In:* WILLIAMS, M., HAYWOOD, A. M., GREGORY, J. & SCHMIDT, D. N. (eds.) *Deep-time perspectives on climate change: marrying the signal from computer models and biological proxies.* London, UK: Micropalaeontological Society (Special Publication), Geol. Soc., 459-480 pp. ISBN.

DOWSETT, H. J., DOLAN, A., ROWLEY, D., MOUCHA, R., FORTE, A. M., MITROVICA, J. X., POUND, M., SALZMANN, U., ROBINSON, M., CHANDLER, M., FOLEY, K. & HAYWOOD, A. 2016. The PRISM4 (mid-Piacenzian) paleoenvironmental reconstruction. *Climate of the Past,* 12 (7)**,** 1519-1538**,** DOI: 10.5194/cp-12-1519-2016.

DOWSETT, H. J., HAYWOOD, A. M., VALDES, P. J., ROBINSON, M. M., LUNT, D. J., HILL, D., STOLL, D. K. & FOLEY, K. M. 2011. Sea surface temperatures of the mid-Piacenzian Warm Period: A comparison of PRISM3 and HadCM3. *Palaeogeography Palaeoclimatology Palaeoecology,* 309 (1-2)**,** 83-91**,** DOI: 10.1016/j.palaeo.2011.03.016.

DOWSETT, H. J. & ROBINSON, M. M. 2009. Mid-Pliocene equatorial Pacific sea surface temperature reconstruction: a multi-proxy perspective. *Philosophical Transactions of the Royal Society a-Mathematical Physical and Engineering Sciences,* 367 (1886)**,** 109-125**,** DOI: 10.1098/rsta.2008.0206.

EBY, M., ZICKFELD, K., MONTENEGRO, A., ARCHER, D., MEISSNER, K. J. & WEAVER, A. J. 2009. Lifetime of anthropogenic climate change: millennial time scales of potential CO_2 and surface temperature perturbations. *Journal of Climate,* 22 (10)**,** 2501-2511**,** DOI: 10.1175/2008jcli2554.1.

EDWARDS, N. & MARSH, R. 2005. Uncertainties due to transport-parameter sensitivity in an efficient 3-D ocean-climate model. *Climate Dynamics,* 24 (4)**,** 415-433**,** DOI: 10.1007/s00382-004-0508-8.

FANTLE, M. S. & TIPPER, E. T. 2014. Calcium isotopes in the global biogeochemical Ca cycle: Implications for development of a Ca isotope proxy. *Earth-Science Reviews,* 129**,** 148-177**,** DOI: 10.1016/j.earscirev.2013.10.004.

FELDMANN, J. & LEVERMANN, A. 2015. Collapse of the West Antarctic ice sheet after local destabilization of the Amundsen Basin. *Proceedings of the National Academy of Sciences of the United States of America,* 112 (46)**,** 14191-14196**,** DOI: 10.1073/pnas.1512482112.

FISH, P., THORNE, M., MOORE, T., PENFOLD, J., RICHARDS, L., LEE, M. & PETHICK, J. 2010. LLWR Environmental Safety Case: Forecasting the Development of the Cumbrian Coastline in the Vicinity of the LLWR Site. *Quintessa Report QRS 1443X 1,* Version 1.

FRIEDLINGSTEIN, P., COX, P., BETTS, R., BOPP, L., VON BLOH, W., BROVKIN, V., CADULE, P., DONEY, S., EBY, M., FUNG, I., BALA, G., JOHN, J., JONES, C., JOOS, F., KATO, T., KAWAMIYA, M., KNORR, W., LINDSAY, K., MATTHEWS, H. D., RADDATZ, T., RAYNER, P.,

REICK, C., ROECKNER, E., SCHNITZLER, K. G., SCHNUR, R., STRASSMANN, K., WEAVER, A. J., YOSHIKAWA, C. & ZENG, N. 2006. Climate-carbon cycle feedback analysis: Results from the C^4MIP model intercomparison. *Journal of Climate,* 19 (14)**,** 3337-3353**,** DOI: 10.1175/Jcli3800.1.

FRIEDLINGSTEIN, P., SOLOMON, S., PLATTNER, G. K., KNUTTI, R., CIAIS, P. & RAUPACH, M. R. 2011. Long-term climate implications of twenty-first century options for carbon dioxide emission mitigation. *Nature Climate Change,* 1 (9)**,** 457-461.

FROLICHER, T. L., WINTON, M. & SARMIENTO, J. L. 2014. Continued global warming after CO_2 emissions stoppage. *Nature Climate Change,* 4 (1)**,** 40-44**,** DOI: 10.1038/Nclimate2060.

GALLEE, H., VANYPERSELE, J. P., FICHEFET, T., MARSIAT, I., TRICOT, C. & BERGER, A. 1992. Simulation of the last glacial cycle by a coupled, sectorially averaged climate-ice sheet model .2. response to insolation and CO_2 variations. *Journal of Geophysical Research-Atmospheres,* 97 (D14)**,** 15713-15740.

GALLEE, H., VANYPERSELE, J. P., FICHEFET, T., TRICOT, C. & BERGER, A. 1991. Simulation of the last glacial cycle by a coupled, sectorially averaged climate-ice sheet model .1. The climate model. *Journal of Geophysical Research-Atmospheres,* 96 (D7)**,** 13139-13161**,** DOI: 10.1029/91jd00874.

GANOPOLSKI, A., WINKELMANN, R. & SCHELLNHUBER, H. J. 2016. Critical insolation-CO_2 relation for diagnosing past and future glacial inception. *Nature,* 529 (7585)**,** 200-203**,** DOI: 10.1038/nature16494.

GEOFFROY, O., SAINT-MARTIN, D., BELLON, G., VOLDOIRE, A., OLIVIE, D. J. L. & TYTECA, S. 2013. Transient climate response in a two-layer energy-balance model. Part II: Representation of the efficacy of deep-ocean heat uptake and validation for CMIP5 AOGCMs. *Journal of Climate,* 26 (6)**,** 1859-1876**,** DOI: 10.1175/Jcli-D-12-00196.1.

GERSHUNOV, A., RAJAGOPALAN, B., OVERPECK, J., GUIRGUIS, K., CAYAN, D., HUGHES, M., DETTINGER, M., CASTRO, C., SCHWARTZ, R. E., ANDERSON, M., RAY, A. J., BARSUGLI, J., CAVAZOS, T. & ALEXANDER, M. 2013. Future Climate: Projected Extremes. *In:* GARFIN, G., JARDINE, A., MERIDETH, R., BLACK, M. & LEROY, S. (eds.) *Assessment of Climate Change in the Southwest United States: A Report Prepared for the National Climate Assessment.* Washington, DC: Island Press.

GOODWIN, P. & RIDGWELL, A. 2010. Ocean-atmosphere partitioning of anthropogenic carbon dioxide on multimillennial timescales. *Global Biogeochemical Cycles,* 24 (2), GB2014**,** DOI: 10.1029/2008gb003449.

GOOSSE, H., BROVKIN, V., FICHEFET, T., HAARSMA, R., HUYBRECHTS, P., JONGMA, J., MOUCHET, A., SELTEN, F., BARRIAT, P. Y., CAMPIN, J. M., DELEERSNIJDER, E., DRIESSCHAERT, E., GOELZER, H., JANSSENS, I., LOUTRE, M. F., MAQUEDA, M. A. M., OPSTEEGH, T., MATHIEU, P. P., MUNHOVEN, G., PETTERSSON, E. J., RENSSEN, H., ROCHE, D. M., SCHAEFFER, M., TARTINVILLE, B., TIMMERMANN, A. & WEBER, S. L. 2010. Description of the Earth system model of intermediate complexity LOVECLIM version 1.2. *Geoscientific Model Development,* 3 (2)**,** 603-633**,** DOI: 10.5194/gmd-3-603-2010.

GORDON, C., COOPER, C., SENIOR, C. A., BANKS, H., GREGORY, J. M., JOHNS, T. C., MITCHELL, J. F. B. & WOOD, R. A. 2000. The simulation of SST, sea ice extents and ocean heat transports in a version of the Hadley Centre coupled model without flux adjustments. *Climate Dynamics,* 16 (2-3)**,** 147-168**,** DOI: 10.1007/s003820050010.

GREGORY, J. M., ANDREWS, T. & GOOD, P. 2015. The inconstancy of the transient climate response parameter under increasing CO_2. *Philosophical Transactions of the Royal Society a-Mathematical Physical and Engineering Sciences,* 373 (2054), 20140417**,** DOI: 10.1098/rsta.2014.0417.

GREGORY, J. M., INGRAM, W. J., PALMER, M. A., JONES, G. S., STOTT, P. A., THORPE, R. B., LOWE, J. A., JOHNS, T. C. & WILLIAMS, K. D. 2004. A new method for diagnosing

radiative forcing and climate sensitivity. *Geophysical Research Letters,* 31 (3), L03205**,** DOI: 10.1029/2003gl018747.
GREVE, R. 2000. On the response of the Greenland ice sheet to greenhouse climate change. *Climatic Change,* 46 (3)**,** 289-303**,** DOI: 10.1023/A:1005647226590.
HALL, A. 2004. The role of surface albedo feedback in climate. *Journal of Climate,* 17 (7)**,** 1550-1568**,** DOI: 10.1175/1520-0442(2004)017<1550:Trosaf>2.0.Co;2.
HAYS, J. D., IMBRIE, J. & SHACKLETON, N. J. 1976. Variations in the earth's orbit: Pacemaker of the Ice Ages. *Science,* 194**,** 1121-1132.
HAYWOOD, A. M., DOWSETT, H. J., DOLAN, A. M., ROWLEY, D., ABE-OUCHI, A., OTTO-BLIESNER, B., CHANDLER, M. A., HUNTER, S. J., LUNT, D. J., POUND, M. & SALZMANN, U. 2016. The Pliocene Model Intercomparison Project (PlioMIP) Phase 2: scientific objectives and experimental design. *Climate of the Past,* 12 (3)**,** 663-675**,** DOI: 10.5194/cp-12-663-2016.
HAYWOOD, A. M., DOWSETT, H. J., OTTO-BLIESNER, B., CHANDLER, M. A., DOLAN, A. M., HILL, D. J., LUNT, D. J., ROBINSON, M. M., ROSENBLOOM, N., SALZMANN, U. & SOHL, L. E. 2010. Pliocene Model Intercomparison Project (PlioMIP): experimental design and boundary conditions (Experiment 1). *Geoscientific Model Development,* 3 (1)**,** 227-242**,** DOI: 10.5194/gmd-3-227-2010.
HAYWOOD, A. M., HILL, D. J., DOLAN, A. M., OTTO-BLIESNER, B. L., BRAGG, F., CHAN, W. L., CHANDLER, M. A., CONTOUX, C., DOWSETT, H. J., JOST, A., KAMAE, Y., LOHMANN, G., LUNT, D. J., ABE-OUCHI, A., PICKERING, S. J., RAMSTEIN, G., ROSENBLOOM, N. A., SALZMANN, U., SOHL, L., STEPANEK, C., UEDA, H., YAN, Q. & ZHANG, Z. 2013. Large-scale features of Pliocene climate: results from the Pliocene Model Intercomparison Project. *Climate of the Past,* 9 (1)**,** 191-209**,** DOI: 10.5194/cp-9-191-2013.
HAYWOOD, A. M. & VALDES, P. J. 2004. Modelling Pliocene warmth: contribution of atmosphere, oceans and cryosphere. *Earth and Planetary Science Letters,* 218 (3-4)**,** 363-377**,** DOI: 10.1016/S0012-821x(03)00685-X.
HELD, I. M., WINTON, M., TAKAHASHI, K., DELWORTH, T., ZENG, F. R. & VALLIS, G. K. 2010. Probing the fast and slow components of global warming by returning abruptly to preindustrial forcing. *Journal of Climate,* 23 (9)**,** 2418-2427**,** DOI: 10.1175/2009jcli3466.1.
HERBERT, T. D., PETERSON, L. C., LAWRENCE, K. T. & LIU, Z. H. 2010. Tropical ocean temperatures over the past 3.5 million years. *Science,* 328 (5985)**,** 1530-1534**,** DOI: 10.1126/science.1185435.
HOLDEN, P. B., EDWARDS, N. R., OLIVER, K. I. C., LENTON, T. M. & WILKINSON, R. D. 2010. A probabilistic calibration of climate sensitivity and terrestrial carbon change in GENIE-1. *Climate Dynamics,* 35 (5)**,** 785-806**,** DOI: 10.1007/s00382-009-0630-8.
HOLLAND, M. M. & BITZ, C. M. 2003. Polar amplification of climate change in coupled models. *Climate Dynamics,* 21 (3-4)**,** 221-232**,** DOI: 10.1007/s00382-003-0332-6.
HONISCH, B., RIDGWELL, A., SCHMIDT, D. N., THOMAS, E., GIBBS, S. J., SLUIJS, A., ZEEBE, R., KUMP, L., MARTINDALE, R. C., GREENE, S. E., KIESSLING, W., RIES, J., ZACHOS, J. C., ROYER, D. L., BARKER, S., MARCHITTO, T. M., MOYER, R., PELEJERO, C., ZIVERI, P., FOSTER, G. L. & WILLIAMS, B. 2012. The Geological Record of Ocean Acidification. *Science,* 335 (6072)**,** 1058-1063**,** DOI: 10.1126/science.1208277.
HUH, Y., CHAN, L. H., ZHANG, L. & EDMOND, J. M. 1998. Lithium and its isotopes in major world rivers: Implications for weathering and the oceanic budget. *Geochimica Et Cosmochimica Acta,* 62 (12)**,** 2039-2051**,** DOI: 10.1016/S0016-7037(98)00126-4.
HUNTER, S. J., GOLDOBIN, D. S., HAYWOOD, A. M., RIDGWELL, A. & REES, J. G. 2013. Sensitivity of the global submarine hydrate inventory to scenarios of future climate change. *Earth and Planetary Science Letters,* 367**,** 105-115**,** DOI: 10.1016/j.epsl.2013.02.017.

HUYBRECHTS, P. & DE WOLDE, J. 1999. The dynamic response of the Greenland and Antarctic ice sheets to multiple-century climatic warming. *Journal of Climate,* 12 (8)**,** 2169-2188**,** DOI: 10.1175/1520-0442(1999)012<2169:Tdrotg>2.0.Co;2.

HUYBRECHTS, P., GOELZER, H., JANSSENS, I., DRIESSCHAERT, E., FICHEFET, T., GOOSSE, H. & LOUTRE, M. F. 2011. Response of the Greenland and Antarctic Ice Sheets to Multi-Millennial Greenhouse Warming in the Earth System Model of Intermediate Complexity LOVECLIM. *Surveys in Geophysics,* 32 (4-5)**,** 397-416**,** DOI: 10.1007/s10712-011-9131-5.

ICRP 2007. The 2007 rcommendations of the International Commission on Radiological Protection. *Annals of the ICRP,* 37 (2-4), Publication 103.

IMBRIE, J. & IMBRIE, J. Z. 1980. Modeling the Climatic Response to Orbital Variations. *Science,* 207 (4434)**,** 943-953**,** DOI: 10.1126/science.207.4434.943.

IPCC 2013. Climate Change 2013: The Physical Science Basis. Contribution of Working Group I to the Fifth Assessment Report of the Intergovernmental Panel on Climate Change. *In:* STOCKER, T. F., QIN, D., PLATTNER, G. K., TIGNOR, M., ALLEN, S. K., BOSCHUNG, J., NAUELS, A., XIA, Y., BEX, V. & MIDGLEY, P. M. (eds.). Cambridge, UK and New York, USA: Cambridge University Press, 1535 pp. ISBN.

JENKYNS, H. C. 1980. Cretaceous Anoxic Events - from Continents to Oceans. *Journal of the Geological Society,* 137 (Mar)**,** 171-188**,** DOI: 10.1144/gsjgs.137.2.0171.

JICKELLS, T. D., AN, Z. S., ANDERSEN, K. K., BAKER, A. R., BERGAMETTI, G., BROOKS, N., CAO, J. J., BOYD, P. W., DUCE, R. A., HUNTER, K. A., KAWAHATA, H., KUBILAY, N., LAROCHE, J., LISS, P. S., MAHOWALD, N., PROSPERO, J. M., RIDGWELL, A. J., TEGEN, I. & TORRES, R. 2005. Global iron connections between desert dust, ocean biogeochemistry, and climate. *Science,* 308 (5718)**,** 67-71**,** DOI: 10.1126/science.1105959.

JOOS, F., BRUNO, M., FINK, R., SIEGENTHALER, U., STOCKER, T. F. & LEQUERE, C. 1996. An efficient and accurate representation of complex oceanic and biospheric models of anthropogenic carbon uptake. *Tellus Series B-Chemical and Physical Meteorology,* 48 (3)**,** 397-417**,** DOI: 10.1034/j.1600-0889.1996.t01-2-00006.x.

JOOS, F., PRENTICE, I. C., SITCH, S., MEYER, R., HOOSS, G., PLATTNER, G. K., GERBER, S. & HASSELMANN, K. 2001. Global warming feedbacks on terrestrial carbon uptake under the Intergovernmental Panel on Climate Change (IPCC) emission scenarios. *Global Biogeochemical Cycles,* 15 (4)**,** 891-907**,** DOI: 10.1029/2000gb001375.

JOOS, F., ROTH, R., FUGLESTVEDT, J. S., PETERS, G. P., ENTING, I. G., VON BLOH, W., BROVKIN, V., BURKE, E. J., EBY, M., EDWARDS, N. R., FRIEDRICH, T., FROLICHER, T. L., HALLORAN, P. R., HOLDEN, P. B., JONES, C., KLEINEN, T., MACKENZIE, F. T., MATSUMOTO, K., MEINSHAUSEN, M., PLATTNER, G. K., REISINGER, A., SEGSCHNEIDER, J., SHAFFER, G., STEINACHER, M., STRASSMANN, K., TANAKA, K., TIMMERMANN, A. & WEAVER, A. J. 2013. Carbon dioxide and climate impulse response functions for the computation of greenhouse gas metrics: a multi-model analysis. *Atmospheric Chemistry and Physics,* 13 (5)**,** 2793-2825**,** DOI: 10.5194/acp-13-2793-2013.

JOSEPH, V. R. & HUNG, Y. 2008. Orthogonal-maximin Latin hypercube designs. *Statistica Sinica,* 18 (1)**,** 171-186.

JOUZEL, J., BARKOV, N. I., BARNOLA, J. M., BENDER, M., CHAPPELLAZ, J., GENTHON, C., KOTLYAKOV, V. M., LIPENKOV, V., LORIUS, C., PETIT, J. R., RAYNAUD, D., RAISBECK, G., RITZ, C., SOWERS, T., STIEVENARD, M., YIOU, F. & YIOU, P. 1993. Extending the Vostok ice-core record of paleoclimate to the penultimate glacial period. *Nature,* 364 (6436)**,** 407-412**,** DOI: 10.1038/364407a0.

JOUZEL, J., MASSON-DELMOTTE, V., CATTANI, O., DREYFUS, G., FALOURD, S., HOFFMANN, G., MINSTER, B., NOUET, J., BARNOLA, J. M., CHAPPELLAZ, J., FISCHER, H., GALLET, J. C., JOHNSEN, S., LEUENBERGER, M., LOULERGUE, L., LUETHI, D., OERTER, H., PARRENIN, F., RAISBECK, G., RAYNAUD, D., SCHILT, A., SCHWANDER, J., SELMO, E., SOUCHEZ, R., SPAHNI, R., STAUFFER, B., STEFFENSEN, J. P., STENNI, B., STOCKER, T. F., TISON, J. L.,

WERNER, M. & WOLFF, E. W. 2007. Orbital and millennial Antarctic climate variability over the past 800,000 years. *Science,* 317 (5839)**,** 793-796**,** DOI: 10.1126/science.1141038.

KAWAMURA, K., PARRENIN, F., LISIECKI, L., UEMURA, R., VIMEUX, F., SEVERINGHAUS, J. P., HUTTERLI, M. A., NAKAZAWA, T., AOKI, S., JOUZEL, J., RAYMO, M. E., MATSUMOTO, K., NAKATA, H., MOTOYAMA, H., FUJITA, S., GOTO-AZUMA, K., FUJII, Y. & WATANABE, O. 2007. Northern Hemisphere forcing of climatic cycles in Antarctica over the past 360,000 years. *Nature,* 448 (7156)**,** 912-914**,** DOI: 10.1038/Nature06015.

KENNEDY, M. C. & O'HAGAN, A. 2000. Predicting the output from a complex computer code when fast approximations are available. *Biometrika,* 87 (1)**,** 1-13**,** DOI: 10.1093/biomet/87.1.1.

KENNETT, J. P. & STOTT, L. D. 1991. Abrupt deep-sea warming, palaeoceanographic changes and benthic extinctions at the end of the Paleocene. *Nature,* 353 (6341)**,** 225-229**,** DOI: 10.1038/353225a0.

KJELLSTRÖM, E., STRANDBERG, G., BRANDEFELT, J., NÄSLUND, J.-O., SMITH, B. & WOHLFARTH, B. 2009. Climate conditions in Sweden in a 100,000-year time perspective, *SKB Report,* Svensk Kärnbränslehantering AB, Stockholm, Sweden. TR-09-04. Available from: www.skb.com/publication/1925516/TR-09-04.pdf.

KNUTTI, R. & RUGENSTEIN, M. A. A. 2015. Feedbacks, climate sensitivity and the limits of linear models. *Philosophical Transactions of the Royal Society a-Mathematical Physical and Engineering Sciences,* 373 (2054), 20150146**,** DOI: 10.1098/rsta.2015.0146.

KOHLER, P., FISCHER, H., MUNHOVEN, G. & ZEEBE, R. E. 2005. Quantitative interpretation of atmospheric carbon records over the last glacial termination. *Global Biogeochemical Cycles,* 19 (4), GB4020**,** DOI: 10.1029/2004gb002345.

KRISHNAN, R. & SUGI, M. 2003. Pacific decadal oscillation and variability of the Indian summer monsoon rainfall. *Climate Dynamics,* 21 (3-4)**,** 233-242**,** DOI: 10.1007/s00382-003-0330-8.

KUMAR, A., PERLWITZ, J., EISCHEID, J., QUAN, X. W., XU, T. Y., ZHANG, T., HOERLING, M., JHA, B. & WANG, W. Q. 2010. Contribution of sea ice loss to Arctic amplification. *Geophysical Research Letters,* 37 L21701**,** DOI: 10.1029/2010gl045022.

KUTZBACH, J. E. 1981. Monsoon climate of the Early Holocene - Climate experiment with the Earths orbital parameters for 9000 years ago. *Science,* 214 (4516)**,** 59-61**,** DOI: 10.1126/science.214.4516.59.

KUTZBACH, J. E. & LIU, Z. 1997. Response of the African monsoon to orbital forcing and ocean feedbacks in the middle Holocene. *Science,* 278 (5337)**,** 440-443**,** DOI: 10.1126/science.278.5337.440.

LAMBECK, K., YOKOYAMA, Y., JOHNSTON, P. & PURCELL, A. 2001. Global ice volumes at the Last Glacial Maximum and early Lateglacial. *Earth and Planetary Science Letters,* 190 (3-4)**,** 275-275**,** DOI: 10.1016/S0012-821x(01)00386-7.

LAMBERT, F., DELMONTE, B., PETIT, J. R., BIGLER, M., KAUFMANN, P. R., HUTTERLI, M. A., STOCKER, T. F., RUTH, U., STEFFENSEN, J. P. & MAGGI, V. 2008. Dust-climate couplings over the past 800,000 years from the EPICA Dome C ice core. *Nature,* 452 (7187)**,** 616-619**,** DOI: 10.1038/nature06763.

LASAGA, A. C., BERNER, R. A. & GARRELS, R. M. 1985. An improved geochemical model of atmospheric CO_2 fluctuations over the past 100 million years. *In:* SUNDQUIST, E. T. & BROECKER, W. S. (eds.) *The Carbon Cycle and Atmospheric CO2: Natural Variations Archean to Present.* American Geophysical Union Monographs.

LASKAR, J., ROBUTEL, P., JOUTEL, F., GASTINEAU, M., CORREIA, A. C. M. & LEVRARD, B. 2004. A long-term numerical solution for the insolation quantities of the Earth. *Astronomy & Astrophysics,* 428 (1)**,** 261-285**,** DOI: 10.1051/0004-6361:20041335.

LAWRENCE, D. M., SLATER, A. G. & SWENSON, S. C. 2012. Simulation of present-day and future permafrost and seasonally frozen ground conditions in CCSM4. *Journal of Climate,* 25 (7), 2207-2225, DOI: 10.1175/Jcli-D-11-00334.1.

LAWRENCE, K. T., HERBERT, T. D., BROWN, C. M., RAYMO, M. E. & HAYWOOD, A. M. 2009. High-amplitude variations in North Atlantic sea surface temperature during the early Pliocene warm period. *Paleoceanography,* 24 Pa2218, DOI: 10.1029/2008pa001669.

LECAIN, G. D. & STUCKLESS, J. S. 2012. Hydrology of the unsaturated zone, Yucca Mountain, Nevada. *In:* STUCKLESS, J. S. (ed.) *Hydrology and Geochemistry of Yucca Mountain and Vicinity, Southern Nevada and California: The Geological Society of America Memoir 209.* The Geological Society of America, 9-72 pp. ISBN.

LECKIE, R. M., BRALOWER, T. J. & CASHMAN, R. 2002. Oceanic anoxic events and plankton evolution: Biotic response to tectonic forcing during the mid-Cretaceous. *Paleoceanography,* 17 (3), 1041, DOI: 10.1029/2001pa000623.

LENTON, T. M. 2000. Land and ocean carbon cycle feedback effects on global warming in a simple Earth system model. *Tellus Series B-Chemical and Physical Meteorology,* 52 (5), 1159-1188, DOI: 10.1034/j.1600-0889.2000.01104.x.

LENTON, T. M. 2006. Climate change to the end of the millennium - An editorial review essay. *Climatic Change,* 76 (1-2), 7-29, DOI: 10.1007/s10584-005-9022-1.

LENTON, T. M. & BRITTON, C. 2006. Enhanced carbonate and silicate weathering accelerates recovery from fossil fuel CO_2 perturbations. *Global Biogeochemical Cycles,* 20 (3), GB3009, DOI: 10.1029/2005gb002678.

LENTON, T. M., WILLIAMSON, M. S., EDWARDS, N. R., MARSH, R., PRICE, A. R., RIDGWELL, A. J., SHEPHERD, J. G., COX, S. J. & TEAM, T. G. 2006. Millennial timescale carbon cycle and climate change in an efficient Earth system model. *Climate Dynamics,* 26 (7-8), 687-711, DOI: 10.1007/s00382-006-0109-9.

LI, C., VON STORCH, J. S. & MAROTZKE, J. 2013. Deep-ocean heat uptake and equilibrium climate response. *Climate Dynamics,* 40 (5-6), 1071-1086, DOI: 10.1007/s00382-012-1350-z.

LISIECKI, L. E. & RAYMO, M. E. 2005. A Pliocene-Pleistocene stack of 57 globally distributed benthic d18O records. *Paleoceanography,* 20 (1), PA1003, DOI: 10.1029/2004pa001071.

LISIECKI, L. E. & RAYMO, M. E. 2007. Plio-Pleistocene climate evolution: trends and transitions in glacial cycle dynamics. *Quaternary Science Reviews,* 26 (1-2), 56-69, DOI: 10.1016/j.quascirev.2006.09.005.

LLWR 2011. Environmental Safety Case - Main Report, LLW Repository Limited. LLWR/ESC/R(11) 10016. Available from: www.llwrsite.com/wp-content/uploads/2013/04/Environmental-Safety-Case-%E2%80%93-Full-Report.pdf.

LOEPPKY, J. L., SACKS, J. & WELCH, W. J. 2009. Choosing the sample size of a computer experiment: A practical guide. *Technometrics,* 51 (4), 366-376, DOI: 10.1198/Tech.2009.08040.

LORD, N. S., CRUCIFIX, M., LUNT, D. J., THORNE, M. C., BOUNCEUR, N., DOWSETT, H., O'BRIEN, C. L. & RIDGWELL, A. 2017. Emulation of long-term changes in global climate: Application to the mid-Pliocene and future. *Climate of the Past,* 13, 1539-1571, DOI: 10.5194/cp-13-1539-2017.

LORD, N. S., RIDGWELL, A., THORNE, M. C. & LUNT, D. J. 2015. The 'long tail' of anthropogenic CO_2 decline in the atmosphere and its consequences for post-closure performance assessments for disposal of radioactive wastes. *Mineralogical Magazine,* 79 (6), 1613-1623, DOI: 10.1180/minmag.2015.079.6.37.

LORD, N. S., RIDGWELL, A., THORNE, M. C. & LUNT, D. J. 2016. An impulse response function for the "long tail" of excess atmospheric CO_2 in an Earth system model. *Global Biogeochemical Cycles,* 30 (1), 2-17, DOI: 10.1002/2014gb005074.

LOUTRE, M. F. 1993. *Paramètres orbitaux et cycles diurne et saisonnier des insolations.* PhD, Université catholique de Louvain.

LOUTRE, M. F. & BERGER, A. 2000a. No glacial-interglacial cycle in the ice volume simulated under a constant astronomical forcing and a variable CO_2. *Geophysical Research Letters,* 27 (6)**,** 783-786**,** DOI: 10.1029/1999gl006081.

LOUTRE, M. F. & BERGER, A. 2000b. Future climatic changes: Are we entering an exceptionally long interglacial? *Climatic Change,* 46 (1-2)**,** 61-90**,** DOI: 10.1023/A:1005559827189.

LU, R. Y., DONG, B. W. & DING, H. 2006. Impact of the Atlantic multidecadal oscillation on the Asian summer monsoon. *Geophysical Research Letters,* 33 (24), L24701**,** DOI: 10.1029/2006gl027655.

LUNT, D. J., DE NOBLET-DUCOUDRE, N. & CHARBIT, S. 2004. Effects of a melted Greenland ice sheet on climate, vegetation, and the cryosphere. *Climate Dynamics,* 23 (7-8)**,** 679-694**,** DOI: 10.1007/s00382-004-0463-4.

LUNT, D. J., HAYWOOD, A. M., SCHMIDT, G. A., SALZMANN, U., VALDES, P. J. & DOWSETT, H. J. 2010. Earth system sensitivity inferred from Pliocene modelling and data. *Nature Geoscience,* 3 (1)**,** 60-64**,** DOI: 10.1038/Ngeo706.

LUTHI, D., LE FLOCH, M., BEREITER, B., BLUNIER, T., BARNOLA, J. M., SIEGENTHALER, U., RAYNAUD, D., JOUZEL, J., FISCHER, H., KAWAMURA, K. & STOCKER, T. F. 2008. High-resolution carbon dioxide concentration record 650,000-800,000 years before present. *Nature,* 453 (7193)**,** 379-382**,** DOI: 10.1038/Nature06949.

MAHOWALD, N., KOHFELD, K., HANSSON, M., BALKANSKI, Y., HARRISON, S. P., PRENTICE, I. C., SCHULZ, M. & RODHE, H. 1999. Dust sources and deposition during the last glacial maximum and current climate: A comparison of model results with paleodata from ice cores and marine sediments. *Journal of Geophysical Research-Atmospheres,* 104 (D13)**,** 15895-15916**,** DOI: 10.1029/1999jd900084.

MAIER-REIMER, E. & HASSELMANN, K. 1987. Transport and storage of CO_2 in the ocean - an inorganic ocean-circulation carbon cycle model. *Climate Dynamics,* 2 (2)**,** 63-90**,** DOI: 10.1007/Bf01054491.

MARTI, O., BRACONNOT, P., BELLIER, J., BENSHILA, R., BONY, S., BROCKMANN, P., CADULE, P., CAUBEL, A., DENVIL, S., DUFRESNE, J. L., FAIRHEAD, L., FILIBERTI, M. A., FOUJOLS, M. A., FICHEFET, T., FRIEDLINGSTEIN, P., GOOSSE, H., GRANDPEIX, J. Y., HOURDIN, F., KRINNER, G., LEVY, C., MADEC, G., MUSAT, I., DE NOBLET, N., POLCHER, J. & TALANDIER, C. 2005. The new IPSL climate system model: IPSL-CM4, Institut Pierre Simon Laplace, Paris.

MARTINEZ-BOTI, M. A., FOSTER, G. L., CHALK, T. B., ROHLING, E. J., SEXTON, P. F., LUNT, D. J., PANCOST, R. D., BADGER, M. P. S. & SCHMIDT, D. N. 2015. Plio-Pleistocene climate sensitivity evaluated using high-resolution CO_2 records. *Nature,* 518 (7537)**,** 49-54**,** DOI: 10.1038/nature14145.

MARZOCCHI, A., LUNT, D. J., FLECKER, R., BRADSHAW, C. D., FARNSWORTH, A. & HILGEN, F. J. 2015. Orbital control on late Miocene climate and the North African monsoon: insight from an ensemble of sub-precessional simulations. *Climate of the Past,* 11 (10)**,** 1271-1295**,** DOI: 10.5194/cp-11-1271-2015.

MASSON-DELMOTTE, V., BRACONNOT, P., HOFFMANN, G., JOUZEL, J., KAGEYAMA, M., LANDAIS, A., LEJEUNE, Q., RISI, C., SIME, L., SJOLTE, J., SWINGEDOUW, D. & VINTHER, B. 2011. Sensitivity of interglacial Greenland temperature and δO^{18}: ice core data, orbital and increased CO_2 climate simulations. *Climate of the Past,* 7 (3)**,** 1041-1059**,** DOI: 10.5194/cp-7-1041-2011.

MATLAB Statistics and Machine Learning Toolbox Release 2012b, The MathWorks, Inc., Natick, Massachusetts, United States.

MCGLADE, C. & EKINS, P. 2015. The geographical distribution of fossil fuels unused when limiting global warming to 2°C. *Nature,* 517 (7533)**,** 187-190**,** DOI: 10.1038/Nature14016.

MCKAY, M. D., BECKMAN, R. J. & CONOVER, W. J. 1979. A comparison of three methods for selecting values of input variables in the analysis of output from a computer code. *Technometrics,* 21 (2)**,** 239-245**,** DOI: 10.2307/1268522.

MEEHL, G. A., COVEY, C., DELWORTH, T., LATIF, M., MCAVANEY, B., MITCHELL, J. F. B., STOUFFER, R. J. & TAYLOR, K. E. 2007. The WCRP CMIP3 multimodel dataset - A new era in climate change research. *Bulletin of the American Meteorological Society,* 88 (9)**,** 1383-1394**,** DOI: 10.1175/Bams-88-9-1383.

MEINSHAUSEN, M., SMITH, S. J., CALVIN, K., DANIEL, J. S., KAINUMA, M. L. T., LAMARQUE, J. F., MATSUMOTO, K., MONTZKA, S. A., RAPER, S. C. B., RIAHI, K., THOMSON, A., VELDERS, G. J. M. & VAN VUUREN, D. P. P. 2011. The RCP greenhouse gas concentrations and their extensions from 1765 to 2300. *Climatic Change,* 109 (1-2)**,** 213-241**,** DOI: 10.1007/s10584-011-0156-z.

MEISSNER, K. J., MCNEIL, B. I., EBY, M. & WIEBE, E. C. 2012. The importance of the terrestrial weathering feedback for multimillennial coral reef habitat recovery. *Global Biogeochemical Cycles,* 26 (3), GB3017**,** DOI: 10.1029/2011gb004098.

MIKOLAJEWICZ, U., GROGER, M., MAIER-REIMER, E., SCHURGERS, G., VIZCAINO, M. & WINGUTH, A. M. E. 2007. Long-term effects of anthropogenic CO_2 emissions simulated with a complex earth system model. *Climate Dynamics,* 28 (6)**,** 599-631**,** DOI: 10.1007/s00382-006-0204-y.

MILANKOVITCH, M. 1941. *Kanon der Erdbestrahlung und seine Anwendung auf das Eiszeitenproblem,* Washington D.C., U.S. Department of Commerce and National Science Foundation.

MODARIA WORKING GROUP 6 2016. Development of a common framework for addressing climate change in post-closure radiological assessment of solid radioactive waste disposal, *Final report of MODARIA Working Group 6*.

MONNIN, E., STEIG, E. J., SIEGENTHALER, U., KAWAMURA, K., SCHWANDER, J., STAUFFER, B., STOCKER, T. F., MORSE, D. L., BARNOLA, J. M., BELLIER, B., RAYNAUD, D. & FISCHER, H. 2004. Evidence for substantial accumulation rate variability in Antarctica during the Holocene, through synchronization of CO_2 in the Taylor Dome, Dome C and DML ice cores. *Earth and Planetary Science Letters,* 224 (1-2)**,** 45-54**,** DOI: 10.1016/j.epsl.2004.05.007.

MONTENEGRO, A., BROVKIN, V., EBY, M., ARCHER, D. & WEAVER, A. J. 2007. Long term fate of anthropogenic carbon. *Geophysical Research Letters,* 34 (19), L19707**,** DOI: 10.1029/2007gl030905.

MULLER, P. J., KIRST, G., RUHLAND, G., VON STORCH, I. & ROSELL-MELE, A. 1998. Calibration of the alkenone paleotemperature index $U_{37}^{K'}$ based on core-tops from the eastern South Atlantic and the global ocean (60°N-60°S). *Geochimica Et Cosmochimica Acta,* 62 (10)**,** 1757-1772**,** DOI: 10.1016/S0016-7037(98)00097-0.

NAAFS, B. D. A., STEIN, R., HEFTER, J., KHELIFI, N., DE SCHEPPER, S. & HAUG, G. H. 2010. Late Pliocene changes in the North Atlantic Current. *Earth and Planetary Science Letters,* 298 (3-4)**,** 434-442**,** DOI: 10.1016/j.epsl.2010.08.023.

NAKIĆENOVIĆ, N. & SWART, R. 2000. *Emissions Scenarios,* Cambridge, Cambridge University Press.

NATIONAL RESEARCH COUNCIL 2011. *Climate stabilization targets: emissions, concentrations, and impacts over decades to millennia,* Washington, D.C., USA, The National Academies Press.

NDA 2010. Geological disposal. An overview of the generic Disposal System Safety Case, Nuclear Decomissioning Agency, Harwell, UK. Report no. NDA/RWMD/010.

NDA 2016. Radioactive wastes in the UK: A summary of the 2016 inventory, Nuclear Decomissioning Agency and Department for Business, Energy and Industrial Strategy. Available from: https://ukinventory.nda.gov.uk/wp-content/uploads/sites/18/2017/03/High-Level-Summary-UK-Radwaste-Inventory-2016.pdf.

NRC 2016. Supplement to the U.S. Department of Energy's Environmental Impact Statement for a Geologic Repository for the Disposal of Spent Nuclear Fuel and High-Level Radioactive Waste at Yucca Mountain, Nye County, Nevada, U.S. Nuclear Regulatory Commission, Washington DC. NUREG-2184. Available from: https://www.nrc.gov/docs/ML1612/ML16125A032.pdf.

OAKLEY, J. & O'HAGAN, A. 2002. Bayesian inference for the uncertainty distribution of computer model outputs. *Biometrika,* 89 (4)**,** 769-784**,** DOI: 10.1093/biomet/89.4.769.

OECHEL, W. C., HASTINGS, S. J., VOURLITIS, G., JENKINS, M., RIECHERS, G. & GRULKE, N. 1993. Recent change of Arctic tundra ecosystems from a net carbon-dioxide sink to a source. *Nature,* 361 (6412)**,** 520-523**,** DOI: 10.1038/361520a0.

PAILLARD, D. 1998. The timing of Pleistocene glaciations from a simple multiple-state climate model. *Nature,* 391 (6665)**,** 378-381**,** DOI: 10.1038/34891.

PAILLARD, D. 2001. Glacial cycles: Toward a new paradigm. *Reviews of Geophysics,* 39 (3)**,** 325-346**,** DOI: 10.1029/2000rg000091.

PAILLARD, D. 2006. What drives the Ice Age cycle? *Science,* 313 (5786)**,** 455-456**,** DOI: 10.1126/science.1131297.

PAILLARD, D. & PARRENIN, F. 2004. The Antarctic ice sheet and the triggering of deglaciations. *Earth and Planetary Science Letters,* 227 (3-4)**,** 263-271**,** DOI: 10.1016/j.epsl.2004.08.023.

PELTIER, W. R. 2004. Global glacial isostasy and the surface of the ice-age earth: The ice-5G (VM2) model and grace. *Annual Review of Earth and Planetary Sciences,* 32**,** 111-149**,** DOI: 10.1146/annurev.earth.32.082503.144359.

PENMAN, D. E., HONISCH, B., ZEEBE, R. E., THOMAS, E. & ZACHOS, J. C. 2014. Rapid and sustained surface ocean acidification during the Paleocene-Eocene Thermal Maximum. *Paleoceanography,* 29 (5)**,** 357-369**,** DOI: 10.1002/2014pa002621.

PETIT, J. R., JOUZEL, J., RAYNAUD, D., BARKOV, N. I., BARNOLA, J. M., BASILE, I., BENDER, M., CHAPPELLAZ, J., DAVIS, M., DELAYGUE, G., DELMOTTE, M., KOTLYAKOV, V. M., LEGRAND, M., LIPENKOV, V. Y., LORIUS, C., PEPIN, L., RITZ, C., SALTZMAN, E. & STIEVENARD, M. 1999. Climate and atmospheric history of the past 420,000 years from the Vostok ice core, Antarctica. *Nature,* 399 (6735)**,** 429-436**,** DOI: 10.1038/20859.

PIMENOFF, N., VENÄLÄINEN, A. & JÄRVINEN, H. 2011. Climate scenarios for Olkiluoto on a time scale of 120,000 years, *Report POSIVA,* Posiva Oy, Eurajoki, Finland. 2011-04. Available from: www.posiva.fi/files/2763/POSIVA_2011-04web.pdf.

PLATTNER, G. K., KNUTTI, R., JOOS, F., STOCKER, T. F., VON BLOH, W., BROVKIN, V., CAMERON, D., DRIESSCHAERT, E., DUTKIEWICZ, S., EBY, M., EDWARDS, N. R., FICHEFET, T., HARGREAVES, J. C., JONES, C. D., LOUTRE, M. F., MATTHEWS, H. D., MOUCHET, A., MULLER, S. A., NAWRATH, S., PRICE, A., SOKOLOV, A., STRASSMANN, K. M. & WEAVER, A. J. 2008. Long-term climate commitments projected with climate-carbon cycle models. *Journal of Climate,* 21 (12)**,** 2721-2751**,** DOI: 10.1175/2007jcli1905.1.

POPE, V. D., GALLANI, M. L., ROWNTREE, P. R. & STRATTON, R. A. 2000. The impact of new physical parametrizations in the Hadley Centre climate model: HadAM3. *Climate Dynamics,* 16 (2-3)**,** 123-146**,** DOI: 10.1007/s003820050009.

PRAHL, F. G., MUEHLHAUSEN, L. A. & ZAHNLE, D. L. 1988. Further evaluation of long-chain alkenones as indicators of paleoceanographic conditions. *Geochimica Et Cosmochimica Acta,* 52 (9)**,** 2303-2310**,** DOI: 10.1016/0016-7037(88)90132-9.

PRELL, W. L. & KUTZBACH, J. E. 1987. Monsoon Variability over the Past 150,000 Years. *Journal of Geophysical Research-Atmospheres,* 92 (D7)**,** 8411-8425**,** DOI: 10.1029/JD092iD07p08411.

PRESCOTT, C. L., HAYWOOD, A. M., DOLAN, A. M., HUNTER, S. J., POPE, J. O. & PICKERING, S. J. 2014. Assessing orbitally-forced interglacial climate variability during the mid-Pliocene Warm Period. *Earth and Planetary Science Letters,* 400**,** 261-271**,** DOI: 10.1016/j.epsl.2014.05.030.

Radioactive Substances Act 1993, Chapter 12. Available from: www.legislation.gov.uk/ukpga/1993/12/contents. (Accessed: 4 September 2017).

RAYMO, M. E., GRANT, B., HOROWITZ, M. & RAU, G. H. 1996. Mid-Pliocene warmth: Stronger greenhouse and stronger conveyor. *Marine Micropaleontology,* 27 (1-4)**,** 313-326**,** DOI: 10.1016/0377-8398(95)00048-8.

RAYNER, N. A., PARKER, D. E., HORTON, E. B., FOLLAND, C. K., ALEXANDER, L. V., ROWELL, D. P., KENT, E. C. & KAPLAN, A. 2003. Global analyses of sea surface temperature, sea ice, and night marine air temperature since the late nineteenth century. *Journal of Geophysical Research-Atmospheres,* 108 (D14), 4407**,** DOI: 10.1029/2002jd002670.

RIDGWELL, A. & HARGREAVES, J. C. 2007. Regulation of atmospheric CO_2 by deep-sea sediments in an Earth system model. *Global Biogeochemical Cycles,* 21 (2), GB2008**,** DOI: 10.1029/2006gb002764.

RIDGWELL, A., HARGREAVES, J. C., EDWARDS, N. R., ANNAN, J. D., LENTON, T. M., MARSH, R., YOOL, A. & WATSON, A. 2007. Marine geochemical data assimilation in an efficient Earth System Model of global biogeochemical cycling. *Biogeosciences,* 4 (1)**,** 87-104**,** DOI: 10.5194/bg-4-87-2007.

RIDGWELL, A. & SCHMIDT, D. N. 2010. Past constraints on the vulnerability of marine calcifiers to massive carbon dioxide release. *Nature Geoscience,* 3 (3)**,** 196-200**,** DOI: 10.1038/Ngeo755.

RIDLEY, J. K., HUYBRECHTS, P., GREGORY, J. M. & LOWE, J. A. 2005. Elimination of the Greenland ice sheet in a high CO_2 climate. *Journal of Climate,* 18 (17)**,** 3409-3427**,** DOI: 10.1175/Jcli3482.1.

ROGNER, H. H. 1997. An assessment of world hydrocarbon resources. *Annual Review of Energy and the Environment,* 22**,** 217-262**,** DOI: 10.1146/annurev.energy.22.1.217.

SACKS, J., WELCH, W. J., MITCHELL, T. J. & WYNN, H. P. 1989. Design and analysis of computer experiments. *Statistical Science,* 4 (4)**,** 409-423**,** DOI: 10.1214/ss/1177012413.

SARMIENTO, J. L., LEQUERE, C. & PACALA, S. W. 1995. Limiting Future Atmospheric Carbon-Dioxide. *Global Biogeochemical Cycles,* 9 (1)**,** 121-137**,** DOI: 10.1029/94gb01779.

SARMIENTO, J. L., ORR, J. C. & SIEGENTHALER, U. 1992. A Perturbation Simulation of CO_2 Uptake in an Ocean General-Circulation Model. *Journal of Geophysical Research-Oceans,* 97 (C3)**,** 3621-3645**,** DOI: 10.1029/91jc02849.

SCHIMEL, D., STEPHENS, B. B. & FISHER, J. B. 2015. Effect of increasing CO_2 on the terrestrial carbon cycle. *Proceedings of the National Academy of Sciences of the United States of America,* 112 (2)**,** 436-441**,** DOI: 10.1073/pnas.1407302112/-/DCSupplemental.

SCHLANGER, S. O. & JENKYNS, H. C. 1976. Cretaceous oceanic anoxic events: Causes and consequences. *Geologie en Mijnbouw,* 55 (3-4)**,** 179-184.

SEKI, O., FOSTER, G. L., SCHMIDT, D. N., MACKENSEN, A., KAWAMURA, K. & PANCOST, R. D. 2010. Alkenone and boron-based Pliocene pCO_2 records. *Earth and Planetary Science Letters,* 292 (1-2)**,** 201-211**,** DOI: 10.1016/j.epsl.2010.01.037.

SHAFFER, G., OLSEN, S. M. & PEDERSEN, J. O. P. 2009. Long-term ocean oxygen depletion in response to carbon dioxide emissions from fossil fuels. *Nature Geoscience,* 2 (2)**,** 105-109**,** DOI: 10.1038/Ngeo420.

SHARPE, S. E. 2007. Using modern through mid-Pleistocene climate proxy data to bound future variation in infiltration at Yucca Mountain, Nevada. *In:* STUCKLESS, J. S. (ed.) *The*

Geology and Climatology of Yucca Mountain and Vicinity, Southern Nevada and California: The Geological Society of America Memoir 199. The Geological Society of America, 155-205 pp. ISBN.

SINGARAYER, J. S. & VALDES, P. J. 2010. High-latitude climate sensitivity to ice-sheet forcing over the last 120 kyr. *Quaternary Science Reviews,* 29 (1-2)**,** 43-55**,** DOI: 10.1016/j.quascirev.2009.10.011.

SITCH, S., HUNTINGFORD, C., GEDNEY, N., LEVY, P. E., LOMAS, M., PIAO, S. L., BETTS, R., CIAIS, P., COX, P., FRIEDLINGSTEIN, P., JONES, C. D., PRENTICE, I. C. & WOODWARD, F. I. 2008. Evaluation of the terrestrial carbon cycle, future plant geography and climate-carbon cycle feedbacks using five Dynamic Global Vegetation Models (DGVMs). *Global Change Biology,* 14 (9)**,** 2015-2039**,** DOI: 10.1111/j.1365-2486.2008.01626.x.

SKB 2011. Long-term safety for the final repository for spent nuclear fuel at Forsmark. Main report of the SR-Site project, Svensk Kärnbränslehantering AB, Stockholm, Sweden. SKB Report TR-11-01. Available from: www.skb.com/publication/2345580.

SKB 2014. Climate and climate-related issues for the safety assessment SR-PSU, Svensk Kärnbränslehantering AB, Stockholm, Sweden. SKB report TR-13-05. Available from: http://skb.se/upload/publications/pdf/TR-13-05.pdf.

SMITH, R. S. & GREGORY, J. 2012. The last glacial cycle: transient simulations with an AOGCM. *Climate Dynamics,* 38 (7-8)**,** 1545-1559**,** DOI: 10.1007/s00382-011-1283-y.

SNL 2008a. Simulation of Net Infiltration for Present-Day and Potential Future Climates, *MDL-NBS-HS-000023 REV 01 ADD 01,* Sandia National Laboratories, Las Vegas, Nevada. ACC: DOC.20080201.0002.

SOLOMON, S., PLATTNER, G. K., KNUTTI, R. & FRIEDLINGSTEIN, P. 2009. Irreversible climate change due to carbon dioxide emissions. *Proceedings of the National Academy of Sciences of the United States of America,* 106 (6)**,** 1704-1709**,** DOI: 10.1073/pnas.0812721106.

STAP, L. B., VAN DE WAL, R. S. W., DE BOER, B., BINTANJA, R. & LOURENS, L. J. 2014. Interaction of ice sheets and climate during the past 800 000 years. *Climate of the Past,* 10 (6)**,** 2135-2152**,** DOI: 10.5194/cp-10-2135-2014.

STATE OF NEVADA 2008. State of Nevada's petition to intervene as a full party. Submitted to the Nuclear Regulatory Commission. In the matter of: U.S. DEPARTMENT OF ENERGY (High Level Waste Repository) ed.: Nuclear Regulatory Commission.

STENNI, B., MASSON-DELMOTTE, V., SELMO, E., OERTER, H., MEYER, H., ROTHLISBERGER, R., JOUZEL, J., CATTANI, O., FALOURD, S., FISCHER, H., HOFFMANN, G., IACUMIN, P., JOHNSEN, S. J., MINSTER, B. & UDISTI, R. 2010. The deuterium excess records of EPICA Dome C and Dronning Maud Land ice cores (East Antarctica). *Quaternary Science Reviews,* 29 (1-2)**,** 146-159**,** DOI: 10.1016/j.quascirev.2009.10.009.

STONE, E. J., LUNT, D. J., RUTT, I. C. & HANNA, E. 2010. Investigating the sensitivity of numerical model simulations of the modern state of the Greenland ice-sheet and its future response to climate change. *Cryosphere,* 4 (3)**,** 397-417**,** DOI: 10.5194/tc-4-397-2010.

STUCKLESS, J. S. 2012. Hydrology and Geochemistry of Yucca Mountain and Vicinity, Southern Nevada and California. *The Geological Society of America Memoir 209.* The Geological Society of America, pp. ISBN.

STUCKLESS, J. S. & LEVICH, R. A. 2007. The Geology and Climatology of Yucca Mountain and Vicinity, Southern Nevada and California. *The Geological Society of America Memoir 199.* The Geological Society of America, pp. ISBN.

SWINGEDOUW, D., FICHEFET, T., HUYBRECHTS, P., GOOSSE, H., DRIESSCHAERT, E. & LOUTRE, M. F. 2008. Antarctic ice-sheet melting provides negative feedbacks on future climate warming. *Geophysical Research Letters,* 35 (L17705), L17705**,** DOI: 10.1029/2008gl034410.

TAYLOR, K. E., STOUFFER, R. J. & MEEHL, G. A. 2012. An Overview of CMIP5 and the experiment design. *Bulletin of the American Meteorological Society,* 93 (4)**,** 485-498**,** DOI: 10.1175/Bams-D-11-00094.1.

TEGEN, I. 2003. Modeling the mineral dust aerosol cycle in the climate system. *Quaternary Science Reviews,* 22 (18-19)**,** 1821-1834**,** DOI: 10.1016/S0277-3791(03)00163-X.

TEXIER, D., DEGNAN, P., LOUTRE, M. F., PAILLARD, D. & THORNE, M. C. 2003. Modelling sequential BIOsphere systems under CLIMate change for radioactive waste disposal. Project BIOCLIM. Proceedings of the 10th International High-Level Waste Management Conference, 30 March – 2 April 2003 Las Vegas, Nevada.

THORNE, M. C. 2013. Book review of Stuckless, J.S. (ed.). *Annals of Nuclear Energy,* 53**,** 545-549.

TONIAZZO, T., GREGORY, J. M. & HUYBRECHTS, P. 2004. Climatic impact of a Greenland deglaciation and its possible irreversibility. *Journal of Climate,* 17 (1)**,** 21-33**,** DOI: 10.1175/1520-0442(2004)017<0021:Cioagd>2.0.Co;2.

TORRENCE, C. & COMPO, G. P. 1998. A practical guide to wavelet analysis. *Bulletin of the American Meteorological Society,* 79 (1)**,** 61-78**,** DOI: 10.1175/1520-0477(1998)079<0061:Apgtwa>2.0.Co;2.

TUENTER, E., WEBER, S. L., HILGEN, F. J. & LOURENS, L. J. 2003. The response of the African summer monsoon to remote and local forcing due to precession and obliquity. *Global and Planetary Change,* 36 (4)**,** 219-235**,** DOI: 10.1016/S0921-8181(02)00196-0.

TURLEY, C., J., B., N., H.-M., E., L., C., L., D., L., P., M., P., N., A., R., T., S., G., T. & S., W. 2010. Carbon uptake, transport and storage by oceans and the consequences of change in carbon capture and storage (CCS). *In:* HARRISON, R. M. & HESTER, R. E. (eds.) *Issues in environmental science and technology (IEST).* Royal Society of Chemistry, 240-284 pp. ISBN.

TYRRELL, T., SHEPHERD, J. G. & CASTLE, S. 2007. The long-term legacy of fossil fuels. *Tellus Series B-Chemical and Physical Meteorology,* 59 (4)**,** 664-672**,** DOI: 10.1111/j.1600-0889.2007.00290.x.

TZEDAKIS, P. C., CHANNELL, J. E. T., HODELL, D. A., KLEIVEN, H. F. & SKINNER, L. C. 2012a. Determining the natural length of the current interglacial. *Nature Geoscience,* 5 (2)**,** 138-141**,** DOI: 10.1038/Ngeo1358.

UNSCEAR 2000. Sources and effects of ionizing radiation, *Report to the General Assembly, with Scientific Annexes,* United Nations, New York, USA. Available from: www.unscear.org/unscear/en/publications/2000_1.

VALDES, P. J., ARMSTRONG, E., BADGER, M. P. S., BRADSHAW, C. D., BRAGG, F., CRUCIFIX, M., DAVIES-BARNARD, T., DAY, J. J., FARNSWORTH, A., GORDON, C., HOPCROFT, P. O., KENNEDY, A. T., LORD, N. S., LUNT, D. J., MARZOCCHI, A., PARRY, L. M., POPE, V., ROBERTS, W. H. G., STONE, E. J., TOURTE, G. J. L. & WILLIAMS, J. H. T. 2017. The BRIDGE HadCM3 family of climate models: HadCM3@Bristol v1.0. *Geoscientific Model Development***,** DOI: 10.5194/gmd-2017-16.

VAN DER SLEEN, P., GROENENDIJK, P., VLAM, M., ANTEN, N. P. R., BOOM, A., BONGERS, F., PONS, T. L., TERBURG, G. & ZUIDEMA, P. A. 2015. No growth stimulation of tropical trees by 150 years of CO_2 fertilization but water-use efficiency increased. *Nature Geoscience,* 8 (1)**,** 24-28**,** DOI: 10.1038/Ngeo2313.

VETTORETTI, G. & PELTIER, W. R. 2011. The impact of insolation, greenhouse gas forcing and ocean circulation changes on glacial inception. *Holocene,* 21 (5)**,** 803-817**,** DOI: 10.1177/0959683610394885.

VIZCAINO, M., MIKOLAJEWICZ, U., GROGER, M., MAIER-REIMER, E., SCHURGERS, G. & WINGUTH, A. M. E. 2008. Long-term ice sheet-climate interactions under anthropogenic greenhouse forcing simulated with a complex Earth System Model. *Climate Dynamics,* 31 (6)**,** 665-690**,** DOI: 10.1007/s00382-008-0369-7.

WALKER, J. C. G., HAYS, P. B. & KASTING, J. F. 1981. A negative feedback mechanism for the long-term stabilization of Earths surface-temperature. *Journal of Geophysical Research-Oceans and Atmospheres,* 86 (Nc10)**,** 9776-9782**,** DOI: 10.1029/Jc086ic10p09776.

WALKER, J. C. G. & KASTING, J. F. 1992. Effects of fuel and forest conservation on future levels of atmospheric carbon-dioxide. *Global and Planetary Change,* 97 (3)**,** 151-189**,** DOI: 10.1016/0921-8181(92)90009-Y.

WARREN, S. G. 1984. Impurities in Snow - Effects on Albedo and Snowmelt Review. *Annals of Glaciology,* 5**,** 177-179.

WEAVER, A. J., EBY, M., WIEBE, E. C., BITZ, C. M., DUFFY, P. B., EWEN, T. L., FANNING, A. F., HOLLAND, M. M., MACFADYEN, A., MATTHEWS, H. D., MEISSNER, K. J., SAENKO, O., SCHMITTNER, A., WANG, H. X. & YOSHIMORI, M. 2001. The UVic Earth System Climate Model: Model description, climatology, and applications to past, present and future climates. *Atmosphere-Ocean,* 39 (4)**,** 361-428.

WILKINSON, R. D. (ed.) 2010. *Bayesian calibration of expensive multivariate computer experiments,* Chichester, UK: John Wiley & Sons, Ltd.

WILLEIT, M., GANOPOLSKI, A., CALOV, R., ROBINSON, A. & MASLIN, M. 2015. The role of CO_2 decline for the onset of Northern Hemisphere glaciation. *Quaternary Science Reviews,* 119**,** 22-34**,** DOI: 10.1016/j.quascirev.2015.04.015.

WILLIAMS, K. D., INGRAM, W. J. & GREGORY, J. M. 2008. Time variation of effective climate sensitivity in GCMs. *Journal of Climate,* 21 (19)**,** 5076-5090**,** DOI: 10.1175/2008jcli2371.1.

WILLIAMS, K. D., SENIOR, C. A. & MITCHELL, J. F. B. 2001. Transient climate change in the Hadley Centre models: The role of physical processes. *Journal of Climate,* 14 (12)**,** 2659-2674**,** DOI: 10.1175/1520-0442(2001)014<2659:Tccith>2.0.Co;2.

WINKELMANN, R., LEVERMANN, A., RIDGWELL, A. & CALDEIRA, K. 2015. Combustion of available fossil-fuel resources sufficient to eliminate the Antarctic ice sheet. *Science Advances,* 1 (8), e1500589**,** DOI: 10.1126/sciadv.1500589.

WINTON, M., TAKAHASHI, K. & HELD, I. M. 2010. Importance of ocean heat uptake efficacy to transient climate change. *Journal of Climate,* 23 (9)**,** 2333-2344**,** DOI: 10.1175/2009jcli3139.1.

WOLFF, E. W., FISCHER, H. & ROTHLISBERGER, R. 2009. Glacial terminations as southern warmings without northern control. *Nature Geoscience,* 2 (3)**,** 206-209**,** DOI: 10.1038/Ngeo442.

YOKOYAMA, Y., LAMBECK, K., DE DECKKER, P., JOHNSTON, P. & FIFIELD, L. K. 2000. Timing of the Last Glacial Maximum from observed sea-level minima. *Nature,* 406 (6797)**,** 713-716**,** DOI: 10.1038/35021035.

YUAN, D. X., CHENG, H., EDWARDS, R. L., DYKOSKI, C. A., KELLY, M. J., ZHANG, M. L., QING, J. M., LIN, Y. S., WANG, Y. J., WU, J. Y., DORALE, J. A., AN, Z. S. & CAI, Y. J. 2004. Timing, duration, and transitions of the Last Interglacial Asian Monsoon. *Science,* 304 (5670)**,** 575-578**,** DOI: 10.1126/science.1091220.

ZACHOS, J. C. & DICKENS, G. R. 2000. An assessment of the biogeochemical feedback response to the climatic and chemical perturbations of the LPTM. *Gff,* 122**,** 188-189.

ZEEBE, R. E. 2013. What caused the long duration of the Paleocene-Eocene Thermal Maximum? *Paleoceanography,* 28 (3)**,** 440-452**,** DOI: 10.1002/Palo.20039.

ZEEBE, R. E. & WOLF-GLADROW, D. A. 2001. *CO_2 in seawater : equilibrium, kinetics, isotopes,* Amsterdam ; New York, Elsevier.

ZEEBE, R. E. & ZACHOS, J. C. 2013. Long-term legacy of massive carbon input to the Earth system: Anthropocene versus Eocene. *Philosophical Transactions of the Royal Society a-Mathematical Physical and Engineering Sciences,* 371 20120006**,** DOI: 10.1098/Rsta.2012.0006.

ZICKFELD, K., EBY, M. & WEAVER, A. J. 2008. Carbon-cycle feedbacks of changes in the Atlantic meridional overturning circulation under future atmospheric CO2. *Global Biogeochemical Cycles,* 22 (3), Gb3024**,** DOI: 10.1029/2007gb003118.

ZICKFELD, K., EBY, M., WEAVER, A. J., ALEXANDER, K., CRESPIN, E., EDWARDS, N. R., ELISEEV, A. V., FEULNER, G., FICHEFET, T., FOREST, C. E., FRIEDLINGSTEIN, P., GOOSSE, H., HOLDEN, P. B., JOOS, F., KAWAMIYA, M., KICKLIGHTER, D., KIENERT, H., MATSUMOTO, K., MOKHOV, I. I., MONIER, E., OLSEN, S. M., PEDERSEN, J. O. P., PERRETTE, M., PHILIPPON-BERTHIER, G., RIDGWELL, A., SCHLOSSER, A., VON DEIMLING, T. S., SHAFFER, G., SOKOLOV, A., SPAHNI, R., STEINACHER, M., TACHIIRI, K., TOKOS, K. S., YOSHIMORI, M., ZENG, N. & ZHAO, F. 2013. Long-Term Climate Change Commitment and Reversibility: An EMIC Intercomparison. *Journal of Climate,* 26 (16)**,** 5782-5809**,** DOI: 10.1175/Jcli-D-12-00584.1.

ZIMOV, S. A., SCHUUR, E. A. G. & CHAPIN, F. S. 2006. Permafrost and the global carbon budget. *Science,* 312 (5780)**,** 1612-1613**,** DOI: 10.1126/science.1128908.